

# **Design, Synthesis, and Host-Guest Properties of Neutral Pd(II) Coordination Cages Supported by Imido-P(V) Anions**

**A Thesis**

**Submitted in Partial Fulfillment of the Requirements**

**for the Degree of**

**Doctor of Philosophy**

**by**

**Meghamala Sarkar**

**ID: 20152023**



**Department of Chemistry  
Indian Institute of Science Education and Research, Pune  
March 2023**

**This Dissertation Is Lovingly Dedicated to My  
Parents, Who Always Encouraged Me to Go on Every  
Adventure, Especially This One...**



भारतीय विज्ञान शिक्षा एवं अनुसंधान संस्थान, पुणे

INDIAN INSTITUTE OF SCIENCE EDUCATION AND RESEARCH (IISER), PUNE

(An Autonomous Institution, Ministry of Human Resource Development, Govt. of India)

Dr. Homi Bhabha Road, Pune 411008.

**Prof. R. Boomi Shankar**

Professor

Department of Chemistry,

IISER Pune

## CERTIFICATE

Certified that the work incorporated in the thesis entitled “***Design, Synthesis, and Host-Guest Properties of Neutral Pd(II) Coordination Cages Supported by Imido-P(V) Anions***” submitted by **Ms. Meghamala Sarkar** was carried out by the candidate, under my supervision. The work presented here or any part of it has not been included in any other thesis submitted previously for the award of any degree or diploma from any other university or institution.

**Date:** 06<sup>th</sup> March 2023

**Place:** Pune

**Prof. R. Boomi Shankar**

**(Research Supervisor)**



## DECLARATION

I declare that this written submission represents my ideas in my own words and where other's ideas have been included; I have adequately cited and referenced the original sources. I also declare that I have adhered to all principles of academic honesty and integrity and have not misrepresented or fabricated or falsified any idea/data/fact/ source in my submission. I understand that violation of the above will be cause for disciplinary action by the Institute and can also evoke penal action from the sources which have thus not been properly cited or from whom proper permission has not been taken when needed.

*Meghamala Sarkar*

**Date:** 06<sup>th</sup> March 2023

**Place:** Pune

**Ms. Meghamala Sarkar**

**ID: 20152023**

## Acknowledgements

*The pages of this thesis represent not only my work within the C-216 lab or at the keyboard, rather, it has also been a personal milestone in more than one way. And while they say pursuing a Ph.D. is often a lonely path, it is never possible to traverse the same without the guidance and support of some indispensable people in life. I sincerely thank every single person who has motivated, encouraged, and lead me to this very moment.*

*My most profound appreciation goes to my Ph.D. supervisor, Prof. R. Boomishankar for his unprecedented support, continuous guidance, and feedback throughout this journey. He has been supportive since the days I began working in this lab as an MS thesis student. While giving me considerable freedom in my research direction, he always made sure that I receive all the necessary resources and exposure needed to pursue my research. I am highly thankful to him for his constant encouragement and leadership which made this long but exciting journey possible. It was a great and inspiring learning experience working under his mentorship.*

*I further express my gratitude to my thesis advisory committee members Prof. V. G. Anand and Dr. Shabana Khan for their encouragement, insightful comments, and thought-provoking questions during the RAC meetings that helped me improve my work. I am grateful to all the faculties of the Chemistry department, IISER Pune for their teachings, mentorship, and support throughout my Masters and for guiding me towards the very first step to pursuing research. I extend my gratitude to Prof. Nirmalya Ballav, Chair Chemistry, and all former Chairs of the Chemistry Department. I acknowledge the Indian Institute of Science Education and Research (IISER), Pune, and its former director Prof. K. N. Ganesh, and present director Prof. J. B. Udgaonkar, and the administration for providing an excellent research environment and a wonderful hostel life.*

*I am most grateful to our collaborator Prof. Evamarie Hey-Hawkins, University of Leipzig for offering me research opportunities in her lab and for her invaluable input while working on diverse exciting projects. Even though for a semester, there is no way to express how much it meant to me to have been a member of her lab.*

*I want to thank IISER Pune and the Department of Chemistry for the experimental and computational facilities that have been made available for research and thanks to all the technicians and staff who keep the facilities operational. I thank Mr. Mayuresh Kulkarni, Ms. Sneha Chordiya, Mr. Prabhakar Anagare, Mr. Tushar Kurulkar, Mr. Mahesh Jadhav, Mr.*

*Yathish, Mr. Sudhir, Mr. Ravinder Malothu, Mrs. Megha Paygude, Mr. Parveen Nasa, Mr. Suresh Prajapat, Mr. Dnyaneshwar, Mr. Ganesh Dimber, Mr. Sandip Kanade, Mr. Sanjay Meena, Mr. Prabhas and others for technical and administrative support. Thanks to CDAC and IISER Pune for access to PARAM Brahma. Also, thanks to the Department of Chemistry, IISER Pune, for the Integrated Ph.D. fellowship and Erasmus+ for the student exchange opportunities.*

*This work would not have been possible without the constant help and support provided by all my lab mates, past and present. I am very grateful to an amazing bunch of seniors from my lab: Dr. Anant, Dr. Ashok, Dr. Mahesh, Dr. Sachin, Dr. Vijaykanth, Dr. Rajasekar, and Dr. Rishabh and my colleagues: Dr. Swati, who has not only been my labmate but also my I-PhD batchmate and a supportive friend; Neetu, Supriya, Rishu, Cavya, Nilotpai, Vikash and Dr. Ranita. A hearty thanks to all the past members who have been with us briefly yet made the research days much brighter- Hrithik, Anupriya, Rani, Sravan, and Kiran. I am also thankful to my other seniors at IISER Pune, Dr. Santosh Panchal, Dr. Madan, Dr. Reshmi, Dr. Manikandan, Dr. Konoya, Dr. Debanjan, and Dr. Prabhat for guiding me in my lab rotation days and helping me out whenever needed.*

*I was fortunate to have met some amazing people during my time with the Hey-Hawkins research group in Germany— especially Saral for helping me out in and out of the lab. I further extend my appreciation to Reike, Axel, Benedict, and Philip for the research inputs, Anastasia, Liridona, Rafaella, Angela, and Ming-Hui for those fun lunch hours and coffee breaks! Some friendships are formed accidentally and yet they stay with you the longest. A big thanks to Rupali (Arora) for taking me around for those trips around the city and guiding me like a big sister throughout my stay abroad.*

*I am highly indebted to the amazing teachers who have helped in and outside of the classroom throughout my shaping years. I would like to thank Dr. Jayashree Laha and Dr. Tridib Tripathy, Midnapore College for constantly motivating me and pushing me towards my goal, till date. I would also like to especially thank Ruma Ma'am, Chail Ma'am, and Devika Ma'am from AGCS, Purulia for guiding and assisting this shy kid throughout her school years!*

*This Ph.D. journey of mine would not have been possible without the constant love and support of the awesome I-PhD batch of 2015. From assignment-solving days to now nearing graduation, this seven-year-long journey has never been tiresome because of their presence.*

*These brilliant friends have endlessly motivated and inspired me over the years: Rayan, Farhan, Avisikta, Swati, Mishika, Rinku, Saptashwa, Unmesh, Abhijit, and Soumodip.*

*A hearty thanks to these amazing people: Rupali (Sathe), Moushila who are more sisters to me than friends, and Debesh- who are always there to pat my back, through all the tough times, successes, and failures. I would also like to thank Neha, Shruti, Moushakhi, and Srijita for the fond memories at the hostel and for being such wonderful companions. Also, thanks to the creators of Spotify, The Big Bang Theory, EXO, and Harry Potter.*

*Last but not least, I am immensely grateful to my parents, who have always walked side-by-side with me and tried their best to enable their daughter in every way possible, and without whom, this journey would not have been possible.*

*And thanks to the almighty for this life full of immense opportunities.*

\*\*\*\*\*

# Contents

Contents	i
Synopsis	iv
Abbreviations	ix
Rights and Permissions	xi
List of Publications	xii
<b>Chapter 1: Introduction</b>	<b>1-36</b>
1.1. Self-assembly	2
1.1.1. Metallo-supramolecular Chemistry	2
1.1.2. Bonding Approaches in Self-assembled Metal-Organic Cages (MOCs)	4
1.2. Host-guest Chemistry	11
1.3. Neutral Metal-Organic Cages (MOCs)	13
1.3.1. Imido-P(V) Anions as Building Blocks to Neutral MOCs	14
1.3.2. Imido-Pd <sub>3</sub> Clusters as Building Blocks for Neutral Polyhedral Cages	22
1.3.3. Host-Guest Studies of the Neutral Tetrahedral Cage	23
1.3.4. Post-assembly Reactions on Pd(II) Neutral Cages	26
1.3.5. Chiral Cages Derived from the Deprotonation of Imido-Pd <sub>3</sub> Clusters	27
1.4. Summary and Outlook	30
1.5. Outline and Objective of Thesis	31
1.6. References	31
<b>Chapter 2: Mapping the Assembly of Neutral Tetrahedral Cages Tethered by Oximido Linkers and Their Guest Encapsulation Studies</b>	<b>37-59</b>
2.1. Introduction	38
2.2. Experimental Details	39
2.2.1. General Remarks	39
2.2.2. Syntheses	40
2.2.3. Crystallography	41
2.2.4. <sup>1</sup> H-2D-DOSY NMR Studies	43
2.2.5. Guest Encapsulation Studies	44
2.2.6. Theoretical Calculations	44
2.3. Results and Discussions	45
2.4. Conclusion	55



# Contents

2.5. References	56
<b>Chapter 3: Mapping the Assembly of Neutral Tetrahedral Cages Tethered by Oximido Linkers and Their Guest Encapsulation Studies</b>	<b>60-80</b>
3.1. Introduction	61
3.2. Experimental Details	63
3.2.1. General Remarks	63
3.2.2. Procedure for In-situ Preparation of Guest $\subset$ Host Complexes	63
3.2.3. Syntheses	64
3.2.4. $^1\text{H}$ -2D-DOSY NMR Studies	64
3.2.5. Theoretical Calculations	65
3.2.6. Crystallography	65
3.3. Results and Discussions	67
3.4. Conclusion	77
3.5. References	78
<b>Chapter 4: Ligand-Guided Synthesis of Ligand-Free Metallocube Built on Imido-Pd(II) Clusters</b>	<b>81-102</b>
4.1. Introduction	82
4.2. Experimental Details	83
4.2.1. General Remarks	82
4.2.2. Syntheses	84
4.2.3. Crystallography	84
4.2.4. $^1\text{H}$ -2D-DOSY NMR Studies	86
4.2.5. Guest Encapsulation Studies	86
4.2.6. Theoretical Calculations	87
4.3. Results and Discussions	87
4.4. Conclusion	100
4.5. References	100
<b>Chapter 5: Selective Self-Sorting Of Tetrahedral And Cubic Pd(II) Neutral Cages With Chiral and Achiral Building Blocks</b>	<b>103-126</b>
5.1. Introduction	104

# Contents

---

<b>5.2.</b> Experimental Details	106
<b>5.2.1.</b> General Remarks	106
<b>5.2.2.</b> Syntheses	106
<b>5.2.3.</b> Crystallography	107
<b>5.2.4.</b> <sup>1</sup> H-2D-DOSY NMR Studies	109
<b>5.2.5.</b> General Procedure for the Chiral Recognition Studies	109
<b>5.2.6.</b> Theoretical Calculations	110
<b>5.3.</b> Results and Discussions	110
<b>5.4.</b> Conclusion	124
<b>5.5.</b> References	125
<b>Chapter 6: Thesis Conclusion and Future Perspectives</b>	<b>127-130</b>
<b>Appendix</b>	<b>131-251</b>
<b>A2.</b> Appendix for Chapter 2	132
<b>A3.</b> Appendix for Chapter 3	155
<b>A4.</b> Appendix for Chapter 4	210
<b>A5.</b> Appendix for Chapter 5	230

\*\*\*\*\*

# Synopsis

*The primary focus of this thesis entitled as “Design, Synthesis, and Host-Guest Properties of Neutral Pd(II) Coordination Cages Supported by Imido-P(V) Anions” is the synthesis of metal-organic cages derived from imido P(V) ligands dictated by various design principles and the studies of their respective host-guest studies and chiral recognition applications.*

## Chapter 1: Introduction

This chapter provides a brief introduction to the concept of self-assembly with respect to the construction of metal-organic cages. It is then followed by a short description of the various bonding techniques reported in literature in order to synthesize these metal-organic cages. A general concept of host-guest chemistry as a pronounced application of supramolecular cages has been introduced with special reference to neutral metal-organic cage systems. Thereafter, a brief description of the deprotonation chemistry of imido-P(V) anions as building blocks to neutral metal-organic cages (MOCs) has been described. The chemistry of the imido-anions of the main group elements has been studied for more than three decades. However, these imido anions are typically generated using strong main group organometallic reagents which has limited their coordination chemistry to reactions in anhydrous aprotic solvents for a few main group metal ions. The efforts made in our group in generating imido P(V) complexes of Pd<sup>+2</sup> ions and further using them as polyhedral building units to synthesize neutral MOCs in a protic and polar medium have been discussed in brief. Finally, a brief outline on the working chapters pertaining to design and synthetic techniques of Pd(II) neutral cages has been given along with their potential applications in host-guest chemistry.

## Chapter 2: Mapping the Assembly of Neutral Tetrahedral Cages Tethered by Oximido Linkers and their Guest Encapsulation Studies

A primary criterion for the design of polyhedral metal-organic cages is the requirement of geometrically matched pairs of metal ions and ligand moieties. However, understanding the pathway it takes to reach the final polyhedral structure can provide more insights into the self-assembly process and improved design strategies. In this regard, we report two neutral tetrahedral cages of formula  $[\{\text{Pd}_3(\text{N}^i\text{Pr})_3\text{PO}\}_4(\text{L}^1)_6]$  (**2.1-TD**) and  $[\{\text{Pd}_3(\text{N}^i\text{Pr})_3\text{PO}\}_4(\text{L}^2)_6]$  (**2.2-TD**) starting from the acetate-bridged cluster  $[\{\text{Pd}_3(\text{N}^i\text{Pr})_3\text{PO}\}_2(\text{OAc})_2(\text{OH})]_2 \cdot 2(\text{CH}_3)_2\text{SO}$  (**HEXA-Pd**) and the respective oxamide precursors  $[\text{L}^1\text{H}_2: \{\text{C}_2(\text{NH}_2)_2\text{O}_2\}]$  and  $[\text{L}^2\text{H}_2:$

# Synopsis

{C<sub>2</sub>(NHMe)<sub>2</sub>O<sub>2</sub>}. By making subtle variations in the reaction conditions two new tetrameric Pd<sub>12</sub>-assemblies,  $[\{\text{Pd}_3(\text{N}^i\text{Pr})_3\text{PO}\}_4(\text{L}^1)_2(\text{OAc})_4(\text{OMe})_4]$  (**2.1-TM**) and  $[\{\text{Pd}_3(\text{N}^i\text{Pr})_3\text{PO}\}_4(\text{L}^2)_2(\text{OAc})_4(\text{OMe})_4]$  (**2.2-TM**), were obtained from the same precursors. Detailed investigations using NMR, mass spectrometry, X-ray crystallography, and computational studies indicate that the macrocyclic complexes **2.1-TM** and **2.2-TM** are the reaction intermediates involved in the formation of the tetrahedral cages **2.1-TD** and **2.2-TD**, respectively. Moreover, the tetrahedral cages **2.1-TD** and **2.2-TD** were found to exhibit an intrinsic cavity of volume  $\sim 85 \text{ \AA}^3$ . Guest encapsulation studies revealed that the cage **2.1-TD** can encapsulate a wide range of guest molecules such as CHCl<sub>2</sub>, CHCl<sub>3</sub>, CCl<sub>4</sub>, C<sub>6</sub>H<sub>6</sub>, and C<sub>6</sub>H<sub>5</sub>F. Interestingly, **2.1-TD** was shown to exhibit a preferential binding of C<sub>6</sub>H<sub>5</sub>F and C<sub>6</sub>H<sub>6</sub> over other halogenated guest molecules as determined from NMR titrations and computational studies (Figure 1).

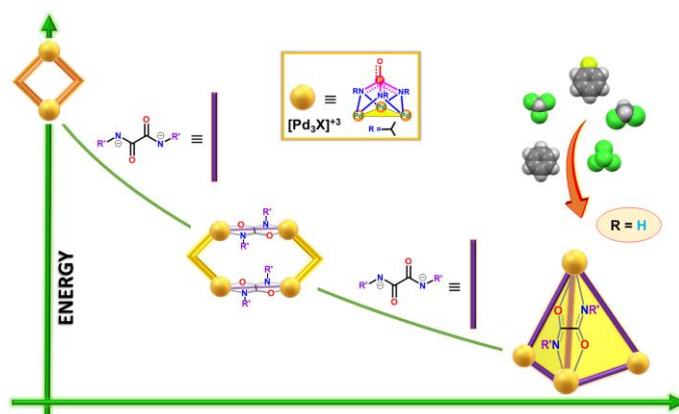


**Figure 1.** Two neutral tetrahedral cages built from trinuclear Pd(II) clusters *cis*-blocked by tris(imido)phosphate trianions and oxamido linkers were synthesized and shown to form via the corresponding tetranuclear macrocyclic intermediates. One of the tetrahedral cages shows interesting guest encapsulation properties at its interior void.

## Chapter 3: Encapsulation Studies on *closo*-Dicarbadodecaborane Isomers in Neutral Tetrahedral Palladium(II) Cages

The encapsulation of icosahedral *closo*-dicarbadodecaborane (*o*-, *m*-, and *p*-carboranes, **Cb**) as guest molecules at the intrinsic cavities of the three isostructural tetrahedral cages  $[\{\text{Pd}_3(\text{N}^i\text{Pr})_3\text{PO}\}_4(\text{Cl-AN})_6]$  (**3.1**),  $[\{\text{Pd}_3(\text{N}^i\text{Pr})_3\text{PO}\}_4(\text{Br-AN})_6]$  (**3.2**) and  $[\{\text{Pd}_3(\text{N}^i\text{Pr})_3\text{PO}\}_4(\text{H-AN})_6]$  (**3.3**) was studied. The formation of definite host–guest assemblies was probed with mass-spectrometric, IR and NMR spectral analysis. The <sup>1</sup>H-2D-DOSY NMR of the **Cb** ⊂ **Cage**

## Synopsis

systems showed similar diffusion coefficient ( $D$ ) values for the host and guest species signifying the encapsulation of these guests inside the cage assemblies. The hydrodynamic radius ( $R_H$ ) derived from the  $D$  values of the host and guest species further confirmed the encapsulation of the **Cb** isomers at the cage pockets. The single molecule energy optimization of the host–guest assemblies indicated the preferential binding of *o*-**Cb** as a guest inside the cages (**3.1**, **3.2**, and **3.3**). The stabilization of these **Cb** guests inside these cages was further attributed to various possible non-classical C-H $\cdots$ X type interactions (Figure 2).

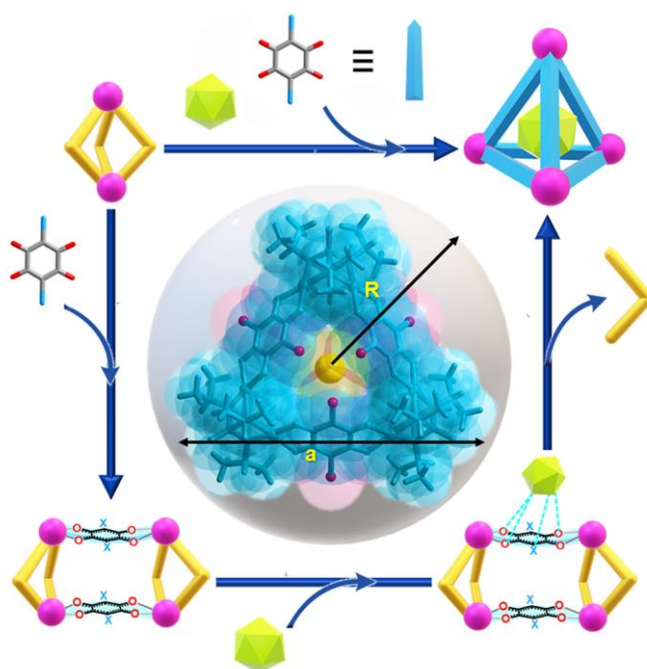


**Figure 2.** A neutral tetrahedral palladium(II) cage encapsulates the three regioisomers of *closo*-dicarbadodecaborane, popularly known as carboranes, in an in-situ pathway. The carborane guests were found to exhibit a high affinity for the host cage molecule in comparison with a tetrameric intermediate via spectral and theoretical studies.

### Chapter 4: Ligand-guided Synthesis of Ligand-Free Metallocube built on Imido-Pd(II) Clusters

The synthesis and guest recognition properties of a neutral 24-atom Pd(II)-cubic cage, **4.1** is reported. The formation of the cubical assembly takes place via an exclusive one-pot template pathway directed by oxamide ligand. The assembly of the linker-free metallocube is initiated by the directing nature of the linear oximido linker which pre-organises the polyhedral building units, resulting in the intermediate **2.1-TM** (vide supra). This intermediate which

## Synopsis

subsequently undergoes dimerization to yield the robust chloride-linked cube. In the absence of a directing linker, no cage formation was observed, and the Pd<sub>6</sub>-precursor was found to undergo self-condensation giving rise to a new pentameric polyhedral building unit. The central cavity of the cube has been probed for guest encapsulation studies which shows a high binding with phenolic guest molecules with an association constant of  $5.0 \times 10^4 \text{ M}^{-1}$ . The favorable formation of host-guest complexes was attributed to the strong hydrogen bonding interactions between the host and guest functional groups (Figure 3).

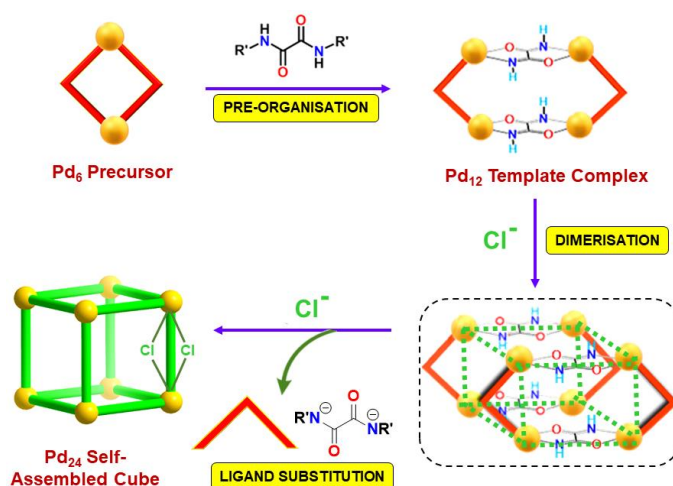


**Figure 3.** A neutral linker free Pd<sub>24</sub>-metallocube forms via a template mediated pathway guided by a dianionic linker.

### Chapter 5: Selective Self-Sorting of Tetrahedral and Cubic Pd(II) Neutral Cages with Chiral and Achiral Building Blocks

The chiral-achiral self-sorting behavior in Pd(II) neutral cages was investigated with equimolar mixtures of chiral and achiral precursors leading to the formation of new assemblies. Variations in linker length, reactivity, and functionalities dictated the geometry and outcome of the major product- either through social (**5.1**) or narcissistic (**5.3**) self-sorting or a mixture of products (**5.2**). The properties and mechanistic pathways leading to the formation of isolated enantiopure and sorted cage compounds were investigated by NMR, mass spectra, and single-crystal X-ray diffraction studies. Further, enantioselective guest recognitions for hydrobenzoin (**HB**), 1-phenyl-1-propanol (**P1P**), and 2-methyl-morpholine (**MP**) were performed with the socially-sorted tetrahedral cage **5.1-R** built with oxalate linker. The highest guest recognition

# Synopsis

of 16.8 was observed with (S)-1-phenyl-1-propanol (**S-P1P**) guest with a binding constant of  $7.2 \times 10^5 \text{ M}^{-1}$  (Figure 4).

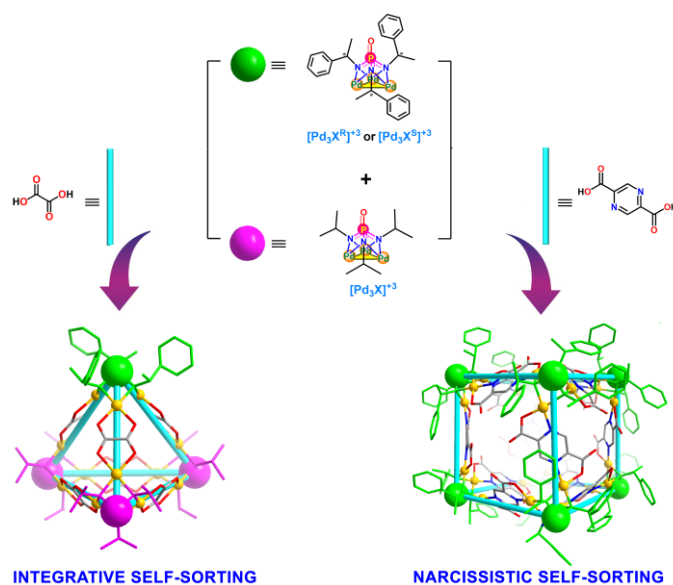


**Figure 4.** Schematic representation depicting the self-sorting behaviour in Pd(II) neutral cage systems.

\*\*\*\*\*

## *Abbreviations*

---

<b>Anal.</b>	Analysis
<b>Calcd.</b>	Calculated
<b>CCDC</b>	Cambridge Crystallographic Data Centre
<b>DFT</b>	Density Functional Theory
<b>DMSO</b>	Dimethyl Sulphoxide
<b>DCM</b>	Dichloromethane
<b>MeOH</b>	Methanol
<b>Ph</b>	Phenyl
<b>ESI</b>	Electron Spray Ionisation
<b>FT-IR</b>	Fourier Transform Infrared Spectroscopy
<b>MALDI-TOF</b>	Matrix Assisted Laser Desorption Ionization-Time Of Flight
<b>MS</b>	Mass Spectrometry
<b>NMR</b>	Nuclear Magnetic Resonance
<b>RT</b>	Room Temperature
<b>SCXRD</b>	Single Crystal X-Ray Diffraction
<b>TGA</b>	Thermogravimetric Analysis
<b>DOSY</b>	Diffusion Ordered Spectroscopy
<b>NOESY</b>	Nuclear Overhauser Effect Spectroscopy
<b>ROESY</b>	Rotating-frame nuclear Overhauser Effect Spectroscopy
<b>mg</b>	Milligram
<b>mmol</b>	Millimole
<b>mm</b>	Millimetre
<b>ml</b>	Millilitre
<b>µl</b>	Microlitre



## *Abbreviations*

---

**ppm**          Parts Per Million

**min**          Minute

**hr**            Hour

**Å**             Angstrom

**°**              Degree

\*\*\*\*\*

# *Rights and Permissions*

---

## Chapter 1

Reprinted (adapted) with permission from “*Chem. Rec.* **2022**, 22, e20210028”.

Copyright © 2021 The Chemical Society of Japan & Wiley-VCH GmbH.

## Chapter 2

Reprinted (adapted) with permission from “*Inorg. Chem.* **2023**, 62, 1855–1863”.

Copyright © 2022 American Chemical Society.

## Chapter 3

Reprinted (adapted) with permission from “*Inorg. Chem.* **2023**, 62, 4035–4042”.

Copyright © 2023 American Chemical Society.

And

Reprinted (adapted) with permission from “*Chem. - Eur. J.* **2020**, 26, 4209– 4213”.

Copyright © 2020 Wiley-VCH Verlag GmbH & Co. KGaA, Weinheim.

\*\*\*\*\*

# List of Publications

## ❖ Contributions Included in the Thesis

1. Polyanionic Imido-P(V) Ligands: From Transition Metal Complexes to Coordination Driven Self-Assemblies  
[M. Sarkar](#), P. Rajasekar, C. Jose, R. Boomishankar\*  
*Chem. Rec.* **2022**, 22, e202100281.
2. Mapping the Assembly of Neutral Tetrahedral Cages Tethered by Oximido Linkers and Their Guest Encapsulation Studies  
[M. Sarkar](#), R. Boomishankar\*  
*Inorg. Chem.* **2023**, 62, 1855-1863.
3. Encapsulation Studies on *closo*-Dicarbadodecaborane Isomers in Neutral Tetrahedral Palladium(II) Cages  
[M. Sarkar](#), E. Hey-Hawkins, R. Boomishankar\*  
*Inorg. Chem.* **2023**, 62, 4035–4042.
4. Ligand-Guided Synthesis of Ligand-Free Metallocube Built on Imido-Pd(II) Clusters  
[M. Sarkar](#), V. Kushwaha, R. Boomishankar\*  
(Manuscript Submitted)
5. Selective Self-Sorting Of Tetrahedral And Cubic Pd(II) Neutral Cages With Chiral And Achiral Building Blocks  
[M. Sarkar](#), V. Kushwaha, P. Rajasekar, C. Jose, R. Boomishankar\*  
(Manuscript Under Preparation)

## ❖ Contributions Not Included in the Thesis

1. Anilate Tethered Neutral Tetrahedral Pd(II) Cages Exhibiting Selective Encapsulation of Xylenes and Mesitylene  
A. Yadav<sup>†</sup>, [M. Sarkar<sup>†</sup>](#), S. Subrahmanyam, A. Chaudhary, E. Hey-Hawkins, R. Boomishankar\*  
*Chem. Eur. J.* **2020**, 26, 4209-4213.
2. Effective Enantioselective Recognition by Chiral Amino-Phosponium Salts  
P. Rajasekar, C. Jose, [M. Sarkar](#), R. Boomishankar\*  
*Angew. Chem. Int. Ed.* **2021**, 60, 4023-4027.

\*\*\*\*\*

# Chapter 1



## Introduction

## 1.1. Introduction

“Supramolecular chemistry” often called “chemistry beyond the molecule”<sup>1</sup> is an interdisciplinary field that explores the assembly of complex molecules through non-covalent interactions and has attracted a lot of attention over the past few decades due to its potential for creating new materials and designing functional devices. Self-assembly is a fundamental concept in supramolecular chemistry that involves the spontaneous formation of a class of well-defined organized entities that result from the association of two or more chemical species held together by intermolecular forces.<sup>2-4</sup> Composed of an amalgamation of several molecules, supramolecular chemistry mainly encompasses the discipline covering the chemistry of high-order molecular structures assembled from simpler building units. While traditional chemistry focuses on the covalent bond, supramolecular chemistry features comparatively weaker and reversible noncovalent interactions between molecules. These interactions account for the existence of a varied class of supra-molecules encompassing a wide range of significant interactions such as hydrogen or anion bonding, dipole–dipole and ion–dipole interactions, van der Waals interactions,  $\pi$ – $\pi$  interactions, electrostatic interactions and coordination bonds between a metal and donor atom.<sup>5</sup> Among these, coordination-driven self-assembly has seen tremendous growth over the last few decades spanning across many subdisciplines of chemistry, leading to the design and synthesis of new and complex architectures and investigating their practical applications.<sup>6-9</sup>

### 1.1.1. Self-assembly of metallo-supramolecular complexes

One of the most interesting and promising areas of supramolecular chemistry is perhaps the development of supramolecular metal organic cages (SMOCs). These cages are three-dimensional structures that are assembled from metal ions and organic ligands through coordination bonds. SMOCs have a wide range of applications, including catalysis, separation, sensing, and drug delivery. The concept of using metal ions and organic ligands to construct three-dimensional structures dates back to the early 20th century. The pioneering work demonstrated by Makoto Fujita laid the foundation of such metal ion based self-assembled architecture in the early 1990s through the formation of the original ‘Fujita square’ (**1.1**) where four palladium(II) metal ions *cis*-capped by ethylene diamine are bridged by *cis*-coordinating 4,4-bipyridine ligands, giving rise to a square macrocycle (Figure 1.1).<sup>10</sup> The Fujita square is a remarkable example of self-assembly in supramolecular chemistry. In addition to being the first demonstration of a self-assembled square made of organic ligands in combination with

transition metal ions and their directional nature, the square metallacycle **1.1** also marked the beginning of utilizing an end-capped (non-naked) transition metal in molecular self-assembly.

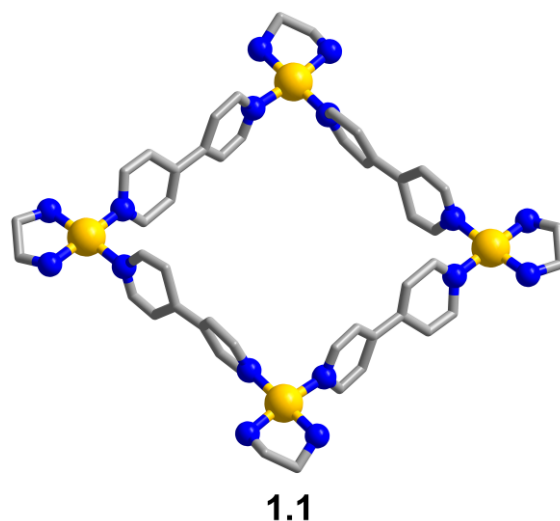


**Figure 1.1.** Crystal structure of the "Fujita square" assembled from *cis*-capped palladium(II) nitrate and 4,4'-bipyridine. Hydrogen atoms and counterions have been omitted for clarity.

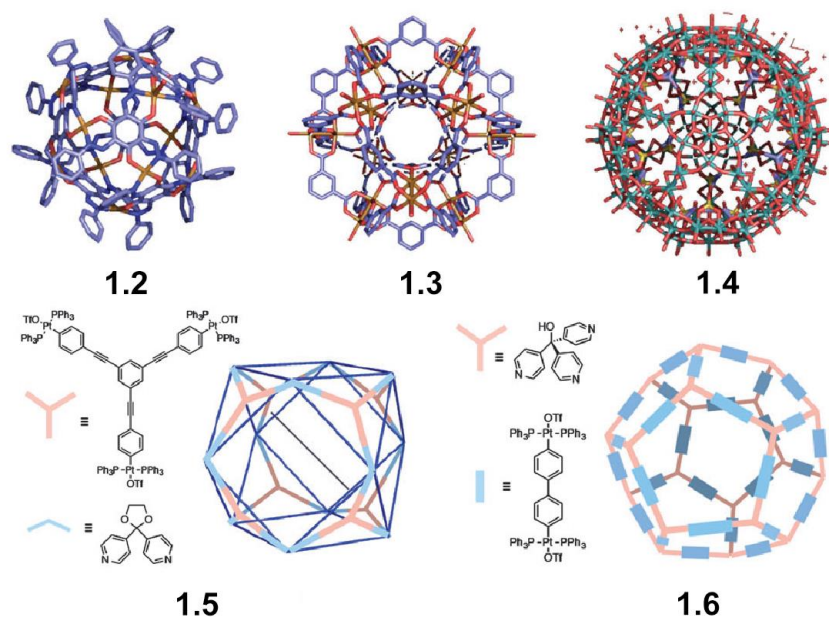


**Figure 1.2.** Some early examples of self-assembled spherical complexes. Reprinted with permission from K. Harris, D. Fujita, M. Fujita, *Chem. Commun.* **2013**, 49, 6703-6712.

Copyright © 2013, Royal Society of Chemistry.<sup>11</sup>

Since then, pioneering works by Fujita<sup>11,12</sup>, Stang<sup>13,14</sup>, Nitschke<sup>15, 16</sup> etc. have further strengthened the realm of metal-organic supramolecular assemblies (Figure 1.2), by developing novel coordination-based compounds with diverse shapes and geometries such as 2D metal-

organic macrocycles (MOMs) common examples of which include triangles<sup>17</sup>, squares<sup>18</sup>, rhomboids<sup>19</sup>, and 3D metal-organic cages (MOCs) such as tetrahedron<sup>20</sup>, cube<sup>21</sup>, octahedron<sup>22</sup>, cuboctahedron<sup>23</sup>, prisms<sup>24,25</sup>, *etc.*

Among these, the MOCs have gained a lot of attention in the past few decades due to the wide variety of shapes, sizes and functionalities exhibited by them. The formation of such metallosupramolecular cages are defined by ligand geometry and the coordination preference and capabilities of the metal ion and the structure of the final product is often decided by both entropic and enthalpic components, as is the case with “Fujita square”. Achieving a proper balance of these components favors the formation of the possible multicyclic product without exerting undue strain on the resulting structure. Thus, in order to simplify and rationalize the formation of a myriad of metal-ligand cages, various strategies have emerged to chaperone the self-assembly process towards the formation of the stable and discrete thermodynamic product.<sup>26-37</sup> Metal–ligand bonding bypasses many of the difficulties that come with controlling the intermolecular interactions by the ‘directional control’ exerted by the well-defined coordination geometries of transition metal ions.

### 1.1.2. Bonding approaches in self-assembled metal-organic cages (MOCs)

#### 1.1.2.1. Directional Bonding

The directional bonding approach is a high-yielding and promising method for the synthesis of a wide variety of 2D macrocycles and 3D MOCs with tailored structures and properties. The rational synthetic strategy of the directional bonding approach gives rise to a combinatorial molecular library consisting of complementary building blocks. In essence, the directional approach is a retrosynthetic way of rationalizing the metal-ligand interactions in order to achieve stable and highly ordered structures.

In the directional bonding method, the key to synthesizing self-assembled architectures lies in the pre-defined geometry and stoichiometry of the donor and acceptors. The donors are usually the organic ligands or linkers that possess two or more binding sites with their angular orientations varying from 0 to 180° while the acceptor sites are the metal ions or metal-containing subunits with available coordination sites (Figure 1.3).

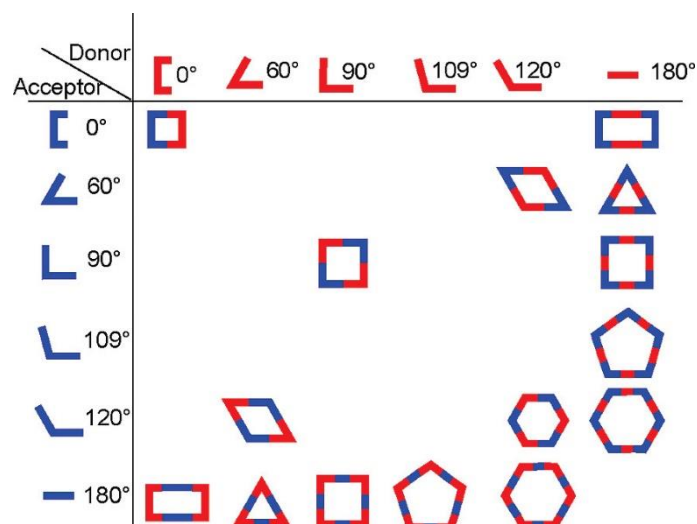


**Figure 1.3.** Combination of various building units for accessing two-dimensional self-assembled architectures. Reprinted with permission from R. Chakrabarty, P. S. Mukherjee, P. J. Stang, *Chem. Rev.* **2011**, *111*, 6810-6918. Copyright © 2011, American Chemical Society.<sup>26</sup>

The fate of the final geometry of the product is decided on the geometry and number of binding sites in the participating moieties. Depending upon whether a 2-fold or greater than 2-fold symmetry axis is present, the resultant structures are either monocyclic or polycyclic assemblies. For example, a molecular rectangle can be obtained by the equimolar combination of two  $0^\circ$  acceptor units with two  $180^\circ$  donor units and vice versa while the synthesis of a molecular triangle requires the combination of three  $60^\circ$  donor units with three  $180^\circ$  acceptors.

On the other hand, the synthesis of three-dimensional architectures requires more complex synthon units and their appropriate combinations. Thus, the two-dimensional acceptors now require angular donor subunits (and vice versa) with more than two binding sites in order to obtain three-dimensional architectures. As shown in Figure 1.4, the simplest platonic solid tetrahedron can be designed by employing four linear  $180^\circ$  ditopic subunits, in combination with six tritopic subunits having an angular disposition of  $60^\circ$ . Similarly, a cube can be synthesized from the combination of twelve  $180^\circ$  ditopic and eight  $90^\circ$  tritopic subunits. Some of these assemblies can also be synthesized by more than one combination of donor-acceptor coordination. For example, a trigonal pyramid can be synthesized simply by a combination of three ditopic subunits at an angular disposition of  $109^\circ$  with two tridentate  $60^\circ$  angular subunits; or it can also be obtained via the coordination between three  $80\text{--}90^\circ$  ditopic units chelated to two orthogonal  $90^\circ$  tritopic subunits.



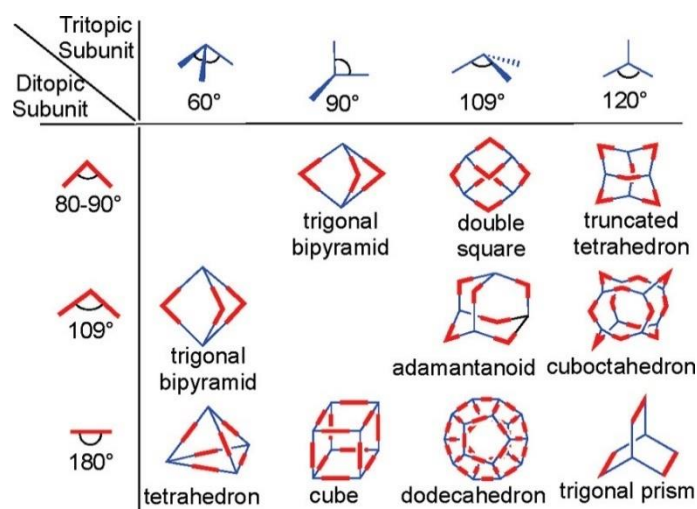


**Figure 1.4.** Combination of various building units for accessing three-dimensional self-assembled polyhedra. Reprinted with permission from R. Chakrabarty, P. S. Mukherjee, P. J. Stang, *Chem. Rev.* **2011**, *111*, 6810-6918. Copyright © 2011, American Chemical Society.<sup>26</sup>

Since transitional metal ions are capable of displaying multiple valencies, and therefore can adapt to a variety of geometries, one specific criterion required for the directional bonding approach is the *cis*-capping of the metal-containing subunits, failure to which leads to the loss in directionality and exclusivity of the predicted architecture.

A classic example of such directionality-dependent architecture can be observed in the work demonstrated by Fujita et. al<sup>38</sup> wherein the change in a single parameter i.e. bite angle in the ligand has controlled the outcome of the self-assembled products. With a single type of metal ion ( $\text{Pd}^{2+}$ ) having a preference towards square-planar coordination, with only the change in ligand curvature can result in self-assembled polyhedrons ranging from simpler octahedra and cubo-octahedra to more complex pseudo-spherical assemblies (Figure 1.5).

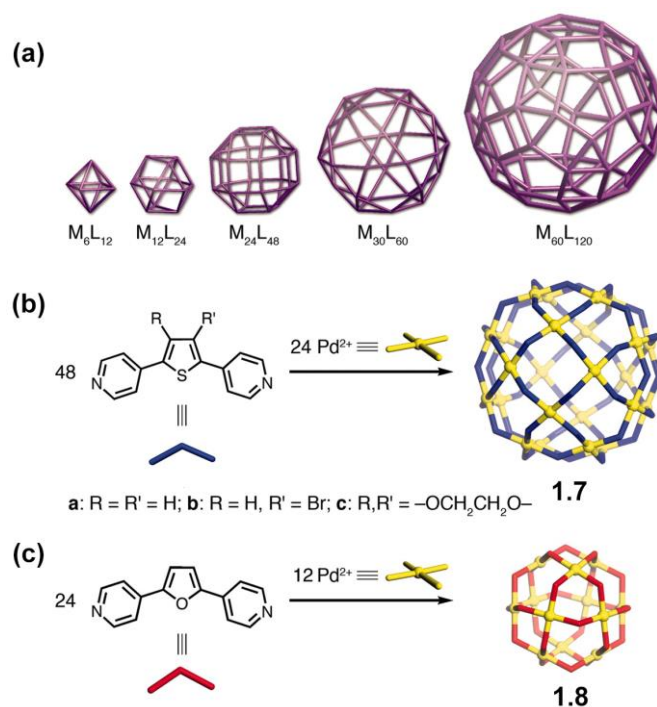


**Figure 1.5.** (a) combinatorial mapping of the family of  $M_nL_{2n}$  polyhedra where metals (denoted by M) and ligands (denoted by L) are located on the vertices and edges of the polyhedra, respectively. (b) Self-assembly of a  $M_{24}L_{48}$  sphere, **1.7** and (C) Self-assembly of a  $M_{12}L_{24}$  cubooctahedra, **1.8**. Reproduced (adapted) from ref. 38, with permission from AAAS.

### 1.1.2.2. Symmetry Interaction Approach

Based on the chelation ability of the organic ligand and the metal ion used, the symmetry interaction approach involves the formation of high-symmetry metallo-supramolecular clusters from a highly symmetric organic subunit chelated to a naked metal center using metal-ligand bonds. This strategy relies on the strong binding affinity and coordination mode of chelating ligands, and the inherent symmetry of the coordination sites available on the naked metal center, although the metal centres may possess ancillary ligands or coordinated solvent molecules. Developed by Raymond and co-workers<sup>29-31</sup>, this method exploits the geometric relationship between the ligand and the metal component using symmetry considerations. For example, to synthesize a  $M_4L_6$  type tetrahedron, the  $C_2$  axes of the tetrahedron should lie within the chelate plane at each of the four metal vertices while the chelate vectors within the ligand lie at an angle of  $70.6^\circ$  (Figure 1.6).

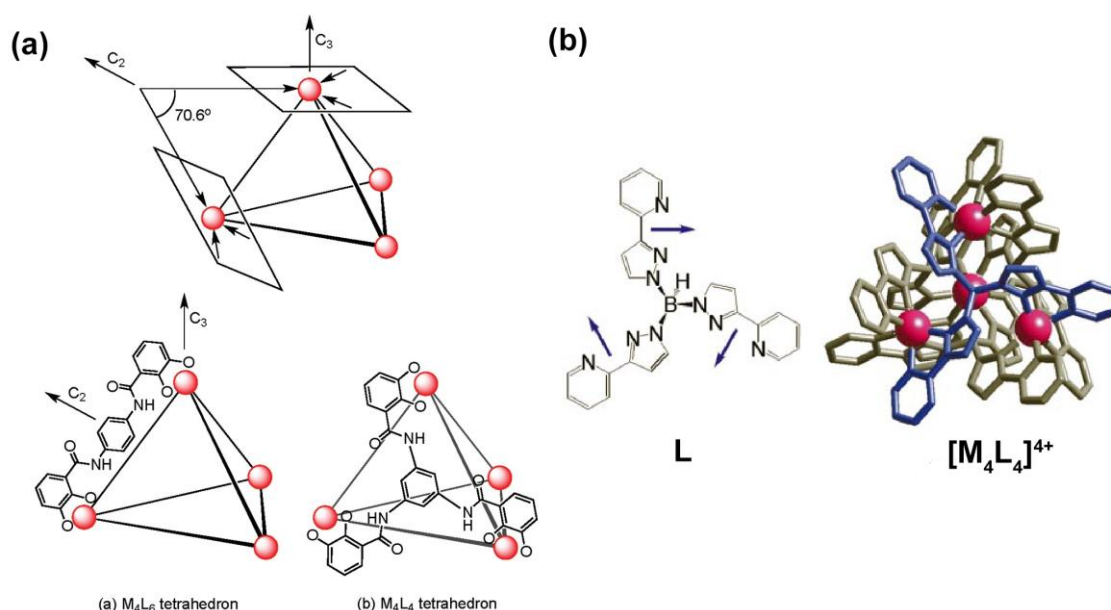


**Figure 1.6.** Schematic diagram of the oramation of the (a)  $M_4L_6$  and  $M_4L_4$  tetrahedra by employing the symmetry interaction design approach. (b) A  $M_4L_4$  type tetrahedron  $[Mn_4L_4]^{4+}$  synthesized via this approach as reported by McCleverty and coworkers. Reprinted with permission from R. Chakrabarty, P. S. Mukherjee, P. J. Stang, *Chem. Rev.* **2011**, *111*, 6810-6918. Copyright © 2011, American Chemical Society,<sup>26</sup> and D. L. Caulder, K. N. Raymond, *J. Chem. Soc., Dalton Trans.* **1999**, 1185-1200. Copyright © 1999, Royal Society of Chemistry.<sup>29</sup>

The various combinations of “naked” metal ions and the chelating ligands can lead to a wide variety of three-dimensional while the flexible nature of the ligands assists in the formation of flexible and more ‘breathable’ cages (that can alter their portal sizes and cavity sizes due to the flexible nature of linkers) capable of accommodating larger guest molecules within their cavity.

### 1.1.2.3. Panelling Approach

In order to create elegant architectures that can mimic the platonic solids, Fujita and co-workers have pioneered<sup>32-34</sup> the paneling method to synthesize metal-organic cages where the required geometries are obtained by the combination of a suitable number of tritopic organic ligands occupying the ‘face’ of the polyhedra with the metal-centers sitting at the respective vertices (Figure 1.7). Usually, *cis*-blocked Pd(II) or Pt(II) centres are used in coordination with organic ligands with a suitable geometry. However, unlike the symmetry interaction approach, the paneling approach do not employ naked metal centres in order to create supramolecular assemblies. Although this method produces rigid assemblies, the *cis*-capping of metals along

with their inherent directionality moulds the convergent geometry around the metal centres and ensures the formation of an exclusive assembly without any undesirable side-product or polymeric assemblies.

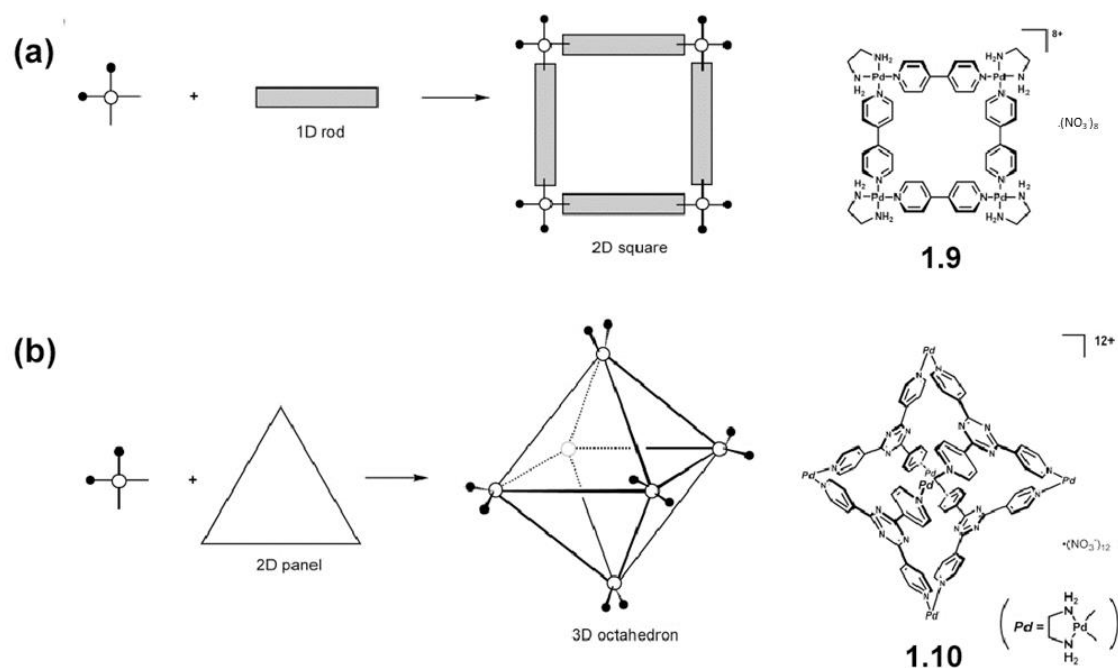


**Figure 1.7.** Schematic representation of molecular paneling approach: (a) from 1D-rods to 2D-molecules and (b) from 2D-panels to 3D-molecules. M. Fujita, K. Umemoto, M.

Yoshizawa, N. Fujita, T. Kusukawa, K. Biradha, *Chem. Commun.* **2001**, 509-518. Copyright © 2001, Royal Society of Chemistry.<sup>33</sup>

#### 1.1.2.4. The Weak-link Approach

In contrast to the above-discussed ‘coordination-driven’ approaches, the weak link approach is a ‘coordination chemistry-driven’ approach wherein the resultant metal-organic assembly depends on the comparative chelating prowess of the organic linkers to the metal centres. Developed by Mirkin and co-workers<sup>35-37</sup>, this approach relies on both the thermodynamic and kinetic control in order to assemble a wide variety of flexible two- and three-dimensional supramolecular architectures with modular properties. The final product is synthesized in a two step pathway where in the first step, the kinetic control leads to the formation of a condensed assembly. This further converts into a flexible, open structure when acted upon hemilabile weak linkers. These weak linkers can further selectively displaced upon treatment with molecules that have stronger affinity for the metal centre, thereby generating the thermodynamic product (Figure 1.8).

One critical feature of this approach is the conformational flexibility of the weak ligands, which not only keeps an open possibility to replace them with stronger linkers thereby generating newer assemblies; but also makes the architecture suitable for applications that require conformational changes, such as in molecular sensing, catalysis, and host–guest chemistry etc.

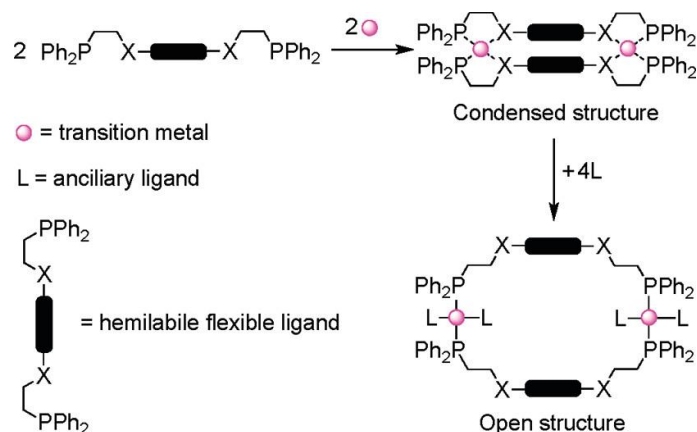


**Figure 1.8.** Schematic representation of the two-step pathway leading to the formation of an open supramolecular assembly by employing the weak link approach. Reprinted with permission from R. Chakrabarty, P. S. Mukherjee, P. J. Stang, *Chem. Rev.* **2011**, *111*, 6810–6918. Copyright © 2011, American Chemical Society.<sup>26</sup>

It is not surprising that the first few steps taken toward the world of self-assembled supramolecular complexes were serendipitous, rather than design. However, extensive research in the past few decades to develop basic design principles behind such complex behaviors has allowed the simplification of process and understanding of the concept of ‘self-assembly’ in a deconstructive approach. This simple idea of the coordination-directed self-assembly has further been extended and well-explored in other sophisticated techniques such as sub-component self-assembly, template effect, self-sorting, guest-induced synthesis<sup>26</sup> etc. in order to create an incredible variety of cage structures, from simple “platonic” solids to more complex “Archimedean” solids.

Though the synthetic strategies of the MOCs are diverse, the successful self-assembly of metal organic cages can still be simplified into a handful of basic factors namely: the well-defined coordination preferences of metal ions, the topicity and denticity of the organic ligands, and the relative spatial orientation of these coordinating donor-acceptor groups. Thus, by a careful selection of appropriate metal and organic ligands, self-assembly pathways leading to the formation of complex metallo-supramolecular architectures can be effectively guided.

## 1.2. Host-Guest Chemistry

In recent years, these metal-organic cages (MOCs) have emerged as a class of self-assembled architectures possessing intrinsic cavities and are easily accessible via a ‘bottom-up’ synthetic strategy of its constituent components. These porous MOCs of myriad shapes and sizes find use in a variety of applications, including catalysis<sup>39-42</sup>, molecular recognition and separations<sup>43-46</sup>, drug delivery<sup>47-50</sup> etc. Though diverse, each of these applications pivots around the properties of the intrinsic cavity of the cage, often called as the ‘microenvironment’, so as to exhibit a distinctively different property from that of the surrounding bulk environment. Thus, featuring one particular area of interest in MOC research called the host-guest chemistry.<sup>51-55</sup>

This refers to the ability of the cage to selectively bind or trap guest molecules within its interior cavity. Guest-binding is a complex process that involves both enthalpic and entropic factors for the encapsulation of the guests and the liberation of solvent molecules (if any) that are already entrapped within the cage cavity. The stability and solubility of hosts in solution media is crucial in promoting guest binding.<sup>56,57</sup> For example, an aqueous media can lead to high-affinity guest binding, either individually or synergistically. Cumulative effects of non-covalent interactions such as hydrogen bonding, ion–dipole and dipole-dipole interactions can promote to effectively bind guests in solution. Water-soluble cages e.g. **1.11** with hydrophobic panels, imparted by the presence of aromatic linkers enclosing their cavities, can successfully encapsulate organic guest molecules driven by the hydrophobic effect (Figure 1.9).<sup>58,59</sup>

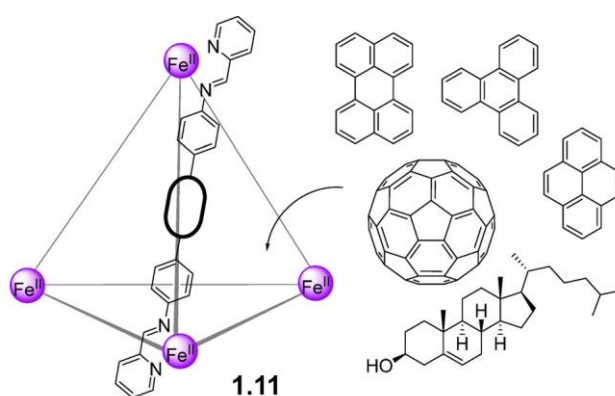


**Figure 1.9.** Structure of the tetrahedra **1.11** possessing aromatic spacer linkers and the various guests investigated for encapsulation. Reprinted (adapted) with permission from D. Zhang, T. K. Ronson, J. R. Nitschke, *Acc. Chem. Res.* **2018**, *51*, 2423-2436. Copyright © 2018, American Chemical Society.<sup>64</sup>

The host-guest chemistry of MOCs is also governed by a number of structural factors such as the size and shape of the cage cavity, and the guest molecule. A good size and shape match between a cavity and guest is often critical to promoting association. A guest that fits too tightly within the host cavity becomes too restricted to move around within the host, leading to an entropic penalty, whereas a guest that fits too loosely can escape away from the cavity causing a loss in the enthalpy of binding.<sup>60</sup> The binding affinity and selectivity of the cage for a particular guest molecule can thus be enhanced through the use of differently-sized functionalized ligands or by incorporating additional binding sites within the cage. In addition to the solvent effect and size complementarity, host-guest interactions are also influenced by the nature of interactions, variation in reaction conditions, chirality, etc. to name a few.<sup>60</sup>

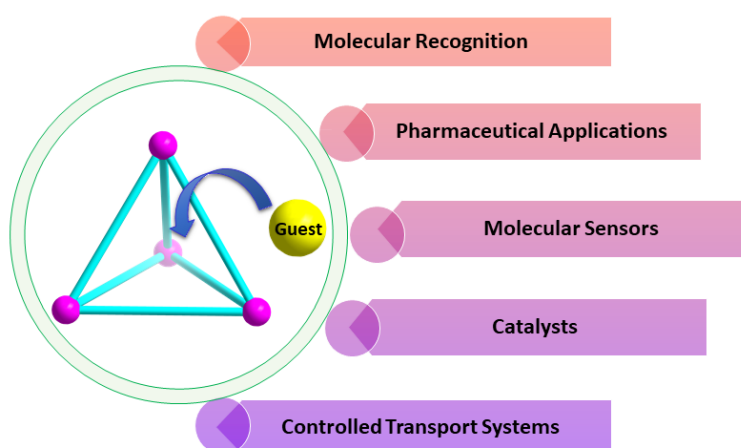


**Figure 1.10.** A schematic representation of host-guest chemistry encompassing a diverse area ranging from molecular recognition to catalytical activities and pharmaceutical applications.

Although the 55% rule originally proposed by Rebek et al<sup>61</sup> provides a good guiding principle in choosing the best host-guest pairs or predicting the binding of the guest(s) within the cage cavity in terms of size complementarity, it is often limited to rigid systems and fails to consider the host flexibility<sup>62,63</sup> and the possible structural adaptations therein in order to accommodate the guest molecules. Therefore, a detailed idea about the host flexibility, characterizations, and host-guest interactions is required in order to employ these MOCs for distinctive purposes. By suitably tuning the physical and chemical properties of the host and the guest, multiple guest binding and their subsequent release can also be achieved. This idea of molecular encapsulation can further be extrapolated towards the idea behind the employment of MOCs in molecular recognition, as organic reaction vessels, in the effective delivery of drug molecules, molecular separations, etc as discussed above (Figure 1.10) which makes the host-guest chemistry of

metal-organic cages is a rich and versatile area of research.

### 1.3. Neutral Metal-Organic Cages

Exploration in the field of metal-organic cages has experienced tremendous growth in the last 20 years. Therefore, in order to understand and appreciate the vast variety of functional properties of these cages, coupled with their design and synthetic aspects, different classification routes have been undertaken, the three most common being - bonding approaches (as briefly discussed in section 1.1), showcasing their utilities (section 1.2) and the synthetic routes taken. Of course, these classification techniques are not mutually exclusive to each other and the boundaries often merge into each other.

One such way of classifying MOCs that is less talked about is the differentiation based on net charge. Synonymous with simple transition metal complexes, MOCs can also be divided into cationic, anionic and neutral cages. While all of these cages can broadly exhibit similar functional characteristic properties, they are often obtained from dissimilar building approaches. In general, coordination-driven self-assembly offers either edge-directed (introduced by Stang<sup>27,28</sup>) or face-directed metal-organic cages (developed by Fujita and co-workers<sup>32-34</sup>). Polyhedral cages synthesized by employing *cis*-blocked and naked metal ions in combination with neutral organic ligands are very well-explored in host-guest chemistry and most of them carry a net positive or negative charge either due to the net positive charge on the metal<sup>64</sup> or by the usage of anionic ligands carrying unrequited negative charge (Figure 1.11)<sup>65</sup>

Even though the diverse design approaches and molecular interactions have given rise to a combinatorial library of interesting architectures, the distribution of these MOCs based on the overall charge of the resultant complex is rather uneven. These net charges on the MOCs are of paramount importance as it imparts the feature of water solubility, thus opening the pathway for an even wider range of exploration including catalyzing chemical reactions in aqueous media and biomedical applications.<sup>63-65</sup> However, statistically, the realm of neutral polyhedral cages has been less explored partly because of the difficulty in synthesizing charge-neutral polyhedral cages by balancing out all residual charges from the participating precursors within a discrete framework; but also the limitations faced in terms of aqueous solubility, the reactivity of metal salts and further their potential applications.



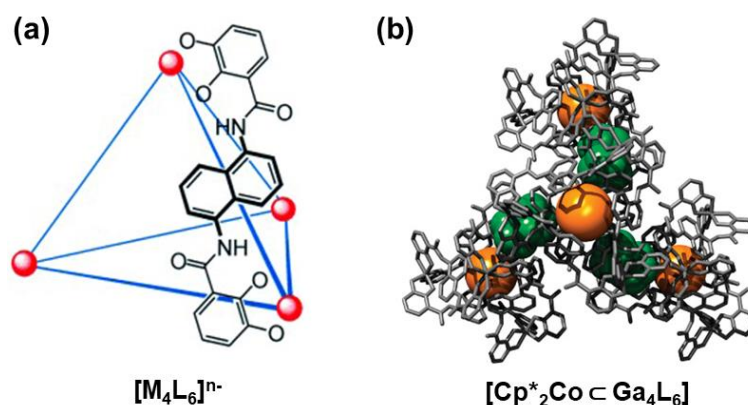


**Figure 1.11.** (a) Schematic representation of the  $M_4L_6$  assembly (b) Molecular structure showing the encapsulation of the  $Cp_2Co^+$  guest within the intrinsic and extrinsic pockets of the anionic cage assembly **1.12**.

In host–guest chemistry, addressing the interactions in the case of neutral guests becomes a key challenge, which renders the design of appropriate host cages more delicate.<sup>66</sup> For example, encapsulation of neutral guests into the cavities of polycationic cages (usually obtained through coordination-driven self-assembly) may get hampered due to the presence of highly competitive counter-anions which obstruct the cavity<sup>26,67</sup>. In this regard, focussing on the design of neutral metal-organic cages through the self-assembled coordination-driven pathway appears promising. While rare, examples of neutral discrete metallo-supramolecular assemblies are still known and have been explored for studying binding affinities of neutral guest molecules.<sup>26,67,68</sup>

In this regard, our group has been interested in generating complex neutral polyhedral cages self-assembled through a ‘three-subunit’ combination of a main-group element-based phosphoramidate ligand, transition metal ( $Pd^{II}$ ), and organic dianionic linkers. The various design principles of such cages and their host-guest studies define the basis of this thesis and will be discussed further in the following sections.

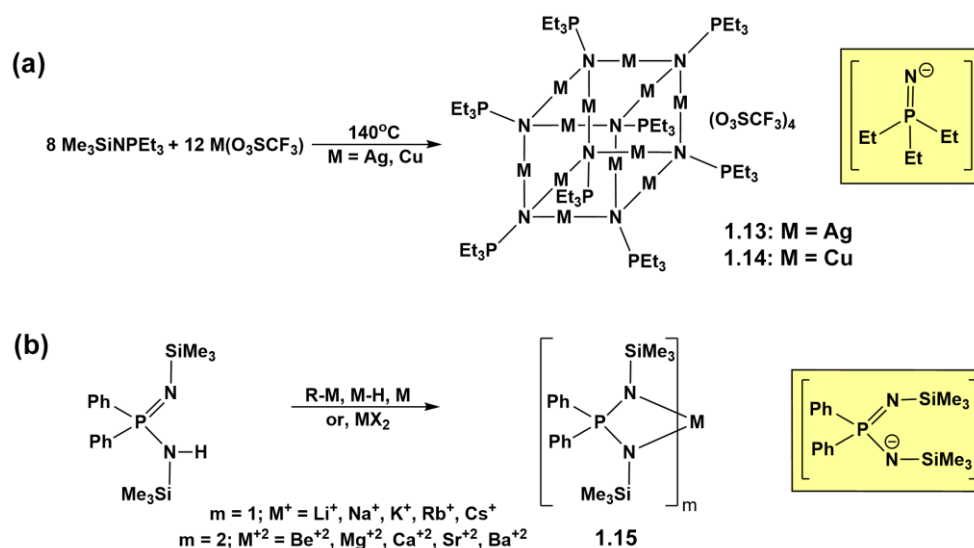
### 1.3.1. Imido-P(V) Anions as Building Blocks to Neutral MOCs

Amido and imido P(V) compounds are one of the most popular classes of P-N based compound in main group chemistry. The P-N bonds are iso-electronic to the Si-O frameworks and exhibit a rich synthetic chemistry. In the last two decades, the imino analogues of p-block oxo-anions containing group 14, 15 and 16 elements and their coordination chemistry have been extensively explored. The replacement of an oxygen centre by =NR group yields the isoelectronic imido group that is capable of forming metal complexes through lone pairs of

electrons available at the nitrogen atom. For example, the P(V)-imido moieties are analogous to the various phosphorus oxo anions derived from phosphoric acid for their isoelectronic relationships and have gained immense attention in coordination chemistry of the main group elements. The coordination chemistry of imido-P(V) anions has been at the forefront of research for more than three decades. Synthetic routes to access these imido-P(V) anions involve the use of highly reactive main-group metal reagents in reaction with a phosphonium salt like  $[(\text{PhNH})_4\text{P}]\text{Cl}$  or phosphoramides of the type  $[(\text{RNH})_3\text{P}=\text{E}]$  ( $\text{E} = \text{NSiMe}_3, \text{O}, \text{S}$  or  $\text{Se}$ ) or with preformed iminophosphanes. Moreover, by changing the different R-groups at the P(V) functionality, it is possible to alter steric bulk, solubility as well as electronic properties of these ligands. However, due to the highly reactive nature of these metal precursors as well as to the presence of residual metal-alkyl/aryl/halide/silylamide bonds in these complexes, the imido ligand chemistry has largely been limited to main-group metal ions in anhydrous aprotic and non-polar solvents.

### 1.3.1.1. Imido-P(V) Anions Derived from Strong Main-Group and Organometallic Bases

Over the years, the research groups of Dehnicke,<sup>69,70</sup> Roesky,<sup>71</sup> Chivers,<sup>72-74</sup> Wright,<sup>75</sup> Stalke,<sup>76</sup> Russell,<sup>77</sup> Steiner,<sup>78</sup> Stahl<sup>79</sup> and few others have elaborated the chemistry of imido analogues of main group oxo anions, particularly relevant to their structural diversities and reactivities.



**Scheme 1.1** (a) Synthesis of Ag(I)- and Cu(I)-phosphoraneiminato complexes. (b) Synthesis of alkali and alkaline earth metal complexes of mono anionic imidophosphinate ion.<sup>80,81</sup>

Dehnicke et al. have studied neutral mono functionalized phosphoramines of the type  $\text{R}_3\text{P}=\text{NSiMe}_3$  under high-temperature conditions for the generation of the mono-anionic ligand

$[\text{R}_3\text{P}=\text{N}]^-$  in the corresponding metal complexes **1.13** and **1.14** via silyl group elimination reaction.<sup>80</sup> Stalke and coworkers have employed the deprotonation reaction of the amino-imino phosphorane precursor  $[\text{Ph}_2\text{P}(\text{NSiMe}_3)(\text{NHSiMe}_3)]$  with alkali-metals or alkali-metal reagents to generate the  $[\text{Ph}_2\text{P}(\text{NSiMe}_3)_2]^-$  mono-anionic imido-phosphinate species, **1.15**, analogous to  $[\text{H}_2\text{PO}_2]^-$  (Scheme 1.1).<sup>81</sup>

In another interesting study, Russell and co-workers have shown the formation of the lithium complex, **1.16** of the imido P(V) dianion  $[\text{HP}(\text{NR})_3]^{2-}$ , analogous to the phosphite anion  $[\text{HPO}_3]^{2-}$ , in a reaction involving  $\text{PCl}_3$  and 2-methoxyaniline followed by the addition of 2 equivalence of  ${}^n\text{BuLi}$ .<sup>83</sup> The proton shift from the amino group to the phosphorus centre was proposed as the origin of phosphitic hydride in its complex. The crystal structure of the complex reveals a dimeric centrosymmetric structure consisting of four  $\text{Li}^+$  ions residing in two different coordinating environments. (Figure 1.12a). Further, Chivers and co-workers have employed the chalcogenido bis(amido)phosphonate ligand,  $[\text{PhP}(\text{E})(\text{N}^t\text{Bu})_2]$  ( $\text{E} = \text{O}, \text{S}$  and  $\text{Se}$ ) in reaction with  ${}^n\text{BuLi}$  to generate the lithium complexes **1.17**, **1.18** and **1.19** respectively of the dianions  $[\text{PhP}(\text{E})(\text{N}^t\text{Bu})_2]^{2-}$  (Figure 1.12b).<sup>84</sup>

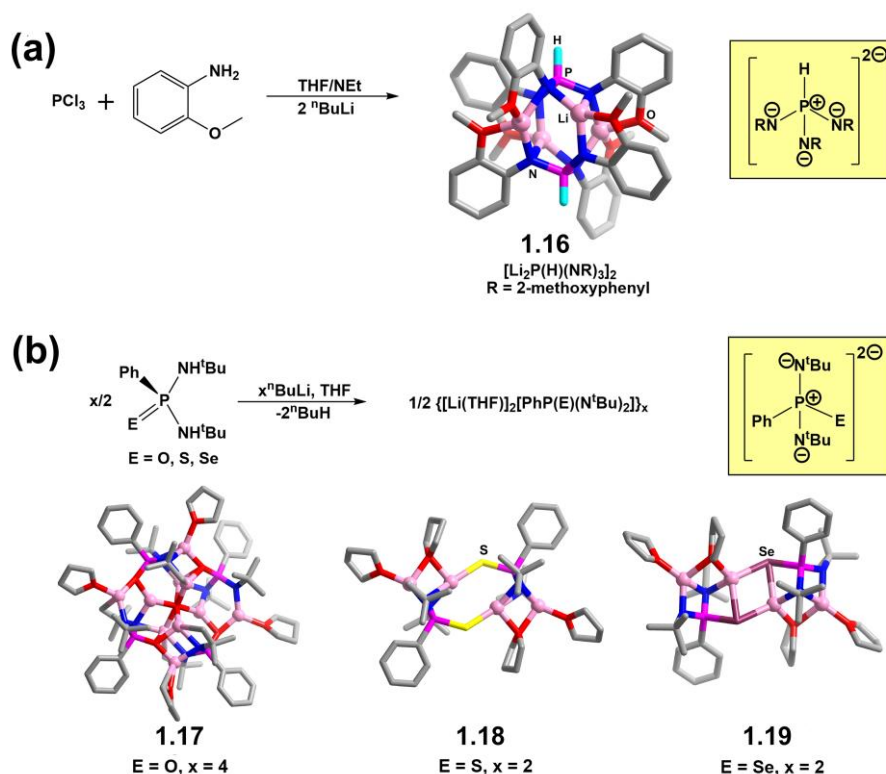


**Figure 1.12** (a) Synthesis and crystal structure of the tetrameric Li-complex **1.16** supported by imido-phosphite dianion. (b) Synthesis and crystal structure of lithium-chalcogenido complexes **1.17-1.19** supported by imido-phosphonate dianions.<sup>83,84</sup>

The first example of the isolation of an imido-P(V) trianion analogous to ortho-phosphate trianion,  $\text{PO}_4^{3-}$  was reported by Steiner, Wright and co-workers in a reaction involving diphosphorus tetraiodide and  $\alpha$ -naphthylamine in the presence of  ${}^n\text{BuLi}$ .<sup>85</sup> The Lithium complex of an unprecedented tetra-imidophosphate trianion was isolated as its solvent separated ion-pair.<sup>86</sup> Further, Chivers et. al. have utilized the tris(amido) phosphate ligand  $[\text{P}(\text{NSiMe}_3)(\text{NH}^t\text{Bu})_3]$  in reaction with excess  ${}^n\text{BuLi}$  to generate the tetra(imido)phosphate trianion<sup>87</sup>,  $[\text{P}(\text{NSiMe}_3)(\text{N}^t\text{Bu})_3]^{3-}$ . The complex **1.20** was the first example of an unsolvated tri-lithium tetrakisimidophosphate, isolated as a hexameric complex consisting of a cyclic ladder shaped  $\text{Li}_6\text{N}_6$  core in which the two  $\text{PNSiMe}_3$  groups cap the hexagonal faces of the cage in a  $\mu_3$  (N, N, N) coordination (Figure 1.13). However, treatment of the analogous  $[\text{PO}(\text{NH}^t\text{Bu})_3]$  with excess  ${}^n\text{BuLi}$  resulted in the formation of the corresponding dianion that stabilizes a tetrameric Lithium complex  $\{\text{Li}_2(\text{THF})\text{P}(\text{O})(\text{N}^t\text{Bu})_2(\text{NH}^t\text{Bu})\}_2$  in a face-sharing double-cubane structure **1.21** in a mixed N,N,O chelating coordination (Figure 1.13). These observations revealed the steric and electronic effects of the non-coordinating imidosilyl group in stabilizing the trianionic ligand,  $[\text{P}(\text{NSiMe}_3)(\text{N}^t\text{Bu})_3]^{3-}$ .

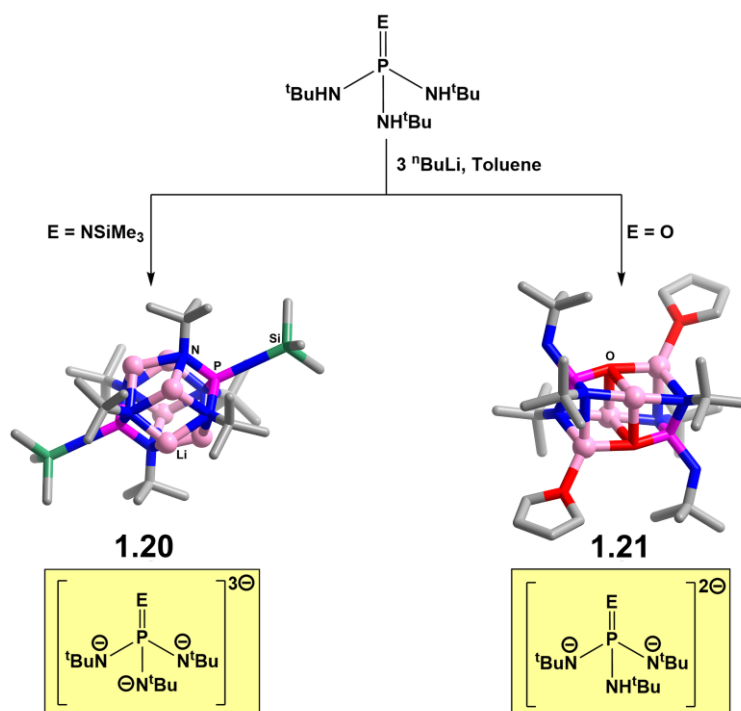


**Figure 1.13.** Synthesis and crystal structure of hexameric Li-complex, **1.20** supported by tris(imido)phosphate trianion and double-cubane Li-complex **1.21** supported by bis(imido)phosphate dianion.<sup>87</sup>

Starting from the same precursor  $[\text{P}(\text{NSiMe}_3)(\text{NH}^t\text{Bu})_3]$ , Roesky et al. have synthesized a trimetallic  $\text{Al}^{\text{III}}\text{-(Li}^{\text{I}})_2\text{-}$ complex of the tetra-imidophosphate trianion containing rare four-membered  $\text{PN}_2\text{Al}$  rings, **1.22-1.25** (Figures 1.14a-d). This is a two-step reaction that involves the initial reaction of  $\text{Me}_3\text{Al}$  with the ligand yielding a monomeric complex of the monoanion  $\{\text{Me}_2\text{Al}[\text{P}(\text{NSiMe}_3)(\text{NH}^t\text{Bu})(\text{NH}^t\text{Bu})_3]\}$ , which on subsequent reaction with  $n\text{-BuLi}$  gives the trimetallic complex  $\{\text{Me}_2\text{Al}[\text{P}(\text{NSiMe}_3)(\text{N}^t\text{Bu})_3]\}$ . In contrast, reaction of  ${}^n\text{Bu}_2\text{Mg}$  with this Al-complex leads to the formation of the corresponding Mg complex of the mono- and dianionic ligand via the displacement of the Al(I) ion in the parent complex. All these complexes were depicted as reagents for various organic syntheses, industrial catalytic processes, precursor for the preparation of Al-N containing materials etc.

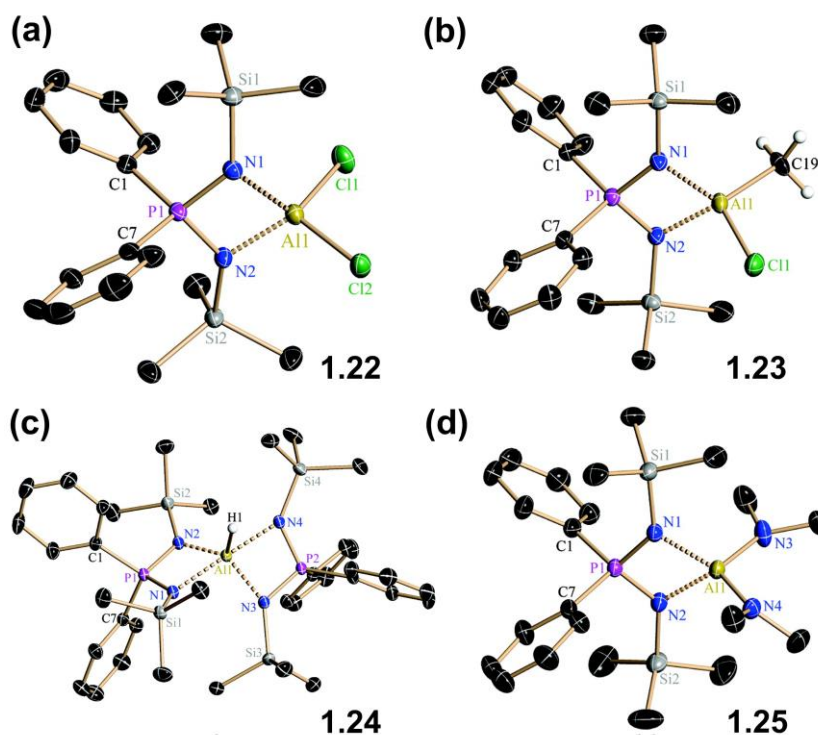


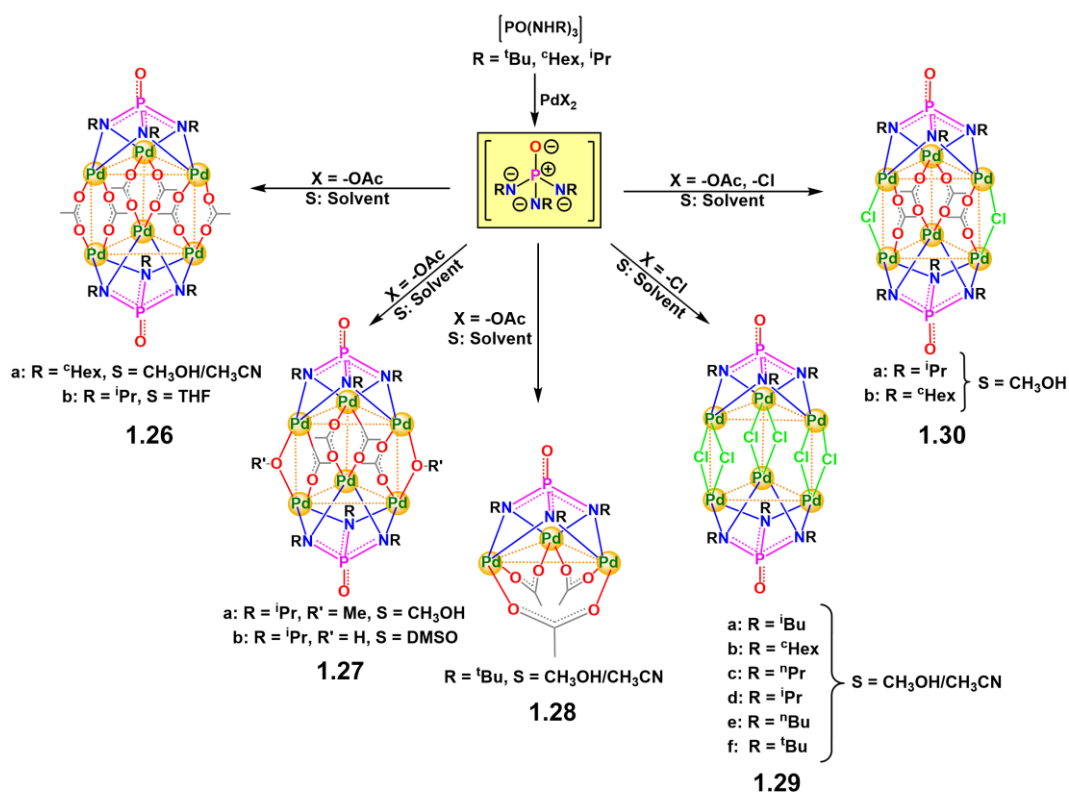
**Figure 1.14.** Crystal structures of Aluminum imidophosphate complexes; (a)  $\text{LAlCl}_2$ , **1.22**; (b)  $\text{LAlClMe}$ , **1.23**; (c)  $\text{L}_2\text{AlH}$ , **1.24**; (d)  $\text{LAl}(\text{NMe}_2)_2$ , **1.25** where  $\text{L} = [\text{Ph}_2\text{P}(\text{NSiMe}_3)_2]$ . Reprinted (adapted) with permission from B. Nekoueishahraki, H. W. Roesky, G. Schwab, D. Stern, D. Stalke *Inorg. Chem.* **2009**, *48*, 9174-9179 Copyright © 2009, American Chemical Society.<sup>88</sup>

Subsequently, Steiner and co-workers showed an elegant sequential deprotonation of the tetraanilino phosphonium cation,  $[\text{P}(\text{NHPh})_4]^+$  with  ${}^n\text{BuLi}$  yielding a series of homoleptic

imido moieties.<sup>89</sup> Alongside, few research groups have contributed to the transition metal complexes of these polyimido anions.<sup>90,91</sup> However, formation of the polyimido anions analogous to the  $\text{HPO}_4^{2-}$  and  $\text{PO}_4^{3-}$  anions remained elusive in these transition metal mediated deprotonation reactions. In fact, Chivers and co-workers have shown use of a strong Lewis acidic metal ion such as  $\text{Cu}^{2+}$  ion to obtain the said polyimido anions has resulted in the P-N bond cleavage reactions.<sup>92</sup>

### 1.3.1.2. Deprotonation of Alkyl phosphoric triamides using Pd(II) salts

Even though a few multi-metallic assemblies were reported by our group based on the deprotonation of the imido-phosphates,<sup>93,94</sup> the imido-trianions related to the *ortho*-phosphate ion,  $(\text{PO}_4)^{3-}$ , remained elusive in all the reactions. Hence, the focus was shifted towards the relatively comparable soft Lewis acidic Pd(II) ions for these deprotonation reactions. Interestingly, treatment of the tris(alkylamido)phosphates with excess of  $\text{Pd}(\text{OAc})_2$  has resulted in the facile one-pot deprotonation of all the three amino-protons in these ligands (Scheme 1.2).<sup>95</sup>



**Scheme 1.2.** Schematic representation of synthesis of tri and hexanuclear Pd(II) clusters supported by tris(imido)phosphate trianion **1.26-1.30**.<sup>94,95</sup>

These tris(imido)phosphate trianions,  $[(RN)_3PO]^{3-}$  ( $R = {}^tBu, {}^cHex, {}^iPr$ ), were isolated as their tri- and hexanuclear Pd(II) clusters of formula  $\{Pd_3[(NR)_3PO](OAc)_3\}_n$ , **1.26** and **1.28** ( $n = 1$  or  $2$ ) (Scheme 1.2). The molecular structure of these assemblies show that each trianionic ligand offers a tripodal hexadentate chelating coordination to three Pd(II) centres on one side of the  $Pd_3$ -plane. The remaining acetate ions act as either chelating or bridging ligand on the other side of the  $Pd_3$ -plane to yield the tri- and hexameric clusters (Figure 1.15a). The arrangement of the two  $Pd_3$  units in the hexamers were found to be in the prismatic geometry (Figure 1.15b). The formation of a smaller trinuclear cluster for the  ${}^tBu$  substituents indicate the role of steric effects in governing the nuclearity of the obtained assemblies in the Pd(II) mediated reactions. Some of these hexanuclear clusters were isolated as their mixed acetate and hydroxy or methoxy-bridged species  $\{Pd_3[(NR)_3PO](OR)(OAc)_2\}_2$ , **1.27** (hereafter called as **HEXA-Pd** to distinguish from the other hexameric complexes) as well depending upon the substituents on the amino group and reaction solvent. Nonetheless, they were chemically similar to their other hexameric counterparts.

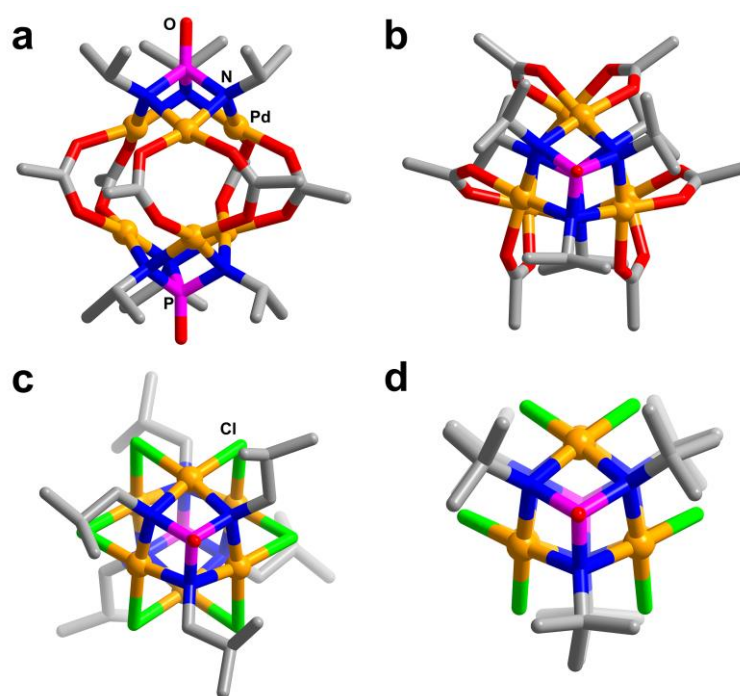
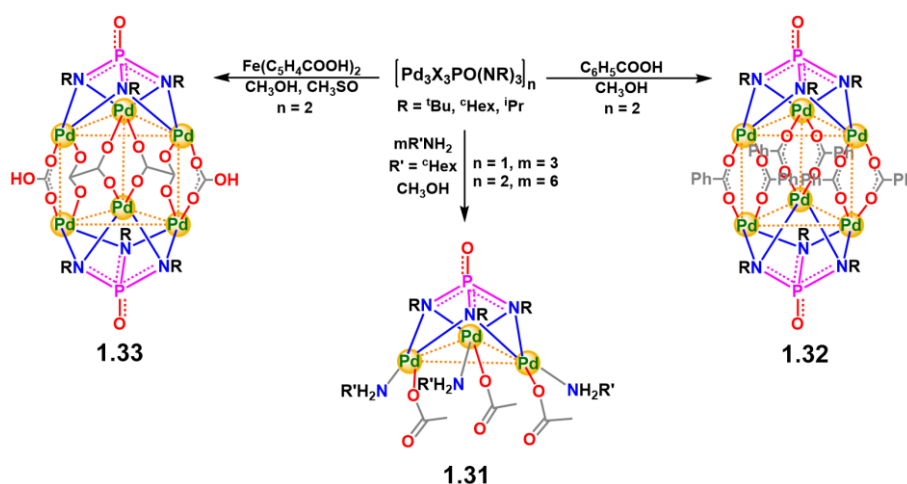


**Figure 1.15.** Molecular structures of acetate- (a-b) and chloro-bridged (c-d) hexa nuclear Pd(II) clusters supported by tris(imido)phosphate trianions.<sup>94,95</sup>

Employing  $PdCl_2$  in place of  $Pd(OAc)_2$  in these reactions results again in the fully deprotonated species  $[(RN)_3PO]^{3-}$ , isolated as their corresponding chloro-bridged hexanuclear clusters  $\{Pd_3[(NR)_3PO](Cl)_3\}_2$ , **1.29** (Scheme 1.2).<sup>96</sup> Detailed structural analysis of these clusters

showed two types of arrangements for the two trinuclear imido-Pd<sub>3</sub>-subunits in them. A staggered arrangement of the two imido-Pd<sub>3</sub> units results in the formation of octahedral clusters (R = <sup>i</sup>Bu, <sup>n</sup>Bu, <sup>c</sup>Hex, <sup>i</sup>Pr, <sup>n</sup>Pr), while an eclipsed conformation (R = <sup>t</sup>Bu) gives rise to prismatic clusters (Figures 1.15c, d). This indicates that the bulky <sup>t</sup>Bu substituent preferred to yield the prismatic cluster, while the smaller substituents on the phosphoramidate precursors yields the octahedral assembly. Though, the *c*-hexyl group is relatively bulkier than the *tert*. -butyl group, the flexibility of this ring to adopt a puckered configuration has indeed favoured the formation of a more-compact octahedral assembly. Interestingly use of a mixture of PdCl<sub>2</sub> and Pd(OAc)<sub>2</sub> in these reactions gave rise to the mixed bridged species {Pd<sub>3</sub>[(NR)<sub>3</sub>PO](Cl)(OAc)<sub>2</sub>}<sub>2</sub>, **1.30** which are structurally similar to the acetate linked clusters.

The reactivity studies of these clusters with nucleophilic reagents such as primary amines (RNH<sub>2</sub>) have led to a symmetric cleaving of the cluster with the formation of the corresponding trimeric species {Pd<sub>3</sub>[(NR)<sub>3</sub>PO](OAc)<sub>3</sub>(R'NH<sub>2</sub>)<sub>3</sub>}, **1.31**. Remarkably, the tripodal coordination of the Pd–N<sub>imido</sub> moieties remained unaffected demonstrating the robustness of the Pd<sub>3</sub>-unit in these clusters. Further, the carboxylate bridges in these hexameric clusters can be successfully replaced with other carboxylate anions upon treatment with their corresponding carboxylic acids.<sup>97</sup> For example, the reaction of benzoic acid with **HEXA-Pd** results in the formation of the corresponding benzoate bridged cluster, **1.32** while the reaction of ferrocene dicarboxylic acid (FDC) resulted in the replacement of four acetate bridges with two FDC bridges, **1.33**. Due to the steric hindrance, the remaining linkages in this cluster are established with chloro- or hydroxy bridges (Scheme 1.3).



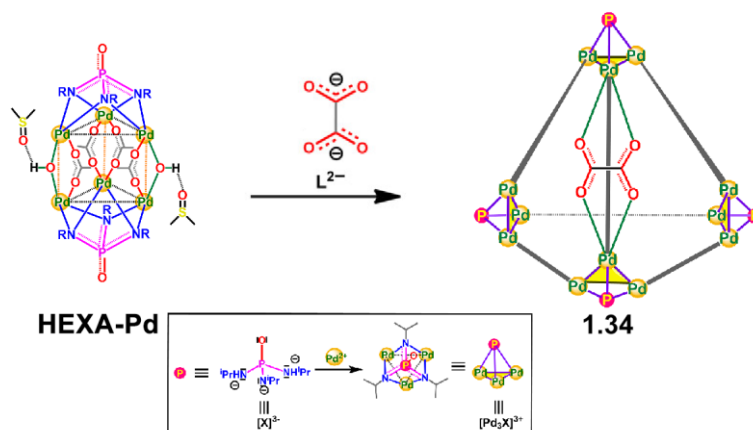
**Scheme 1.3.** Schematic representation for the ligand exchange reaction for the tri- and hexanuclear clusters leading to the complexes **1.31-1.33**.<sup>97</sup>



Thus, in contrast to the usual deprotonation pathways, our group has emphasized the use of salts of certain soft transition metal ions as a source of base to generate the P(V) bound polyimido species in polar medium. Especially, the propensity of the Pd(II) salts to yield the highly basic imido-trianions, which are otherwise accessible only in the presence of highly reactive organolithium reagents.

### 1.3.2. Imido-Pd<sub>3</sub> Clusters as Building Blocks for Neutral Polyhedral Cages

It is hereby interesting to note that each trianionic ligand in the hexanuclear imido-Pd (II) clusters offers a hexadentate cisoidal coordination to the three Pd(II) centers. The labile nature of the residual acetate ligands thus opens up free bidentate chelating sites at an angle of 90° on each Pd (II) centers that makes these imido-Pd<sub>3</sub> clusters as potential building units for coordination driven self-assemblies in the presence of suitable ligands. Accordingly, treatment of the hexameric cluster {Pd<sub>3</sub>[(N<sup>i</sup>Pr)<sub>3</sub>PO](OAc)<sub>2</sub>(OH)<sub>2</sub>}<sub>2</sub> **HEXA-Pd** with 1.5 equivalents of oxalic acid gave an oxalate linked cage molecule {Pd<sub>3</sub>[(N<sup>i</sup>Pr)<sub>3</sub>PO]<sub>4</sub>(C<sub>2</sub>O<sub>4</sub>)<sub>6</sub>}, **1.34** in tetrahedral topology (Scheme 1.4).<sup>97</sup>



**Scheme 1.4.** Schematic representation for the neutral cage formation reaction, starting from the hexameric precursor **HEXA-Pd**, leading to the tetrahedral cage **1.34**.<sup>97</sup>

The structural analysis revealed that the cage consists of four [Pd<sub>3</sub>(N<sup>i</sup>Pr)<sub>3</sub>PO]<sup>3+</sup> (denoted as [Pd<sub>3</sub>X]<sup>3+</sup>) units at the corners of the tetrahedron and six oxalate, [C<sub>2</sub>O<sub>4</sub>]<sup>2-</sup>, ions at the tetrahedral edges. The vertices of these cages comprise of a trinuclear polyhedral building unit (PBU) of composition [Pd<sub>3</sub>X]<sup>3+</sup> in which the trianionic [PO(N<sup>i</sup>Pr)<sub>3</sub>]<sup>3-</sup> motif (denoted as X<sup>3-</sup>) acts as a *cis*-capping ligand for a planar Pd<sub>3</sub>-unit. These *cis*-blocked PBUs act as 60° acceptors and spontaneously self-assemble in the presence of 180° wide-angle chelating oxalate linkers to yield charge-neutral tetrahedral cage of composition [(Pd<sub>3</sub>X)<sub>4</sub>(C<sub>2</sub>O<sub>4</sub>)<sub>6</sub>]. Although Pd(II) based

cationic cages were well known in the literature, robust, charge neutral cages are scarce. Hence, use of the  $[\text{Pd}_3\text{X}]^{3+}$  PBUs in combination with chelating anionic linkers serves as a powerful approach to access neutral tetrahedral Pd(II) cages.

Alternately, all this tetrahedral cluster cage also can be synthesized in a one-pot reaction involving the phosphoramidate ligand  $[\text{PO}(\text{NH}^i\text{Pr})_3]$ ,  $\text{Pd}(\text{OAc})_2$  and oxalic acid. The intrinsic cavity in **1.34** was found to be  $\sim 85 \text{ \AA}^3$  as determined from MSROLL calculations.<sup>99,100</sup> The gas sorption analysis of the desolvated phase of **1.34** revealed a major pore of  $5 \text{ \AA}$  diameter for this cage, which matches well with its observed central portal distances along the four tetrahedral faces.

### 1.3.3. Host-Guest Studies of the Neutral Tetrahedral Cage

The molecular structure of **1.34** was found to contain a molecule of DMSO at its intrinsic cavity (Figure 1.16a). Thereafter, the guest-free cage was generated easily by re-crystallizing it from methanol. Spurred by the availability of a small cavity and by the presence of encapsulated DMSO molecule, the host-guest chemistry of **1.34** was probed for certain neutral solvents. The mass-spectrum of the cage in the presence of guest molecules such as  $\text{CH}_2\text{Cl}_2$ ,  $\text{CHCl}_3$ ,  $\text{CCl}_4$ ,  $\text{C}_6\text{H}_6$ ,  $\text{C}_7\text{H}_8$ ,  $\text{C}_5\text{H}_{10}$  and  $\text{C}_6\text{H}_{12}$  showed peaks due to the respective guest  $\subset$  **1.34** species (Figure 1.16). Further studies indicated that this oxalate linked tetrahedral cage can accommodate only suitable small guest molecules, while larger molecules such as toluene ( $\text{C}_7\text{H}_8$ ) and cyclohexane ( $\text{C}_6\text{H}_{12}$ ) could not enter the intrinsic cavity of the cage. The presence of these guest molecules at the internal void of **1.34** was confirmed by single-crystal X-ray diffraction analysis and diffusion ordered NMR spectroscopy (DOSY).

When a single species is present in the solution, DOSY-NMR 2D-plot gives a single band-like appearance, and the D-value can be obtained from the corresponding f1-axis. However, due to the presence of two or more kinds of species are present in the host-guest mixture, it becomes difficult to resolve the individual D-values from the 2D plot, especially in case of a fast exchange. Thus, the “T1/T2” module in Topspin 4.1 software is used for regression analysis to calculate the diffusion coefficient for each integral region or individual selected peak. The fitting of the diffusion dimension in the 2D-DOSY spectra is carried out using a one-parameter mono-exponential (equation 1) or a two-parameter biexponential fit (equation 2).

$$I = I_0 \exp[-D\gamma^2 g^2 \delta^2 (\Delta - \delta/3)] \quad (1)$$

$$I = I_{0A} \exp[-D_A \gamma^2 g^2 \delta^2 (\Delta - \delta/3)] + I_{0B} \exp[-D_B \gamma^2 g^2 \delta^2 (\Delta - \delta/3)] \quad (2)$$

which gives us distinct D-values for free, bound, or any other intermediate species present in the solution. From this  $^1\text{H}$ -2D-DOSY data analysis two diffusion coefficient values can be obtained for each of the guests studied for the cages: one with a faster diffusion rate which is attributed to the free guest molecule in solution and one with a slow diffusion rate for the host-bound guest molecule.

Often in supramolecular systems, the diffusion coefficient value not only provides information about the diffusion rates of the different species but they are often used to extract hydrodynamic radii and molecular mass of the respective molecules as well. A free guest molecule is usually much smaller in size and has a small molecular mass and thus can diffuse at a faster rate than the supramolecular host assembly. However, the same guest, when encapsulated within the cavity of the host, diffuses at a much slower rate along with the host molecule as one single 'Guest⊂Host' entity. This moiety and its constituent components including the guest now possess properties (size, mass, etc) comparable to that of the host itself. Thus, when the guest peaks (from the host-guest NMR spectra) are integrated and are fitted into the bi-exponential equation (2) via the T1/T2 analysis, a faster D-value shows up due to the presence of free independent guest that is present in the solution outside the cavity of the host whereas the slower D-value obtained gets assigned to the guest molecule that is present within the 'Guest⊂Host' entity. Similarly, the cages also exhibit two diffusion coefficient values pertaining to a free (fast-moving) and a guest-bound (slow-moving) host (Figure 1.17). However, the difference in the two D-values (free and bound) for the host cage is less drastic as compared to the guest due to a more prominent difference in size occurring in the latter during the encapsulation process. Furthermore, a comparison of the diffusion coefficients of the different bound guests also provides a qualitative idea about the guest binding strength. A pair of closely related D-values from the bound host and guest species is suggestive of a tighter host-guest binding (e.g.  $\text{C}_6\text{H}_6$ ,  $\text{C}_5\text{H}_{10}$ ,  $\text{CHCl}_3$  in Figure 1.17) as compared to slightly different D-values ( $\text{CH}_2\text{Cl}_2$  in Figure 1.17) which suggests a weaker host-guest binding which is possible if either the guest is too small and thus can escape easily from the host cavity or the guest is too large and is not fully encapsulated into the host cavity.

Competitive binding experiments proved the selective encapsulation of benzene over all the other examined solvents and among the chlorinated solvents,  $\text{CCl}_4$  was found to be selective as determined by mass-spectral analysis. These observations were further confirmed by theoretical binding energy calculations as well wherein the highest binding energies of -154.01

and  $-107.36 \text{ kJmol}^{-1}$  were obtained for  $\text{C}_6\text{H}_6 \subset \mathbf{1.34}$  and  $\text{CCl}_4 \subset \mathbf{1.34}$ , respectively.

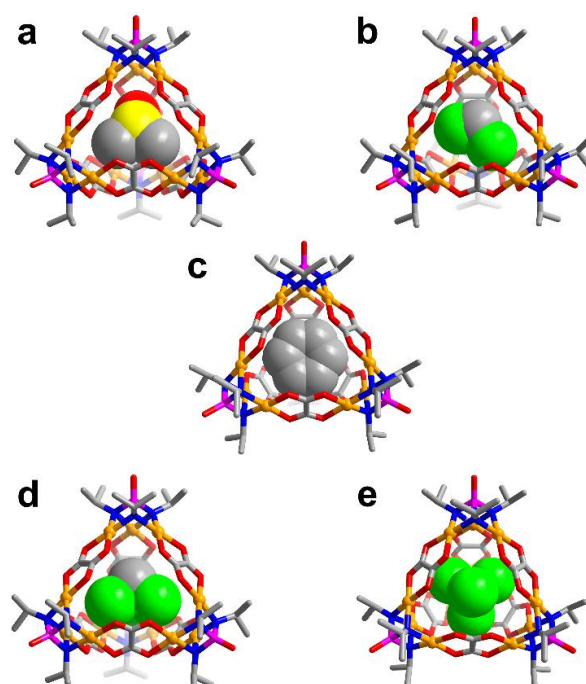


**Figure 1.16.** SCXRD Structures of guest  $\subset \mathbf{1.34}$  complexes with the following guests: (a) DMSO (b)  $\text{CH}_2\text{Cl}_2$  (c)  $\text{C}_6\text{H}_6$  (d)  $\text{CHCl}_3$  (e)  $\text{CCl}_4$ .<sup>97</sup>

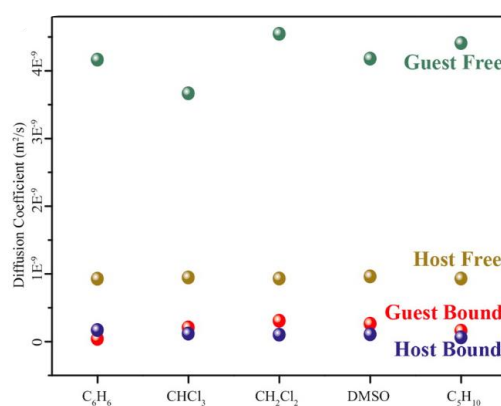


**Figure 1.17.** A summary of host guest studies of  $\mathbf{1.34}$  as derived from 2D-DOSY NMR studies. Reprinted (adapted) with permission from A. K. Gupta, A. Yadav, A. K. Srivastava, K. R. Ramya, H. Paithankar, S. Nandi, J. Chugh, R. Boomishankar, *Inorg. Chem.* **2015**, *54*, 3196-3202. Copyright © 2015, American Chemical Society.<sup>97</sup>

Spurred by the guest encapsulating ability of  $\mathbf{1.34}$ , larger neutral polyhedral cages built with the same imido- $\text{Pd}_3$  subunit, tethered by anilic acid-based linkers were synthesized. With intrinsic cavity volume more than  $200 \text{ \AA}^3$ , these cages were further probed for the encapsulation of certain substituted aromatic hydrocarbons and have shown excellent selectivity towards

encapsulation of isomeric xylenes and mesitylene. The ability of the host to selectively recognize the guest molecules was attributed to the difference in portal size of these cages. Further, the formation of stable host-guest assemblies were probed by crystallography, NMR titration, DOSY-NMR and theoretical binding energy calculations.<sup>98</sup>

Robust, neutral polyhedral-cage assemblies capable of binding guest molecules based on physical interactions, size, and shape are highly desirable as they offer a great control for the recognition of small molecules in organic solvents.

### 1.3.4. Post-assembly Reactions on Pd(II) Neutral Cages

Structural transformations of cages involving post-assembly functionalization, cage-conversions and growth into hierarchical networks play an important role in the synthesis of complex metal-organic materials.<sup>101,102</sup> Having established the utility of the imido-Pd<sub>3</sub> motifs in the formation of various tetrahedral cages attention was paid to understand the role of these PBU in aiding the post-assembly reactions. In this effort, a 42-component cubic cage assembly, was synthesized based on these imido-Pd<sub>3</sub> PBUs and 2,5-pyrazine dicarboxylate linkers (Figure 1.18).<sup>103</sup> The cubic assembly of formula [(Pd<sub>3</sub>X)<sub>8</sub>(PZDC)<sub>12</sub>], **1.35** was obtained by the treatment of the hexameric cluster, **HEXA-Pd** and 2,5-pyrazinedicarboxylic acid (PZDC-2H). Each PZDC ligand in it provides two chelating N, and O-coordinating sites to two opposite Pd(II) ions. In addition, one of the carboxylate oxygen atoms on each PZDC ligand is uncoordinated, which leaves the cage with twenty-four vacant coordination sites for post-assembly reactions via hetero-metal ion coordination.

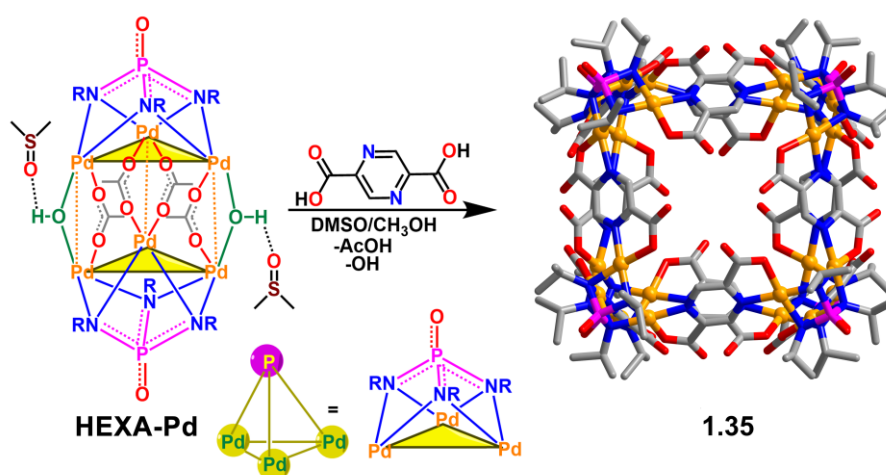


**Figure 1.18.** Schematic representation showing the formation of cubic cage assembly **1.35**.<sup>103</sup>

Treatment of divalent metal ion derived reagents such as  $\text{Fe}(\text{OTf})_2$  and  $\text{Zn}(\text{NO}_3)_2$  under methanol reflux conditions resulted in the conversion of this cubic cage into 3D-metal organic frameworks, **1.36** and **1.37** respectively. In both frameworks the basic structural unit is the heterocubane of the type  $[\text{M}_4(\text{Pd}_3\text{X})_4(\text{PZDC})_6]$  in which the  $\text{M}(\text{II})$  ions bridge between the tetrahedral faces by coordinating with the free carboxylate O-atoms in their triangular faces (Figure 1.19). This indicates the robustness of the  $[\text{Pd}_3\text{X}]$  building blocks, which further aided in the isolation of various intermediates in discrete, 1D and 2D-cage networks.<sup>103</sup>

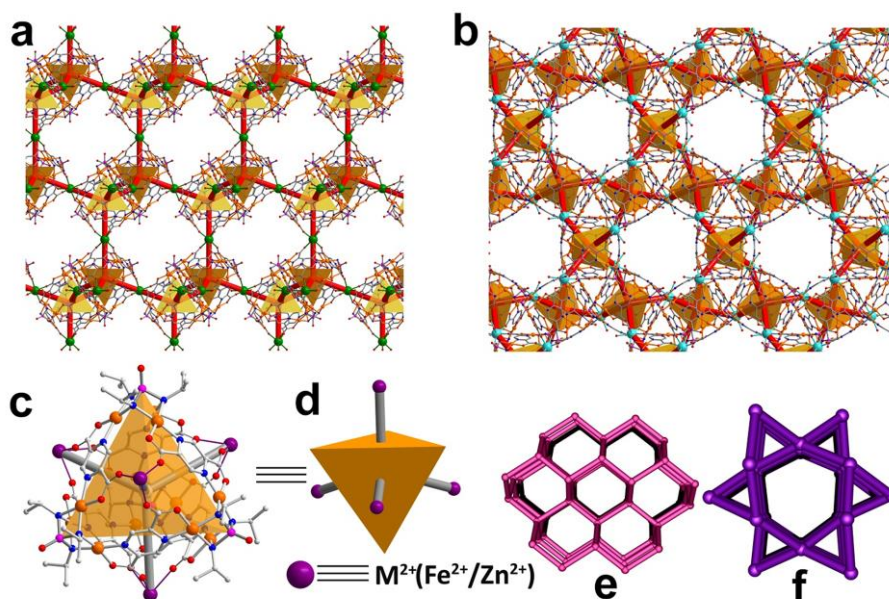


**Figure 1.19.** Crystal Structures of (a) **1.36** and (b) **1.37** showing the network structures. Green and cyan coloured spheres represent Fe (II) and Zn (II) atoms. Reprinted (adapted) with permission from Boomishankar et al. *Chem. -Eur. J.* **2017**, *23*, 18296-18302.<sup>103</sup>

### 1.3.5. Chiral Cages Derived from the Deprotonation of Imido-Pd<sub>3</sub> Clusters

Further developments in the chemistry of imido-Pd<sub>3</sub> derived assemblies were also aimed at the development of chiral tetrahedral cages. For this purpose, enantiopure phosphoric triamide ligands having  $\alpha$ -methyl benzyl substituents were synthesized and subjected to the cage formation reactions in the presence of  $\text{Pd}(\text{OAc})_2$  and oxalic acid to yield the chiral cages **1.38-R** and **1.38-S** of formula  $[(\text{Pd}_3\text{X}^*)_4(\text{C}_2\text{O}_4)_6]$ , ( $[\text{X}^*]^{3-} = \text{RRR-}$  or  $\text{SSS-}[\text{PO}(\text{N}(\text{*CH}(\text{CH}_3)\text{Ph})_3)]^{3-}$ ) (Figures 1.20a, b).<sup>104</sup> Use of chloranilic acid instead of oxalic acid gave the corresponding larger cages of formula  $[(\text{Pd}_3\text{X}^*)_4(\text{C}_6\text{O}_4\text{Cl}_2)_6]$ , **1.39-R** and **1.39-S** (Figures 1.21a, b).<sup>105</sup> The structures of the oxalate-linked cages were solved in the face-centered cubic chiral space group  $F23$  while the larger chloranilate based cages were solved in the cubic body-centered chiral

space group  $I23$ . This signifies that the non-centrosymmetric T-symmetry of the cages were retained by their crystal lattice as well. Also, these cages possess additional rotational chirality as the chiral  $\alpha$ -methyl benzyl amino groups in these cages are oriented in the clockwise (for R-cages) or anti-clockwise (for S-cages) direction.

Further, the chiral discrimination and separation capabilities of all these enantiomeric pure cages were examined. The oxalate cages were tested for certain small racemic compounds such as Epichlorohydrin (epi),  $\beta$ -Butyrolactone (BBL), 3-Methyl cyclopentanone (3-Me-cp) and 3-Ethyl cyclopentanone (3-Et-cp). From the chiral GC analysis, the enantiomeric excess values of 6, 34, 14 and 12 % were obtained for the excess R-enantiomers of epi, BBL, 3-Me-cp and 3-Et-cp guests using the host **1.38-R**. Similarly, for the excess enantiomers of epi, BBL, 3-Me-cp and 3-Et-cp guests, the %ee values of 10, 14, 16 and 14 were obtained by employing the host **1.38-S**. These observed separation efficiencies were further comparable with some of the efficient discrete coordination assemblies.<sup>106,107</sup>

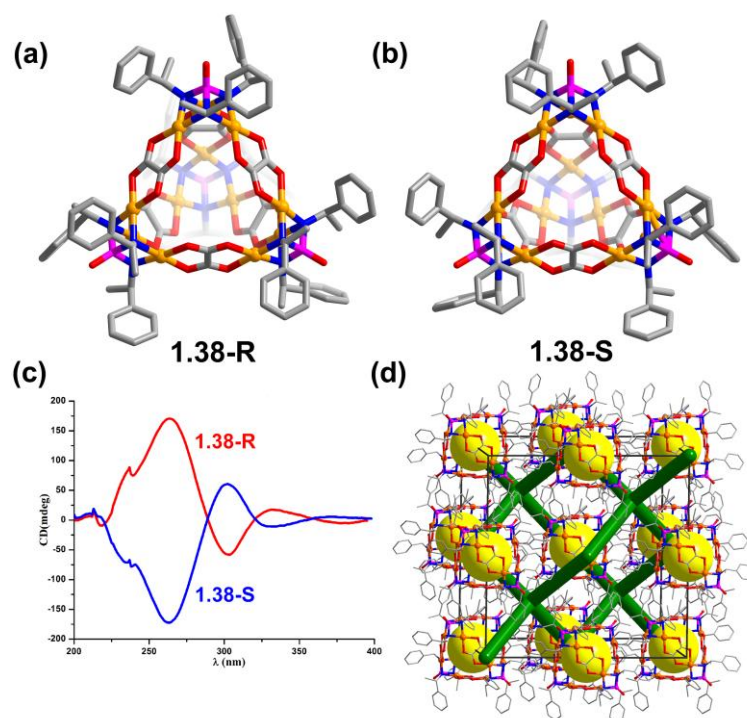


**Figure 1.20.** Molecular Structures of (a) **1.38-R** (b) **1.38-S** (c) their corresponding Circular Dichroism (CD) spectra and (d) packing structure of **1.38-S** showing the presence of diamondoid channels connecting the intrinsic voids of the cages. Reprinted (adapted) with permission from Boomishankar et al. *Chem. Commun.* **2018**, 54, 1873-1876.<sup>104</sup>

Owing to the presence of larger cavities and quinonoid portals, the enantio-separation capabilities of the anilate linked cages (**1.39-R** and **1.39-S**) were probed for the more exotic and challenging aryl oxiranes (also named as styrene oxides). Thus, the representative racemic ( $\pm$ ) mixtures of styrene oxide (SO), 4-fluoro styrene oxide (F-SO), 4-chloro styrene oxide (Cl-SO), 4-bromo styrene oxide (Br-SO) were individually subjected for the crystallization inclusion process with the hosts wherein a highest %ee value of 80 was obtained for +F-SO desorbed from **1.39-R** and a closely similar value of 78 was again obtained for the +F-SO using **1.39-S**. Notably, the empty cages can be easily regenerated in all the above instances and reused for several separation cycles without the loss of the ee values. Separation of oxiranes using non-HKR methods are very challenging and hence a good separation of the enantiomers of the styrene oxides using metal-ligand cages serves as an attractive proof of concept protocol.

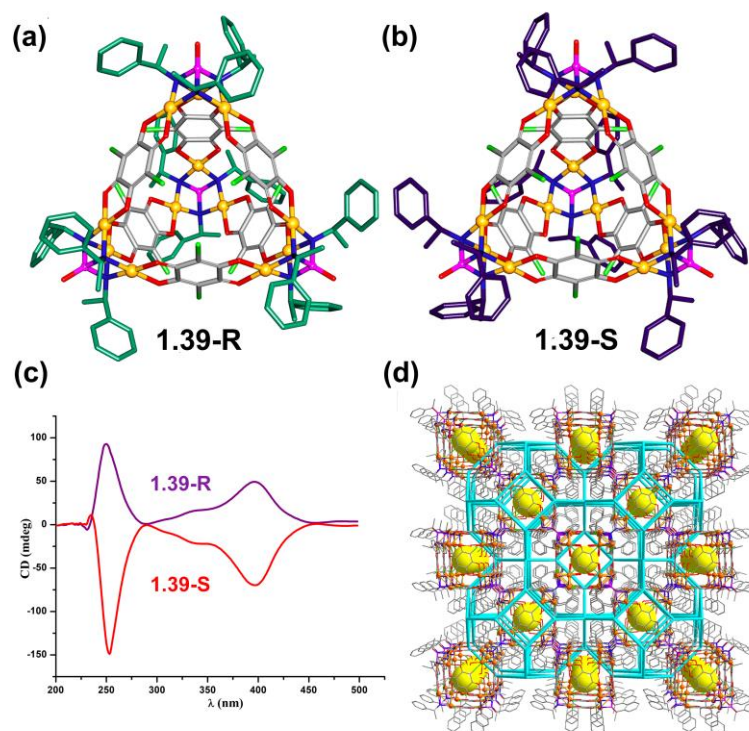


**Figure 1.21.** Molecular Structures of (a) **1.39-R** (b) **1.39-S** (c) their corresponding Circular Dichroism (CD) spectra and (d) packing structure of **1.39-S** showing the extrinsic of sodalite channels. Reprinted (adapted) with permission from P. Rajasekar, S. Pandey, J. D. Ferrara, M. Del Campo, P. Le Magueres, R. Boomishankar, *Inorg. Chem.* **2019**, 58, 15017-15020.

Copyright © 2019, American Chemical Society.<sup>105</sup>



## 1.4. Summary and Outlook

Self-assembly encompasses the ability of a system to spontaneously organize itself into an ordered aggregate by a rational combination of complimentary components. Metal-organic cages (MOCs) are one such important class of compounds constructed from metal ions and organic ligands by myriad coordination-driven self-assembly processes. These assemblies possess the advantages of exhibiting distinct portals and well-defined permanent intrinsic cavities, which makes them excellent candidates for exploring host-guest chemistry with high affinity and selectivity for the recognition of guest molecules. Particularly, neutral polyhedral cages have become one of the emerging classes of supramolecular cages owing to their interesting chemistry, charge neutrality and excellent host-guest properties.

In this regard, our group has focused on the main group-based imido-P(V) anions as suitable co-ligands for the construction of neutral polyhedral cages for Pd(II) ions in an effective manner. While historically, the generation of poly-imido anions has been difficult by utilizing reactive organometallic reagents of the alkali, alkaline earth and reactive main-group metals; subsequent efforts were made in our laboratory to synthesize the transition-metal complexes of imido-P(V) anions in a straight-forward facile way. Using the salts of Pd(II) ions in combination with phosphoric triamide ligands with aliphatic substituents, an effortless deprotonation path for generating the highly basic tris(imido)phosphate trianions was developed in polar and protic medium. The anions were isolated as their tri- and hexanuclear Pd(II) complexes. Replacement of the residual acetate bridges in these clusters with wide-angle chelating dicarboxylate ligands has yielded polyhedral neutral assemblies in tetrahedral or cubic topologies. Thus, the use of  $180^\circ$  linkers such as oxalates and anilates has led to the formation of tetrahedral cages, while the  $120^\circ$  linkers like pyrazine dicarboxylate ions gave rise to a cubic cage assembly. These cages were further able to exhibit guest encapsulation behavior, and chiral separation abilities and generate 2D and 3D network structures via the post-assembly pathway, all while keeping the basic Pd-complexed tris(imido)phosphate trianionic moiety intact. Thus, by utilizing and modifying the well-known directional bonding techniques along with employing the imido analogs of main group oxo anions as suitable directing subunits, a series of neutral Pd(II) cages were successfully synthesized.

In addition, there exists plenty of room for the development of the imido-P(V) anions supported by other soft metal ions from both the main group and transition metal series that can give rise to novel structural assemblies and functional materials.

## 1.5. Outline and Objective of Thesis

The aforementioned lack of neutral cages in literature prompted us to design new robust polyhedral assemblies by a simplified pathway. Through the appropriate combination of the imido-Pd<sub>3</sub> PBUs with suitable organic linkers, a number of neutral MOCs have been synthesized over the last few years and their host-guest properties explored. However, in terms of employing and understanding various synthetic and mechanistic strategies, there are still a lot of unexplored opportunities.

This thesis demonstrates a few of those design principles and synthetic strategies in order to create new imido-Pd<sub>3</sub>-based polyhedral neutral cages and explore their host-guest properties, beginning with a study of the mechanistic pathways and the intermediates behind the self-assembly of these cage assemblies, together with their structural and reactivity details (Chapter 2). This idea will further be extended into the synthesis of cages with larger cavities and an elaborate study on the encapsulation of larger, regio-isomeric carborane molecules (Chapter 3). Further along, in Chapter 4 a template mediated pathway to synthesize linker-free, halide-linked neutral metallo-cube from a condensed linker-bound tetrameric precursor. Additionally, the guest binding abilities of this cubic cage towards a number of polar guest molecules will be discussed. Finally, three distinct cases of chiral-achiral subunit self-sorting behaviour of these cages will be described resulting in newer hitherto-unknown assemblies (Chapter 5).

Thus, broadly, this thesis will showcase some of the new findings that has been brought by the development of the imido-P(V) anion chemistry of Pd(II) metal ions. Particularly, the use of imido-Pd<sub>3</sub>-PBUs for the synthesis of neutral polyhedral cages with diverse structural features and exploring their inherent chemistry from a mechanistic point of view. Eventually, the host-guest properties of these new assemblies shall be demonstrated according to their characteristic abilities aided by a number of structural, spectral and theoretical techniques.

## 1.6. References

1. F. Huang, E. V. Anslyn, *Chem. Rev.* **2015**, *115*, 6999-7000.
2. J.-M. Lehn, *Supramolecular Chemistry: Concepts and Perspectives*; VCH: Weinheim, **1995**
3. J.-M. Lehn, *Science* **1985**, *227*, 849–856.
4. J. W. Steed, J. L. Atwood, *Supramolecular Chemistry*; Wiley: Chichester, **2009**.
5. J.-M. Lehn, *Angew. Chem., Int. Ed. Engl.* **1988**, *27*, 89-112.

6. L. Chen, Q. Chen, M. Wu, F. Jiang, M. Hong, *Acc. Chem. Res.* **2015**, *48*, 201-210.
7. L. Xu, Y.-X. Wang, L.-J. Chen, H.-B. Yang, *Chem. Soc. Rev.* **2015**, *44*, 2148-2167.
8. L. Xu, Y.-X. Wang, H.-B. Yang, *Dalton Trans.* **2015**, *44*, 867-890.
9. H. Li, Z.-J. Yao, D. Liu, G.-X. Jin, *Coord. Chem. Rev.* **2015**, *293-294*, 139-157.
10. M. Fujita, O. Sasaki, T. Mitsuhashi, T. Fujita, J. Yazaki, K. Yamaguchi, K. Ogura, *Chem. Commun.* **1996**, 1535-1536.
11. K. Harris, D. Fujita, M. Fujita, *Chem. Commun.* **2013**, *49*, 6703-6712.
12. M. Fujita, M. Tominaga, A. Hori, B. Therrien, *Acc. Chem. Res.* **2005**, *38*, 369-378.
13. T. R. Cook, P. J. Stang, *Chem. Rev.* **2015**, *115*, 7001-7045.
14. P. J. Stang, B. Olenyuk, *Acc. Chem. Res.* **1997**, *30*, 502-518.
15. M. M. J. Smulders, I. A. Riddell, C. Browne, J. R. Nitschke, *Chem. Soc. Rev.* **2013**, *42*, 1728-1754.
16. J. R. Nitschke, *Acc. Chem. Res.* **2007**, *40*, 103-112.
17. Z. Zhou, D.-G. Chen, M. L. Saha, H. Wang, X. Li, P.-T. Chou, P. J. Stang, *J. Am. Chem. Soc.* **2019**, *141*, 5535-5543.
18. A. Garci, K. J. Castor, J. Fakhoury, J.-L. Do, J. Di Trani, P. Chidchob, R. S. Stein, A. K. Mittermaier, T. Frišćić, H. Sleiman, *J. Am. Chem. Soc.* **2017**, *139*, 16913-16922.
19. G.-F. Huo, X. Shi, Q. Tu, Y.-X. Hu, G.-Y. Wu, G.-Q. Yin, X. Li, L. Xu, H.-M. Ding, H.-B. Yang, *J. Am. Chem. Soc.* **2019**, *141*, 16014-16023.
20. A. J. Musser, P. P. Neelakandan, J. M. Richter, H. Mori, R. H. Friend, J. R. Nitschke, *J. Am. Chem. Soc.* **2017**, *139*, 12050-12059.
21. B. S. Pilgrim, D. A. Roberts, T. G. Lohr, T. K. Ronson, J. R. Nitschke, *Nat. Chem.* **2017**, *9*, 1276-1281.
22. I. M. Müller, S. Spillmann, H. Franck, R. Pietschnig, *Chem. Eur. J.* **2004**, *10*, 2207-2213.
23. Q.-F. Sun, S. Sato, M. Fujita, *Nat. Chem.* **2012**, *4*, 330-333.
24. N. Liu, T. Lin, M. Wu, H.-K. Luo, S.-L. Huang, T. S. A. Hor, *J. Am. Chem. Soc.* **2019**, *141*, 9448-9452.
25. G. Yu, B. Zhu, L. Shao, J. Zhou, M. L. Saha, B. Shi, Z. Zhang, T. Hong, S. Li, X. Chen, P. J. Stang, *Proc. Natl. Acad. Sci. U.S.A.* **2019**, *116*, 6618-6623.
26. R. Chakrabarty, P. S. Mukherjee, P. J. Stang, *Chem. Rev.* **2011**, *111*, 6810-6918.
27. P. J. Stang, *J. Org. Chem.* **2009**, *74*, 2-20.
28. B. H. Northrop, D. Chercka, P. J. Stang, *Tetrahedron* **2008**, *64*, 11495-11503.
29. D. L. Caulder, K. N. Raymond, *J. Chem. Soc., Dalton Trans.* **1999**, 1185-1200.

30. D. L. Caulder, K. N. Raymond, *Acc. Chem. Res.* **1999**, *32*, 975-982.
31. D. L. Caulder, C. Brückner, R. E. Powers, S. König, T. N. Parac, J. A. Leary, K. N. Raymond, *J. Am. Chem. Soc.* **2001**, *123*, 8923-8938.
32. M. Fujita, M. Tominaga, A. Hori, B. Therrien, *Acc. Chem. Res.* **2005**, *38*, 369-378.
33. M. Fujita, K. Umemoto, M. Yoshizawa, N. Fujita, T. Kusakawa, K. Biradha, *Chem. Commun.* **2001**, 509-518.
34. M. Fujita, *Chem. Soc. Rev.* **1998**, *27*, 417-425.
35. C. G. Oliveri, P. A. Ulmann, M. J. Wiester, C. A. Mirkin, *Acc. Chem. Res.* **2008**, *41*, 1618-1629.
36. N. C. Gianneschi, M. S. Masar, C. A. Mirkin, *Acc. Chem. Res.* **2005**, *38*, 825-837.
37. B. J. Holliday, C. A. Mirkin, *Angew. Chem. Int. Ed.* **2001**, *40*, 2022-2043.
38. Q.-F. Sun, J. Iwasa, D. Ogawa, Y. Ishido, S. Sato, T. Ozeki, Y. Sei, K. Yamaguchi, M. Fujita, *Science* **2010**, *328*, 1144-1147.
39. M. Yoshizawa, J. K. Klosterman, M. Fujita, *Angew. Chem. Int. Ed.* **2009**, *48*, 3418-3438.
40. C. J. Brown, F. D. Toste, R. G. Bergman, K. N. Raymond, *Chem. Rev.* **2015**, *115*, 3012-3035.
41. M. Raynal, P. Ballester, A. Vidal-Ferran, P. W. N. M. van Leeuwen, *Chem. Soc. Rev.* **2014**, *43*, 1734-1787.
42. S. Qin, Y. Lei, J. Guo, J.-F. Huang, C.-P. Hou, J.-M. Liu, *ACS Appl. Mater. Interfaces* **2021**, *13*, 25960-25971.
43. D. Zhang, T. K. Ronson, Y.-Q. Zou, J. R. Nitschke, *Nat. Rev. Chem.* **2021**, *5*, 168-182.
44. W. Xuan, M. Zhang, Y. Liu, Z. Chen, Y. Cui, *J. Am. Chem. Soc.* **2012**, *134*, 6904-6907.
45. T. Kida, T. Iwamoto, H. Asahara, T. Hinoue, M. Akashi, *J. Am. Chem. Soc.* **2013**, *135*, 3371-3374.
46. J. K. Clegg, J. Cremers, A. J. Hogben, B. Breiner, M. M. J. Smulders, J. D. Thoburn, J. R. Nitschke, *Chem. Sci.* **2013**, *4*, 68-76.
47. C.-Y. Zhu, M. Pan, C.-Y. Su, *Isr. J. Chem.* **2019**, *59*, 209-219.
48. S. M. McNeill, D. Preston, J. E. M. Lewis, A. Robert, K. Knerr-Rupp, D. O. Graham, J. R. Wright, G. I. Giles, J. D. Crowley, *Dalton Trans.* **2015**, *44*, 11129-11136.
49. J. E. M. Lewis, E. L. Gavey, S. A. Cameron, J. D. Crowley, *Chem. Sci.* **2012**, *3*, 778-784.
50. J. W. Yi, N. P. E. Barry, M. A. Furrer, O. Zava, P. J. Dyson, B. Therrien, B. H. Kim, *Bioconjugate Chem.* **2012**, *23*, 461-471.

51. A. Jiménez, R. A. Bilbeisi, T. K. Ronson, S. Zarra, C. Woodhead, J. R. Nitschke, *Angew. Chem. Int. Ed.* **2014**, *53*, 4556-4560.
52. M. Whitehead, S. Turega, A. Stephenson, C. A. Hunter, M. D. Ward, *Chem. Sci.* **2013**, *4*, 2744-2751.
53. A. J. McConnell, C. M. Aitchison, A. B. Grommet, J. R. Nitschke, *J. Am. Chem. Soc.* **2017**, *139*, 6294-6297.
54. A. M. Castilla, T. K. Ronson, J. R. Nitschke, *J. Am. Chem. Soc.* **2016**, *138*, 2342-2351.
55. N. Busschaert, C. Caltagirone, W. Van Rossom, P. A. Gale, *Chem. Rev.* **2015**, *115*, 8038-8155.
56. A. J. Metherell, W. Cullen, N. H. Williams, M. D. Ward, *Chem. Eur. J.* **2018**, *24*, 1554-1560.
57. J. H. Jordan, B. C. Gibb, *Chem. Soc. Rev.* **2015**, *44*, 547-585.
58. F. Diederich, *Angew. Chem., Int. Ed. Engl.* **1988**, *27*, 362-386.
59. C. J. Hastings, M. D. Pluth, S. M. Biros, R. G. Bergman, K. N. Raymond, *Tetrahedron* **2008**, *64*, 8362-8367.
60. F. J. Rizzuto, L. K. S. von Krbek, J. R. Nitschke, *Nat. Rev. Chem.* **2019**, *3*, 204-222.
61. S. Mecozzi, J. J. Rebek, *Chem. Eur. J.* **1998**, *4*, 1016-1022.
62. F. Feixas, S. Lindert, W. Sinko, J. A. McCammon, *Biophys. Chem.* **2014**, *186*, 31-45.
63. A. E. Martín Díaz, J. E. M. Lewis, *Front. Chem.* **2021**, *9*.
64. D. Zhang, T. K. Ronson, J. R. Nitschke, *Acc. Chem. Res.* **2018**, *51*, 2423-2436.
65. M. D. Pluth, D. W. Johnson, G. Szigethy, A. V. Davis, S. J. Teat, A. G. Oliver, R. G. Bergman, K. N. Raymond, *Inorg. Chem.* **2009**, *48*, 111-120.
66. G. Szalóki, V. Croué, M. Allain, S. Goeb, M. Sallé, *Chem. Commun.* **2016**, *52*, 10012-10015.
67. P. Thanasekaran, C.-H. Lee, K.-L. Lu, *Coord. Chem. Rev.* **2014**, *280*, 96-175.
68. S. A. Boer, K. F. White, B. Slater, A. J. Emerson, G. P. Knowles, W. A. Donald, A. W. Thornton, B. P. Ladewig, T. D. M. Bell, M. R. Hill, A. L. Chaffee, B. F. Abrahams, D. R. Turner, *Chem. Eur. J.* **2019**, *25*, 8489-8493.
69. K. Dehnicke, F. Weller, *Coord. Chem. Rev.*, **1997**, *158*, 103-169.
70. K. Dehnicke, M. Krieger, W. Massa, *Coord. Chem. Rev.* **1999**, *182*, 19-65.
71. M. Witt, H. W. Roesky, *Chem. Rev.* **1994**, *94*, 1163-1181.
72. J. K. Brask, T. Chivers, *Angew. Chem. Int. Ed.* **2001**, *40*, 3960-3976.
73. T. Chivers, *Top. Curr. Chem.* **2003**, *229*, 143-159.

74. T. Chivers, R. W. Hilts, *Coord. Chem. Rev.* **1994**, *137*, 201-232.
75. M. A. Beswick, D. S. Wright, *Coord. Chem. Rev.* **1998**, *176*, 373-406.
76. R. Fleischer, D. Stalke, *Coord. Chem. Rev.* **1998**, *176*, 431-450.
77. G. M. Aspinall, M. C. Copley, A. P. Leedham, C. A. Russell, *Coord. Chem. Rev.* **2002**, *227*, 217-232.
78. A. Steiner, S. Zacchini, P. I. Richards, *Coord. Chem. Rev.* **2002**, *227*, 193-216.
79. L. Stahl, *Coord. Chem. Rev.* **2000**, *210*, 203-250.
80. U. Riese, N. Faza, W. Massa, K. Dehnicke, *Angew. Chem. Int. Ed. Engl.*, **1999**, *38*, 528-531.
81. A. Steiner, D. Stalke, *Inorg. Chem.* **1993**, *32*, 1977-1981.
82. M. Sarkar, P. Rajasekar, C. Jose, R. Boomishankar, *Chem. Rec.* **2021**, e202100281
83. L. T. Burke, E. Hevia-Freire, R. Holland, J. C. Jeffery, A. P. Leedham, C. A. Russell, A. Steiner, A. Zagorski, *Chem. Commun.* **2000**, 1769-1770.
84. G. G. Briand, T. Chivers, M. Krahn, M. Parvez, *Inorg. Chem.* **2002**, *41*, 6808-6815.
85. P. R. Raithby, C. A. Russell, A. Steiner, D. S. Wright, *Angew. Chem. Int. Ed. Engl.* **1997**, *36*, 649-650.
86. R. Fleischer, D. Stalke, *Inorg. Chem.* **1997**, *36*, 2413-2419.
87. A. Armstrong, T. Chivers, M. Krahn, M. Parvez, G. Schatte, *Chem. Commun.* **2002**, 2332-2333.
88. B. Nekoueishahraki, H. W. Roesky, G. Schwab, D. Stern, D. Stalke, *Inorg. Chem.* **2009**, *48*, 9174-9179.
89. J. F. Bickley, M. C. Copley, J. C. Jeffery, A. P. Leedham, C. A. Russell, D. Stalke, A. Steiner, T. Stey, S. Zacchini, *Dalton Trans.* **2004**, 989-995.
90. R. L. Stapleton, J. Chai, N. J. Taylor, S. Collins, *Organomet.* **2006**, *25*, 2514-2524.
91. D. N. Woodruff, E. J. L. McInnes, D. O. Sells, R. E. P. Winpenny, R. A. Layfield, *Inorg. Chem.* **2012**, *51*, 9104-9109.
92. T. Chivers, Z. Fu, L. K. Thompson, *Chem. Commun.* **2005**, 2339-2341
93. A. K. Gupta, F. A. S. Chipem, R. Boomishankar, *Dalton Trans.* **2012**, *41*, 1848-1853.
94. A. K. Gupta, A. Steiner, R. Boomishankar, *Dalton Trans.* **2012**, *41*, 9753-9759.
95. A. K. Gupta, S. A. D. Reddy, R. Boomishankar, *Inorg. Chem.* **2013**, *52*, 7608-7614.
96. A. K. Gupta, S. A. D. Reddy, P. Rajasekar, P. Prakash, R. Boomishankar, *Chem. Select.* **2017**, *2*, 10636-10641.

97. A. K. Gupta, A. Yadav, A. K. Srivastava, K. R. Ramya, H. Paithankar, S. Nandi, J. Chugh, R. Boomishankar, *Inorg. Chem.* **2015**, *54*, 3196-3202
98. A. Yadav, M. Sarkar, S. Subrahmanyam, A. Chaudhary, E. Hey-Hawkins, R. Boomishankar, *Chem. -Eur. J.* **2020**, *26*, 4209-4213.
99. M. L. Connolly, *J. Mol. Graphics* **1993**, *11*, 139– 141
100. L. J. Barbour, *Chem. Commun.* **2006**, 1163– 1168
101. M. Han, D. M. Engelhard, G. H. Clever, *Chem. Soc. Rev.* **2014**, *43*, 1848-1860.
102. D. Samanta, P. S. Mukherjee, *Chem. -Eur. J.* **2014**, *20*, 12483-12492
103. A. Yadav, A. K. Gupta, A. Steiner, R. Boomishankar, *Chem. -Eur. J.* **2017**, *23*, 18296-18302.
104. P. Rajasekar, S. Pandey, H. Paithankar, J. Chugh, A. Steiner, R. Boomishankar, *Chem. Commun.* **2018**, *54*, 1873-1876.
105. P. Rajasekar, S. Pandey, J. D. Ferrara, M. Del Campo, P. Le Magueres, R. Boomishankar, *Inorg. Chem.* **2019**, *58*, 15017-15020.
106. W. Xuan, M. Zhang, Y. Liu, Z. Chen, Y. Cui, *J. Am. Chem. Soc.* **2012**, *134*, 6904-6907.
107. J. Dong, Y. Zhou, F. Zhang, Y. Cui, *Chem. -Eur. J.* **2014**, *20*, 6455-6461.

 End of Chapter 1 

# Chapter 2



## **Mapping the Assembly of Neutral Tetrahedral Cages Tethered by Oximido Linkers and Their Guest Encapsulation Studies**



## 2.1. Introduction

The formation of architecturally complex polyhedral coordination cages, from a combination of labile metal ions and simple organic bridging ligands, has continued to fascinate supramolecular chemists for quite a few decades now.<sup>1-7</sup> One of the powerful strategies for the efficient synthesis of such supramolecular assemblies involves the use of well-arranged polyhedral building units (PBUs) in combination with suitable linker motifs leading to self-assembled cages with specifically desired geometries and functions.<sup>8,9</sup> Thus, cages with cationic, anionic, and neutral frameworks can be synthesized by the selection of appropriate PBU precursors and linker ligands.<sup>10,11</sup> Apart from the topological feasibilities,<sup>12,13</sup> the reactivities of the participating moieties also determine the pathway and consequently, the product formation in the molecular self-assembly.<sup>14-16</sup> Factors such as the concentration of the reactants,<sup>17-20</sup> external stimuli,<sup>21-30</sup> reaction templates<sup>31-35</sup> and post-assembly transformations,<sup>36-39</sup> etc. are some of the most important ones that affect the component reactivity and the formation of the suitable products. Nevertheless, the precise understanding of the synthetic pathways of these cage assemblies together with their structural and reactivity details have provided deep insights into the mechanistic pathways behind the self-assembly process.<sup>40-44</sup>

Neutral metal-organic cages are an attractive class of compounds as they can emulate the functional properties of both the metal-organic frameworks (MOFs) and metal-organic polyhedra (MOPs). Our group has been engaged in synthesizing one such class of neutral polyhedral cluster cages built from trinuclear Pd(II) motifs<sup>45</sup> of the type  $[\text{Pd}_3(\text{N}^i\text{Pr})_3\text{PO}]^{3+}$  (denoted as  $\text{Pd}_3\text{X}$  PBUs), *cis*-protected by tris-imido(phosphate)trianions of formula  $[(\text{N}^i\text{Pr})_3\text{PO}]^{3-}$  marked as  $[\text{X}]^{3-}$  and wide-angled chelating linkers such as oxalate,<sup>46,47</sup> anilates,<sup>48</sup> and other dianionic dicarboxylate motifs.<sup>49</sup> These cages have shown interesting host-guest chemistry, chiral recognition and separation, and post-assembly reactions.<sup>50</sup> The formation of these cages can be understood from the geometric parameters provided by the  $\text{Pd}_3$ -clusters and the linker motifs via a directional bonding approach. However, an understanding of their step-wise construction from the building blocks has so far been not possible due to the high reactivity of the imido- $\text{Pd}_3$  precursors with the employed linker ligands. Oxamide and its N-substituted derivatives are analogous to oxalate ions for their coordination abilities, except that they can exhibit less reactivity due to the presence of amide bonds in them. Hence, we set out to test these somewhat less reactive linker ligands in pursuit of isolating certain intermediate

species involved in these cage-formation reactions.

Herein, we report two new tetrahedral cages  $[\{\text{Pd}_3(\text{N}^i\text{Pr})_3\text{PO}\}_4(\text{L}^1)_6]$  (**2.1-TD**) and  $[\{\text{Pd}_3(\text{N}^i\text{Pr})_3\text{PO}\}_4(\text{L}^2)_6]$  (**2.2-TD**) obtained from the reaction of the dimeric imido-Pd<sub>3</sub> precursor  $[\{\text{Pd}_3(\text{N}^i\text{Pr})_3\text{PO}\}_2(\text{OAc})_2(\text{OH})]_2 \cdot 2(\text{CH}_3)_2\text{SO}$  (**HEXA-Pd**) and oxamide  $[\text{L}^1: \{\text{C}_2(\text{NH})_2\text{O}_2\}^{2-}]$  and N, N'-dimethyl oxamide  $[\text{L}^2: \{\text{C}_2(\text{NMe})_2\text{O}_2\}^{2-}]$  linkers, respectively. By performing the reaction at a slightly lower temperature, the tetrameric macrocycles  $[\{\text{Pd}_3(\text{N}^i\text{Pr})_3\text{PO}\}_4(\text{L}^1)_2(\text{OAc})_4(\text{OMe})_4]$  (**2.1-TM**) and  $[\{\text{Pd}_3(\text{N}^i\text{Pr})_3\text{PO}\}_4(\text{L}^2)_2(\text{OAc})_4(\text{OMe})_4]$  (**2.2-TM**) were isolated. Interestingly, conversion of **2.1-TM** to **2.1-TD** and **2.2-TM** to **2.2-TD** have been realized when their corresponding reaction mixtures were heated at slightly elevated temperatures. These observations were supported by monitoring their reactions by NMR and mass-spectrometric techniques and by understanding their relative energies through computational studies. Investigation of the host-guest properties of these cages showed the efficient binding of guest molecules such as benzene, fluorobenzene, and small-sized halogenated solvents at the intrinsic cavity of **2.1-TD**. These observations will inspire the use of these unique Pd<sub>3</sub>X PBUs for the design of cage assemblies of various topologies and functions.

## 2.2. Experimental Details

### 2.2.1. General Remarks

All manipulations involving phosphorus halides were performed under a dry nitrogen atmosphere in standard Schlenk glassware. Dry Solvents were purchased from local vendors and used without further purification. The isopropylamine, methylamine, oxamide, oxalyl chloride, palladium acetate were purchased from Aldrich and used as received. POCl<sub>3</sub> was purchased locally and was distilled prior to use. The ligand  $[\text{PO}(\text{N}^i\text{Pr})_3]$  and the PBU precursor, **HEXA-Pd**  $[\{\text{Pd}_3(\text{N}^i\text{Pr})_3\text{PO}\}_2(\text{OAc})_2(\text{OH})]_2 \cdot 2(\text{CH}_3)_2\text{SO}$ , was prepared by the earlier reported procedures.<sup>45,46</sup> The linker L<sup>2</sup>H<sub>2</sub> was synthesized according to the earlier reported procedure from the reaction of oxalyl chloride and methylamine.<sup>51</sup> NMR spectra were recorded on a Bruker or Jeol 400 MHz spectrometer (<sup>1</sup>H NMR: 400.13 MHz, <sup>13</sup>C{<sup>1</sup>H} NMR: 100.62 MHz, <sup>31</sup>P{<sup>1</sup>H} NMR: 161.97 MHz) spectrometer at room temperature using TMS (<sup>1</sup>H, <sup>13</sup>C) and 85% H<sub>3</sub>PO<sub>4</sub> (<sup>31</sup>P). The mass spectra were obtained on an Applied Bio system matrix-assisted laser desorption ionization time-of-flight (MALDI-TOF)/TOF spectrometer. For mass spectral measurements, both 2,5-dihydroxybenzoic acid (DHB) and α-cyano-4-hydroxy-cinnamic acid (CHCA) matrix or a 1:1 mixture of them has been used as the matrix. Thermal analysis (TGA)

data have been obtained from a PerkinElmer STA-6000 thermogravimetric analyzer. Elemental analyses were performed on a Vario-EL cube elemental analyzer.

### 2.2.2. Syntheses

**2.2.2.1. Synthesis of 2.1-TM:** To a stirred solution of **HEXA-Pd**, (20 mg, 0.0140 mmol) in 1:1 DMSO-MeOH at room temperature, oxamide (1.85 mg, 0.0210 mmol) was added. The resultant mixture was heated at 65°C for 30 min to yield a yellow-colored precipitate. The precipitated compound was recovered by filtration, washed with 2-5ml methanol several times, and dried under vacuum. Yellow needle-like crystals were obtained from its methanol-chloroform solution (by solvent evaporation method) after 7-10 days. Yield: 68% (based on P). MALDI-TOF/TOF: Expected- 2685.52, Found- 2686.24 [M+H]<sup>+</sup>. <sup>31</sup>P NMR (161 MHz, CDCl<sub>3</sub>): δ 74.20; <sup>1</sup>H NMR (400 MHz, CDCl<sub>3</sub>): δ 1.24 (d, *J* = 6.8 Hz, CH<sub>3</sub>), 2.30 (b, NH), 2.92 (s, OCOCH<sub>3</sub>), 3.38 (m, CH), 3.68 (s, OCH<sub>3</sub>); <sup>13</sup>C NMR (100 MHz, CDCl<sub>3</sub>): δ 23.84, 26.79, 51.27, 171.03, 173.45. Elemental Analysis (%): Calcd for C<sub>52</sub>H<sub>115</sub>N<sub>16</sub>O<sub>20</sub>P<sub>4</sub>Pd<sub>12</sub>: C, 23.26; H, 4.32; N, 8.35. Found: C, 23.22; H, 4.45; N, 8.41.

**2.2.2.2. Synthesis of 2.2-TM:** To a stirred solution of **HEXA-Pd**, (20 mg, 0.0140 mmol) in 1:1 DMSO-MeOH at room temperature, N, N'-dimethyl oxamide (2.45 mg, 0.0210 mmol) was added. The resultant mixture was heated at 65°C for 30 min to yield a yellowish-orange colored precipitate. The precipitated compound was recovered by filtration, washed with 2-5ml methanol several times, and dried under vacuum. Orange needle-shaped crystals were obtained from its methanol-chloroform solution (by solvent evaporation method) after 7-10 days. Yield: 72% (based on P). MALDI-TOF/TOF: Expected- 2740.63, Found- 2740.99 [M]<sup>+</sup>. <sup>31</sup>P NMR (161 MHz, CDCl<sub>3</sub>): δ 74.62; <sup>1</sup>H NMR (400 MHz, CDCl<sub>3</sub>): δ 1.25 (d, *J* = 6.8 Hz, CH<sub>3</sub>), 2.65 (s, NCH<sub>3</sub>), 2.91 (s, OCOCH<sub>3</sub>), 3.39 (m, CH), 3.90 (s, OCH<sub>3</sub>); <sup>13</sup>C NMR (100 MHz, CDCl<sub>3</sub>): δ 23.61, 25.98, 34.41, 50.88, 170.76, 173.81. Elemental Analysis (%): Calcd for C<sub>56</sub>H<sub>123</sub>N<sub>16</sub>O<sub>20</sub>P<sub>4</sub>Pd<sub>12</sub>: C, 24.53; H, 4.52; N, 8.17. Found: C, 24.47; H, 4.64; N, 8.23.

**2.2.2.3. Synthesis of 2.1-TD:** To a methanolic solution of **HEXA-Pd**, (20 mg, 0.0140 mmol) at room temperature, oxamide (1.85 mg, 0.0210 mmol) was added. The resultant mixture was heated at 85°C for 4 hours to yield a yellow-colored precipitate. The precipitated compound was recovered by filtration, washed with 2-5ml methanol several times, and dried under vacuum. Yellow square-shaped crystals were obtained from its chloroform mixture (by solvent evaporation method) after 15-20 days. Yield: 73% (based on P). MALDI-TOF/TOF: Expected- 2669.38, Found- 2708.55 [M+K]<sup>+</sup>. <sup>31</sup>P NMR (161 MHz, CDCl<sub>3</sub>): δ 73.00; <sup>1</sup>H NMR (400 MHz,

$\text{CDCl}_3$ ):  $\delta$  1.74 (d,  $J = 6.6$  Hz,  $\text{CH}_3$ ), 2.88 (m, CH);  $^{13}\text{C}$  NMR (100 MHz,  $\text{CDCl}_3$ ):  $\delta$  27.14, 30.55, 177.12. Elemental Analysis (%): Calcd for  $\text{C}_{48}\text{H}_{96}\text{N}_{24}\text{O}_{16}\text{P}_4\text{Pd}_{12}$ : C, 21.62; H, 3.63; N, 12.61. Found: C, 21.58; H, 3.77; N, 12.67.

**2.2.2.4. Synthesis of 2.2-TD:** To a methanolic solution of **HEXA-Pd**, (20 mg, 0.0140 mmol) at room temperature, N, N'-dimethyloxamide (2.45 mg, 0.0210 mmol) was added. The resultant mixture was heated at 85°C for 4 hours resulting in a yellowish-orange clear solution. The solution was filtered through celite. Orange-colored square-shaped crystals were obtained from its methanol solution (by solvent evaporation method) after 15-20 days. Yield: 80% (based on P). MALDI-TOF/TOF: Expected- 2834.71, Found- 2834.58  $[\text{M}]^+$ .  $^{31}\text{P}$  NMR (161 MHz,  $\text{CDCl}_3$ ):  $\delta$  72.46;  $^1\text{H}$  NMR (400 MHz,  $\text{CDCl}_3$ ):  $\delta$  1.75 (d,  $J = 6.6$  Hz,  $\text{CH}_3$ ), 2.62 (s,  $\text{NCH}_3$ ), 2.96 (m, CH);  $^{13}\text{C}$  NMR (100 MHz,  $\text{CDCl}_3$ ):  $\delta$  27.67, 30.15, 34.29, 178.83. Elemental Analysis (%): Calcd for  $\text{C}_{60}\text{H}_{120}\text{N}_{24}\text{O}_{16}\text{P}_4\text{Pd}_{12}$ : C, 25.42; H, 4.27; N, 11.86. Found: C, 25.37; H, 4.40; N, 12.02.

### 2.2.3. Crystallography

Reflections were collected on a Bruker Smart Apex Duo diffractometer at 100 K using Mo  $K\alpha$  radiation ( $\lambda = 0.71073$  Å). All structures were solved using intrinsic phasing method and refined by full-matrix least-squares on  $F^2$  (G. M. Sheldrick, SHELX-2014, program for crystal structure refinement, University of Gottingen, Germany, 2015).<sup>52</sup> Crystallographic data for all these compounds are listed in Table 2.1 and 2.2. All non-hydrogen atoms were refined anisotropically if not stated otherwise. The crystals of **2.1-TM** diffracted very weakly at higher angles and hence its data is truncated to  $2\theta = 50^\circ$ . Hydrogen atoms were constrained in geometric positions to their parent atoms. The diffuse solvent molecules in both **2.1-TM** and **2.1-TD** could not be modeled appropriately. Hence, these were treated as diffuse contributions to the overall scattering and removed by the SQUEEZE/PLATON for better refinement data. The squeezed volume in **2.1-TM** was found to be  $755\text{Å}^3$  which corresponds approximately to 10 water molecules and 8 methanol molecules. The squeezed volume in **2.1-TD** was found to be  $1376.5\text{Å}^3$  which accounted for approximately 40 water molecules. The disordered DMSO guest in **2.1-TD** was modelled using similar distance and similar U-restraint (SAME/SIMU) command of the SHELX. In the final refinements, OMIT command was used to remove a number of reflections for which  $I(\text{obs})$  and  $I(\text{calc})$  differed more than 10 times SigmaW (the latter being the square root of  $1.0/\text{weight}$  for that reflection in the L.S. refinement).

Table 2.1. Crystallographic Data for 2.1-TM and 2.1-TD

Compound	2.1-TM	2.1-TD
Chemical formula	$C_{52}H_{112}N_{16}O_{20}P_4Pd_{12}$	$C_{50}H_{102}N_{24}O_{17}P_4Pd_{12}S$
Formula weight	2682.25	2744.29
Temperature	100(2) K	100(2)K
Crystal system	Triclinic	Monoclinic
Space group	$P\bar{1}$	$P2_1/n$
a (Å); $\alpha$ (°)	11.86(2); 102.49(3)	18.332(19); 90
b (Å); $\beta$ (°)	14.59(3); 103.26(3)	23.777(3); 107.165(3)
c (Å); $\gamma$ (°)	17.38(3); 107.70(4)	30.101(3); 90
V (Å <sup>3</sup> ); Z	2651(8); 1	12537(2); 4
$\rho$ (calc.) mg m <sup>-3</sup>	1.680	1.454
$\mu$ (Mo K $\alpha$ ) mm <sup>-1</sup>	2.097	1.792
$2\theta_{max}$ (°)	50.084	56.774
R(int)	0.2471	0.2818
Data / param.	9351 / 469	31223 / 969
GOF	0.945	1.022
R1 [F > 4 $\sigma$ (F)]	0.0962	0.0631
wR2 (all data)	0.3228	0.2114
max. peak/hole (e.Å <sup>-3</sup> )	1.537/-1.297	1.311/-1.170

Table 2.2. Crystallographic Data for 2.2-TM and 2.2-TD

Compound	2.2-TM	2.2-TD
Chemical formula	C <sub>56</sub> H <sub>116</sub> N <sub>16</sub> O <sub>20</sub> P <sub>4</sub> Pd <sub>12</sub>	C <sub>60</sub> H <sub>120</sub> N <sub>24</sub> O <sub>16</sub> P <sub>4</sub> Pd <sub>12</sub>
Formula weight	2734.32	2837.55
Temperature	100(2)K	100(2)K
Crystal system	Monoclinic	Triclinic
Space group	<i>P2<sub>1</sub>/c</i>	<i>P-1</i>
a (Å); α (°)	18.391(3); 90	19.008(7); 60.091(17)
b (Å); β (°)	17.306(3); 118.714(3)	19.016(8); 60.102(11)
c (Å); γ (°)	18.358(3); 90	19.056(5); 60.103(17)
V (Å <sup>3</sup> ); Z	5124.2(13); 2	4881(3); 2

#### 2.2.4. <sup>1</sup>H-2D-DOSY NMR Studies

The <sup>1</sup>H-2D-DOSY NMR experiments were carried out on a Bruker AVANCE III NMR spectrometer operating at a <sup>1</sup>H frequency of 600 MHz, and a constant temperature of 298 K. 2.0 mM solutions of the participating species and host-guest complexes were prepared in CDCl<sub>3</sub> and allowed to equilibrate for 30 minutes before data acquisition. Diffusion Ordered Spectroscopy (DOSY) experiments were performed by varying gradient strength. The standard Bruker protocol using Topspin 2.1 software was used for processing the DOSY data. The fitting of the diffusion dimension in the 2D-DOSY spectra was carried out using a one-parameter mono-exponential (equation 1) or two-parameter biexponential fits (equation 2).

$$I = I_0 \exp[-D\gamma^2 g^2 \delta^2 (\Delta - \delta/3)] \dots \dots (1)$$

$$I = I_{0A} \exp[-D_A \gamma^2 g^2 \delta^2 (\Delta - \delta/3)] + I_{0B} \exp[-D_B \gamma^2 g^2 \delta^2 (\Delta - \delta/3)] \dots \dots (2)$$

In this equation, I is the observed integral, I<sub>0</sub>, I<sub>0A</sub> and I<sub>0B</sub> are the reference or un-attenuated integrals, D, D<sub>A</sub>, and D<sub>B</sub> are the diffusion coefficients, γ is the gyromagnetic ratio of the

detected nucleus,  $g$  is the gradient strength,  $\delta$  the length of the gradient pulse, and  $\Delta$  the diffusion time.

### 2.2.5. Guest Encapsulation Studies

**2.2.5.1 General procedure for preparation of Guest  $\subset$  2.1-TD Complexes:** 50  $\mu$ l of the guest solvent was added to 10 mg of **2.1-TD**. The resulting solution was stirred further for 30 mins at 35°C. The obtained mixture was analyzed by MALDI-TOF and  $^1\text{H}$ -2D-DOSY NMR spectroscopy which revealed the formation of host-guest complexes.

**2.2.5.2. Procedure for the  $^1\text{H}$ -NMR titration of Guest  $\subset$  2.1-TD Complexes** To perform the  $^1\text{H}$ -NMR titrations, a  $10^{-3}$  M solution of **2.1-TD** was prepared in  $\text{CDCl}_3$ . To this, subsequent equivalents of each of the guest molecules were added. Downfield shifts were observed for the successfully encapsulated systems whereas the unsuccessful ones gave overlapping chemical shifts with respect to the guest proton peak positions. The titration experiment was continued until the peak shifts finally became constant indicating completion of the encapsulation process. The data were then analyzed and fitted in a 1:1 host-guest binding ratio using the Bindfit<sup>53-55</sup> web calculator which gave the final binding constant values.

### 2.2.6. Theoretical Calculations

The gas-phase single-molecule optimization energies of all the participating species and the host-guest systems were calculated theoretically by using the Gaussian 09 software.<sup>56, 57</sup> These energies were computed by DFT methods by employing the b97d3 functional. Energy calculations were performed using the basis set Lanl2dz for Pd in conjunction with the cc-pvtz basis set (for all other atoms).

For the host-guest complexes, the energies of the host cage **2.1-TD**, guest solvents, and host-guest complexes were separately calculated and the binding energy of a given complex was calculated by using the following equation.

$$\text{Binding energy} = E_{\text{Guest} \subset \text{2.1-TD}} - (E_{\text{2.1-TD}} + E_{\text{Guest}})$$

To determine the structural changes associated with the encapsulation of guests in the host cage **2.1-TD**, deformation energies<sup>58</sup> were calculated by the following equation-

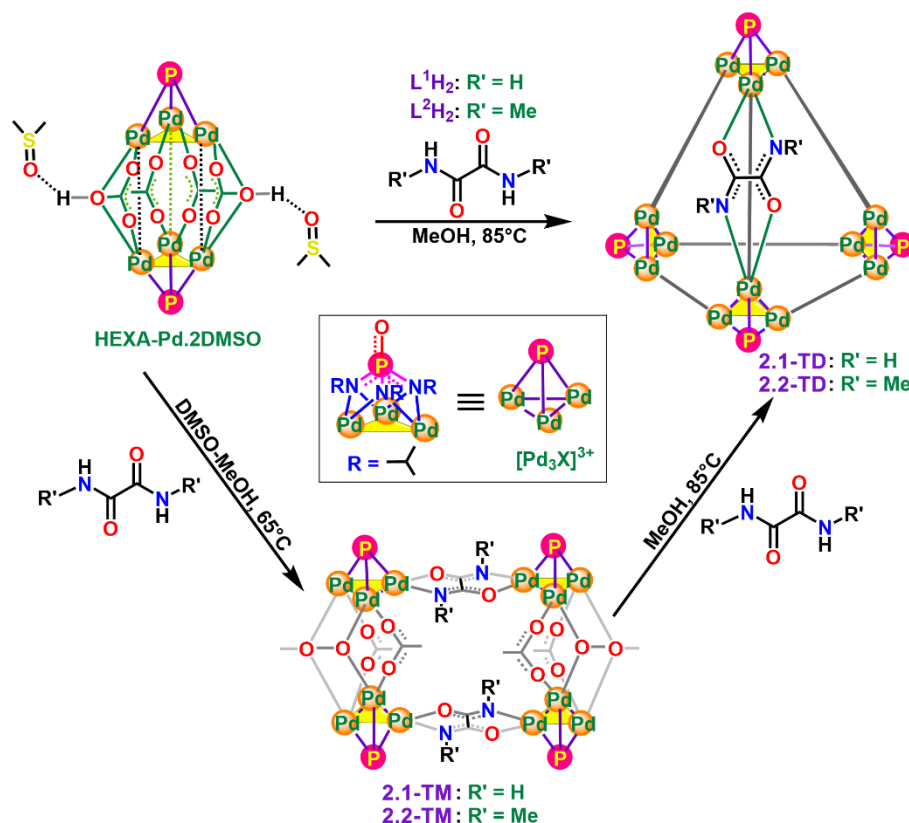
$$\text{Deformation energy} = E_{\text{2.1-TD}} - E_{\text{2.1-TD}}^{\text{enc}}$$

Here,  $E_{2.1-TD}$  is the total energy of the optimized empty cage, and  $E_{2.1-TD}^{enc}$  is obtained by removal of the guest molecule from the host cage followed by a single-point energy calculation on the corresponding structure.

## 2.3. Results and Discussions

### 2.3.1. Synthesis and Structures

The previously reported tetrahedral cage  $\{[Pd_3(N^iPr)_3PO]_4(L)_6\}$  (**2.3-TD**) based on the oxalate linkers ( $L: [C_2O_4]^{2-}$ ) was obtained by the treatment of **HEXA-Pd** with oxalic acid at  $65^\circ C$ .<sup>46</sup> However, treatment of the  $Pd_3$ -dimer with the oxamide ligands  $L^1H_2$  and  $L^2H_2$  at  $65^\circ C$  resulted in the formation of the tetrameric assemblies **2.1-TM** and **2.2-TM** (Scheme 2.1).



**Scheme 2.1.** Synthetic pathway depicting the formation of tetramers **2.1-TM**, **2.2-TM**, and tetrahedral assemblies **2.1-TD**, **2.2-TD** from precursor **HEXA-Pd**.

The  $^{31}P$ -NMR spectra of **2.1-TM** and **2.2-TM** gave a single peak at 74.20 ppm and 74.62 ppm, respectively (Figures A2.1-A2.4, Appendix 2). The MALDI-TOF mass spectra showed peaks centered at  $m/z$  values 2686.24 and 2740.99 for the parent ions of  $[2.1-TM+H]^+$  and  $[2.2-TM]^+$ , respectively (Figures A2.5-A2.6, Appendix 2). Slowly heating the methanolic



solution/suspension of **2.1-TM** and **2.2-TM** at 85°C in a screw-capped vial yielded the respective tetrahedral cages **2.1-TD** and **2.2-TD**.

The cages **2.1-TD** and **2.2-TD** can also be synthesized directly from the corresponding reaction of  $L^1H_2$  and  $L^2H_2$  with the precursor **HEXA-Pd** in MeOH at 85 °C (Scheme 2.1). The  $^{31}P$ -NMR spectra of **2.1-TD** and **2.2-TD** gave peaks at 73.00 and 72.46 ppm, respectively, showing a marginal upfield shift with respect to the signals obtained for **2.1-TM** and **2.2-TM** (Figures A2.7-A2.10, Appendix 2). The MALDI-TOF mass spectra showed peaks centered at  $m/z$  values 2708.55 and 2834.58 for the parent ions of  $[2.1-TD+K]^+$  and  $[2.2-TD]^+$ , respectively (Figures A2.11-A2.12, Appendix 2).

The single crystals of **2.1-TM** and **2.2-TM** were obtained by slow evaporation of their corresponding solutions in methanol-chloroform mixtures. The single crystals of **2.1-TD** were obtained from their chloroform solution, while the crystals of **2.2-TD** were grown from their methanol solution. The crystals of **2.2-TM** were heavily twinned and hence reliable final refinement parameters could not be obtained for its structure. Similarly, **2.2-TD** diffracted very weakly and hence the structural parameters are very weak for this cage. However, both of them show reliable connectivity patterns for their constituent atoms. An overview of the structural descriptions of these structures are provided in Table 2.1 and 2.2.

The molecular structure of **2.1-TM** was solved in the triclinic space group  $P-1$ , and that of **2.2-TM** was obtained in the monoclinic  $P2_1/c$  space group. The asymmetric unit in them contains one-half of the molecule consisting of six Pd-atoms, two imido-phosphate ligands, one oximido dianion, two acetates, and two methoxy groups. The structural determination reveals that both **2.1-TM** and **2.2-TM** are isostructural consisting of four  $Pd_3X$  PBUs, two oximido, and four acetate linkers in their molecular core. In addition, there are four methoxy bridges in the structures of **2.1-TM** and **2.2-TM** to neutralize the charge and coordination at the metal centers (Figure 2.1a and Figures A2.13a, A2.14a, Appendix 2). The origin of methoxy groups can be tracked to the deprotonation of the methanol solvent during these reactions. These tetrameric assemblies are considered as the dimerization products of the precursor complexes, where two acetate groups in each of these dimeric motifs are replaced with the mixed N, O-coordination of the oxamide linkers. Importantly, the coordination of the imido-phosphate ligand remains intact in the tetrameric assemblies of **2.1-TM** and **2.2-TM** preventing the formation of higher-ordered structures for them. The packing structures of **2.1-TM** and **2.2-TM** show the absence of any intrinsic voids in them (Figures A2.15-A2.16,

Appendix 2). However, they exhibit extrinsic cavities of volumes 722.84 and 1066.77 Å<sup>3</sup>, which are about 27.2% and 20.8 % of the overall volumes of their unit cell structures.

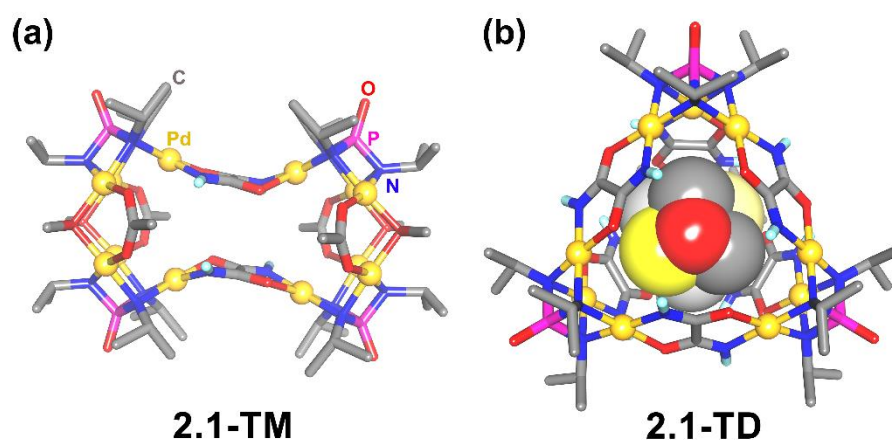


**Figure 2.1.** Molecular structures of (a) **2.1-TM** and (b) **2.1-TD**. The atoms depicted in space-fill model shows the encapsulated DMSO molecules at the intrinsic cavity of **2.1-TD**; one of the disordered fragments of DMSO has been depicted as semi-transparent spheres.

The molecular structure of **2.1-TD**·(CH<sub>3</sub>)<sub>2</sub>SO·(s)<sub>x</sub> was solved in the monoclinic  $P2_1/n$  space group, while that of **2.2-TD**·(s)<sub>x</sub> was solved in the triclinic space group  $P-1$  (the species denoted with ‘s’ are the unassigned solvent molecules). The asymmetric unit in both of them contains the entire cage consisting of twelve Pd-atoms, four imido-phosphate ligands, and six oximido linkers. The cage frameworks in both **2.1-TD** and **2.2-TD** are similar to the earlier reported oxalate-derived cage **2.3-TD**.<sup>46</sup> Each vertex of the cage comprises of the Pd<sub>3</sub>X PBU, in which the three Pd(II) centers are involved in coordination with the tris(imido)phosphate motifs in a *cis*-orientation. The two remaining sites at each of the Pd-sites are located at an angle of 90° and interact with the oximido linkers through the wide-angle chelating N, O-coordination. Thus, each dianionic oximido motif provides an almost linear (180°) linkage to two opposite Pd(II) centers. Six such dianionic linkers connect the four tri-cationic [Pd<sub>3</sub>X]<sup>3+</sup> vertices along the six edges of a tetrahedron leading to the formation of the neutral cage assemblies **2.1-TD** and **2.2-TD**. In contrast, the oximido linkers in both **2.1-TM** and **2.2-TM** are located in a strained coordination geometry due to the presence of shorter acetate and methoxy bridges at the other sides of the macrocycle. The average Pd-N-O-Pd dihedral angle in **2.1-TM** is 17.42° while that found in **2.1-TD** is 2.30° (Figures A2.13c, A2.13d Appendix 2). Further, MSROLL calculations<sup>59,60</sup> performed on the structures of **2.1-TD** and **2.2-TD** showed a void volume of 86.92 and 84.68 Å<sup>3</sup>, respectively, at the interiors of these cages (Table A2.3, A2.4 Appendix 2). The average portal distances at the trigonal faces of **2.1-TD** and **2.2-TD** were measured to

be 4.598 and 2.873 Å, respectively. The smaller portal widths found in the case of **2.2-TD** are attributed to the presence of three oximido-bound methyl groups at each of its triangular faces. The intrinsic cavity of **2.1-TD** was found to contain one molecule of disordered DMSO (Figures 2.1b and A2.17, Appendix 2). The lattice packing of the cages **2.1-TD** and **2.2-TD** showed that they exhibit large exterior voids in addition to their intrinsic cavities (Figures A2.18-A2.19, Appendix 2). These voids account for about 37.2 and 24.4% of the unit cell volume (4658.17 and 1191.42 Å<sup>3</sup>, respectively).

### 2.3.2. Solution Phase Conversions from TM to TD assembly.

It is evident that the macrocyclic products **2.1-TM** and **2.2-TM** are the intermediates associated with the formation of the corresponding tetrahedral cages **2.1-TD** and **2.2-TD**. In order to check the possible existence of any other species in the solution, we set out to investigate the time-dependent <sup>31</sup>P-NMR shifts for the reaction mixtures of **HEXA-Pd** and the oxamide ligands L<sup>2</sup>H<sub>2</sub> at 85°C in d<sub>4</sub>-methanol. These experiments gave a good spectral profile for the reaction involving the **HEXA-Pd** and L<sup>2</sup>H<sub>2</sub>, as both **2.2-TM** and **2.2-TD** exhibit good solubility in MeOH.

As seen in Figure 2, the formation of **2.2-TM** is observed within 15 minutes of the reaction at 85°C and the disappearance of the peak due to the precursor (**HEXA-Pd**) at 30 minutes. Soon after, the peak due to the tetrahedral cage **2.2-TD** appears at 45 minutes of the reaction, whose intensity increases slowly with time. Finally, at the end of 240 minutes, the peak due to **2.2-TM** disappears completely, while **2.2-TD** remains the only product in the solution. Also, no other products were observed during the intermediate time intervals indicating the direct conversion of **2.2-TM** to **2.2-TD** at this temperature. The reaction was stirred for another half an hour and the subsequent analysis of the product isolated from the reaction mixture exhibits identical NMR (both <sup>1</sup>H and <sup>31</sup>P) and MALDI-TOF spectral signatures as that of as-made **2.2-TD** crystals. The conversion from **2.2-TM** to **2.2-TD** was also mapped by the MALDI-TOF spectral profiles collected at various stages of their respective reactions (Figure A2.20, Appendix 2). Similarly, the conversion of **2.1-TM** to **2.1-TD** was also mapped by taking aliquots of the reaction mixture in methanol at regular intervals. The <sup>31</sup>P-NMR data were recorded by diluting the aliquot with CHCl<sub>3</sub> and by using a sealed capillary of CDCl<sub>3</sub> as an external locking standard (Figure A2.21, Appendix 2).

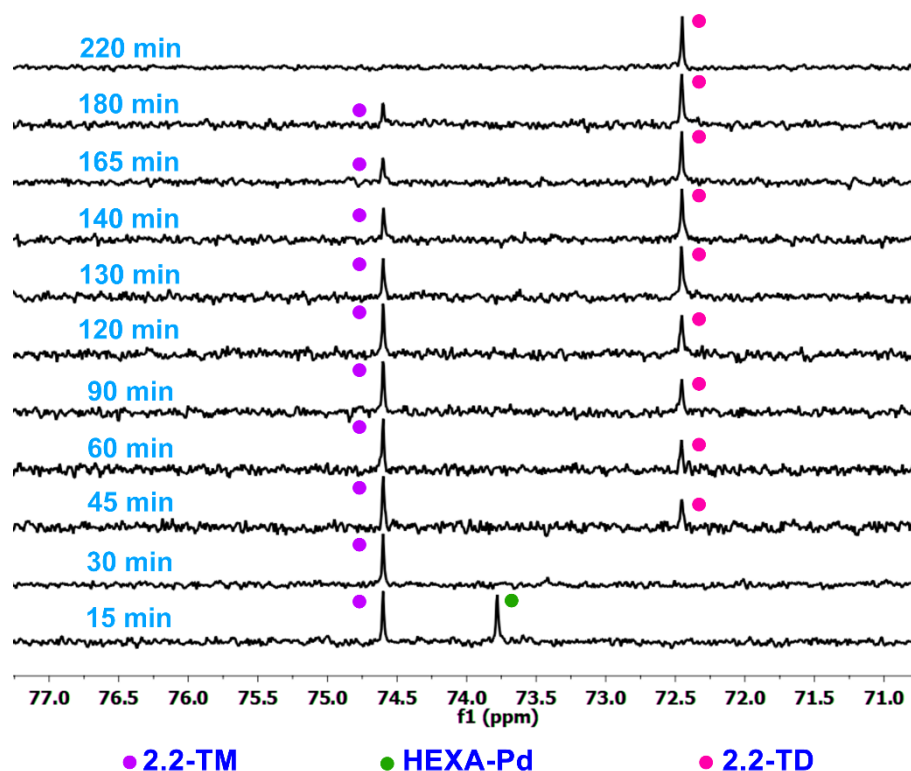


**Figure 2.2.**  $^{31}\text{P}$ -NMR peak intensity changes as **2.2-TM** gradually converts to **2.2-TD**.

Since the  $^1\text{H}$ -NMR spectra showed overlapping peaks for both the **2.2-TM** and **2.2-TD** complexes, the  $^1\text{H}$  2D-diffusion ordered spectroscopy (DOSY) experiment was performed to analyze the mixture of these products. For this experiment, the decay profile of the methyl protons on the  $^i\text{Pr}$  group of the phosphoramidate ligand was studied. As evident from Figure 2.3a, two diffusion coefficient values of  $D = 1.32 \times 10^{-09} \text{ m}^2/\text{s}$  and  $6.87 \times 10^{-10} \text{ m}^2/\text{s}$  were noted for the overlapping peaks of the species **2.2-TM** and **2.2-TD**, respectively. These  $D$  values were found to be closely matched with those observed for pure samples **2.2-TM** and **2.2-TD**, which again exhibit single  $D$  values of  $1.03 \times 10^{-09} \text{ m}^2/\text{s}$  and  $7.91 \times 10^{-10} \text{ m}^2/\text{s}$ , respectively, for their methyl protons (Figures 2.3b, 2.3c). These observations clearly indicate that no other products or intermediates exist in the solution apart from these two compounds (Figure A2.22, Appendix 2).

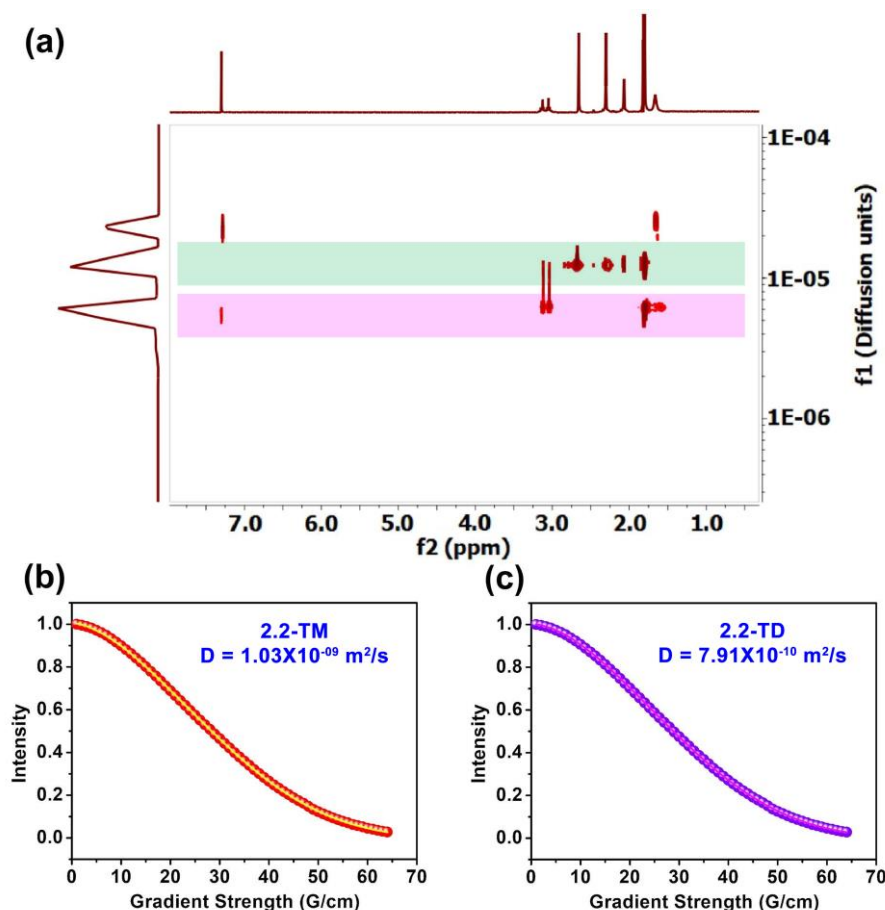


**Figure 2.3.**  $^1\text{H}$  2D-DOSY NMR of (a) mixture of **2.2-TM** and **2.2-TD** after 125 min of stirring. The DOSY band due to **2.2-TM** is being highlighted in green while the band due to **2.2-TD** is highlighted in pink. Integral decay profile of  $-\text{CH}_3$  proton of (b) pure **2.2-TM** ( $\delta$  1.25,  $\text{CDCl}_3$ , 298K) and (c) pure **2.2-TD** cage ( $\delta$  1.75,  $\text{CDCl}_3$ , 298K).

### 2.3.3. Single Molecule Energy Optimization studies for the TM/TD assemblies.

The tendency of formation of the tetrahedral cages from the tetrameric macrocycles shows the better thermodynamic stability and robustness of the former over the latter complexes. This prompted us to look into the gas-phase energies of these complexes obtained from their optimized structures using DFT methods.<sup>56,57</sup> The energy minimized structures of all these four assemblies and the precursor **HEXA-Pd** were found to exhibit similar structural features to those of their corresponding crystal structures (Figure A2.23, Appendix 2). Figure 2.4 shows the graphical representation of the relative energies of these different species. It is evident that the **HEXA-Pd** precursor shows the highest energy of  $-1.77 \times 10^6$  kcal/mol, while the energies for the cages **2.1-TD** ( $-3.46 \times 10^6$  kcal/mol) and **2.2-TD** ( $-3.53 \times 10^6$  kcal/mol), lay at the bottom with the most negative values (Table A2.5 and Figure A2.24, Appendix 2). Intermediate

energies of  $-2.65 \times 10^6$  and  $-3.06 \times 10^6$  kcal/mol were obtained for the macrocycles **2.1-TM** and **2.2-TM**, respectively, which are considerably higher in energy than their tetrahedral counterparts though they are much more stable than the **HEXA-Pd**.

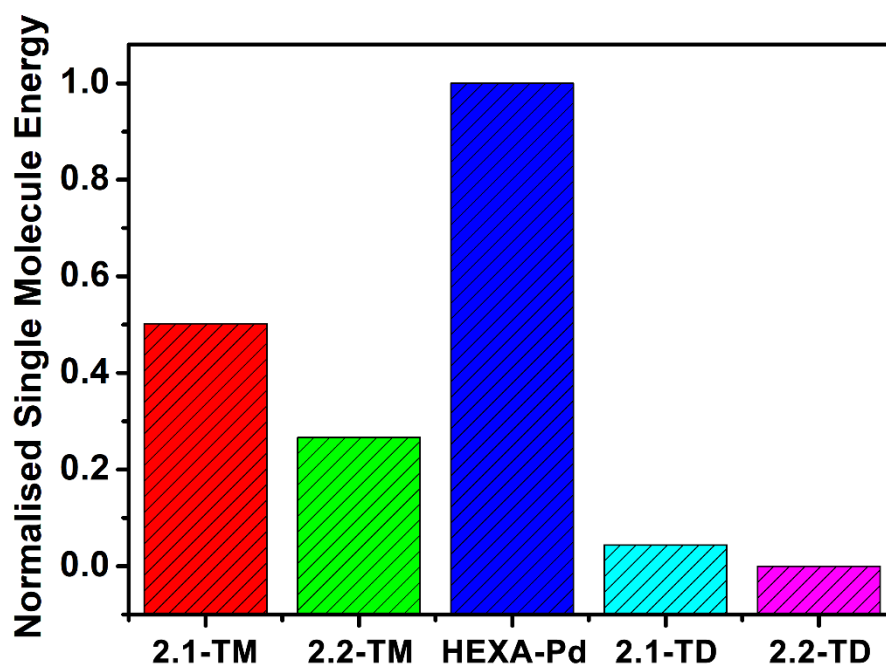


**Figure 2.4.** Graphical Representation of the normalized optimized energies of the participating complexes.

The comparatively higher energy of the macrocycles (**2.1-TM** and **2.2-TM**) over the tetrahedral cages (**2.1-TD** and **2.2-TD**) could be due to the fact that the oxamide linkers are located in a slightly bent conformation in the former complexes than in the latter. The puckered coordination not only imposes a strain on the entire molecule but also narrows the voids located at their internal cavities. However, these linkers are not bent in the tetrahedral cages indicating the reduction of strain in these polyhedral cages and the concomitant lowering of their energies.

Thus, based on structural, spectral, and computational studies, the step-wise formation of these tetrahedral cages can be understood as follows. The sluggish reactivity of the oxamide linkers, irrespective of the stoichiometry of the reaction, replaces only two acetate groups on each of the two dimeric clusters, while the other acetate and methoxy groups on them remain intact. The structure of the as-formed tetramers can be visualized as the dimer of dimeric clusters. Further activation of these tetramers, however, destroys the dimeric sub-units within them and yields the tetrahedral cages in a spontaneous pathway replacing all the remaining acetate and methoxy groups with the oxamide linkers.

However, it is to be noted that all these assemblies (**2.1-TM**, **2.1-TD**, **2.2-TM**, and **2.2-TD**) display excellent thermal stability as determined by the TGA analysis. (Figures A2.25-A2.26, Appendix 2)

### 2.3.4. Guest Encapsulation studies.

Inspired by the excellent guest encapsulation capabilities of the oxalate-bridged cage **1.34**,<sup>46</sup> we set out to investigate the host-guest behavior of both **2.1-TD** and **2.2-TD**. Owing to the presence of intrinsic hydrophobic cavities in them, the encapsulation of a few aliphatic and aromatic solvents such as dichloromethane ( $\text{CH}_2\text{Cl}_2$ ), chloroform ( $\text{CHCl}_3$ ), tetrachloromethane ( $\text{CCl}_4$ ), benzene ( $\text{C}_6\text{H}_6$ ), fluorobenzene ( $\text{C}_6\text{H}_5\text{F}$ ) and chlorobenzene ( $\text{C}_6\text{H}_5\text{Cl}$ ) were investigated.

The initial formation of definite host-guest complexes of **2.1-TD** was investigated using mass spectrometry. Prior to the experiments, the guest solvents were added in excess to the **2.1-TD** host and equilibrated adequately. The MALDI-TOF spectra of these host-guest mixtures showed peaks at  $m/z$  values 2750.87, 2785.13, 2822.27, 2746.23, 2762.11 for host-guest complexes of  $[\text{CH}_2\text{Cl}_2\text{c}2.1\text{-TD}]^+$ ,  $[\text{CHCl}_3\text{c}2.1\text{-TD}]^+$ ,  $[\text{CCl}_4\text{c}2.1\text{-TD}+\text{H}]^+$ ,  $[\text{C}_6\text{H}_6\text{c}2.1\text{-TD}+\text{H}]^+$  and  $[\text{C}_6\text{H}_5\text{F}\text{c}2.1\text{-TD}]^+$ , respectively (Figures A2.27-A2.31, Appendix 2). The signature host-guest peaks were not observed in the case of  $\text{C}_6\text{H}_5\text{Cl}$  indicating the absence of its encapsulation within the cavity of the **2.1-TD** cage. This may be attributed to the larger size of the  $\text{C}_6\text{H}_5\text{Cl}$  guest, which requires a larger volume than that is computed for the intrinsic cavity of the host (**2.1-TD**) system. Although the isostructural cage **2.2-TD** exhibits an almost identical cavity volume as that of **2.1-TD**, it showed poor guest encapsulation capabilities due to the protrusion of the methyl groups on the oxamide linkers at the triangular cage portals preventing access to the incoming guest molecules.

The host-guest behavior of all these Guest  $\text{c}$  **2.1-TD** systems was further probed by the DOSY NMR analysis (Figure A2.32, Appendix 2). For these experiments, diffusion of the isopropyl methyl protons on the cage core and the protons of the guest molecules were monitored by the DOSY technique. Interestingly, the plot of the integral decay profile as a function of the gradient strength fits to bi-exponential decay curves in all the successful encapsulation events. Subsequently, two diffusion coefficient ( $D$ ) values were extracted for both the host and guest protons under study from these curves (Figures 2.5a-c). A closer look at the  $D$ -values reveals that the host and guest protons diffuse at the same rate in the bound state, while faster diffusion rates are observed for both of them in the free state.

Figure 2.5d shows a summarized form of the D values for the host and guest protons studied for the **Guest**  $\subset$  **2.1-TD** systems. The closest value of the bound guest and the bound host was found for the  $\text{C}_6\text{H}_6 \subset \text{2.1-TD}$  system, which indicates that in the bound phase the **2.1-TD** and  $\text{C}_6\text{H}_6$  protons diffuse at closely similar rates signifying a tight association between them. Similar trends in diffusion were observed for all the other guest molecules exhibiting two D-values in the solution media, pertaining to the free and bound states.

In contrast, the DOSY profiles for the **2.1-TD**+ $\text{C}_6\text{H}_5\text{Cl}$  mixture gave a single D-value for each of the host and guest protons suggesting the lack of guest encapsulation in it (Table A2.6, Appendix 2). Also, due to the absence of protons in  $\text{CCl}_4$ , the diffusion coefficients of only the cage in the free and bound state were observed for the  $\text{CCl}_4 \subset \text{2.1-TD}$  system.

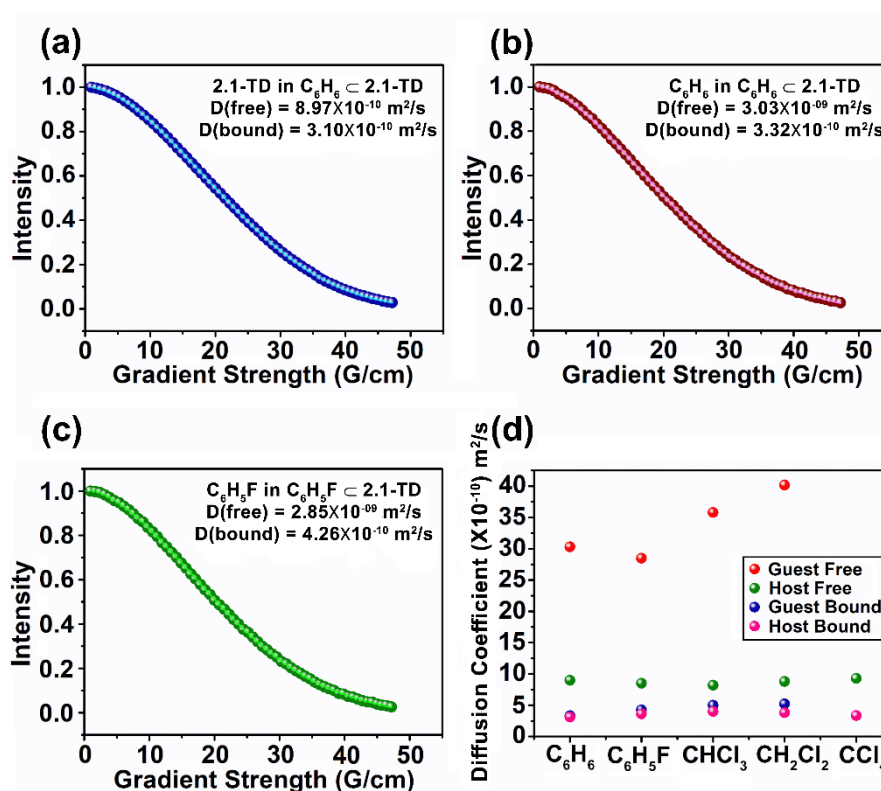


**Figure 2.5.** Integral decay profile of (a) **2.1-TD** in  $\text{C}_6\text{H}_6 \subset \text{2.1-TD}$  ( $\delta$  1.74,  $\text{CDCl}_3$ , 298K) (b)  $\text{C}_6\text{H}_6$  in  $\text{C}_6\text{H}_6 \subset \text{2.1-TD}$  ( $\delta$  7.40,  $\text{CDCl}_3$ , 298K) (c)  $\text{C}_6\text{H}_5\text{F}$  in  $\text{C}_6\text{H}_5\text{F} \subset \text{2.1-TD}$  ( $\delta$  7.35,  $\text{CDCl}_3$ , 298K) (d) Summary of the D values for the host and guest protons studied for the **Guest**  $\subset$  **2.1-TD** systems.

To further evaluate the binding capabilities,  $^1\text{H-NMR}$  titrations were performed for the **2.1-TD** cage with  $\text{C}_6\text{H}_6$  and  $\text{C}_6\text{H}_5\text{F}$  guests. For these titrations, successive equivalents of guest molecules were added gradually to a  $10^{-3} \text{ M}$   $\text{CDCl}_3$  solution of **2.1-TD**. A small but steady



downfield shift was observed for the guest protons in both cases (Figures 2.6a, b). These shifts could be attributed to hydrogen-bonding and non-covalent interactions of the guests within the cage cavity. The association constants derived from the mole fractions of the host and host-guest mixtures, as calculated by the online Bindfit software<sup>53-55</sup> were found to be 27.39 and 25.80 M<sup>-1</sup> for the 1:1 binding of C<sub>6</sub>H<sub>6</sub>  $\subset$  2.1-TD and C<sub>6</sub>H<sub>5</sub>F  $\subset$  2.1-TD systems, respectively (Figures 2.6c, d).

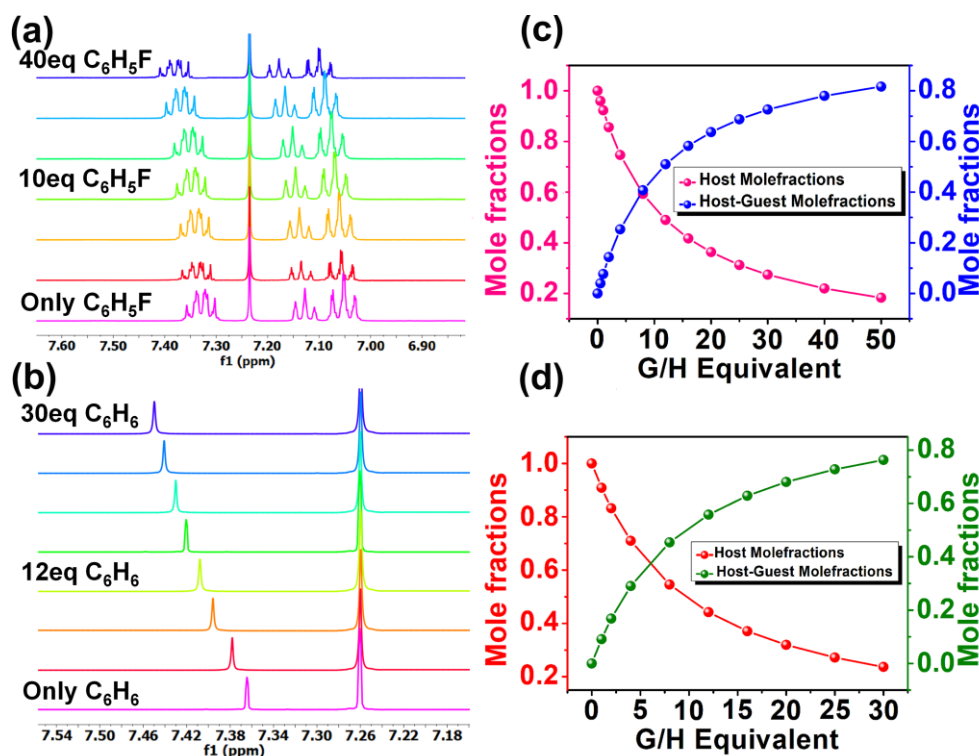


**Figure 2.6.** <sup>1</sup>H-NMR (CDCl<sub>3</sub>, 298K) titration plots for host-guest complexes of (a) C<sub>6</sub>H<sub>5</sub>F  $\subset$  2.1-TD, (b) C<sub>6</sub>H<sub>6</sub>  $\subset$  2.1-TD. Mole fractions of the host (H) and host-guest complexes (HG) against equivalence of guest added in (c) C<sub>6</sub>H<sub>5</sub>F  $\subset$  2.1-TD, (d) C<sub>6</sub>H<sub>6</sub>  $\subset$  2.1-TD.

To further probe only the internal binding of the guest molecule, we performed mass spectral studies wherein the guests C<sub>6</sub>H<sub>6</sub> and C<sub>6</sub>H<sub>5</sub>F were added in lesser equivalents (~0.5 eq) per 1eq of host molecule. The resultant mixture was then studied which revealed the presence of both empty host and guest $\subset$ 2.1-TD peaks corresponding to interior encapsulation in appropriate ratios (Figure A2.33, Appendix 2).

Furthermore, the gas-phase energies were computed to gain deeper insights into the nature and strength of binding of the guest molecules within the cage cavity (Figure A2.34, Appendix 2). The DFT calculations were performed with all the free and bound systems using Gaussian 09 software<sup>56,57</sup> (Table 2.3). Deformation energies<sup>58</sup> were calculated to determine the extent of

structural change in **2.1-TD** on guest encapsulation. The highest binding energies of -37.244 and -40.572 kcal/mol were obtained for **C<sub>6</sub>H<sub>6</sub> ⊂ 2.1-TD** and **C<sub>6</sub>H<sub>5</sub>F ⊂ 2.1-TD** species respectively, while the halogenated aliphatic solvents showed very closely related binding energies indicating their similar encapsulation strengths. The deformation energy was highest (0.78 kcal/mol) for the **C<sub>6</sub>H<sub>5</sub>F ⊂ 2.1-TD** system indicating the highest deviation of the guest-bound cage from the empty cage, showing the tighter binding of C<sub>6</sub>H<sub>5</sub>F with the **2.1-TD** over C<sub>6</sub>H<sub>6</sub> (Figure A2.35, Appendix 2). However, all the deformation energy values were less than 1 kcal/mol, which is too low to cause any significant structural change indicating the facile entry and exit of these guest molecules at the cavity of the **2.1-TD** cage.

**Table 2.3. Binding and deformation energies of Guest ⊂ 2.1-TD complexes calculated from DFT analysis**

Guest ⊂ 2.1-TD complex	Binding Energy (kcal/mol)	Deformation Energy (kcal/mol)
<b>C<sub>6</sub>H<sub>6</sub> ⊂ 2.1-TD</b>	-37.244	0.30
<b>C<sub>6</sub>H<sub>5</sub>F ⊂ 2.1-TD</b>	-40.572	0.78
<b>CHCl<sub>3</sub> ⊂ 2.1-TD</b>	-26.071	0.55
<b>CH<sub>2</sub>Cl<sub>2</sub> ⊂ 2.1-TD</b>	-23.688	0.58
<b>CCl<sub>4</sub> ⊂ 2.1-TD</b>	-29.015	0.48

## 2.4. Conclusion

In summary, we have synthesized two new tetrahedral cages based on P(V)-imido-Pd<sub>3</sub> clusters and oximido linkers. The moderate reactivity of the oxamide ligands with the Pd(II) precursor complex assists in the isolation of the corresponding intermediate macrocyclic compounds that can eventually be converted into the cage compounds upon increasing the reaction temperatures. These transformations were successfully mapped using spectral studies and these conversions are rationalized via computational studies. Further, guest encapsulation studies at the intrinsic cavity of the **2.1-TD** cage were probed by using small organic solvents. These studies showed a slightly better binding of organic guest molecules such as benzene and fluorobenzene over halogenated solvents such as dichloromethane, chloroform and carbon

tetrachloride. This study provides groundwork to understand how subtle variations in linker functionalization and external reaction conditions can lead to the isolation of stable intermediates. In the realm of supramolecular chemistry, this may further lead to development of new polyhedral structures with better functional properties. All these observations are believed to provide key insights on the reaction pathways leading up to the formation of supramolecular cages and stable intermediates with interesting properties and applications.

## 2.5. References

1. R. Chakrabarty, P. S. Mukherjee, P. J. Stang, P. J., *Chem. Rev.* **2011**, *111*, 6810-6918.
2. R. W. Saalfrank, N. Löw, B. Demleitner, D. Stalke, M. Teichert, *Chem. Eur. J.* **1998**, *4*, 1305-1311.
3. R. W. Saalfrank, N. Löw, S. Trummer, G. M. Sheldrick, M. Teichert, D. Stalke, *Eur. J. Inorg. Chem.* **1998**, *1998*, 559-563.
4. J. J. Perry Iv, J. A. Perman, M. J. Zaworotko, *Chem. Soc. Rev.* **2009**, *38*, 1400-1417.
5. M. D. Ward, *Chem. Commun.* **2009**, 4487-4499.
6. M. M. J. Smulders, I. A. Riddell, C. Browne, J. R. Nitschke, *Chem. Soc. Rev.* **2013**, *42*, 1728-1754.
7. M. Scherer, D. L. Caulder, D. W. Johnson, K. N. Raymond, *Angew. Chem. Int. Ed.* **1999**, *38*, 1587-1592.
8. M. D. Ward, P. R. Raithby, *Chem. Soc. Rev.* **2013**, *42*, 1619-1636.
9. D. Zhang, T. K. Ronson, J. R. Nitschke, *Acc. Chem. Res.* **2018**, *51*, 2423-2436.
10. K. Wu, B. Zhang, C. Drechsler, J. J. Holstein, G. H. Clever, *Angew. Chem. Int. Ed.* **2021**, *60*, 6403-6407.
11. S. Samantray, S. Bandi, D. K. Chand, *Beilstein J. Org. Chem.* **2019**, *15*, 1129-1140.
12. P. Howlader, P. Bhandari, D. Chakraborty, J. K. Clegg, P. S. Mukherjee, *Inorg. Chem.* **2020**, *59*, 15454-15459.
13. D. Preston, P. E. Kruger, *Chem. Eur. J.* **2019**, *25*, 1781-1786.
14. T. R. Cook, Y.-R. Zheng, P. J. Stang, *Chem. Rev.* **2013**, *113*, 734-777.

15. S. Komine, T. Tateishi, T. Kojima, H. Nakagawa, Y. Hayashi, S. Takahashi, S. Hiraoka, *Dalton Trans.* **2019**, 48, 4139-4148.
16. D. Bardhan, D. K. Chand, *Chem. Eur. J.* **2019**, 25, 12241-12269.
17. A. J. McConnell, C. S. Wood, P. P. Neelakandan, J. R. Nitschke, *Chem. Rev.* **2015**, 115, 7729-7793.
18. K. Harano, S. Hiraoka, M. Shionoya, *J. Am. Chem. Soc.* **2007**, 129, 5300-5301.
19. X. Lu, X. Li, K. Guo, T.-Z. Xie, C. N. Moorefield, C. Wesdemiotis, G. R. Newkome, *J. Am. Chem. Soc.* **2014**, 136, 18149-18155.
20. D. K. Chand, R. Manivannan, H. S. Sahoo, K. Jeyakumar, *Eur. J. Inorg. Chem.* **2005**, 3346-3352.
21. O. Gidron, M. Jirásek, N. Trapp, M.-O. Ebert, X. Zhang, F. Diederich, *J. Am. Chem. Soc.* **2015**, 137, 12502-12505.
22. K. Suzuki, M. Kawano, M. Fujita, *Angew. Chem. Int. Ed.* **2007**, 46, 2819-2822.
23. M. Fujita, F. Ibukuro, H. Hagihara, K. Ogura, *Nature* **1994**, 367, 720-723.
24. J. Ramírez, A.-M. Stadler, N. Kyritsakas, J.-M. Lehn, *Chem. Commun.* **2007**, 237-239.
25. J.-H. Fu, Y.-H. Lee, Y.-J. He, Y.-T. Chan, *Angew. Chem. Int. Ed.* **2015**, 54, 6231-6235.
26. M. J. Wiester, A. B. Braunschweig, H. Yoo, C. A. Mirkin, *Inorg. Chem.* **2010**, 49, 7188-7196.
27. H. Lee, P. Elumalai, N. Singh, H. Kim, S. U. Lee, K.-W. Chi, *J. Am. Chem. Soc.* **2015**, 137, 4674-4677.
28. D. Samanta, P. S. Mukherjee, *J. Am. Chem. Soc.* **2014**, 136, 17006-17009.
29. S. Chen, L.-J. Chen, H.-B. Yang, H. Tian, W. Zhu, *J. Am. Chem. Soc.* **2012**, 134, 13596-13599.
30. A. Kumar, P. S. Mukherjee, *Chem. Eur. J.* **2020**, 26, 4842-4849.
31. I. A. Riddell, M. M. J. Smulders, J. K. Clegg, Y. R. Hristova, B. Breiner, J. D. Thoburn, J. R. Nitschke, *Nat. Chem.* **2012**, 4, 751-756.
32. R. Sekiya, M. Fukuda, R. Kuroda, *J. Am. Chem. Soc.* **2012**, 134, 10987-10997.

33. R. Zhu, J. Lübben, B. Dittrich, G. H. Clever, *Angew. Chem. Int. Ed.* **2015**, *54*, 2796-2800.
34. K. Oji, A. Igashira-Kamiyama, N. Yoshinari, T. Konno, *Angew. Chem. Int. Ed.* **2014**, *53*, 1992-1996.
35. X. Bai, C. Jia, Y. Zhao, D. Yang, S.-C. Wang, A. Li, Y.-T. Chan, Y.-Y. Wang, X.-J. Yang, *Angew. Chem. Int. Ed.* **2018**, *57*, 1851-1855.
36. J. Mosquera, T. K. Ronson, J. R. Nitschke, *J. Am. Chem. Soc.* **2016**, *138*, 1812-1815.
37. W.-X. Gao, H.-J. Feng, Y.-J. Lin, G.-X. Jin, *J. Am. Chem. Soc.* **2019**, *141*, 9160-9164.
38. D. A. Roberts, B. S. Pilgrim, J. R. Nitschke, J. R., *Chem. Soc. Rev.* **2018**, *47*, 626-644.
39. A. M. Lifschitz, M. S. Rosen, C. M. McGuirk, C. A. Mirkin, *J. Am. Chem. Soc.* **2015**, *137*, 7252-7261.
40. S. Hiraoka, S. Takahashi, H. Sato, *Chem. Rec.* **2021**, *21*, 443-459.
41. L.-X. Cai, D.-N. Yan, P.-M. Cheng, J.-J. Xuan, S.-C. Li, L.-P. Zhou, C.-B. Tian, Q.-F. Sun, *J. Am. Chem. Soc.* **2021**, *143*, 2016-2024.
42. W. Cullen, C. A. Hunter, M. D. Ward, *Inorg. Chem.* **2015**, *54*, 2626-2637.
43. S. Sudan, R. -J. Li, S. M. Jansze, A. Platzek, R. Rudolf, *J. Am. Chem. Soc.* **2021**, *143*, 1773-1778.
44. H. Dasary, D.K. Chand, *Isr. J. Chem.* **2019**, *59*, 248-256.
45. A.K. Gupta, S. A. D. Reddy, R. Boomishankar, *Inorg. Chem.* **2013**, *52*, 7608-7614.
46. A.K. Gupta, A. Yadav, A.K. Srivastava, K.R. Ramya, H. Paithankar, S. Nandi, J. Chugh, R. Boomishankar, *Inorg. Chem.* **2015**, *54*, 3196-3202.
47. P. Rajasekar, S. Pandey, H. Paithankar, J. Chugh, A. Steiner, R. Boomishankar, *Chem. Commun.* **2018**, *54*, 1873-1876.
48. A. Yadav, M. Sarkar, S. Subrahmanyam, A. Chaudhary, E. Hey-Hawkins, R. Boomishankar, *Chem. Eur. J.* **2020**, *26*, 4209-4213.
49. A. Yadav, A.K. Gupta, A. Steiner, R. Boomishankar, *Chem. Eur. J.* **2017**, *23*, 18296-18302.

50. M. Sarkar, P. Rajasekar, C. Jose, R. Boomishankar, *Chem. Rec.* **2022**, *22*, e202100281.
51. M.D. Santana, G. García, M. Julve, F. Lloret, J. Pérez, M. Liu, F. Sanz, J. Cano, G. López, *Inorg. Chem.* **2004**, *43*, 2132-2140.
52. G. Sheldrick, *Acta Crystallogr. Sect. A* **2008**, *64*, 112-122.
53. <http://supramolecular.org>
54. P. Thordarson, *Chem. Soc. Rev.* **2011**, *40*, 1305-1323.
55. D. Brynn Hibbert, P. Thordarson, *Chem. Commun.* **2016**, *52*, 12792-12805.
56. M.J. Frisch et al. *Gaussian 09*, Revision C.01; Gaussian, Inc.: Wallingford, CT, 2016.
57. S. Grimme, *J. Comput. Chem.* **2006**, *27*, 1787-1799.
58. K. R. Ramya, A. Venkatnathan, A., *Comput. Theor. Chem.* **2013**, *1023*, 1-4.
59. M.L. Connolly, *J. Mol. Graph.* **1993**, *11*, 139-141.
60. L. J. Barbour, *Chem. Commun.* **2006**, 1163-1168.

 End of Chapter 2 

# Chapter 3



## Encapsulation Studies On *Closo*-Dicarbadoodecaborane Isomers In Neutral Tetrahedral Palladium(II) Cages

### 3.1. Introduction

Discrete self-assembled architectures and polyhedral metal-ligand cages are a notable class of compounds in supramolecular chemistry.<sup>1-4</sup> They find enormous applications<sup>5,6</sup> in host–guest chemistry,<sup>7-11</sup> molecular recognition,<sup>12-15</sup> catalysis in confined space,<sup>16-19</sup> electroactivity,<sup>20-23</sup> drug delivery<sup>24-27</sup>, etc. One of the hallmark properties of these compounds over polymeric framework solids is their solution-phase behavior, which can be studied using various techniques. These cages can exhibit a wide variety of functionalities in solution depending on their structural architectures, stability, and chemical properties.<sup>28-32</sup> The extensive analysis of the behavior of supramolecular moieties, such as the polyhedral cages, in the solution phase along with their structural details, is not only essential to predict the mechanism of their formation but also to understand their host–guest chemistry.<sup>33,34</sup> Typically, the interaction between host and guest molecules is one of the main driving forces that control guest encapsulation studies. Notably, the strength and stability of guest bindings inside or outside of a self-assembled moiety can depend on various factors such as the size of the guests, the portal window of the hosts, the stoichiometry of the reaction mixtures, and the reaction conditions.<sup>35</sup> In several instances, the early addition of guest molecules, say at the beginning of the self-assembly process, is vital for developing unique host–guest systems, which are otherwise difficult to access under normal circumstances.<sup>36</sup>

Recently, we have reported the selective encapsulation of isomeric xylenes and mesitylene utilizing a family of neutral tetrahedral Pd<sup>II</sup> cages.<sup>37</sup> In this work, three isostructural tetrahedral cages were synthesized by employing the imido-Pd<sub>3</sub> trimeric polyhedral building units (PBUs) in association with a family of anilic acid derivatives: chloranilic acid (**3.1**), bromanilic acid (**3.2**) and dihydroxybenzoquinone (**3.3**). The intrinsic cavities in these cages are hydrophobic due to their benzenoid portals and exhibited a cavity volume of over 200 Å<sup>3</sup> respectively which prompted us to examine these cages for encapsulation of aromatic guests such as isomeric xylenes and mesitylene. The tetrahedral cages **3.1**, **3.2**, and **3.3** containing chloranilate, bromanilate and anilate linkers exhibited selective encapsulation of *o*-xylene, *p*-xylene, and mesitylene respectively, over other analogous aromatic hydrocarbons. These selective encapsulations were driven by the variations in the portal diameters present at each of these cages and their interactions with the hydrocarbon guests. These findings further encouraged us to explore the guest-binding abilities of these assemblies towards the encapsulation of larger guest molecules.



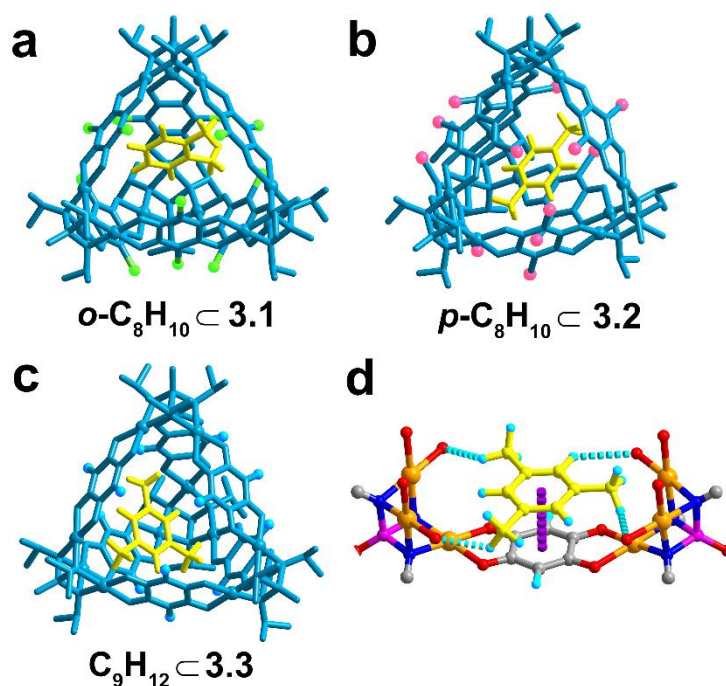


**Figure 3.1.** Selective binding of the aromatic guests driven by the variations in the portal diameters controlled by the substituents on the anilate backbones: (a)  $o\text{-C}_8\text{H}_{10} \subset 3.1$  (b)  $p\text{-C}_8\text{H}_{10} \subset 3.2$  (c)  $\text{C}_9\text{H}_{12} \subset 3.3$  and (d) potential non-covalent interactions that can stabilize the host–guest assemblies shown for  $\text{C}_9\text{H}_{12} \subset 3.3$ .

*Closo*-dicarbadoecaboranes (carboranes) of formula  $\text{C}_2\text{B}_{10}\text{H}_{12}$  are stable polyhedral boron-carbon hydride clusters known for almost sixty years.<sup>38,39</sup> Several of their derivatives are investigated extensively for boron neutron capture therapy.<sup>40-44</sup> They exhibit charge-neutral structures similar to those of aromatic hydrocarbons. However, unlike the aromatic hydrocarbons and fullerenes, the host–guest chemistry of these icosahedral carboranes is far less studied.<sup>45-50</sup> Three isomeric forms, termed *o*-, *m*- and *p*-carboranes, where the carbon atoms are located at 1,2- or 1,7- and 1,12- positions of the icosahedral structure, respectively, are known. Notably, the *m*- and *p*-isomers are synthesized via the heating of *o*-carborane. As a result, their purification requires removing isomeric impurities using complicated processes leading to loss of yields.<sup>38</sup> Hence, employing supramolecular self-assemblies for the selective encapsulation and separation of these isomeric carboranes via host–guest chemistry is a worthwhile process.

Herein, we present the in-situ solution phase binding of the isomers of carboranes within the intrinsic cavities of three iso-structural tetrahedral neutral cages,  $[\{\text{Pd}_3(\text{N}^i\text{Pr})_3\text{PO}\}_4(\text{Cl-AN})_6]$  (**3.1**),  $[\{\text{Pd}_3(\text{N}^i\text{Pr})_3\text{PO}\}_4(\text{Br-AN})_6]$  (**3.2**) and  $[\{\text{Pd}_3(\text{N}^i\text{Pr})_3\text{PO}\}_4(\text{H-AN})_6]$  (**3.3**) built on the

anilate (AN) ligands ( $X\text{-AN}^{2-}$ ;  $X = \text{Cl, Br or, H}$ ). All three cages were found to preferentially encapsulate *o*-carborane over its other two isomers, attributed to the effective non-classical interactions between the host and guest moieties. A combination of mass-spectral, NMR (NOESY/ROESY and DOSY) data and hydrodynamic radii calculations confirm the encapsulation of *o/m/p*-carboranes as guests in these cages. The DFT-optimized structures of the host-guest complexes provided insights into the nature of non-classical interactions present in these assemblies. These results pave the way for exploring discrete supramolecular systems toward the purification of isomeric carboranes.

## 3.2. Experimental Details

### 3.2.1. General Remarks

All manipulations involving phosphorus halides were performed under a dry nitrogen atmosphere in standard Schlenk glassware. Dry Solvents were purchased from local vendors and used without further purification. Isopropylamine, chloranilic acid, bromanilic acid, dihydroxy benzoquinone and palladium acetate were purchased from Aldrich and used as received.  $\text{POCl}_3$  was purchased locally and was distilled prior to use. The ligand  $[\text{PO}(\text{NH}^i\text{Pr})_3]$ , the PBU precursor, **HEXA-Pd**  $[\text{Pd}_3\{(\text{N}^i\text{Pr})_3\text{PO}\}(\text{OAc})_2(\text{OH})]_2 \cdot 2(\text{CH}_3)_2\text{SO}$  was prepared by the earlier reported procedure.<sup>51</sup> NMR spectra were recorded on a Bruker or Jeol 400 MHz spectrometer ( $^1\text{H}$  NMR: 400.13 MHz,  $^{13}\text{C}\{^1\text{H}\}$  NMR: 100.62 MHz,  $^{31}\text{P}\{^1\text{H}\}$  NMR: 161.97 MHz,  $^{11}\text{B}\{^1\text{H}\}$  NMR: 128.43 MHz) at room temperature using TMS ( $^1\text{H}$ ,  $^{13}\text{C}$ ) and 85%  $\text{H}_3\text{PO}_4$  ( $^{31}\text{P}$ ) as reference. The mass spectra were obtained on an Applied Bio system matrix-assisted laser desorption ionization time-of-flight (MALDI-TOF)/TOF spectrometer. For mass spectral measurements, both 2,5-dihydroxybenzoic acid (DHB) and  $\alpha$ -cyano-4-hydroxy-cinnamic acid (CHCA) matrix or a 1:1 mixture of them has been used as the matrix. Fourier-transform infrared (FTIR) spectra were obtained with a Bruker Alpha-E Fourier transform infrared spectrometer. Elemental Analyses were performed with the VARIO-EL CUBE elemental analyzer.

### 3.2.2. Procedure for the in-situ preparation of *o*-/*m*-/*p*-Cb $\subset$ Host complexes:

***o*-/*m*-/*p*-Cb  $\subset$  3.1:** Chloranilic acid (4.40 mg, 0.0210 mmol) and *o*-/*m*-/*p*-Cb (20.20 mg, 0.14 mmol) were added to a stirred solution of **HEXA-Pd**, (20 mg, 0.0140 mmol) in MeOH at room temperature. The resultant mixture was heated at 80 °C for 4 hours to yield a brown precipitate. The precipitate was recovered by filtration, washed with 2-5ml methanol several times, and

dried under vacuum. The obtained mixture was analyzed by MALDI-TOF, NMR, and  $^1\text{H}$ -2D-DOSY NMR spectroscopy, which revealed the formation of host–guest complexes.

***o*-/m-/p-Cb**  $\subset$  **3.2**: Bromanilic acid (6.25 mg, 0.0210 mmol) and *o*-/m-/p-Cb (20.20 mg, 0.14 mmol) were added to a stirred solution of **HEXA-Pd**, (20 mg, 0.0140 mmol) in MeOH at room temperature. The resultant mixture was heated at 85 °C for 4 hours to yield a reddish-brown precipitate. The precipitate was recovered by filtration, washed with 2-5ml methanol several times, and dried under vacuum. The obtained mixture was analyzed by MALDI-TOF, NMR, and  $^1\text{H}$ -2D-DOSY NMR spectroscopy, which revealed the formation of host–guest complexes.

***o*-/m-/p-Cb**  $\subset$  **3.3**: Dihydroxybenzoquinone (3.00 mg, 0.0210 mmol) and *o*-/m-/p-Cb (20.20 mg, 0.14 mmol) were added to a stirred solution of **HEXA-Pd**, (20 mg, 0.0140 mmol) in MeOH at room temperature. The resultant mixture was heated at 80 °C for 1 hour to yield a dark brown precipitate. The precipitate was recovered by filtration, washed with 2-5ml methanol several times, and dried under vacuum. The obtained mixture was analyzed by MALDI-TOF, IR, NMR, and  $^1\text{H}$ -2D-DOSY NMR spectroscopy, which revealed the formation of host–guest complexes.

### 3.2.3. Synthesis of 3.2-TM:

Bromanilic acid (6.25 mg, 0.0210 mmol) was added to a stirred solution of **HEXA-Pd**, (20.00 mg, 0.0140 mmol) in MeOH at room temperature. The resultant mixture was heated at 60 °C for 2 hours to yield a reddish-brown precipitate. The precipitate was recovered by filtration, washed with 3-5ml of methanol several times, and dried under vacuum. Reddish-brown needle-like crystals were obtained from a methanol-chloroform solution (by solvent evaporation method) after one month at room temperature. Yield: 60% (based on P). MALDI-TOF/TOF: Expected- 3046.11, Found- 3047.03 [M+H]<sup>+</sup>.  $^{31}\text{P}\{^1\text{H}\}$  NMR (161 MHz,  $\text{CDCl}_3$ ):  $\delta$  76.0;  $^1\text{H}$  NMR (400 MHz,  $\text{CDCl}_3$ ):  $\delta$  1.75 (d,  $J = 6.6$  Hz,  $\text{CH}_3$ ), 2.88 (m, CH), 3.95 (s,  $\text{OCOCH}_3$ );  $^{13}\text{C}\{^1\text{H}\}$  NMR (100 MHz,  $\text{CDCl}_3$ ):  $\delta$  21.2, 24.7, 56.7, 121.8, 147.5, 166.4, 192.7. Elemental Analysis (%): Calcd for  $\text{C}_{56}\text{H}_{100}\text{Br}_4\text{N}_{12}\text{O}_{24}\text{P}_4\text{Pd}_{12}$ : C, 22.08; H, 3.31; N, 5.52. Found: C, 22.02; H, 3.47; N, 5.57.

### 3.2.4. $^1\text{H}$ -2D-DOSY NMR studies:

The  $^1\text{H}$ -2D-DOSY NMR experiments were carried out on a Bruker AVANCE III NMR spectrometer operating at a  $^1\text{H}$  frequency of 400 MHz at a constant temperature of 298K. 3.0 mM solutions of the participating species and host–guest complexes were prepared in  $\text{CDCl}_3$

and allowed to equilibrate for 30 minutes before data acquisition. Diffusion-Ordered Spectroscopy (DOSY) experiments were performed by varying gradient strength.

The “T1/T2” module in Topspin 4.1 software was used for regression analysis to calculate the diffusion coefficient for each integral region or individual selected peak. The fitting of the diffusion dimension in the 2D-DOSY spectra was carried out using a one-parameter mono-exponential (equation 1) or a two-parameter biexponential fit (equation 2).

$$I = I_0 \exp[-D\gamma^2 g^2 \delta^2 (\Delta - \delta/3)] \dots \dots \dots (1)$$

$$I = I_{0A} \exp[-D_A \gamma^2 g^2 \delta^2 (\Delta - \delta/3)] + I_{0B} \exp[-D_B \gamma^2 g^2 \delta^2 (\Delta - \delta/3)] \dots \dots \dots (2)$$

In these equations, I is the observed integral,  $I_0$ ,  $I_{0A}$  and  $I_{0B}$  are the reference or un-attenuated integrals,  $D$ ,  $D_A$ , and  $D_B$  are the diffusion coefficients,  $\gamma$  is the gyromagnetic ratio of the detected nucleus,  $g$  is the gradient strength,  $\delta$  the length of the gradient pulse, and  $\Delta$  the diffusion time.

### 3.2.5. Theoretical calculations:

The gas-phase single molecule energies of all the participating species and the host–guest systems were calculated by using the Gaussian 09 software<sup>52,53</sup> These energies were computed by DFT methods by employing the b97d3 functional. Energy calculations were performed using the basis set Lanl2dz for Pd, Cl and Br in conjunction with the cc-pvtz basis set (for all other atoms). For the host–guest complexes, the energies of the host cage **3.1**, **3.2**, **3.3** and **3.2-TM**, the guests *o*-/*m*-/*p*-carboranes, and the host–guest complexes were separately calculated and the binding energy of a given complex was calculated by equation 3:

$$\text{Binding energy} = E_{\text{Guest} \subset \text{Host}} - (E_{\text{Host}} + E_{\text{Guest}}) \quad (3)$$

To determine the structural changes associated with the encapsulation of guests in the host cages **3.1**, **3.2** and **3.3**, deformation energies<sup>54</sup> were calculated by equation 4:

$$\text{Deformation energy} = E_{\text{Host}} - E_{\text{Host}}^{\text{enc}} \quad (4)$$

Here,  $E_{\text{Host}}$  is the total energy of the optimized empty cage, and  $E_{\text{Host}}^{\text{enc}}$  is obtained by removal of the guest molecule from the host cage followed by a single-point energy calculation on the corresponding structure.

### 3.2.6. Crystallography

Reflections for **3.2-TM** were collected on a Bruker Smart Apex Duo diffractometer at 100 K using Mo K $\alpha$  radiation microfocus source ( $\lambda = 0.71073 \text{ \AA}$ ) with 60.00sec exposure and a CMOS

detector. The structure was solved using the intrinsic phasing method and refined by full-matrix least-squares on  $F^2$ .<sup>55</sup> Crystallographic data for **3.2-TM** are listed in Table 3.1. All non-hydrogen atoms were refined anisotropically if not stated otherwise. The crystals of **3.2-TM** diffracted very weakly at higher angles and hence its data is truncated to  $2\theta = 50^\circ$ . Hydrogen atoms were constrained in geometric positions to their parent atoms. The diffuse solvent molecules in **3.2-TM** could not be modelled appropriately. Hence, these were treated as diffuse contributions to the overall scattering and removed by SQUEEZE/PLATON for better refinement data. The squeezed volume was found to be  $1261 \text{ \AA}^3$ , which corresponds approximately to 10 water molecules and 8 methanol molecules. In the final refinements, OMIT command was used to remove a number of reflections for which  $I(\text{obs})$  and  $I(\text{calc})$  differed more than 10 times  $\text{SigmaW}$  (the latter being the square root of  $1.0/\text{weight}$  for that reflection in the L.S. refinement).

**Table 3.1. Crystallographic Data for 3.2-TM**

<b>Compound: 3.2-TM</b>	
Chemical formula	$\text{C}_{56}\text{H}_{100}\text{Br}_4\text{N}_{12}\text{O}_{24}\text{P}_4\text{Pd}_{12}$
Formula weight	3045.79
Temperature	100(2) K
Crystal system	Monoclinic
Space group	$P2_1/n$
$a$ (Å); $\alpha$ (°)	12.247(5); 90
$b$ (Å); $\beta$ (°)	34.25(1); 114.407(9)
$c$ (Å); $\gamma$ (°)	14.316(5); 90
$V$ (Å <sup>3</sup> ); $Z$	5468(4); 2

$\rho$ (calc.) $\text{mg m}^{-3}$	1.850
$\mu(\text{Mo K}\alpha)$ $\text{mm}^{-1}$	3.500
$2\theta_{\text{max}}$ ( $^{\circ}$ )	45.03
R(int)	0.3531
Data / param.	7152 / 493
GOF	1.021
R1 [ $F > 4\sigma(F)$ ]	0.1113
wR2 (all data)	0.3121
max. peak/hole ( $\text{e} \cdot \text{\AA}^{-3}$ )	1.440 / -1.171

### 3.3. Results and Discussions

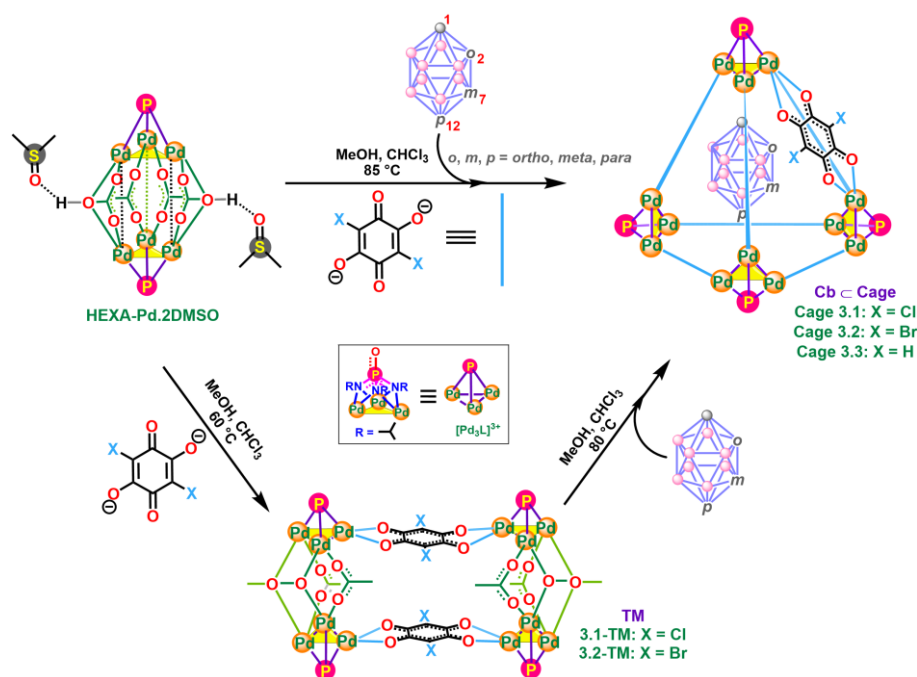
#### 3.3.1. Synthesis, Structure, and Characterization.

The encapsulation capabilities for the carborane guests were probed using both post-assembly and in-situ methods. In the post-assembly method, the preformed cages were treated with the carborane (**Cb**) guests. The tetrahedral cages **3.1**, **3.2** and **3.3**, consisting of the trinuclear  $\text{Pd}^{\text{II}}$  cluster units, *cis*-protected by the tris(imido)phosphate trianions and the anilate linkers, were synthesized by adopting the procedure reported by us earlier.<sup>37</sup> The mass spectra of the reaction mixture of the preformed cage **3.3** with **Cb** guests gave clear peaks due to the host-guest assemblies indicating the encapsulation of the carboranes in cage **3.3** in the post-assembly method. In contrast, the mass-spectral analyses revealed the absence of peaks due to the guest-bound cages for **3.1** and **3.2** indicating the inability of **Cb** guests to enter the intrinsic cavities of these cages. This could be attributed to smaller portals present in cages **3.1** and **3.2**. Hence, we turned our attention to the in-situ method, in which the respective cages were synthesized in the presence of carborane guests starting from the hexanuclear  $\text{Pd}^{\text{II}}$  precursor  $[\{\text{Pd}_3(\text{N}^{\text{i}}\text{Pr})_3\text{PO}\}_2(\text{OAc})_2(\text{OH})]_2 \cdot 2(\text{CH}_3)_2\text{SO}$  (**HEXA-Pd**) and the corresponding anilic acid ( $\text{C}_6\text{H}_2\text{X}_2\text{O}_4$ ; X = Cl, Br or H). However, heating the host-guest assemblies of **Cb**  $\subset$  **3.3** (at 80  $^{\circ}\text{C}$ ) for a longer period releases these guest molecules from the cavities of **3.3** as evidenced by the  $^1\text{H-NMR}$  and mass-spectral data.

Treatment of a methanolic mixture of **HEXA-Pd** and anilic acids (X-AN-2H; X = Cl, Br or H) with a chloroform solution of *o*-carborane (***o*-Cb**) at 85 °C resulted in the in-situ formation of the host–guest complex, ***o*-Cb**  $\subset$  **Cage (3.1, 3.2 or 3.3)** (Pathway A, Scheme 3.1). The MALDI-TOF mass-spectral analysis revealed the formation of the host–guest assemblies yielding *m/z* peaks centered at 3574.9, 4070.7, and 3145.3 for the [***o*-Cb**  $\subset$  **3.1**+K]<sup>+</sup>, [***o*-Cb**  $\subset$  **3.2**+H]<sup>+</sup> and [***o*-Cb**  $\subset$  **3.3**+Na]<sup>+</sup> species, respectively. Similar in-situ experiments were performed to study the encapsulation of *m*- and *p*-carboranes in these cages. Here, the formation of host–guest assemblies with ***m*-Cb** and ***p*-Cb** guests was also observed from the MALDI-TOF spectral data, with the corresponding *m/z* peaks centered at 3536.1, 4069.8, and 3123.9 for the [***m*-Cb**  $\subset$  **3.1**]<sup>+</sup>, [***m*-Cb**  $\subset$  **3.2**]<sup>+</sup> and [***m*-Cb**  $\subset$  **3.3**+H]<sup>+</sup> ions, respectively, and at 3536.2, 4069.7, and 3145.3 for the [***p*-Cb**  $\subset$  **3.1**]<sup>+</sup>, [***p*-Cb**  $\subset$  **3.2**]<sup>+</sup> and [***p*-Cb**  $\subset$  **3.3**+Na]<sup>+</sup> ions, respectively (Figures A3.1-A3.9, Appendix 3).

The IR spectrum shows a significant shift of 35 cm<sup>-1</sup> towards the lower energy side for the  $\nu_{\text{C-H}}$  signal of the carborane and a shift of 25.2 cm<sup>-1</sup> towards the higher energy side for the  $\nu_{\text{B-H}}$  band (Figure A3.11, Appendix 3). This observation is consistent with the involvement of the C-H bonds in nonclassical hydrogen bonding observed for other host-guest assemblies involving carboranes.<sup>47</sup>

To understand the stepwise formation and the nature of host–guest assemblies present in the solution, the in-situ reactions were then performed at lower temperatures. Thus, the treatment of **HEXA-Pd** with Br-AN-2H in the presence ***o*-Cb** at 60 °C shows the formation of a tetrameric Pd<sub>12</sub> macrocyclic assembly [**{Pd<sub>3</sub>(N<sup>i</sup>Pr)<sub>3</sub>PO}**]<sub>4</sub>(Br-AN)<sub>2</sub>(OAc)<sub>4</sub>(OH)<sub>4</sub> (**3.2-TM**), an intermediate species for the tetrahedral cage **3.2** (Pathway B, Scheme 3.1). The MALDI-TOF spectrum of the reaction mixture via pathway B showed peaks at *m/z* values centered at 3047.03 and 3190.32, for the species [**3.2-TM**+H]<sup>+</sup> and [**3.2-TM**·***o*-Cb**]<sup>+</sup>, respectively (Figure A3.10, Appendix 3). Since **3.2-TM** does not possess any significant internal cavity (*vide supra*), the association of **3.2-TM** with ***o*-Cb** is expected to occur at the exteriors of the macrocycle. Further heating of the reaction mixture containing **3.2-TM**·***o*-Cb** has expectedly yielded the ***o*-Cb**  $\subset$  **3.2** complex via pathway C.



**Scheme 3.1.** Schematic representation showing the direct and stepwise pathways of in-situ guest binding.

Although attempts to obtain single crystals of **Cb** ⊂ **Cage** and **3.2-TM-*o*-Cb** were unsuccessful, the guest-free **3.2-TM** complex was crystallized upon performing the reaction in the absence of the **Cb** guests. The structure of **3.2-TM** was solved in the monoclinic space group  $P2_1/n$ . Its core structure is similar to the earlier reported tetrameric motifs known with the oxamide linkers.<sup>56</sup> The molecular structure of **3.2-TM** consists of four  $[Pd_3(N^iPr)_3PO]^{3+}$  units connected with two bromanilate ( $Br-AN^{2-}$ ) linkers, four acetate and four hydroxido bridges (Figures 3.2a and A3.12-A3.15, Appendix 3). Though the intrinsic space between the two  $(Br-AN)^{2-}$  panels is too small to host any guest molecules, the small bowl-like cavity generated in the exterior of the tetramer (Figure A3.16, Appendix 3) can interact with the **Cb** guests and can act as a control-assembly to spectrally distinguish the exo-cage binding from the endo-cage binding observed with the tetrahedral cages. Similarly, the formation of the intermediate **3.1-TM** was observed in the  $^{31}P\{^1H\}$ -NMR spectrum. However, the complex could not be isolated due to the higher reactivity of Cl-AN-2H with the **HEXA-Pd** precursor. In the absence of any X-ray-derived structures, all the energy-minimized structures of host-guest complexes were obtained by DFT methods<sup>52,53</sup> (Figures 3.2b and A3.17-A3.20, Appendix 3).



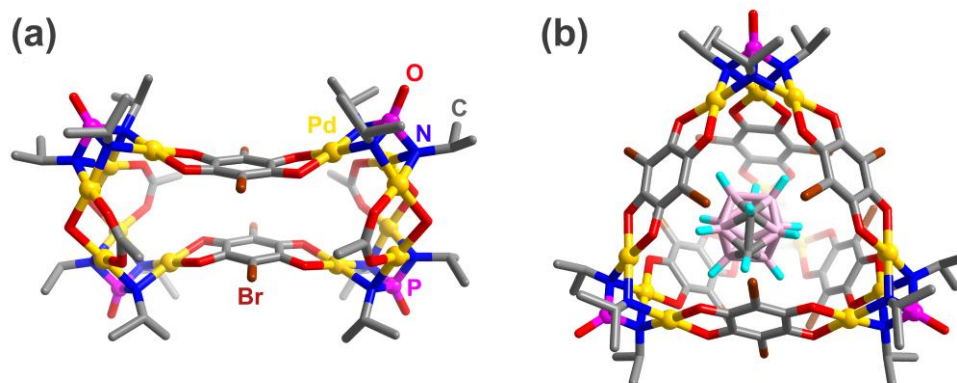


**Figure 3.2.** (a) Crystal structure of **3.2-TM** and (b) Single Molecule Energy Optimized structure of *o*-**Cb** c **3.2**.

The  $^{31}\text{P}\{^1\text{H}\}$ -NMR spectra of all the isolated host–guest complexes gave a single peak due to the imido(phosphate) trianion motifs located at the cage vertices. Thus, peaks at  $\delta$  72.6, 72.6, 72.8, 73.7, 73.9, 73.8, 70.4, 70.5, 70.4, 76.1, 76.3 and 76.2 are observed for the respective *o*-**Cb** c **3.1**, *m*-**Cb** c **3.1**, *p*-**Cb** c **3.1**, *o*-**Cb** c **3.2**, *m*-**Cb** c **3.2**, *p*-**Cb** c **3.2**, *o*-**Cb** c **3.3**, *m*-**Cb** c **3.3**, *p*-**Cb** c **3.3**, **3.2-TM**·*o*-**Cb**, **3.2-TM**·*m*-**Cb** and **3.2-TM**·*p*-**Cb** assemblies (Figures A3.21-A3.32, Appendix 3). Notably, cage **3.3** with the least electronegative substituent ( $X = \text{H}$ ) shows the highest upfield chemical shifts for all the **Cb** c **3.3** systems. Furthermore, the gradual conversion of **3.2-TM** to **3.2**, in pathway C, both in the absence and presence of *o*-**Cb**, was monitored via  $^{31}\text{P}\{^1\text{H}\}$ -NMR spectral studies (Figures A3.33-A3.34, Appendix 3). These studies indicate that the conversion of **3.2-TM** to **3.2** was not disrupted due to the presence of the *o*-**Cb** guest molecules. However, the broadened nature of the  $^{31}\text{P}\{^1\text{H}\}$ -NMR peaks in the presence of *o*-**Cb** guests suggests the existence of both the guest-bound and guest-free cages in the reaction mixture.

All the guest-encapsulated cages (**3.1**, **3.2** and **3.3**), when synthesized with excess (~20 eq.) *o*-, *m*- and *p*-**Cb**, show prominent upfield shifts in the  $^1\text{H}$ -NMR for the carborane and cage protons. Significant  $^1\text{H}$ -shifts were observed for the C-H and B-H hydrogens of **Cb**, indicating that the **Cb** moieties are efficiently shielded within the cavities and interact with the quinoid portals of the cage. For cages, the shifts were observed for the  $^i\text{Pr}$  groups of the imido- $\text{P}^{\text{V}}$  ligands and the hydrogens of the anilate linker in the case of cage **3.3** (Figure 3.3). However, two sets of protons were observed for the **Cb** guests and cage **3.3** indicating the presence of a free cage in addition to the bound cage in the reaction mixture. This could be attributed to the higher reactivity of the anilate linker that forms empty cage **3.3** at a much faster rate than the

other two halogenated-anilate linkers employed for obtaining **3.1** and **3.2**. However, the use of lesser amounts (5-7 eq.) of **Cb** guests results in two sets of peaks for cages **3.1** and **3.2** as well due to the distinction between bound and free host cages (Figures A3.35-A3.43, Appendix 3). In all encapsulation processes, while *o*- and *m*-**Cb** readily engaged, *p*-**Cb** required longer reaction times for the formation of the host–guest assemblies. Also, a single set of host peaks and only small upfield shifts in the  $^1\text{H}$ -NMR signals were observed for the guest hydrogens (both C-H and B-H) of the **3.2-TM**·*o*-**Cb** system, indicative of a weakly bound externally situated guest molecule in the assembly (Figure A3.44, Appendix 3). Further, since **3.2-TM** was identified as the stable intermediate of the tetrahedral cage reaction pathway, the entire stepwise conversion of **3.2-TM** to **3.2** was monitored in a time-dependent fashion in the presence of all three isomers of **Cb**. These studies showed a continuous and gradual upfield shift of the **Cb** guest protons until the end of the in-situ encapsulation process (Figure A3.45, Appendix 3).

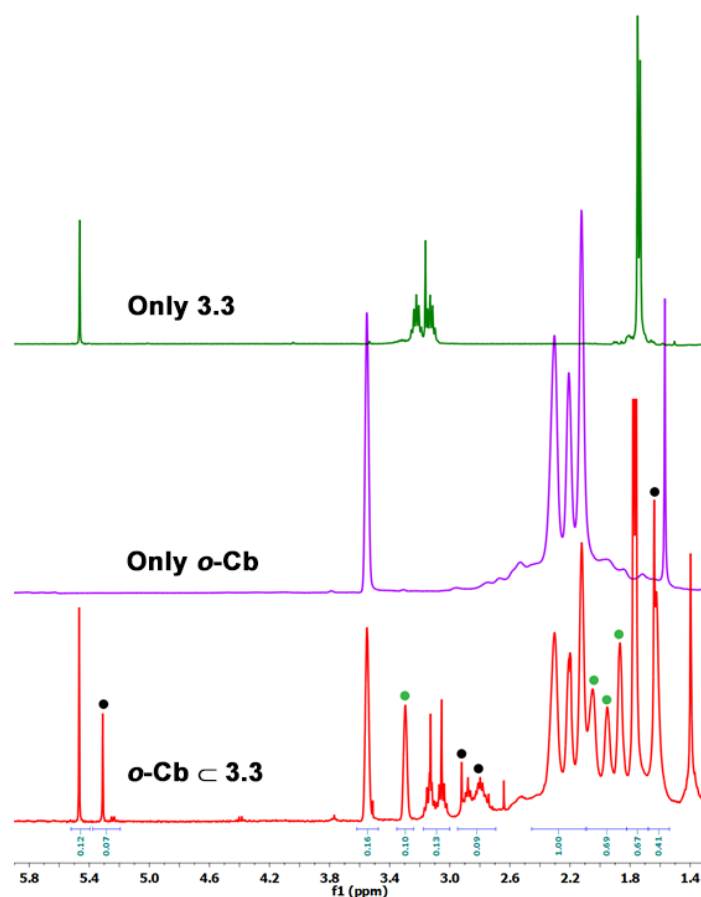


**Figure 3.3.** Partial  $^1\text{H}\{^{11}\text{B}\}$ -NMR profile of *o*-**Cb** c **3.3** compared with pure *o*-**Cb** and empty cage **3.3**. The black and green dots represent the host and guest protons in their respective bound states.

Compared to the  $^1\text{H}$ -NMR spectra, the  $^{11}\text{B}\{^1\text{H}\}$ -NMR spectra showed characteristic resonances in all the cases in the range between  $-2.3$  and  $-14.8$  ppm with small shifts proving the integrity of the *closo*-carborane guests within the cage cavities. The non-classical interactions of the hydridic B-H groups with the cage moieties seemingly have little effect on the  $^{11}\text{B}$  signals (Figures A3.46-A3.48, Appendix 3).

Furthermore,  $^1\text{H}$ - $^1\text{H}$ -NOESY and/or ROESY-NMR spectroscopy was performed for the **Cb**  $\subset$  **3.3** systems as the host cages and **Cb** guests are expected to be in close proximity to each other in the host-guest complexes. Since cages **3.1** and **3.2** did not possess any protons in the anilate backbone that can effectively interact with the encapsulated **Cb** guests, NOESY-NMR experiments were performed only with the *o*-**Cb**  $\subset$  **3.3**, *m*-**Cb**  $\subset$  **3.3** and *p*-**Cb**  $\subset$  **3.3** host-guest complexes. NOe cross-peaks were observed between the H-AN linker proton at  $\delta$  5.45 and carborane C-H peaks at  $\delta$  3.55, 3.42 and 3.38 for *o*-, *m*- and *p*-**Cb** respectively, which confirmed the strong host-guest interactions at the intrinsic voids of the cages (Figures A3.49-A3.51, Appendix 3).

### 3.3.2. $^1\text{H}$ -2D-DOSY NMR Studies.

$^1\text{H}$ -2D-DOSY NMR spectroscopy experiments were performed to understand further the intrinsic vs. extrinsic binding of **Cb** guests in the host-guest complexes. Due to the broadened nature of peaks in the host-guest spectra the “T1/T2” module in Topspin 4.1 software was used for regression analysis to calculate the most accurate diffusion coefficient for each integral region or individual selected peak. In these studies, the signals of the host and guest hydrogen atoms as well as those in the host-guest complexes were independently monitored as a function of gradient strength. While the quantitative analysis of the DOSY NMR profiles gave a single diffusion coefficient ( $D$ ) value for the independent host and guest systems (Figure A3.52, Appendix 3), two distinct diffusion coefficients ( $D$ ) were observed for the bound and free host and guest species in the in-situ formed host-guest solution. The DOSY NMR data for the *o*-**Cb**  $\subset$  **3.1** system shows very similar diffusion coefficient values of  $4.55 \times 10^{-10}$  and  $4.51 \times 10^{-10}$   $\text{m}^2/\text{s}$  for the bound *o*-**Cb** and **3.1**, respectively (Figures 3.4a and A3.53, Appendix 3). Similarly, the  $D$  values of  $4.30 \times 10^{-10}$   $\text{m}^2/\text{s}$  (for bound *o*-**Cb**) and  $4.27 \times 10^{-10}$   $\text{m}^2/\text{s}$  (for bound **3.2**) and  $4.35 \times 10^{-10}$   $\text{m}^2/\text{s}$  (for bound *o*-**Cb**) and  $4.31 \times 10^{-10}$   $\text{m}^2/\text{s}$  (for bound **3.3**) were obtained for the other *o*-**Cb**  $\subset$  **Cage** systems of **2** and **3** (Figures 3.4b, 3.4c and A3.56 and A3.59, Appendix 3). This indicates that the host and guest molecules diffuse together at the same rate.

In contrast, distinctively different  $D$  values were observed for the *o*-Cb species ( $11.60 \times 10^{-10}$ ,  $11.33 \times 10^{-10}$ , and  $10.15 \times 10^{-10}$  m<sup>2</sup>/s) in host cages **3.1** ( $4.98 \times 10^{-10}$  m<sup>2</sup>/s), **3.2** ( $4.68 \times 10^{-10}$  m<sup>2</sup>/s) and **3.3** ( $4.76 \times 10^{-10}$  m<sup>2</sup>/s) for their respective unbound forms (Figure 3.4c).

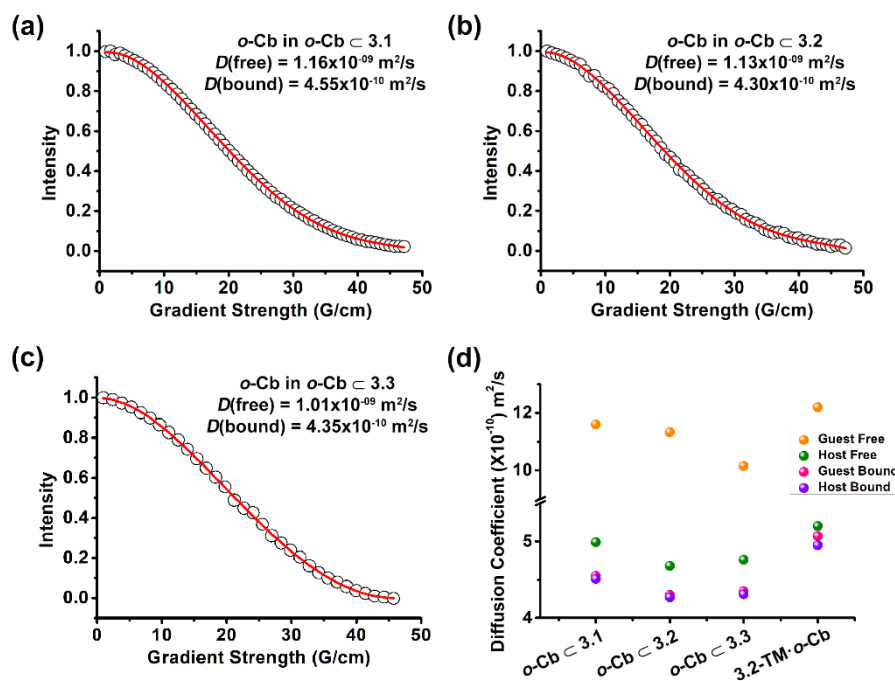


**Figure 3.4.** Integral decay profile of the C-H protons of *o*-Cb in (a) *o*-Cb **3.1**, (b) *o*-Cb **3.2** and (c) *o*-Cb **3.3** (CDCl<sub>3</sub>, 298K); (d) Summary of the  $D$  values for selected host and guest protons studied for the *o*-Cb **Cage** host–guest systems.

The complexes *m*-Cb **3.1**, *m*-Cb **3.2**, and *m*-Cb **3.3** also showed closely comparable  $D$  values for the host and guest systems in the encapsulated state (Figures A3.54, A3.57 and A3.60, Appendix 3). Amongst all, the closest  $D$  values for the host and guest moieties were observed for the *o*-Cb **3.2** system indicating a more efficient encapsulation of the *o*-Cb guest in the larger cage **3.2**. However, DOSY data for *p*-Cb in all three cages show that the *p*-Cb guest and the host cages diffuse at slightly different rates at the encapsulated state (Figures A3.55, A3.58 and A3.61, Appendix 3). These variations could be due to its loose binding at the cavities of the cages.

In contrast to the tetrahedral cages, the DOSY NMR analyses of the **3.2-TM**·*o*-Cb system show that even though the cavitand **3.2-TM** exhibits very similar diffusion rates in the free and the bound state, the guest *o*-Cb diffuses at a much slower rate in the encapsulated state, suggesting a weak complexation with the host system (Figure A3.62, Appendix 3).<sup>57</sup> It is evident that the  $D(\text{bound})$  values for *o*-Cb guests obtained via pathway B are higher than those

obtained via pathway A. This can be attributed to the fact that somewhat loose guest binding occurs in pathway B and the externally bound *o*-Cb guests undergo faster exchange with free *o*-Cb guests present in the solution compared to the guests located inside the tetrahedral cages. Moreover, the interactions of *o*-Cb guests with the tetrahedral cages (with six anilate moieties) are better than the interactions with **3.2-TM** (with one or two anilate moieties).

Having observed the diffusion behavior of the guest **Cb** with different hosts (Table A3.4 and Figures A3.63, Appendix 3), we sought to investigate the DOSY NMR spectra of the reaction mixture, consisting of **HEXA-Pd**, Br-AN-2H, and *o*-Cb, which was monitored from the beginning until the formation of the final *o*-Cb  $\subset$  **3.2** product in order to probe the host–guest interactions in solution. These experiments indicated a gradual decrease in the  $D(\text{bound})$  values for *o*-Cb (from  $13.6 \times 10^{-10} \text{ m}^2/\text{s}$  to  $4.30 \times 10^{-10} \text{ m}^2/\text{s}$ ) as the reaction proceeded from **HEXA-Pd** to **3.2** via **3.2-TM** showing the gradual encapsulation and stepwise formation of the host–guest assemblies in solution accompanied by a better interaction between the host and guest systems (Figures A3.64, Appendix 3).

### 3.3.3. Calculation for hydrodynamic radius using DOSY data.

Additionally, to confirm the formation of definite host–guest assemblies, the hydrodynamic radius ( $R_H$ ) of the diffusing particles was calculated,<sup>58</sup> which gave a clear distinction between the internally encapsulated and externally bound **Cb** guests. Using the Stoke-Einstein equation, the  $R_H$  values can be extracted from the  $D$  values obtained by DOSY NMR. Thus, two independent  $R_H$  values have been obtained for each of the host and guest species in the bound and free states. For example, for the *o*-Cb  $\subset$  **3.2** system, the  $R_H$  values of 11.13 (free) and 11.95 Å (bound) were obtained for cage **3.2** and the  $R_H$  values of 5.89 (free) and 11.90 Å (bound) were observed for *o*-Cb. Notably, closely comparable  $R_H$  values (11.95 and 11.90 Å) were observed for the host and the guest species in the bound state thereby confirming the encapsulation of *o*-Cb at the intrinsic cavity of **3.2** (Table 3.2). Similar observations have been made for the rest of the *o*-Cb  $\subset$  **3.2**, *o*-Cb  $\subset$  **3.3**, *m*-Cb  $\subset$  **3.1**, *m*-Cb  $\subset$  **3.2**, *m*-Cb  $\subset$  **3.3**, *p*-Cb  $\subset$  **3.1**, *p*-Cb  $\subset$  **3.2** and *p*-Cb  $\subset$  **3.3** systems as well (Table A3.5 and Figure A3.65, Appendix 3). Moreover, the hydrodynamic radii for the free and bound cage systems obtained from DOSY NMR were consistent with the radii of the circumscribed sphere calculated for their respective energy-minimized models (Table A3.6, Appendix 3). For the tetrameric **3.2-TM**·*o*-Cb system, the **3.2-TM** showed a large hydrodynamic radius consistent with its crystal structure.

However, the  $R_H$  (bound) value for the *o*-Cb guest (10.35 Å) in the **3.2-TM**·*o*-Cb complex is somewhat different from that of the *o*-Cb  $\subset$  **3.2** (11.90 Å), which can be attributed to the loose association of *o*-Cb at the exterior of **3.2-TM** (Table 3.2).

**Table 3.2.** Selected hydrodynamic radii values for the tightest host-guest bound pairs

Guest $\subset$ Host complex	Hydrodynamic Radius (Free, Å)		Hydrodynamic Radius (Bound, Å)	
	Host	Guest	Host	Guest
<i>o</i> -Cb $\subset$ <b>3.1</b>	10.61	5.80	11.44	11.38
<i>o</i> -Cb $\subset$ <b>3.2</b>	11.13	5.89	11.95	11.90
<i>o</i> -Cb $\subset$ <b>3.3</b>	10.98	6.34	11.87	11.78
<b>3.2-TM</b> · <i>o</i> -Cb	10.26	5.61	10.77	10.35

### 3.3.4. Single-molecule Optimization Studies.

Further insights into the host-guest binding scenario of **Cb**  $\subset$  **Cage** were obtained from the computed single-molecule energy optimization studies. Figure 3.5 shows the graphical representation of the binding energies of the various host-guest complexes studied. Most stable host-guest complexes with the lowest (most negative) energies were observed for *o*-Cb  $\subset$  **Cage** complexes of **3.1**, **3.2** and **3.3** with the respective binding energies of -661.54, -660.28, and -501.12 kcal/mol. The energies of *m/p*-Cb  $\subset$  **Cage** were slightly higher than the *o*-Cb  $\subset$  **Cage** systems, and the energies of the host-guest assemblies were lowered in the order *p*-Cb  $>$  *m*-Cb  $>$  *o*-Cb. In contrast, all **3.2-TM**·Cb systems exhibit much higher (less negative) optimized energies (in the range of -81.13 to -101.47 kcal/mol) than all the **Cb**  $\subset$  **Cage** systems (Table A3.7, Appendix 3). Among the cavity-bound host-guest systems, the tightest binding was observed for the *o*-Cb  $\subset$  **3.1** system with the deformation energy<sup>54</sup> of 0.98 kcal/mol closely followed by *o*-Cb  $\subset$  **3.2** (1.15 kcal/mol). However, all the deformation energy values were  $\approx$  1 kcal/mol (Table A3.8, Appendix 3), which is too low to cause any significant structural change to the main cage motif.

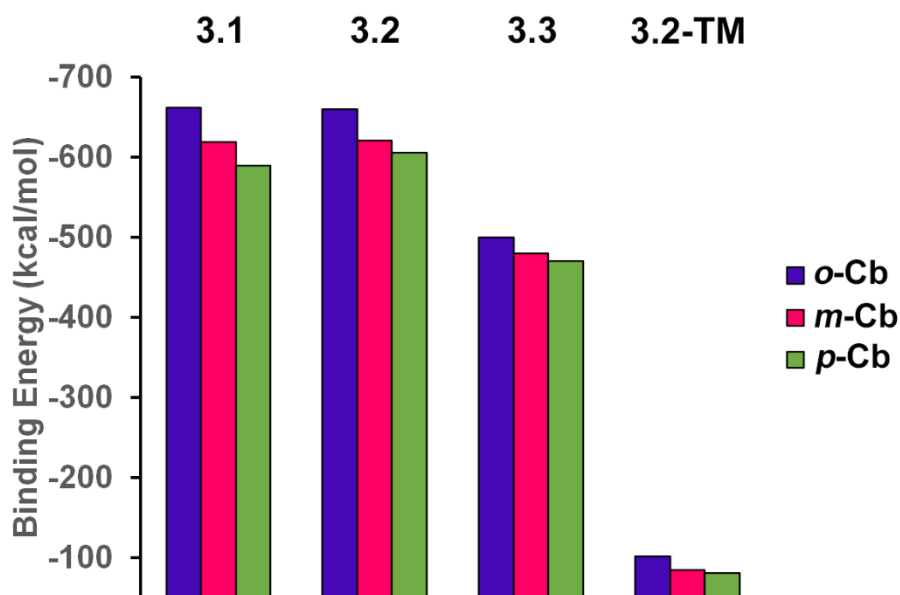


**Figure 3.5.** Graphical representation of the binding energies of the various host–guest complexes optimized for the hosts **3.1**, **3.2**, **3.3** and **3.2-TM**.

Figure 3.6 shows the DFT-optimized structures for *o*-Cb  $\subset$  **3.1** and *o*-Cb  $\subset$  **3.2**, with all major possible interactions (see Figures A3.66–A3.77, Appendix 3 for all the other optimized Cb  $\subset$  Cage structures). A closer inspection of these optimized structures shows the interactions responsible for forming stable host–guest moieties. In all the optimized assemblies, effective C–H $\cdots$ O and C–H $\cdots$ Cl or C–H $\cdots$ Br interactions of the carborane guest molecules with one or more of the anilate edges of the cage were found to be responsible for the formation of the highly stable host–guest entity. However, unlike the DOSY NMR analysis, the DFT-based host–guest studies were indicative of Cb  $\subset$  **3.1** assembly being energetically more stable than Cb  $\subset$  **3.2** assemblies, which are in turn more stable than Cb  $\subset$  **3.3**. This could be attributed to relatively stronger C–H $\cdots$ Cl interactions in the Cb  $\subset$  **3.1** system over the corresponding C–H $\cdots$ Br or C–H $\cdots$ O interactions in **3.2** and **3.3**, respectively.

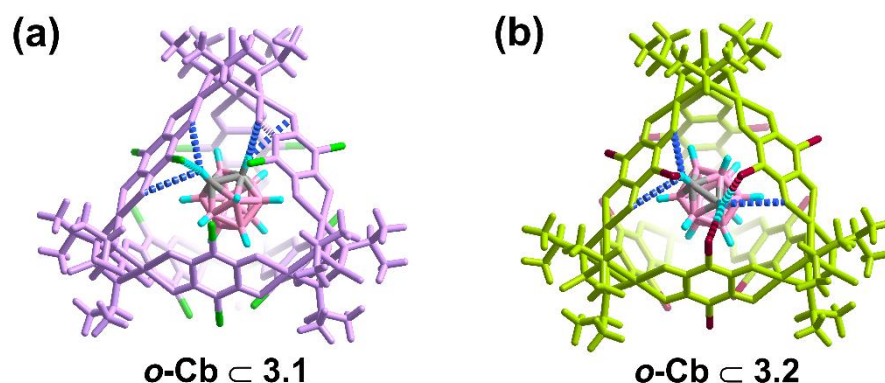


**Figure 3.6.** Possible non-covalent interactions responsible for the stabilization of the host-guest assemblies of (a)  $o\text{-Cb} \subset 3.1$ , and (b)  $o\text{-Cb} \subset 3.2$ .

### 3.4. Conclusion

In summary, this study shows the efficient encapsulation of the carborane isomers at the intrinsic pockets of neutral tetrahedral cages built from  $\text{Pd}^{\text{II}}$  ions stabilized by tris(imido)phosphate trianions and anilate linkers. A combination of mass spectrometry, IR spectroscopy, NOESY and/or ROESY- and DOSY-NMR and computational studies confirmed the definite encapsulation of *o*-, *m*- and *p*-isomers of the **Cb** guests within the cavities of cages **3.1**, **3.2** and **3.3**. Notably, from the DOSY NMR analysis it is evident that host cages and **Cb** guest isomers diffuse at the same rate in the encapsulated state. Moreover, the DOSY-derived hydrodynamic radii of the guests in the bound states closely match the radii of the bound hosts, which confirms the encapsulation of these **Cb** guests within the intrinsic cavity of the cages. The radii of the cages in the free and bound states also match with those calculated from their crystal and optimized structures, thus confirming the structural integrity of the cage with and without guest encapsulation. In contrast, the intermediate tetrameric complex **3.2-TM** shows evidence of **Cb** guest binding at the exteriors of the cavitand and acts as a ‘control group’ to distinguish extrinsic guest binding from the typical intrinsic ones. All these observations clearly show the merits of in-situ synthesis of host-guest assemblies as an efficient means of capturing larger guest molecules in the cage cavities that were otherwise impossible to achieve by conventional post-assembly methods. Neutral host-guest systems based on  $\text{Pd}^{\text{II}}$  ions are relatively under-explored; but with subtle variations in the synthetic approaches, these imido- $\text{P}^{\text{V}}$  supported  $\text{Pd}^{\text{II}}$  systems can be credited as promising building blocks for developing new functional molecules with interesting features and applications.



### 3.5. References

1. R. Chakrabarty, P. S. Mukherjee, P. J. Stang, *Chem. Rev.* **2011**, *111*, 6810-6918.
2. J. J. Perry Iv, J. A. Perman, M. J. Zaworotko, *Chem. Soc. Rev.* **2009**, *38*, 1400-1417.
3. M. D. Ward, *Chem. Commun.* **2009**, 4487-4499.
4. M. M. J. Smulders, I. A. Riddell, C. Browne, J. R. Nitschke, *Chem. Soc. Rev.* **2013**, *42*, 1728-1754.
5. M. D. Ward, P. R. Raithby, *Chem. Soc. Rev.* **2013**, *42*, 1619-1636.
6. D. Zhang, T. K. Ronson, J. R. Nitschke, *Acc. Chem. Res.* **2018**, *51*, 2423-2436.
7. A. Jiménez, R. A. Bilbeisi, T. K. Ronson, S. Zarra, C. Woodhead, J. R. Nitschke, *Angew. Chem. Int. Ed.* **2014**, *53*, 4556-4560.
8. M. Whitehead, S. Turega, A. Stephenson, C. A. Hunter, M. D. Ward, *Chem. Sci.* **2013**, *4*, 2744-2751.
9. A. J. McConnell, C. M. Aitchison, A. B. Grommet, J. R. Nitschke, *J. Am. Chem. Soc.* **2017**, *139*, 6294-6297.
10. A. M. Castilla, T. K. Ronson, J. R. Nitschke, *J. Am. Chem. Soc.* **2016**, *138*, 2342-2351.
11. N. Busschaert, C. Caltagirone, W. Van Rossom, P. A. Gale, *Chem. Rev.* **2015**, *115*, 8038-8155.
12. D. Zhang, T. K. Ronson, Y.-Q. Zou, J. R. Nitschke, *Nat. Rev. Chem.* **2021**, *5*, 168-182.
13. W. Xuan, M. Zhang, Y. Liu, Z. Chen, Y. Cui, *J. Am. Chem. Soc.* **2012**, *134*, 6904-6907.
14. T. Kida, T. Iwamoto, H. Asahara, T. Hinoue, M. Akashi, *J. Am. Chem. Soc.* **2013**, *135*, 3371-3374.
15. J. K. Clegg, J. Cremers, A. J. Hogben, B. Breiner, M. M. J. Smulders, J. D. Thoburn, J. R. Nitschke, *Chem. Sci.* **2013**, *4*, 68-76.
16. M. Yoshizawa, J. K. Klosterman, M. Fujita, *Angew. Chem. Int. Ed.* **2009**, *48*, 3418-3438.
17. C. J. Brown, F. D. Toste, R. G. Bergman, K. N. Raymond, *Chem. Rev.* **2015**, *115*, 3012-3035.
18. M. Raynal, P. Ballester, A. Vidal-Ferran, P. W. N. M. van Leeuwen, *Chem. Soc. Rev.* **2014**, *43*, 1734-1787.
19. S. Qin, Y. Lei, J. Guo, J.-F. Huang, C.-P. Hou, J.-M. Liu, *ACS Appl. Mater. Interfaces* **2021**, *13*, 25960-25971.
20. X. Jing, C. He, L. Zhao, C. Duan, *Acc. Chem. Res.* **2019**, *52*, 100-109.

21. F. J. Rizzuto, D. M. Wood, T. K. Ronson, J. R. Nitschke, *J. Am. Chem. Soc.* **2017**, *139*, 11008-11011.
22. C. Ji, W. Wang, E.-S. M. El-Sayed, G. Liu, Y. Si, K. Su, Z. Ju, F. Wu, D. Yuan, *Appl. Catal. B.* **2021**, *285*, 119782.
23. S. Goeb, S. Bivaud, V. Croué, V. Vajpayee, M. Allain, M. Sallé, *Materials*, **2014**, *7*, 611-622.
24. C.-Y. Zhu, M. Pan, C.-Y. Su, *Isr. J. Chem.* **2019**, *59*, 209-219.
25. S. M. McNeill, D. Preston, J. E. M. Lewis, A. Robert, K. Knerr-Rupp, D. O. Graham, J. R. Wright, G. I. Giles, J. D. Crowley, *Dalton Trans.* **2015**, *44*, 11129-11136.
26. J. E. M. Lewis, E. L. Gavey, S. A. Cameron, J. D. Crowley, *Chem. Sci.* **2012**, *3*, 778-784.
27. J. W. Yi, N. P. E. Barry, M. A. Furrer, O. Zava, P. J. Dyson, B. Therrien, B. H. Kim, *Bioconjugate Chem.* **2012**, *23*, 461-471.
28. G. Liu, Y. Di Yuan, J. Wang, Y. Cheng, S. B. Peh, Y. Wang, Y. Qian, J. Dong, D. Yuan, D. Zhao, *J. Am. Chem. Soc.* **2018**, *140*, 6231-6234.
29. D. Li, J. Zhang, K. Landskron, T. Liu, *J. Am. Chem. Soc.* **2008**, *130*, 4226-4227.
30. V. Brega, M. Zeller, Y. He, H. Peter Lu, J. K. Klosterman, *Chem. Commun.* **2015**, *51*, 5077-5080.
31. G. A. Craig, P. Larpent, S. Kusaka, R. Matsuda, S. Kitagawa, S. Furukawa, *Chem. Sci.* **2018**, *9*, 6463-6469.
32. R. W. Larsen, *J. Am. Chem. Soc.* **2008**, *130*, 11246-11247.
33. A. J. McConnell, *Chem. Soc. Rev.* **2022**, *51*, 2957-2971.
34. S. A. Kadam, K. Haav, L. Toom, T. Haljasorg, I. Leito, *J. Org. Chem.* **2014**, *79*, 2501-2513.
35. F. J. Rizzuto, L. K. S. von Krbek, J. R. Nitschke, *Nat. Rev. Chem.* **2019**, *3*, 204-222.
36. E. G. Percástegui, *Eur. J. Inorg. Chem.* **2021**, *2021*, 4425-4438.
37. A. Yadav, M. Sarkar, S. Subrahmanyam, A. Chaudhary, E. Hey-Hawkins, R. Boomishankar, *Chem. Eur. J.* **2020**, *26*, 4209-4213.
38. R. N. Grimes, *Carboranes*, 3rd ed.; Grimes, R. N., Ed.; Academic Press: Boston, 2016.
39. M. Scholz, E. Hey-Hawkins, *Chem. Rev.* **2011**, *111*, 7035-7062.
40. P. Stockmann, M. Gozzi, R. Kuhnert, M. B. Sárosi, E. Hey-Hawkins, *Chem. Soc. Rev.* **2019**, *48*, 3497-3512.
41. R. F. Barth, P. Mi, W. Yang, *Cancer Commun.* **2018**, *38*, 35.

42. Z. J. Leśnikowski, *J. Med. Chem.* **2016**, *59*, 7738-7758.
43. M. F. Hawthorne, *Angew. Chem. Int. Ed. Engl.* **1993**, *32*, 950-984.
44. F. Issa, M. Kassiou, L. M. Rendina, *Chem. Rev.* **2011**, *111*, 5701-5722.
45. T. Kusukawa, M. Fujita, *Angew. Chem. Int. Ed.* **1998**, *37*, 3142-3144.
46. E. V. Peresyphkina, C. Heindl, A. Schindler, M. Bodensteiner, A. V. Virovets, M. Scheer, *Z. Kristallogr. - Cryst. Mater.*, **2014**, *229*, 735-740.
47. R. J. Blanch, M. Williams, G. D. Fallon, M. G. Gardiner, R. Kaddour, C. L. Raston, *Angew. Chem. Int. Ed. Engl.* **1997**, *36*, 504-506.
48. A. Kataki-Anastasakou, J. C. Axtell, S. Hernandez, R. M. Dziedzic, G. J. Balaich, A. L. Rheingold, A. M. Spokoyny, E. M. Sletten, *J. Am. Chem. Soc.* **2020**, *142*, 20513-20518.
49. T. E. Clark, M. Makha, C. L. Raston, A. N. Sobolev, *Dalton Trans.* **2006**, 5449-5453.
50. C. Carruthers, J. Fisher, L. P. Harding, M. J. Hardie, *Dalton Trans.* **2010**, *39*, 355-357.
51. A.K. Gupta, S. A. D. Reddy, R. Boomishankar, *Inorg. Chem.* **2013**, *52*, 7608-7614.
52. M. J. Frisch, Gaussian 03 Rev. C.01, Gaussian, Inc., Wallingford CT, 2016.
53. S. Grimme, *J. Comput. Chem.* **2006**, *27*, 1787-1799.
54. K. R. Ramya, A. Venkatnathan, *Comput. Theor. Chem.* **2013**, *1023*, 1-4.
55. G. Sheldrick, *Acta Crystallogr. Sect. A* **2008**, *64*, 112-122.
56. M. Sarkar, R. Boomishankar, *Inorg. Chem.* **2023**, *62*, 1855-1863.
57. With the two other isomers of carboranes, only one *D* value associated with each of the free *m-Cb* and *p-Cb* guests was obtained in the DOSY NMR. Likewise, a single *D* value (ca.  $5.1 \times 10^{-10}$  m<sup>2</sup>/s) was obtained for the tetramer **3.2-TM** indicating an absence of the formation of **3.2-TM·m-Cb** and **3.2-TM·p-Cb** complexes (Table A3.4, Figures A3.36-A3.47, Appendix 3).
58.  $D = (kT)/(6\pi\eta R_H)$ , where *D* is the diffusion coefficient, *k* is the Boltzman constant, *T* is the temperature in Kelvin,  $\eta$  is the viscosity of the solution, and *R<sub>H</sub>* is the radius of the molecular sphere.

 End of Chapter 3 

# Chapter 4



## Ligand-Guided Synthesis of Ligand-Free Metallocube Built on Imido-Pd(II) Clusters

## 4.1. Introduction

Supramolecular chemistry encompasses a vast range of sophisticated assemblies and frameworks built from the interaction of non-covalent intermolecular forces between smaller components. The supramolecular structural features and their wide range of functional properties along with the stored molecular information can be manipulated through the appropriate combination of these secondary interactions.<sup>1-3</sup> In metal-ligand cage chemistry, the geometry of building units and the nature of the coordinating ligands drive the formation of well-defined polyhedral assemblies. However, such high-symmetric cages are not simply obtained in a one-step spontaneous pathway. Instead, they are assembled in a step-wise fashion involving various stable or transient intermediate structures under different equilibrium conditions.<sup>4</sup> The nature of intermediates in a reaction typically depends on parameters such as concentrations and stoichiometries of the components, temperature, presence of secondary components, etc.<sup>5-9</sup> Additionally certain intermediates can sometimes act as kinetic products with temporal information (with respect to the metal-ligand interaction and subsequent preorganization) and further undergo sequential modifications before reaching the final target architecture. In this respect, the template effect in combination with self-organization has become one of the emerging synthetic approaches for constructing supramolecular cages, which would otherwise be impossible to synthesize.<sup>10-13</sup> The template effect is a key synthetic approach to control the arrangement of building blocks in cage assemblies.<sup>14-19</sup> In this approach, the building units of a cage are pre-organized into an ideal geometry by a well-designed organic primary linker which is subsequently replaced by a secondary stronger linker leading to the formation of unusual architectures as the final product.

Halides, especially, chlorides are one such category of non-directing secondary and are well-known for acting as templates for forming multinuclear cage complexes, via anion recognition.<sup>20-22</sup> As bridging ligands in coordination chemistry, they are known to form various macrocyclic structures or cluster cages with transition metals involving  $\mu_n$ -Cl linkages.<sup>23-26</sup> However, in most polyhedral and macrocyclic assemblies, the chloride ions exist as complementary ligands along with other appropriate organic linkers<sup>27-31</sup>. However, polyhedral coordination cages solely based on chloride bridges have not been well-explored, although polynuclear metal-chloride clusters are widely known in the literature.

Herein, we report the synthesis and guest recognition properties of a neutral 24-atom Pd(II)-cubic cage,  $[\{\text{Pd}_3(\text{N}^i\text{Pr})_3\text{PO}\}_8(\mu_2\text{-Cl})_{24}]$  (**4.1**), built by 24  $\mu_2\text{-Cl}$  bridges. Treatment of the hexanuclear precursor,  $[\{\text{Pd}_3(\text{N}^i\text{Pr})_3\text{PO}\}_2(\text{OAc})_2(\text{OH})]_2 \cdot 2(\text{CH}_3)_2\text{SO}$  (**HEXA-Pd**) with chloride ions in the presence of oxamide linkers leads to the formation of the cubic cage **4.1** as a thermodynamically stable product. Analyzing the reaction mixtures in the intermediate stages shows the formation of the assemblies **2.1-TM** and **2.1-TD** as intermediates. A rare prismatic assembly of formula  $[\{\text{Pd}_3(\text{N}^i\text{Pr})_3\text{PO}\}_6(\mu_2\text{-Cl})_{18}]$  as a transient intermediate is also proposed during the conversion of **2.1-TD** to **4.1**. These observations suggest that the formation of imido-Pd(II) derived cubic cage **4.1** involves a template-mediated pathway, in which the anionic oximido ligands act both as a template and as a primary linker for the intermediates. In contrast, in the absence of the oxamide ligand as a directing template, cage formation does not occur. Instead, the **HEXA-Pd** undergoes a self-condensation reaction forming a pentameric cluster, **4.2**. These observations were supported by X-ray diffraction data, NMR, and mass spectrometric techniques and by understanding their relative energies through computational studies. The host-guest studies of **4.1** are further explored with polar phenolic guest molecules resorcinol (**RC**), hydroquinone (**HQ**), and pyrogallol/pyrogallic acid (**PY**) at its intrinsic cavity. These guest molecules show a high binding affinity due to effective hydrogen bonding interactions between the host and guest systems.

## 4.2. Experimental Details

### 4.2.1. General Remarks

All manipulations involving phosphorus halides were performed under a dry nitrogen atmosphere in standard Schlenk glassware. Dry solvents were purchased from local vendors and used without further purification. The chemicals, isopropylamine, methylamine, oxamide, palladium acetate, resorcinol, hydroquinone, and pyrogallol, were purchased from Sigma-Aldrich and used as received.  $\text{POCl}_3$  was purchased locally and was distilled prior to use. The ligand  $[\text{PO}(\text{N}^i\text{Pr})_3]$  and the PBU precursor, **HEXA-Pd**  $[\{\text{Pd}_3(\text{N}^i\text{Pr})_3\text{PO}\}_2(\text{OAc})_2(\text{OH})]_2 \cdot 2(\text{CH}_3)_2\text{SO}$ , were prepared by the earlier reported procedures.<sup>32</sup> NMR spectra were recorded on a Bruker 400 MHz spectrometer ( $^1\text{H}$  NMR: 400.13 MHz,  $^{13}\text{C}\{^1\text{H}\}$  NMR: 100.62 MHz,  $^{31}\text{P}\{^1\text{H}\}$  NMR: 161.97 MHz) spectrometer at room temperature using TMS ( $^1\text{H}$ ,  $^{13}\text{C}$ ) and 85%  $\text{H}_3\text{PO}_4$  ( $^{31}\text{P}$ ). The mass spectra were obtained on an Applied Bio system matrix-assisted laser desorption ionization time-of-flight (MALDI-TOF)/TOF spectrometer. For mass spectral measurements, both 2,5-dihydroxybenzoic acid

(DHB) and  $\alpha$ -cyano-4-hydroxy-cinnamic acid (CHCA) matrix or a 1:1 mixture of them has been used as the matrix. Elemental analyses were performed on a Vario-EL cube elemental analyzer.

### 4.2.2. Syntheses

**4.2.2.1. Synthesis of 4.1:** To a stirred solution of **HEXA-Pd**, (20.10 mg, 0.0140 mmol) in 5:1 DMSO-MeOH solution at room temperature, oxamide (1.85 mg, 0.0210 mmol) was added. The resultant mixture was initially heated at 80°C for 30 min to yield a yellow-colored precipitate following which isopropyl ammonium chloride (4.00 mg, 0.0421 mmol) was added and the temperature was raised up to 120°C. A brown precipitated compound was obtained after 12 hours, which was recovered by filtration and dried under vacuum. Orange-brown square-like crystals were obtained from its DMSO-chloroform solution (by solvent evaporation method) after 7-10 days. Yield: 65% (based on P). MALDI-TOF/TOF: Expected- 5151.97, Found- 5255.5 [M+DMSO+Na]<sup>+</sup>. <sup>31</sup>P NMR (161 MHz, CDCl<sub>3</sub>):  $\delta$  76.52; <sup>1</sup>H NMR (400 MHz, CDCl<sub>3</sub>):  $\delta$  1.63 (d,  $J$  = 6.8 Hz, CH<sub>3</sub>), 3.72 (m, CH); <sup>13</sup>C NMR (100 MHz, CDCl<sub>3</sub>):  $\delta$  26.39, 43.78. Elemental Analysis (%): Calcd for C<sub>72</sub>H<sub>168</sub>Cl<sub>24</sub>N<sub>24</sub>O<sub>8</sub>P<sub>8</sub>Pd<sub>24</sub>: C, 16.79; H, 3.29; N, 6.53. Found: C, 16.65; H, 3.40; N, 6.58.

**4.2.2.2. Synthesis of 4.2:** To a stirred solution of **HEXA-Pd**, (20.10 mg, 0.0140 mmol) in 5:1 DMSO-MeOH solution at room temperature, isopropyl ammonium chloride (4.00 mg, 0.0421 mmol) was added and the reaction mixture was stirred for 45min at 60°C. A yellow-colored clear solution was obtained, which was filtered through celite and kept for crystallization. Yellow triangular shaped crystals were obtained from the resulting solution after 4-5 days (by solvent evaporation method). Yield: 70% (based on P). MALDI-TOF/TOF: 1125.20 [M+Na]<sup>+</sup>. <sup>31</sup>P NMR (161 MHz, CDCl<sub>3</sub>):  $\delta$  73.44; <sup>1</sup>H NMR (400 MHz, CDCl<sub>3</sub>):  $\delta$  1.14 (d,  $J$  = 6.8 Hz, CH<sub>3</sub>), 3.06 (s, OCOCH<sub>3</sub>), 3.38 (m, CH); <sup>13</sup>C NMR (100 MHz, CDCl<sub>3</sub>):  $\delta$  27.58, 27.59, 43.87, 54.21, 172.46. Elemental Analysis (%): Calcd for C<sub>22</sub>H<sub>45</sub>N<sub>6</sub>O<sub>8</sub>P<sub>2</sub>Pd<sub>5</sub>: C, 23.68; H, 4.07; N, 7.53. Found: C, 23.52; H, 4.18; N, 7.60.

### 4.2.3. Crystallography

Reflections were collected on a Bruker Kappa Apex Duo diffractometer at 100 K using Mo K $\alpha$  radiation ( $\lambda$  = 0.71073 Å). All structures were solved using intrinsic phasing method and refined by full-matrix least-squares on F<sup>2</sup> (G. M. Sheldrick, SHELX-2014, program for crystal structure refinement, University of Gottingen, Germany, 2015).<sup>33</sup> Crystallographic data for all these compounds are listed in Table 4.1.

All non-hydrogen atoms were refined anisotropically if not stated otherwise. The crystals of **4.1** diffracted very weakly at higher angles and hence its data is truncated to  $2\theta = 45^\circ$ . Hydrogen atoms were constrained in geometric positions to their parent atoms. The diffuse solvent molecules in both **4.1** and **4.2** could not be modeled appropriately. Hence, these were treated as diffuse contributions to the overall scattering and removed by the SQUEEZE/PLATON for better refinement data. The squeezed volume in **4.1** was found to be  $2165 \text{ \AA}^3$  which corresponds approximately to 40 water molecules and 20 methanol molecules. The squeezed volume in **4.2** was found to be  $180 \text{ \AA}^3$  which accounted for approximately 6 water molecules. In the final refinements of **4.1**, OMIT command was used to remove some reflections for which  $I(\text{obs})$  and  $I(\text{calc})$  differed more than 10 times SigmaW (the latter being the square root of  $1.0/\text{weight}$  for that reflection in the L.S. refinement).

**Table 4.1. Crystallographic Data for 4.1 and 4.2**

Compound	4.1	4.2
Chemical formula	$\text{C}_{72}\text{H}_{168}\text{Cl}_{24}\text{N}_{24}\text{O}_8\text{P}_8\text{Pd}_{24}$	$\text{C}_{22}\text{H}_{45}\text{N}_6\text{O}_8\text{P}_2\text{Pd}_5$
Formula weight	5150.45	1115.58
Temperature	100(2) K	100(2) K
Crystal system	Triclinic	Orthorhombic
Space group	<i>P</i> -1	<i>Pnma</i>
a (Å); $\alpha$ (°)	18.719(9); 119.610(9)	24.318(3); 90
b (Å); $\beta$ (°)	18.828(9); 105.303(9)	17.135(2); 90
c (Å); $\gamma$ (°)	18.866(9); 102.192(9)	9.5649(11); 90
V (Å <sup>3</sup> ); Z	5091(4); 1	3985.7(8); 4
$\rho$ (calc.) mg m <sup>-3</sup>	1.680	1.859
$\mu(\text{Mo K}\alpha)$ mm <sup>-1</sup>	2.472	2.336
$2\theta_{\text{max}}$ (°)	45.028	56.692



R(int)	0.2573	0.0554
Data / param.	13326 / 745	5117 / 212
GOF	0.975	1.035
R1 [F>4σ(F)]	0.0783	0.0324
wR2 (all data)	0.2406	0.0752
max. peak/hole (e.Å <sup>-3</sup> )	2.215/-1.165	1.229/-0.767

#### 4.2.4. <sup>1</sup>H-2D-DOSY NMR Studies

The <sup>1</sup>H-2D-DOSY NMR experiments were carried out on a Bruker AVANCE III NMR spectrometer operating at a <sup>1</sup>H frequency of 400 MHz at a constant temperature of 298K. 3.0 mM solutions of the participating species and host–guest complexes were prepared in CDCl<sub>3</sub> and allowed to equilibrate for 30 minutes before data acquisition. Diffusion-Ordered Spectroscopy (DOSY) experiments were performed by varying gradient strength. The “T1/T2” module in Topspin 4.1 software was used for regression analysis to calculate the diffusion coefficient for each integral region or individual selected peak. The fitting of the diffusion dimension in the 2D-DOSY spectra was carried out using a one-parameter mono-exponential (equation 1) or a two-parameter biexponential fit (equation 2).

$$I = I_0 \exp[-D\gamma^2 g^2 \delta^2 (\Delta - \delta/3)] \dots (1)$$

$$I = I_{0A} \exp[-D_A \gamma^2 g^2 \delta^2 (\Delta - \delta/3)] + I_{0B} \exp[-D_B \gamma^2 g^2 \delta^2 (\Delta - \delta/3)] \dots (2)$$

In this equation, I is the observed integral, I<sub>0</sub>, I<sub>0A</sub> and I<sub>0B</sub> are the reference or un-attenuated integrals, D, D<sub>A</sub>, and D<sub>B</sub> are the diffusion coefficients, γ is the gyromagnetic ratio of the detected nucleus, g is the gradient strength, δ the length of the gradient pulse, and Δ the diffusion time.

#### 4.2.5. Guest Encapsulation Studies

**4.2.5.1 General procedure for preparation of Guest ⊂ 4.1 Complexes:** 2-2.5mg of the guest was added to 10 mg of 4.1 in 1ml CDCl<sub>3</sub>. The resulting solution was stirred further for one hour at room temperature. The obtained mixture was analyzed by MALDI-TOF and <sup>1</sup>H-2D-DOSY NMR spectroscopy which revealed the formation of host-guest complexes.

**4.2.5.2. Procedure for the UV titration of Guest  $\subset$  4.1 Complexes:** The stock solutions of RC, HQ, and PY in 2 mM concentrations were freshly prepared by dissolving them in chloroform (HPLC grade). Separate stock solutions of **4.1** (4 mM) in chloroform were freshly prepared at room temperature. For all three guests, the host solution of **4.1** of concentration 2.5  $\mu$ M in 2 mL of solvent (1:1 MeOH-CHCl<sub>3</sub>) was placed in a 10 mm cuvette (2.0 mL), and the guest solutions of RC, HQ, and PY (0.5eq-100eq) was added by using micro pipette. The entire UV-Vis spectra in titration experiments were collected at room temperature after stirring the sample solution for ca. 3 min. The changes in the absorption maxima values of the host were monitored. Based on the data obtained in the 220-800 nm range, the binding constants were calculated by using the online Bindfit tool. The values of the binding constants were presented as mean  $\pm$  standard deviation in all these independent experiments.

### 4.2.6. Theoretical Calculations

The gas-phase single-molecule optimization energies of all the participating species and the host-guest systems were calculated theoretically by using the Gaussian 09 software.<sup>37, 38</sup> These energies were computed by semi-empirical PM6 calculations. For the host-guest complexes, the energies of the host cage **4.1**, guest molecules, and host-guest complexes were separately calculated and the binding energy of a given complex was calculated by using the following equation.

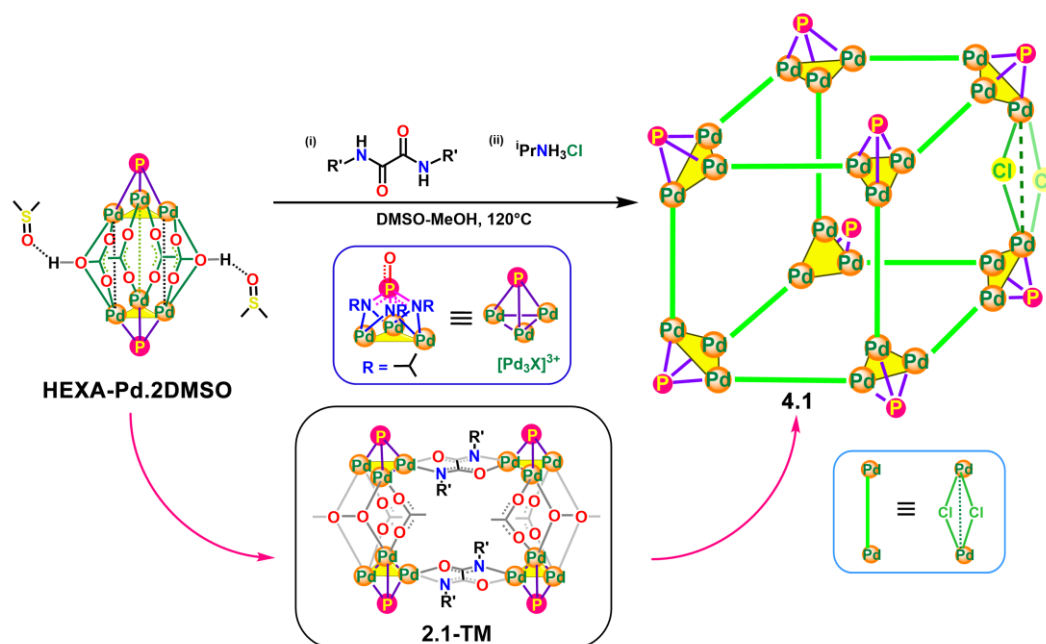
$$\text{Binding energy} = E_{\text{Guest} \subset 4.1} - (E_{4.1} + E_{\text{Guest}})$$

## 4.3. Results and Discussions

### 4.3.1. Synthesis

Treatment of **HEXA-Pd** with <sup>1</sup>PrNH<sub>3</sub>Cl in the presence of oxamide linker [ $\{C_2(NH)_2O_2\}^{2-}$ ] in DMSO/MeOH mixture at 120 °C resulted in the formation of cubical assembly **4.1** in an in-situ post-assembly modification manner (Scheme 4.1). Cube **4.1** was characterized in solution by NMR spectroscopy and MALDI-TOF mass spectrometry (Figures A4.1-A4.4, Appendix 4). The <sup>31</sup>P-NMR spectra displayed a single peak at 76.52 ppm while <sup>1</sup>H-NMR spectra gave well-resolved signals corresponding to the isopropyl groups. The mass spectral analysis showed a peak centered at an m/z value of 5255.5 corresponding to [**4.1**+DMSO+Na]<sup>+</sup> species. The **HEXA-Pd** precursor consisting of two [Pd<sub>3</sub>X]<sup>3+</sup> units is a very versatile building block in forming neutral cages with varied topologies as reported earlier due to the presence of labile acetate and hydroxy linkages present in it.<sup>39-41</sup> However, the reaction of the analogous chloro-

bridged precursor  $[\{\text{Pd}_3(\text{N}^i\text{Pr})_3\text{PO}\}(\text{Cl})_6]_2$ , **HEXA-Pd-Cl (1.29)**<sup>32</sup> under similar conditions did not yield the product **4.1** due to the higher strength of Pd-Cl bonds present in the precursor unit compared to the oxamide ligands employed for the template procedure.<sup>42</sup>



**Scheme 4.1.** Synthetic pathway depicting the formation of chloro-bridged cubical assembly **4.1** via the formation of the template tetrameric cluster **2.1-TM**.

### 4.3.2. The Template Effect

To understand the function of the oxamide linker in the formation of **4.1**, the reaction was monitored in a step-wise fashion via MALDI-TOF spectrometry and 2D-DOSY NMR studies. It was observed that in the initial stages of the reaction, treatment of **HEXA-Pd** with oxamide in methanol leads to the formation of the tetrameric complex (**2.1-TM**) which has been previously established as a stable intermediate in the formation of corresponding oxamide-tethered neutral tetrahedral cages.<sup>41</sup> Figure 4.1 shows the MALDI-TOF mass spectra of the reaction mixtures taken at different time intervals.

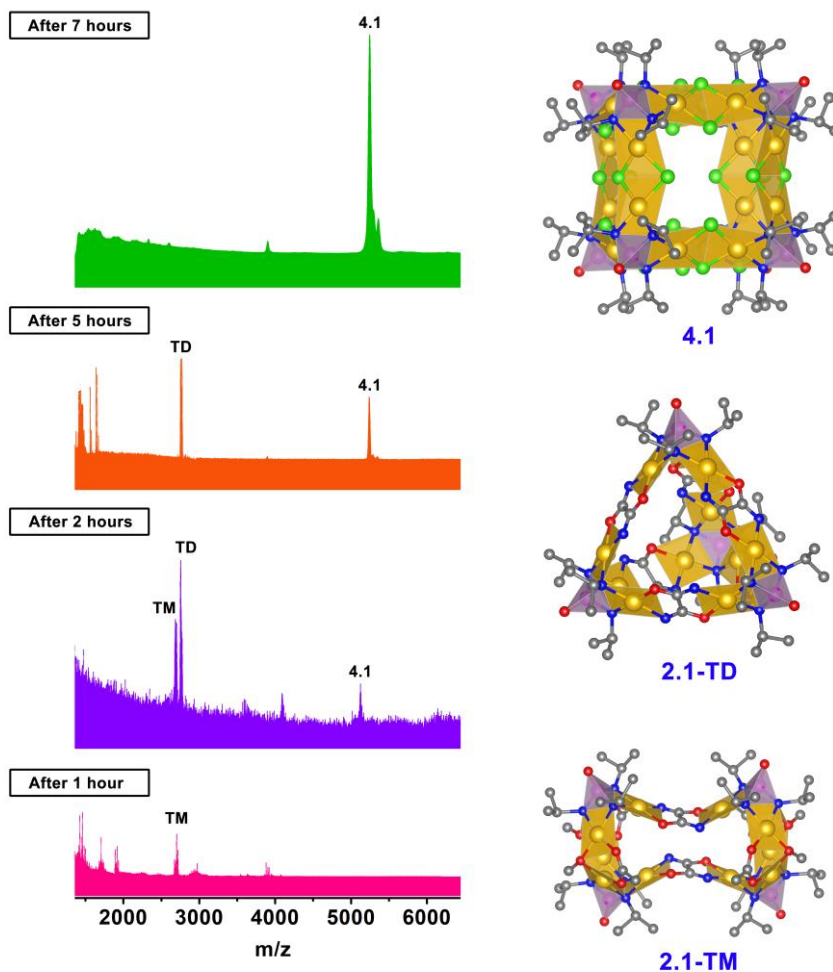


**Figure 4.1.** MALDI-TOF mass spectra of the template reaction taken at various intervals (left). Structures of all of the associated cage complexes of this pathway are shown for comparison (right).

The early reaction mixture after 1h shows the formation of **2.1-TM** giving peaks at  $m/z$  values centered at 2703.89, which subsequently converts to **2.1-TD** ( $m/z$ : 2763.21) and finally to **4.1** as the sole product at the signature  $m/z$  value of 5254.31. Further, under the applied reaction conditions, the oxamide and acetate linkages were replaced by chloride anions, and the cubical assembly **4.1** was obtained as a sole product after 7 hours. Further evidence was also obtained from the 2D-DOSY-NMR of the reaction at various stages showing the D-values corresponding to **2.1-TM**, **2.1-TD** and **4.1**. While **2.1-TM** was obtained at lower temperatures (65°C) as an isolable intermediate, the presence of  $\text{Cl}^-$  ions and a higher temperature (120°C) expedited the dimerization of the **2.1-TD** and rapidly converts it into cage **4.1** (Figure 4.2). The structure of **2.1-TM** has already been described in Chapter 2 and its structure in the isolated solid was again confirmed by verifying the unit cell parameters of its single crystal (Table 4.2).

In addition to mass and DOSY-NMR, the formation of **2.1-TM** and its subsequent conversions to **2.1-TD** and **4.1** has also been observed by  $^{31}\text{P}$ -NMR spectroscopy (Figure A4.5 and A4.6, Appendix 4).

**Table 4.2. Unit Cell Parameters observed for 2.1-TM.**

Compound	2.1-TM (This Work)	2.1-TM (Reported in Chapter 2)
a (Å); $\alpha$ (°)	11.93(3); 102.57(4)	11.86(2); 102.49(3)
b (Å); $\beta$ (°)	14.71(3); 103.22(3)	14.59(3); 103.26(3)
c (Å); $\gamma$ (°)	17.49(4); 107.56(4)	17.38(3); 107.70(4)
V (Å <sup>3</sup> )	2710(2)	2651(8)

It was thus proposed that the tetrameric assembly **2.1-TM**, formed from the labile **HEXA-Pd** complex acts as a template cage in bringing the  $[\text{Pd}_3\text{X}]^{3+}$  polyhedral building units (PBUs) in a pre-organized fashion, which would not be possible in the presence of only a non-directing monoanionic ligand such as  $\text{Cl}^-$  ion. Further, the presence of oxamide-tethered tetrahedral cage **2.1-TD**<sup>41</sup> as a minor intermediate was observed from the spectral data due to excess oxamide dianions in the solution. Even though **2.1-TD** acts as a transient intermediate under the given reaction conditions, the final product was not a tetrahedral cage chloro-linkers (**TD-Cl**) because of the high torsional strain that ensues in the Pd-Cl linkages, which could not be alleviated in **TD-Cl** in the absence of any wide-angle chelating ligand such as oxamide (*vide supra*). Thus, the replacement of oxamide linkages and the subsequent dimerization of two molecules of **TD-Cl** in the final step of the reaction led to the formation of **4.1** with the most stable cubical geometry.

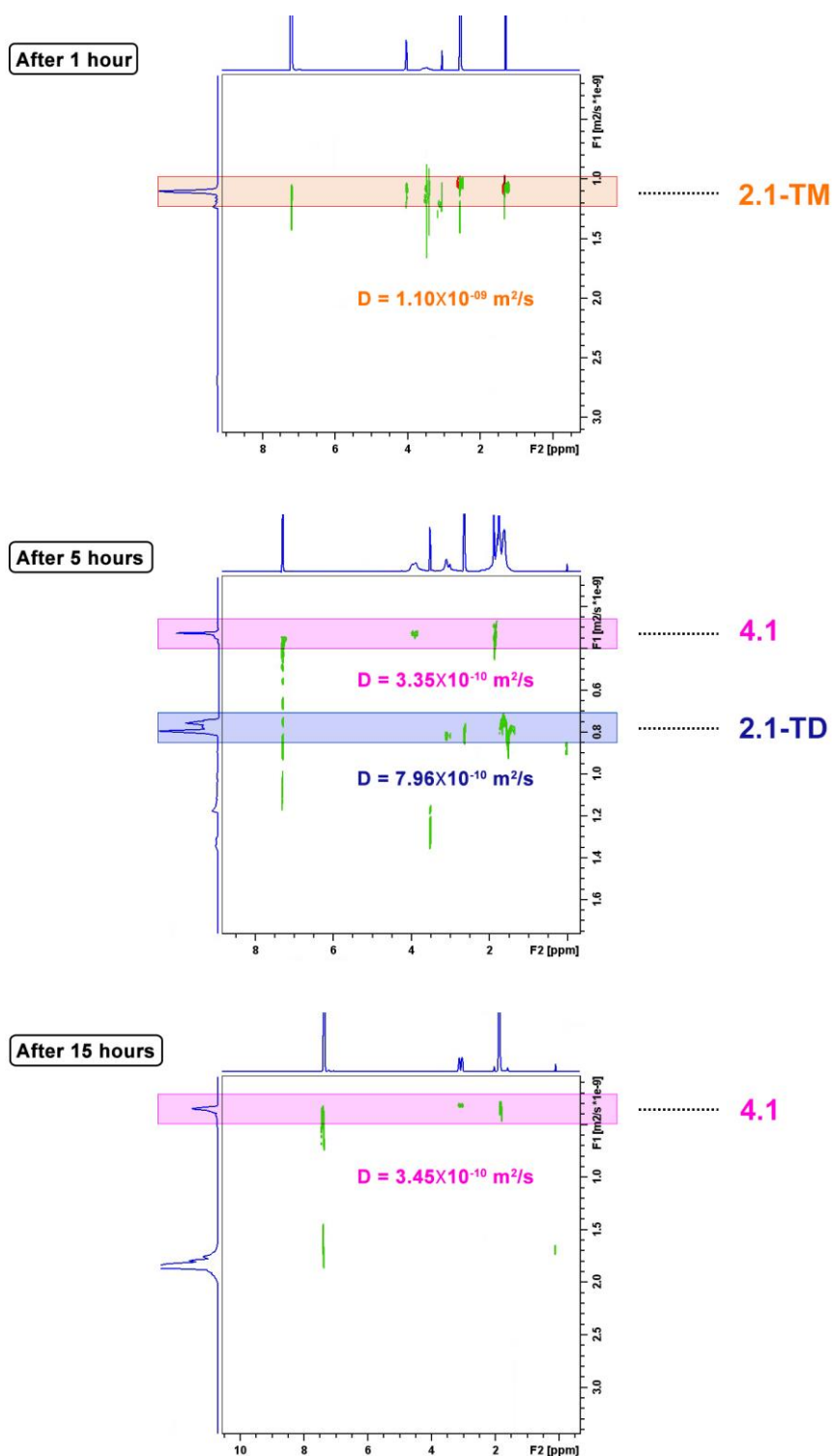


**Figure 4.2.**  $^1\text{H}$ -2D-DOSY NMR of the template pathway taken at different stages of the reaction.

Further to corroborate the results of the template effect, a control reaction was performed without the oxamide linker. As expected, the formation of the cubic assembly of **4.1** was not observed in the absence of pre-organized PBUs. Instead, the **HEXA-Pd** cluster was found to

transform into a pentameric Pd-cluster **4.2** of formula  $[\text{Pd}_5\{(\text{N}^i\text{Pr})_3\text{PO}\}_2(\text{OH})_2(\text{OAc})_2]$  with no chloride linkages (Figure 4.3, Figures A4.7-A4.10, Appendix 4). The molecular structure of **4.2** with the formula  $[\text{Pd}_5\{(\text{N}^i\text{Pr})_3\text{PO}\}_2(\text{OH})_2(\text{OAc})_2]$  was solved in the orthorhombic *Pnma* space group featuring half of the molecule in the asymmetric unit. Careful analysis of the molecular structure revealed **4.2** to be a self-condensed product formed by eliminating one molecule of  $\text{Pd}(\text{OAc})_2$  from the **HEXA-Pd** cluster. Unlike the trigonal arrangement of the Pd-atoms in  $[\text{Pd}_3\text{X}]^{3+}$  subunit, **4.2** accommodated five Pd-atoms in a square pyramidal arrangement with the apex consisting of a single Pd-atom shared by the two condensed  $[\text{Pd}_3\text{X}]^{3+}$  units (Figure A4.11, Appendix 4). This self-condensation reaction could be attributed to the combined effects of the thermal reaction conditions and the absence of a directing linker.

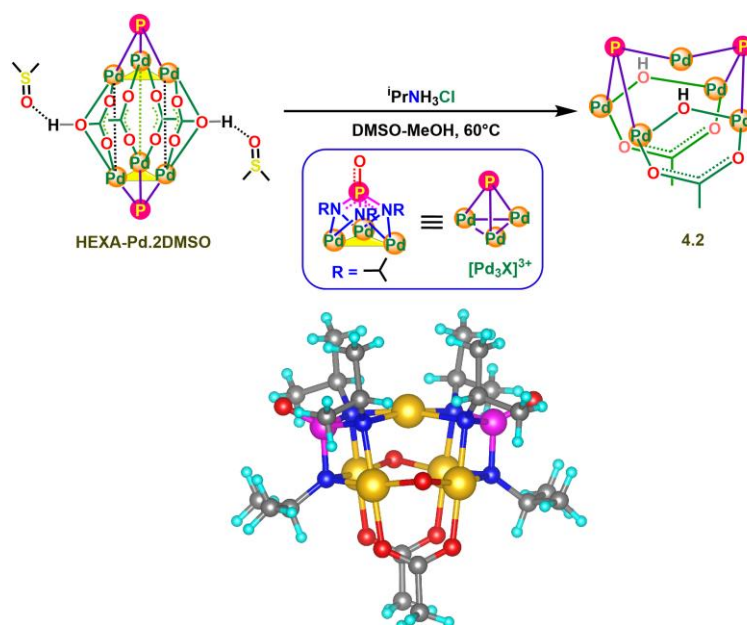


**Figure 4.3.** Synthetic pathway depicting the formation of pentameric cluster **4.2** (top) and its molecular structure (below).

### 4.3.3. Structural Analysis of 4.1

The single-crystal of **4.1** was obtained from the slow evaporation of its solution in a DMSO- $\text{CHCl}_3$  mixture. The molecular structure of **4.1** was solved in the Triclinic *P-1* space group. The asymmetric unit featured half of the cage molecule consisting of four units of  $\text{Pd}_3\text{X}$  motifs, *cis*-protected by the hexadentate coordination of tris(imido)phosphate trianions, and twelve chloride ions (Figure 4.4). Each of the  $\text{Pd}_3\text{X}$  clusters along the eight corners of the cube is tricationic, amounting to an overall cationic charge of twenty-four. The charge balance in the cage is restored by twenty-four chloride ions located along the twelve edges of the cube.

Moreover, the stability of the cage arises from twenty-four strong Pd-Cl bonds, which compensates for the loss of stability due to the removal of wide-angle chelation of the oxamide linkers. Further, the tendency of the Pd(II) ion to maintain the stable square planar coordination environment forming a compact cubic assembly has led to the slight concaving of the Pd-Cl linkages by an angle of  $10.71^\circ$  (Figure A4.12-A4.14, Appendix 4). Single-molecule energy optimization calculations by DFT showed that compared to **4.1** ( $E_{\text{opt}} = -8.11 \times 10^8$  kcal/mol), a hypothetical tetrahedral cage **TD-Cl**\* would have much higher energy ( $E_{\text{opt}} = -4.95 \times 10^5$  kcal/mol) due to the absence of twelve additional Pd-Cl linkages in the latter (Figure A4.15, Appendix 4) corroborating the exclusive formation of **4.1** in the template pathway.

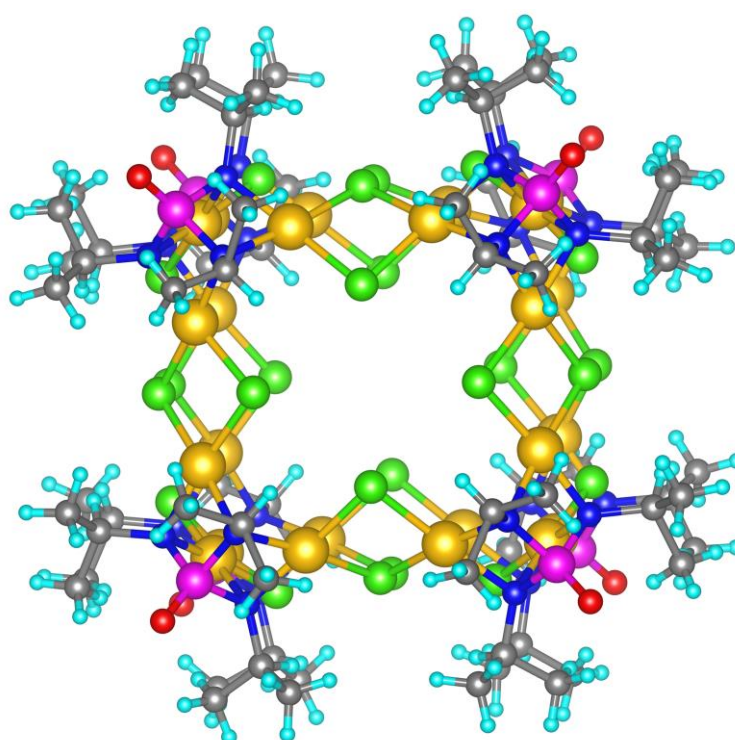


**Figure 4.4.** SCXRD derived molecular structure of **4.1** (Colour code: C, grey; H, cyan; N, blue; O, red; P, magenta; Pd, golden-yellow; Cl, light-green).

Further structural analysis revealed that the phosphoramidate units situated in the diagonally opposite vertices of **4.1** adopt a staggered arrangement as opposed to an eclipsed/prismatic arrangement observed in a previously reported cubic cage  $[\text{Pd}_{24}(\text{PZDC})_{12}]$ , **1.35** supported by the O, N-chelating coordination of the pyrazine dicarboxylate (PZDC) linkers.<sup>40</sup> This is also evident from the structure of their hexameric counterparts, **HEXA-Pd** and **HEXA-Pd-Cl**, (**1.29**)<sup>32</sup> where the two  $[\text{Pd}_3\text{X}]^{3+}$  PBUs were arranged in an eclipsed and staggered manner respectively. (Figure 4.5). Thus, it was inferred that even with identical geometries adopted by



the cages, the spatial arrangement of respective  $[\text{Pd}_3\text{X}]^{3+}$  PBUs was depended on the nature of metal-to-linker linkages and not the starting material. It is evident that the longer Pd-O / Pd-N linkages favored an eclipsed arrangement, the shorter and comparatively stronger Pd-Cl linkages favored the staggered one. This complementarity was further reflected in the average inter-planar Pd-Pd distance and the corresponding  $\langle\text{Pd-P-Pd}\rangle$  angle of **4.1** which was found to be 3.15(4) Å and 71.23(2)°, which closely matched with those observed for the **HEXA-Pd-Cl** precursor (**1.29**) ( $\text{Pd-Pd}_{\text{avg.}} = 3.13(1)$  Å and  $\langle\text{Pd-P-Pd}\rangle_{\text{avg.}} = 69.60(2)^\circ$ ).<sup>42</sup>

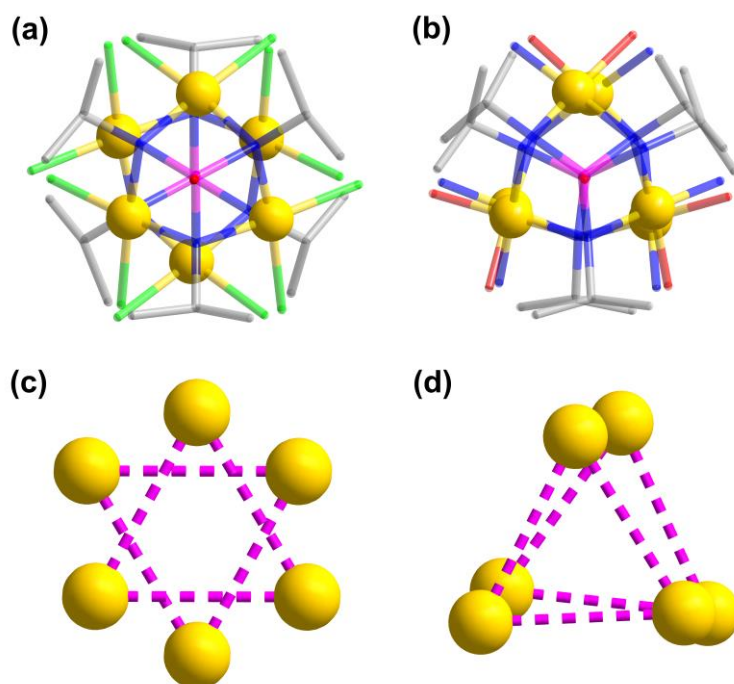
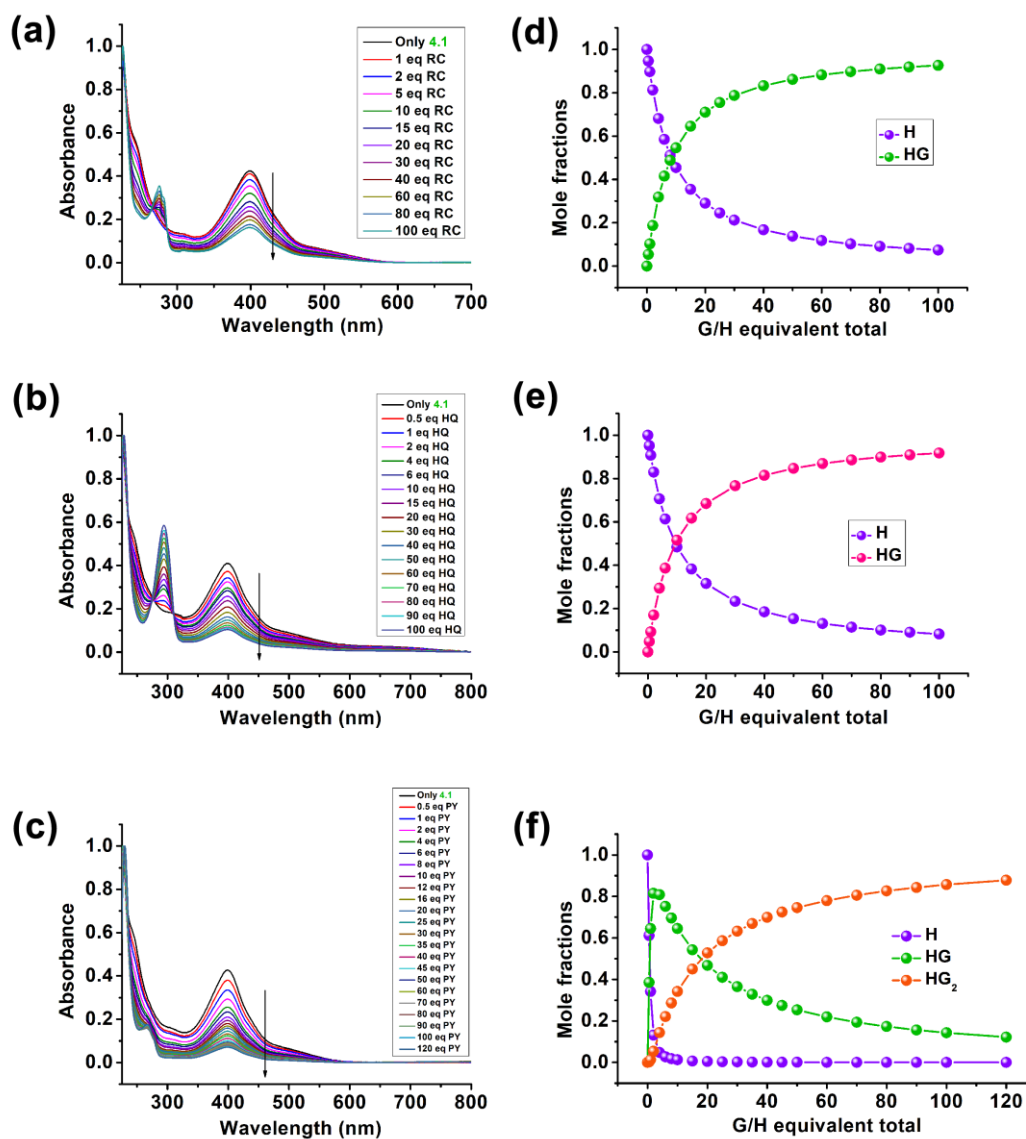


**Figure 4.5.** Partial molecular structures of (a) Cl-linked cubical assembly **4.1** and (b) PZDC tethered O, N-linked cubical assembly<sup>40</sup> showing the respective staggered and eclipsed arrangement of the two diagonally opposite Pd<sub>3</sub> subunits in them. View of the cluster core in (c) cube **4.1** and (d) PZDC tethered O, N-linked cubical assembly.<sup>40</sup>

#### 4.3.4. Guest encapsulation studies of **4.1**

Molecular packing indicated the presence of both intrinsic and extrinsic voids in **4.1**. The volume of the intrinsic cavity in **4.1** was found to be 275.09 Å<sup>3</sup> (Table 4.3, Appendix 4) as determined by MSROLL calculations<sup>43,44</sup> which prompted us to further employ this cage for guest encapsulation purposes. Guest recognition and encapsulation studies were performed with three phenolic guests of varied polarities, resorcinol (**RC**), hydroquinone (**HQ**), and pyrogallol/pyrogallic acid (**PY**) using mass spectrometry, titration experiments, and DOSY-NMR analysis. The mass spectral analysis showed broad peaks of  $m/z$  values centered around

5260.81, 5261.15, and 5402.46 for **RC**, **HQ**, and **PY**, respectively while the  $^1\text{H-NMR}$  of the host-guest mixture showed prominent upfield shift for the guest protons (Figure A4.16-A4.21, Appendix 4).

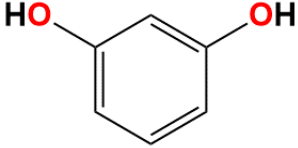
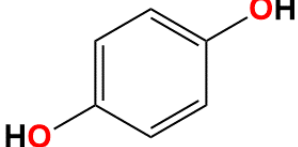
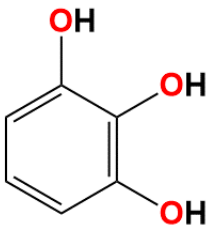


**Figure 4.6.** UV-VIS titration plots for the host-guest complexes of (a)  $\text{RC} \subset \mathbf{4.1}$ , (b)  $\text{HQ} \subset \mathbf{4.1}$ , and (c)  $\text{PY} \subset \mathbf{4.1}$  systems. Bind fit plot for (d)  $\text{RC} \subset \mathbf{4.1}$ , (e)  $\text{HQ} \subset \mathbf{4.1}$ , and (f)  $\text{PY} \subset \mathbf{4.1}$  systems.

However, since the host **4.1** did not possess any protons on its linkers, therefore, to analyze the binding capabilities of **4.1** towards these phenolic guest molecules, UV/Visible titrations were performed by adding 100 equivalents of the guest molecules in successive steps to a  $10^{-6}$  M solution of **4.1** and monitoring a gradual decrease in the host absorbance value (Figure 4.6). The Binding constants ( $K_a$ ) were further extracted by fitting the peak intensity gradients using

the online Bindfit Tool<sup>34-36</sup>, which revealed an overall strong 1:1 binding of all the host-guest assemblies of **4.1**. The highest binding with a  $K_{11}$  value of  $5.0 \times 10^4 \text{ M}^{-1}$  was obtained for the guest **RC**. In comparison, the guest **HQ** showed a somewhat weaker binding towards **4.1** with a  $K_{11}$  value of  $2.8 \times 10^4 \text{ M}^{-1}$ . Unlike **RC** and **HQ**, **PY** showed both 1:1 and 1:2 type binding to **4.1** with a  $K_{11}$  value of  $1.4 \times 10^4 \text{ M}^{-1}$  and a much weaker  $K_{12}$  value of  $5.75 \text{ M}^{-1}$ .

**Table 4.2.** Binding constants obtained for the host-guest bound pairs from UV-visible titration experiments.

Host-Guest Systems	Binding Constant, $K_{11}$ ( $\text{M}^{-1}$ )
<b>RC</b> $\subset$ <b>4.1</b> 	$5.0 \times 10^4$
<b>HQ</b> $\subset$ <b>4.1</b> 	$2.8 \times 10^4$
<b>PY</b> $\subset$ <b>4.1</b> 	$1.4 \times 10^4$

The much higher values of host-guest binding constants as compared to other neutral host-guest systems reported by us were attributed to the presence of the slightly concaved nature of the  $\mu_2$ -Cl linkages in the host which imparted strong and effective hydrogen bonding interactions with the polar O-H groups present in the encapsulated guest molecules.

As compared to the diols, the lesser binding of **PY** to **4.1** could be attributed to its bulky nature owing to the presence of a third O-H functional group in the guest. Additionally, these

hydrogen bonding interactions also imparted air stability to the phenolic guest molecules, especially pyrogallol which is known to auto-oxidize to the brown-colored pyrogallol-quinone in the open air. Further from the UV spectral data of the **PY**  $\subset$  **4.1** system taken in various intervals of time, it was also evident that pyrogallol did not auto-oxidize in its encapsulated state within the intrinsic cavity of the cage and was air-stable in an open vial even after a period of one month (Figure 4.7).

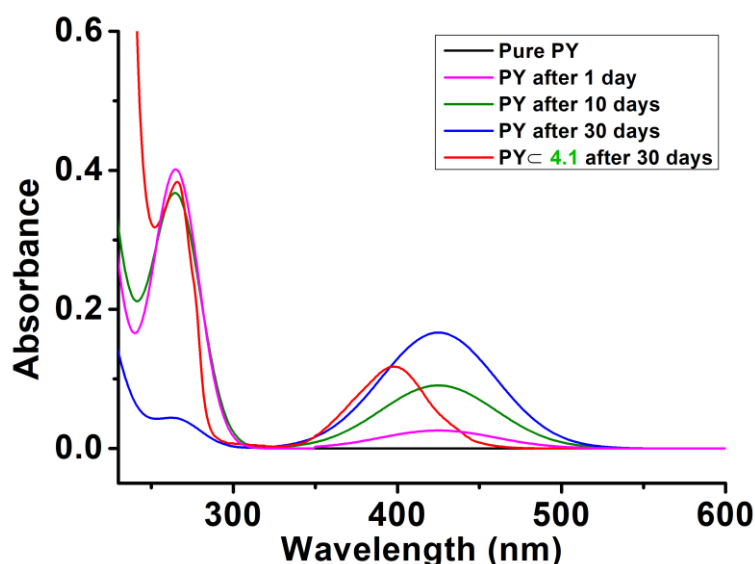


**Figure 4.7.** UV-visible spectral data of the **PY**  $\subset$  **4.1** system taken in various intervals of time showing the stability of PY within the cage cavity as compared to free PY (shown in blue).

To understand the nature of the host-guest complexes, the diffusion coefficient ( $D$ ) values were extracted from the 2D-DOSY-NMR analysis of the host-guest mixture. The strongest guest-to-host binding was observed for the **PY**  $\subset$  **4.1** system with a lower  $D(\text{bound})$  value of  $7.60 \times 10^{-11}$   $\text{m}^2/\text{s}$  closely followed by **RC** with a  $D(\text{bound})$  value of  $8.15 \times 10^{-11}$   $\text{m}^2/\text{s}$  (Figure 4.8). Comparatively, **HQ** showed a loose binding to **4.1** with a higher  $D(\text{bound})$  value of  $1.02 \times 10^{-10}$   $\text{m}^2/\text{s}$  (Figures A4.22-4.24, Table A4.4, Appendix 4). In contrast to the binding constants, the much lower  $D$ -value of the **PY**  $\subset$  **4.1** system arose from the fact that PY could simultaneously bind with **4.1** from within the cavity as well as the exterior of the cage as depicted by its 1:2 binding nature. This, in turn, slows the diffusion of the **PY**  $\subset$  **4.1** moiety to a higher extent than the other guest diols.

Further, the calculation of the hydrodynamic radius ( $R_H$ )<sup>45</sup> of the guests from their respective bound  $D$ -values indicated a large radius much different from those obtained from free guests.

Particularly, the  $R_H$  for the bound host and bound-guests obtained from DOSY NMR for **RC**  $\subset$  **4.1** and **PY**  $\subset$  **4.1** were consistent with the radii of the circumscribed sphere calculated from the single-crystal structure of **4.1**, which further indicated the presence of the guests within the intrinsic cavity of **4.1** (Figure A4.25, Appendix 4). However, **HQ** in the **HQ**  $\subset$  **4.1** mixture showed a somewhat smaller  $R_H$  value than that obtained for the host cage (Table 4.2). This could be attributed to the smaller size of **HQ** as compared to **RC** or **PY**, which led to the rapid exchange of the free and encapsulated **HQ** from within the cage cavity giving rise to a faster diffusion rate.

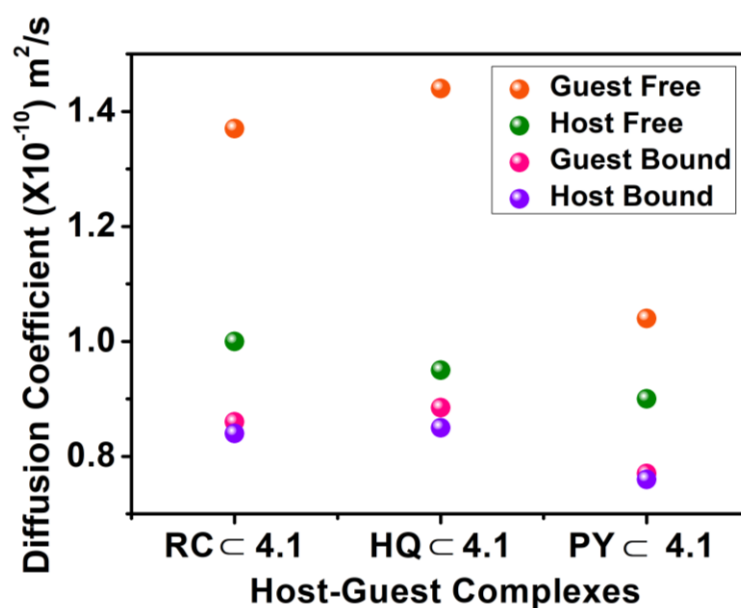


**Figure 4.8.** Summary of the D values for the host and guest protons studied for the Guest  $\subset$  **4.1** systems.

**Table 4.2.** Hydrodynamic radii values for the host-guest bound pairs.

Host–Guest Systems	Hydrodynamic Radius (Å)				Optimized Radii of Guest $\subset$ <b>4.1</b> Systems (Å)
	Host		Guest		
	Free	Bound	Free	Bound	
<b>RC</b> $\subset$ <b>4.1</b>	12.18(2)	14.12(3)	2.17(1)	13.95(1)	14.75
<b>HQ</b> $\subset$ <b>4.1</b>	12.78(2)	14.03(4)	9.20(3)	13.60(3)	14.54
<b>PY</b> $\subset$ <b>4.1</b>	13.36(3)	15.37(5)	11.88(5)	15.24(1)	14.88

#### 4.3.5. Single Molecule Energy Optimization studies for the Guest $\subset$ 4.1 assemblies

To understand the nature of interactions for the host-guest complexes, energy-minimized models were obtained for **RC**  $\subset$  **4.1**, **HQ**  $\subset$  **4.1**, and **PY**  $\subset$  **4.1** by semi-empirical PM6 calculations. It was observed that in presence of the guest molecules, the host portal window size increases from 5.20 Å to 7.31 Å on an average in presence of the guest molecules. Additionally, the  $\langle \text{Pd-P-Pd}_{\text{avg.}} \rangle$  also increases from the usual 71.23(2)° to 85.74(2)°. This makes the Pd<sub>3</sub>-trimeric unit to open up and accommodate the structural changes without disrupting the integrity of the cage. Figures 4.9a and 4.9b shows the comparison of portal size for an empty host and a guest-encapsulated-host. This structural flexibility in the cube arises from the non-directional nature of the monoanionic Cl<sup>-</sup> linkages which in presence of guests can adopt a convex conformation ( $\langle \text{Cl-Pd-Pd}_{\text{avg.}} \rangle = 9.46^\circ$ ) thereby facilitating then smooth uptake and exchange of guests from the external media (Figure A4.26, Appendix 4).

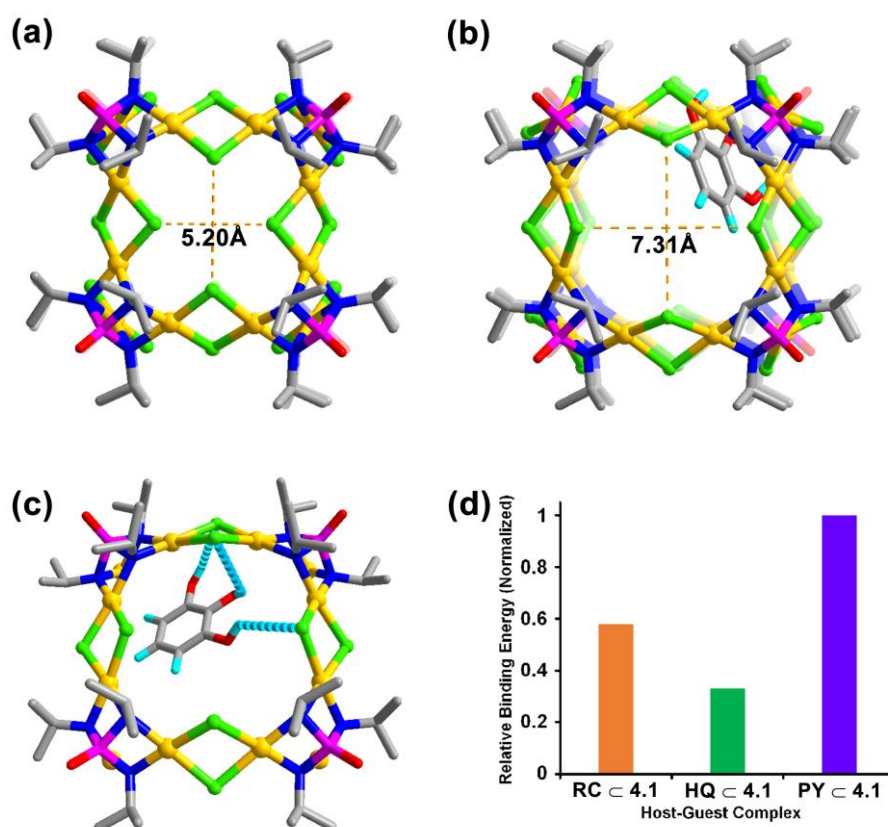


**Figure 4.9.** Portal window size of the host in (a) absence of guest and (b) presence of guest. (c) Potential hydrogen bonding interactions responsible for the stabilization of the host-guest assembly in **PY**  $\subset$  **4.1**. Only the interacting segment of the cage framework is shown for clarity. (d) Relative binding energy plots for the various optimized guest  $\subset$  **4.1** complexes.

Figure 4.9c shows the energy-minimized structural model of the **PY**  $\subset$  **4.1** complex (only the interacting segment has been shown). The various possible O-H...Cl interactions have been shown by the blue dotted lines. The observed strong guest binding values obtained from titration studies could be attributed to the presence of strong hydrogen bonding interactions between the  $\mu_2$ -Cl linkages of the host and guest O-H groups. A relative binding energy calculation (Figure 4.9d) showed the highest binding energy for the **PY**  $\subset$  **4.1** system owing to the presence of a greater number of interactions between the guest and the host (Figure A4.27-A4.29, Appendix 4).

#### 4.4. Conclusion

In summary, we report the synthesis of an unusual linker-free neutral metallocube, **4.1** by an exclusive template pathway directed by oxamide ligand. The robust nature of the metallocube is attributed to the presence of 24 strong Pd-( $\mu_2$ )-Cl linkages and is proposed to be the dimerization product of the intermediate **2.1-TM**. In the absence of a directing linker, no cage formation was observed, and the precursor HEXA-Pd undergoes self-condensation giving rise to a new pentameric polyhedral building unit (PBU), **4.2**. Further, **4.1** showed high binding to phenolic guest molecules as supported by  $^1\text{H-NMR}$ -titration and DOSY-NMR analysis. The favorable formation of host-guest complexes was attributed to the strong hydrogen bonding interactions between the host and guest functional groups.

#### 4.5. References

1. L. Jean-Marie, *Rep. Prog. Phys.* **2004**, *67*, 249
2. J.-M. Lehn, *Proc. Natl. Acad. Sci. U.S.A.* **2002**, *99*, 4763-4768.
3. N. J. Turro, *Proc. Natl. Acad. Sci. U.S.A.* **2005**, *102*, 10766-10770.
4. Y. Domoto, M. Abe, M. Fujita, *J. Am. Chem. Soc.* **2021**, *143*, 8578-8582.
5. A. Sautter, D. G. Schmid, G. Jung, F. Würthner, *J. Am. Chem. Soc.* **2001**, *123*, 5424-5430.
6. T. Weilandt, R. W. Troff, H. Saxell, K. Rissanen, C. A. Schalley, *Inorg. Chem.* **2008**, *47*, 7588-7598.
7. M. Ferrer, A. Pedrosa, L. Rodríguez, O. Rossell, M. Vilaseca, *Inorg. Chem.* **2010**, *49*, 9438-9449.
8. C. J. Kuehl, S. D. Huang, P. J. Stang, *J. Am. Chem. Soc.* **2001**, *123*, 9634-9641.

9. A. Kumar, R. Banerjee, E. Zangrando, P. S. Mukherjee, *Inorg. Chem.* **2022**, *61*, 2368-2377.
10. D. Philp, J. F. Stoddart, *Angew. Chem., Int. Ed. Engl.* **1996**, *35*, 1154-1196.
11. S. R. Batten, R. Robson, in *Molecular Catenanes, Rotaxanes and Knots*, **1999**, pp. 77-106.
12. K. I. Arias, E. Zysman-Colman, J. C. Loren, A. Linden, J. S. Siegel, *Chem. Commun.* **2011**, *47*, 9588-9590.
13. M. Fukuda, R. Sekiya, R. Kuroda, *Angew. Chem., Int. Ed.* **2008**, *47*, 706-710.
14. J.-F. Ayme, J. E. Beves, C. J. Campbell, D. A. Leigh, *Chem. Soc. Rev.* **2013**, *42*, 1700-1712.
15. L. H. Foianesi-Takeshige, S. Takahashi, T. Tateishi, R. Sekine, A. Okazawa, W. Zhu, T. Kojima, K. Harano, E. Nakamura, H. Sato, S. Hiraoka, *Commun. Chem.* **2019**, *2*, 128.
16. J. F. Woods, L. Gallego, P. Pfister, M. Maaloum, A. Vargas Jentzsch, M. Rickhaus, *Nat. Commun.* **2022**, *13*, 3681.
17. J. Guo, P. C. Mayers, G. A. Breault, C. A. Hunter, *Nat. Chem.* **2010**, *2*, 218-222.
18. Y. Domoto, M. Abe, T. Kikuchi, M. Fujita, *Angew. Chem., Int. Ed.* **2020**, *59*, 3450-3454.
19. J. Wang, F. Wang, Q. Dong, M. Chen, Z. Jiang, H. Zhao, D. Liu, Z. Jiang, P. Su, Y. Li, Q. Liu, H. Liu, P. Wang, *Inorg. Chem.* **2022**, *61*, 5343-5351.
20. B. Hasenknopf, J.-M. Lehn, B. O. Kneisel, G. Baum, D. Fenske, *Angew. Chem., Int. Ed. Engl.* **1996**, *35*, 1838-1840.
21. S. Sudan, D. W. Chen, C. Berton, F. Fadaei-Tirani, K. Severin, *Angew. Chem., Int. Ed.* **2023**, *62*, e202218072.
22. K. Bowman-James, *Science* **2019**, *365*, 124-125.
23. S. Bhattacharya, U. Basu, M. Haouas, P. Su, M. F. Espenship, F. Wang, A. Solé-Daura, D. H. Taffa, M. Wark, J. M. Poblet, J. Laskin, E. Cadot, U. Kortz, *Angew. Chem., Int. Ed.* **2021**, *60*, 3632-3639.
24. D. Preston, A. Fox-Charles, W. K. C. Lo, J. D. Crowley, *Chem. Commun.* **2015**, *51*, 9042-9045.
25. J. C. Röder, F. Meyer, H. Pritzkow, *Chem. Commun.* **2001**, 2176-2177.
26. J. Liang, J. Yin, Z. Li, C. Zhang, D. Wu, S. H. Liu, *Dyes and Pigments* **2011**, *91*, 364-369.



27. G. Liu, Y. Di Yuan, J. Wang, Y. Cheng, S. B. Peh, Y. Wang, Y. Qian, J. Dong, D. Yuan, D. Zhao, *J. Am. Chem. Soc.* **2018**, *140*, 6231-6234.
28. G. Liu, Z. Ju, D. Yuan, M. Hong, *Inorg. Chem.* **2013**, *52*, 13815-13817.
29. S. Freye, R. Michel, D. Stalke, M. Pawliczek, H. Frauendorf, G. H. Clever, *J. Am. Chem. Soc.* **2013**, *135*, 8476-8479.
30. M. Frank, J. M. Dieterich, S. Freye, R. A. Mata, G. H. Clever, *Dalton Trans.* **2013**, *42*, 15906-15910.
31. S. Freye, D. M. Engelhard, M. John, G. H. Clever, *Chem. Eur. J.* **2013**, *19*, 2114-2121.
32. A.K. Gupta, S. A. D. Reddy, R. Boomishankar, *Inorg. Chem.* **2013**, *52*, 7608-7614.
33. G. Sheldrick, *Acta Crystallogr. Sect. A* **2008**, *64*, 112-122.
34. <http://supramolecular.org>
35. P. Thordarson, *Chem. Soc. Rev.* **2011**, *40*, 1305-1323.
36. D. Brynn Hibbert, P. Thordarson, *Chem. Commun.* **2016**, *52*, 12792-12805.
37. M.J. Frisch et al. *Gaussian 09*, Revision C.01; Gaussian, Inc.: Wallingford, CT, 2016.
38. S. Grimme, *J. Comput. Chem.* **2006**, *27*, 1787-1799.
39. A.K. Gupta, A. Yadav, A.K. Srivastava, K.R. Ramya, H. Paithankar, S. Nandi, J. Chugh, R. Boomishankar, *Inorg. Chem.* **2015**, *54*, 3196-3202
40. A. Yadav, A.K. Gupta, A. Steiner, R. Boomishankar, *Chem. Eur. J.* **2017**, *23*, 18296-18302
41. M. Sarkar, R. Boomishankar, *Inorg. Chem.* **2023**, *62*, 1855-1863.
42. A. K. Gupta, S. A. D. Reddy, P. Rajasekar, P. Prakash, R. Boomishankar, *ChemistrySelect* **2017**, *2*, 10636-10641.
43. M.L. Connolly, *J. Mol. Graph.* **1993**, *11*, 139-141.
44. L. J. Barbour, *Chem. Commun.* **2006**, 1163-1168.
45.  $D = (kT)/(6\pi\eta R_H)$ , where  $D$  is the diffusion coefficient,  $k$  is the Boltzman constant,  $T$  is the temperature in Kelvin,  $\eta$  is the viscosity of the solution, and  $R_H$  is the radius of the molecular sphere.

🌀 End of Chapter 4 🌀

# Chapter 5



## **Selective Self-Sorting Of Tetrahedral And Cubic Pd(II) Neutral Cages With Chiral And Achiral Building Blocks**

## 5.1. Introduction

The self-assembly of supramolecular assemblies is known to occur by an amalgamation of multiple species directed into multi-component structures aided by the cumulative contributions of weak non-covalent interactions.<sup>1</sup> A major challenge in designing such self-assembled cages is the inclusion of multiple types of ligands within one species giving a higher degree of complexity and functionality.<sup>2</sup> Merging different ligands into a single system can give rise to emergent properties, although, incorporating and integrating them along with their functionalities in a single system is challenging.

Self-sorting is a burgeoning phenomenon in supramolecular chemistry to incorporate multiple components with distinct functionalities in a single self-assembled system. In supramolecular metal-ligand cages, self-sorting has been known to yield social or narcissistic products or a combination of both leading to homo and heteroleptic assemblies. Social self-sorting involves an integrative (unequal) or a statistical (mostly equal) incorporation of the sub-components into a single cage. In contrast, narcissistic sorting involves a self-recognition of the sub-components leading to a heterogeneous mixture of homoleptic cages. To design well-ordered heteroleptic cages governed by the chemical and topological properties of the sub-components, different self-sorting pathways have been developed based on steric interactions, geometric differences and reactivity of ligands, solvent effects, guest inclusion<sup>3-7</sup>, etc. The phenomena of self-sorting is well-explored for discrete cages with organic and inorganic substrates<sup>8-16</sup>. Chiral self-sorting is one of the strategies for building heteroleptic discrete structures in which the chirality becomes the differentiating factor for selectivity.<sup>17-22</sup> These protocols can lead to supramolecular assemblies composed of the same enantiomers (narcissistic, homochiral self-sorting) or different enantiomers (social, heterochiral self-sorting) or a mixture of both depending on the system being employed (Figure 5.1). Apart from determining the above factors, self-sorted assemblies can also be constructed based on thermodynamic or kinetic considerations.<sup>11</sup> Moreover, the self-sorting is unique to the nature and variability of the systems that can determine the outcome of the final product. Thus, studying self-sorting in any multi-component self-assembled system is attractive to understanding the generation of new complex structures and their functional behaviour especially on chirality-dependent properties in multicomponent mixtures.

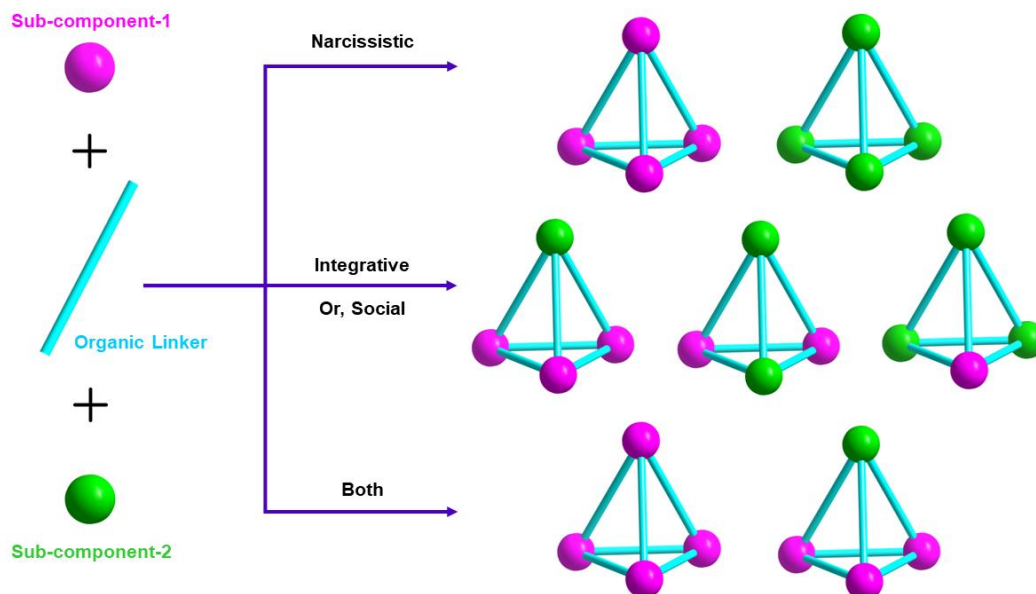


**Figure 5.1.** Schematic representation of a reaction between equimolar mixture of two different sub-components and a common organic linker resulting in the formation of various possible self-sorted tetrahedral cages via narcissistic self-sorting (resulting in homoleptic cages), social self-sorting (resulting in heteroleptic cages) or a mixture of both.

Over the years, our group has studied various neutral Pd(II) based cages with different chiral and achiral polyhedral building units (PBUs) forming a wide range of discrete supramolecular assemblies with distinct structural and functional properties.<sup>23-27</sup> Herein, we report self-sorting behavior in tetrahedral and cubic cages built from achiral and chiral imido-P(V) motifs that adopts a social or narcissistic distribution depending on the choice of the linker ligands. Socially self-sorted tetrahedral cage, **5.1**  $[\{\text{Pd}_3(\text{N}^i\text{Pr})_2(\text{N}\alpha\text{MeBn})\text{PO}\}_4(\text{L})_6]$  where  $\text{L} = \text{C}_2\text{O}_4^{2-}$  consisting of one chiral and three achiral PBUs are formed via the treatment of the PBU precursors  $[\{\text{Pd}_3(\text{N}^i\text{Pr})_3\text{PO}\}_2(\text{OAc})_2(\text{OH})]_2$  (**HEXA-Pd**) and  $[\{\text{Pd}_3(\text{N}\alpha\text{MeBn})_3\text{PO}\}_2(\text{OAc})_2(\text{OH})]_2$  (**HEXA-Pd\***) and oxalic acid. A similar treatment of **HEXA-Pd** and **HEXA-Pd\*** with 2,5-pyrazine dicarboxylic acid linker (PZDC-2H) results in the formation of a narcissistically sorted new chiral cage  $[\text{Pd}_3\{\text{PO}(\text{N}\alpha\text{MeBn})_3\}_8(\text{PZDC})_{12}]$  (**5.3**). In contrast, the reaction of **HEXA-Pd** and **HEXA-Pd\*** with the chloranilic acid (Cl-AN-2H) linker leads to a mixture of both social and narcissistic self-sorted cages. These observations highlight that the steric and electronic factors governed by the ligands play a crucial role in the self-sorting phenomena. Furthermore, we show a preliminary chiral guest recognition study of the chiral socially self-sorted tetrahedral cage **5.1-R**.

## 5.2. Experimental Details

### 5.2.1. General Remarks

All manipulations involving phosphorus halides were performed under a dry nitrogen atmosphere in standard Schlenk glassware. Dry Solvents were purchased from local vendors and used without further purification. Isopropylamine, R/S- $\alpha$ -methylbenzylamine, oxalic acid, 2,5-pyrazinedicarboxylic acid and palladium acetate were purchased from Aldrich and used as received. POCl<sub>3</sub> was purchased locally and was distilled prior to use. The phosphoramidate ligands- [PO(NH<sup>i</sup>Pr)<sub>3</sub>], the chiral phosphoramidate precursors, (*R,R,R*)-(+)-*N,N',N''*- and (*S,S,S*)-(-)-*N,N',N''*-[PO{NH(\*CH(CH<sub>3</sub>)Ph)}<sub>3</sub>], denoted as X<sup>R</sup>H<sub>3</sub> and X<sup>S</sup>H<sub>3</sub>, the achiral PBU precursor, [Pd<sub>3</sub>{(N<sup>i</sup>Pr)<sub>3</sub>PO}(OAc)<sub>2</sub>(OH)]<sub>2</sub>·2(CH<sub>3</sub>)<sub>2</sub>SO (**HEXA-Pd**) were prepared by the earlier reported procedures.<sup>25,28</sup> NMR spectra were recorded on a Bruker or Jeol 400 MHz spectrometer (<sup>1</sup>H NMR: 400.13 MHz, <sup>13</sup>C{<sup>1</sup>H} NMR: 100.62 MHz, <sup>31</sup>P{<sup>1</sup>H} NMR: 161.97 MHz) at room temperature using TMS (<sup>1</sup>H, <sup>13</sup>C) and 85% H<sub>3</sub>PO<sub>4</sub> (<sup>31</sup>P) as reference. The mass spectra were obtained on an Applied Bio system matrix-assisted laser desorption ionization time-of-flight (MALDI-TOF)/TOF spectrometer. For mass spectral measurements, both 2,5-dihydroxybenzoic acid (DHB) and  $\alpha$ -cyano-4-hydroxy-cinnamic acid (CHCA) matrix or a 1:1 mixture of them has been used as the matrix. CD spectra were measured in a JASCO J815 spectrometer from 400 nm to 190 nm. Elemental Analyses were performed with the VARIO-EL CUBE elemental analyzer.

### 5.2.2. Syntheses

**5.2.2.1. Synthesis of 5.1:** The ligand X<sup>R</sup>H<sub>3</sub> (0.050 mmol) and Palladium acetate (0.150 mmol) in DMSO were stirred in a closed cap vial for 1 hour to yield a dark orange-colored precipitate composed of the species [{Pd<sub>3</sub>(N $\alpha$ MeBn)<sub>3</sub>PO}<sub>2</sub>(OAc)<sub>2</sub>(OH)]<sub>2</sub> (denoted as **HEXA-Pd**\*). To this product, an equimolar quantity of **HEXA-Pd** (0.025 mmol) in methanol was added and the mixture was further stirred at room temperature to yield a homogeneous solution. Treatment of this solution with oxalic acid (0.113 mmol) at 60°C for 2 hours yields the self-sorted cage **5.1** as a yellowish-orange precipitate. The precipitated compound was recovered by filtration, washed with 2-5ml methanol 2-3 times, and dried under a vacuum. Yield: 75% (based on P). MALDI-TOF/TOF: Expected- 2863.30, Found- 2864.88 (M+H)<sup>+</sup>. <sup>31</sup>P{<sup>1</sup>H}-NMR (161 MHz, CDCl<sub>3</sub>):  $\delta$  71.67, 73.43. <sup>1</sup>H-NMR (400 MHz, CDCl<sub>3</sub>):  $\delta$  1.52 (d, *J* = 6.6 Hz, CH<sub>3</sub>), 1.78 (d, *J* = 6.8 Hz, CH<sub>3</sub>), 3.01 (m, CH), 3.67-3.83 (m, CH), 7.76-7.78 (d, *J* = 2.0 Hz, aromatic), 7.48-7.54

(m, aromatic). Elemental Analysis (%): Calcd for  $C_{63}H_{89}N_{12}O_{28}P_4Pd_{12}$ : C, 26.43; H, 3.13; N, 5.87. Found: C, 26.20; H, 3.08; N, 5.80.

**5.2.2.2. Synthesis of 5.2:** The ligand  $X^R H_3$  (0.050 mmol) and Palladium acetate (0.150 mmol) in DMSO were stirred in a closed cap vial for 1 hour to yield a dark orange-colored precipitate composed of the species  $[Pd_3(N\alpha MeBn)_3PO]_2(OAc)_2(OH)_2$  (denoted as **HEXA-Pd\***). To this product, an equimolar quantity of **HEXA-Pd** (0.025 mmol) in methanol was added and the mixture was further stirred at room temperature to yield a homogeneous solution. Treatment of this solution with chloranilic acid (0.113 mmol) at 85°C for 4 hours yields a mixture of self-sorted cages including the statistically sorted cage **5.2** and the narcissistically sorted chloranilate-linked cages **3.1** and **1.39**. Crude yield: 80% (based on P). MALDI-TOF/TOF: 3764.13, 3432.59, 4148.33.  $^{31}P\{^1H\}$ -NMR (161 MHz,  $CDCl_3$ ):  $\delta$  69.78, 71.01, 72.34.  $^1H$ -NMR (400 MHz,  $CDCl_3$ ):  $\delta$  1.48 (d,  $J = 6.6$  Hz,  $CH_3$ ), 1.74 (d,  $J = 6.8$  Hz,  $CH_3$ ), 2.86-2.98 (m, CH), 4.02-4.11 (m, CH), 7.74-7.75 (d,  $J = 2.0$  Hz, aromatic), 7.43-7.49 (m, aromatic).

**5.2.2.4. Synthesis of 5.3:** The ligand  $X^R H_3$  (0.050 mmol) and Palladium acetate (0.150 mmol) in DMSO were stirred in a closed cap vial for 1 hour to yield a dark orange-colored precipitate composed of the species  $[Pd_3(N\alpha MeBn)_3PO]_2(OAc)_2(OH)_2$  (denoted as **HEXA-Pd\***). To this product, an equimolar quantity of **HEXA-Pd** (0.025 mmol) in methanol was added and the mixture was further stirred at room temperature to yield a homogeneous solution. This solution was stirred with 2,5-pyrazinedicarboxylic acid (0.225 mmol) at room temperature for 1 hour, filtered and kept for crystallization. The cage assembly **5.3** was separated from its achiral counterpart **1.35** via crystallized from slow evaporation of its DMSO solution after 15-20 days. Crude yield: 82% (based on P). MALDI-TOF/TOF: Expected- 7820.10, Found- 7820.41 (M)<sup>+</sup>.  $^{31}P\{^1H\}$ -NMR (161 MHz,  $CDCl_3$ ):  $\delta$  72.78.  $^1H$ -NMR (400 MHz,  $CDCl_3$ ):  $\delta$  1.22 (d,  $J = 6.8$  Hz,  $CH_3$ ), 3.95-4.02 (m, CH), 7.74-7.76 (d,  $J = 2.0$  Hz, aromatic), 7.46-7.50 (m, aromatic), 8.81 (s, aromatic).

### 5.2.3. Crystallography

Reflections were collected on a Bruker Smart Apex Duo diffractometer at 100 K using Mo  $K\alpha$  radiation ( $\lambda = 0.71073$  Å). All structures were solved using intrinsic phasing method and refined by full-matrix least-squares on  $F^2$  (G. M. Sheldrick, SHELX-2014, program for crystal structure refinement, University of Gottingen, Germany, 2015).<sup>29</sup> Crystallographic data for all these compounds are listed in Table 5.1 and 5.2. All non-hydrogen atoms were refined anisotropically if not stated otherwise. Hydrogen atoms were constrained in geometric

positions to their parent atoms. The diffuse solvent molecules in the crystals could not be modeled appropriately. Hence, these were treated as diffuse contributions to the overall scattering and removed by the SQUEEZE/PLATON for better refinement data. The squeezed volume in **5.3** was found to be 4695 Å<sup>3</sup> which corresponds approximately to 50 water molecules and 70 methanol molecules. In the final refinements, OMIT command was used to remove a number of reflections for which I(obs) and I(calc) differed more than 10 times SigmaW (the latter being the square root of 1.0/weight for that reflection in the L.S. refinement).

**Table 5.1. Crystallographic Data for 5.1-rac and 5.3**

Compound	5.1-rac	5.3
Chemical formula	C <sub>63</sub> H <sub>89</sub> N <sub>12</sub> O <sub>28</sub> P <sub>4</sub> Pd <sub>12</sub>	C <sub>264</sub> H <sub>240</sub> N <sub>48</sub> O <sub>56</sub> P <sub>8</sub> Pd <sub>24</sub>
Formula weight	2863.14	7782.39
Temperature	100(2) K	100(2)K
Crystal system	Monoclinic	Tetragonal
Space group	<i>P</i> 2 <sub>1</sub> / <i>n</i>	<i>I</i> 422
a (Å); α (°)	17.983(4); 90	23.462(4); 90
b (Å); β (°)	28.833(6); 107.038(7)	23.462(4); 90
c (Å); γ (°)	29.930(8); 90	37.479(11); 90
V (Å <sup>3</sup> ); Z	12265(5); 4	20632(8); 2
ρ (calc.) mg m <sup>-3</sup>	1.551	1.253
μ(Mo K <sub>α</sub> ) mm <sup>-1</sup>	4.375	1.104
2θ <sub>max</sub> (°)	56.72	57.04
R(int)	0.1756	0.2439
Data / param.	30484 / 947	12991 / 441

GOF	1.009	0.986
R1 [ $F > 4\sigma(F)$ ]	0.0762	0.0537
wR2 (all data)	0.2441	0.1504
max. peak/hole ( $\text{e.}\text{\AA}^{-3}$ )	1.590/-1.397	0.621/-0.653

#### 5.2.4. $^1\text{H}$ -2D-DOSY NMR Studies

The  $^1\text{H}$ -2D-DOSY NMR experiments were carried out on a Bruker AVANCE III NMR spectrometer operating at a  $^1\text{H}$  frequency of 600 MHz, and a constant temperature of 298 K. 2.0 mM solutions of the participating species and host-guest complexes were prepared in  $\text{CDCl}_3$  and allowed to equilibrate for 30 minutes before data acquisition. Diffusion Ordered Spectroscopy (DOSY) experiments were performed by varying gradient strength. The standard Bruker protocol using Topspin 2.1 software was used for processing the DOSY data. The fitting of the diffusion dimension in the 2D-DOSY spectra was carried out using a one-parameter mono-exponential (equation 1) or two-parameter biexponential fits (equation 2).

$$I = I_0 \exp[-D\gamma^2 g^2 \delta^2 (\Delta - \delta/3)] \dots \dots (1)$$

$$I = I_{0A} \exp[-D_A \gamma^2 g^2 \delta^2 (\Delta - \delta/3)] + I_{0B} \exp[-D_B \gamma^2 g^2 \delta^2 (\Delta - \delta/3)] \dots \dots (2)$$

In this equation,  $I$  is the observed integral,  $I_0$ ,  $I_{0A}$  and  $I_{0B}$  are the reference or un-attenuated integrals,  $D$ ,  $D_A$ , and  $D_B$  are the diffusion coefficients,  $\gamma$  is the gyromagnetic ratio of the detected nucleus,  $g$  is the gradient strength,  $\delta$  the length of the gradient pulse, and  $\Delta$  the diffusion time.

#### 5.2.5. General Procedure for the Chiral Recognition Studies with 5.1-R

The chiral recognition capability of the self-sorted chiral cage **5.1-R** was evaluated for the enantiomeric R- and S-isomers of hydrobenzoin (**HB**), 1-phenyl-1-propanol (**P1P**) and 2-methyl morpholine (**MP**) using UV-Visible titrations. The change in absorption values was monitored during the UV-Visible titration experiments. The obtained data were then analyzed and fitted in a 2:1 host-guest binding ratio using the Bindfit<sup>30-32</sup> web calculator which gave the final binding constant values.

**5.2.5.1. Procedure for the UV-Visible titration:** Individual stock solutions of R and S- **HB**, **P1P**, and **MP** in 2 mM concentrations were freshly prepared by dissolving them in chloroform



(HPLC grade). Separate stock solutions of **5.1-R** (4 mM) in chloroform were freshly prepared at room temperature. For all three guests, the host solution of concentration 2.0  $\mu\text{M}$  in 2 mL of solvent was placed in a 10 mm cuvette, and the guest solutions of RS- **HB**, **P1P**, and **MP** (0.5eq-100eq) were added by using a micro pipette. The entire UV-Vis spectra in titration experiments were collected at room temperature after stirring the sample solution for ca. 3 min. The changes in the absorption maxima values of the host were monitored. Based on the data obtained in the 220-800 nm range, the binding constants were calculated by using the online Bindfit tool. The values of the binding constants were presented as mean  $\pm$  standard deviation in all these independent experiments.

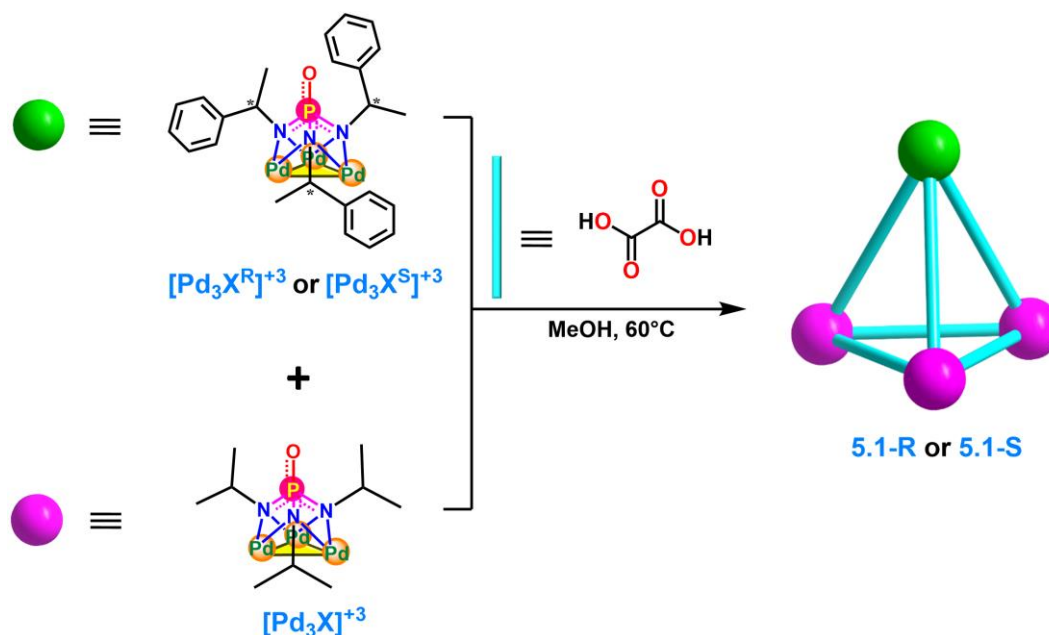
### 5.2.6. Theoretical Calculations

The gas-phase single-molecule optimization energies of the self-sorted cage systems were calculated theoretically by using the Gaussian 09 software.<sup>33,34</sup> These energies were computed by DFT methods by employing the b97d3 functional. Energy calculations were performed using the basis set Lanl2dz for Pd in conjunction with the cc-pvtz basis set (for all other atoms).

## 5.3. Results and Discussions

### 5.3.1. Synthesis and Structures

**5.3.1.1. Case 1- With oxalate linker:** Treatment of an equimolar mixture of chiral  $[\text{Pd}_3\text{X}^*]^{+3}$  and achiral  $[\text{Pd}_3\text{X}]^{+3}$  precursors with a stoichiometric amount of oxalic acid resulted in the formation of an exclusive socially sorted tetrahedral cage, **5.1**.  $^{31}\text{P}\{^1\text{H}\}$ -NMR spectral observations revealed two peaks at 71.6 and 73.4 ppm in a 1:3 ratio corresponding to their chiral and achiral subunits, respectively. Similar observations were made as well from their  $^1\text{H}$ -NMR spectral profiles confirming the ratio of the chiral and achiral subunits. MALDI-TOF mass spectra showed characteristic  $m/z$  peaks centered at 2864 corresponding to the  $[\text{M}+\text{H}]^+$  ion, which is also in good accordance with the NMR data (Figure A5.1-A5.3, Appendix 5). Both the isomers of this chiral cage, (**5.1-R** and **5.1-S**) were independently constructed based on the chirality of the chiral precursor used (Scheme 5.1). Their enantio-enriched nature was confirmed by CD spectra and were compared with those of the pure chiral cages<sup>25</sup> (Figure 5.2 and Figure A5.4, Appendix 5). The peak at 271 nm originates from the corresponding  $\pi-\pi^*$  transitions while those at 303 and 332 nm originate from the MLCT transitions. The optical rotation measurements on **5.1-R** and **5.1-S** gave the specific rotation ( $\alpha_{\text{D}}$ ) values of  $+555.3^\circ$  and  $-542.7^\circ$  further confirming their enantio-enriched nature.



**Scheme 5.1.** Synthetic pathway depicting the formation of self-sorted tetrahedral cages **5.1-R**, and **5.1-S**, from an equimolar mixture of chiral and achiral precursors.

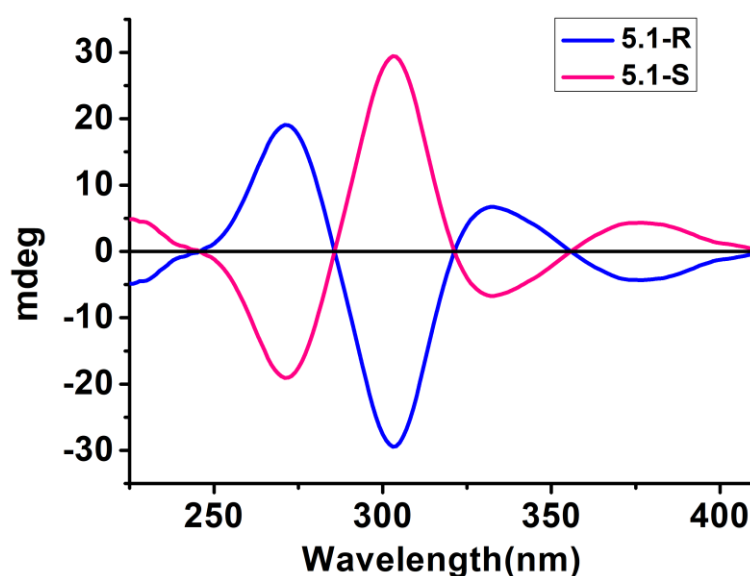


**Figure 5.2.** Circular dichroism spectra of the self-sorted tetrahedral cages **5.1-R** and **5.1-S**.

Furthermore,  $^1\text{H}$  diffusion ordered spectroscopy (DOSY) of the tetrahedral cage **5.1** (R or S) revealed the same diffusion coefficient values for each of the protons pertaining to the chiral subunits as well as the achiral subunits. This further proved the exclusivity of the reaction product as a single D-value is consistent with the presence of a single species in solution (Figure 5.3).

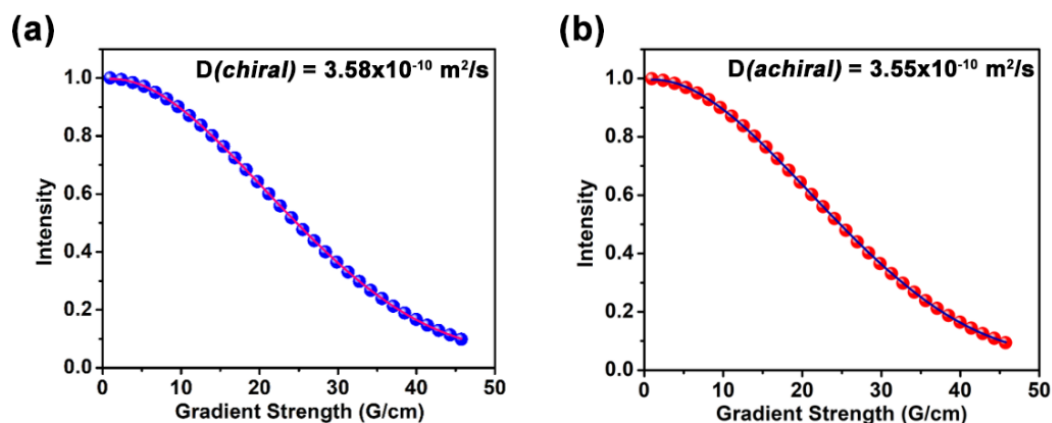


**Figure 5.3.** Integral decay profile of the protons (a)  $\delta$  7.80 (chiral) and (b)  $\delta$  1.78 (achiral) ( $\text{CDCl}_3$ , 298 K) in the tetrahedral cage **5.1**.

Single crystals of the socially sorted cage **5.1** were obtained by the slow evaporation of its chloroform solution. Although initial attempts to crystallize the enantiopure cages **5.1-R/S** were unsuccessful in a three-solvent mixture of DMSO, chloroform, and dichloromethane, the racemic cage **5.1-rac** was found to crystallize in the centrosymmetric  $P2_1/n$  space group. As expected from spectral data, the molecular structure of **5.1-rac** displayed a 1:3 distribution of the  $\text{Pd}_3$ -subunits, where three out of four vertices of the tetrahedron are occupied by the achiral  $\text{Pd}_3$ -subunit and the chiral  $\text{Pd}_3$ -subunit takes up at only one of the cage vertices. These subunits are further connected by the bridging interaction of the six oxalate linkers completing the tetrahedral structure for the cage assembly. The asymmetric unit of **5.1-rac** consists of one cage and within the chiral  $[\text{Pd}_3\text{X}^*]^{+3}$  subunit, all three chiral imido centers adopt the same R configuration (Figure 5.4a). However, the packing structure revealed the presence of a racemic mixture in which chiral  $\text{Pd}_3$  subunit of the cages in one layer faces the chiral subunits of the adjacent layer in a “head-on” fashion thereby giving rise to a centrosymmetric crystal structure for **5.1** (Figure 5.4b and 5.4c).

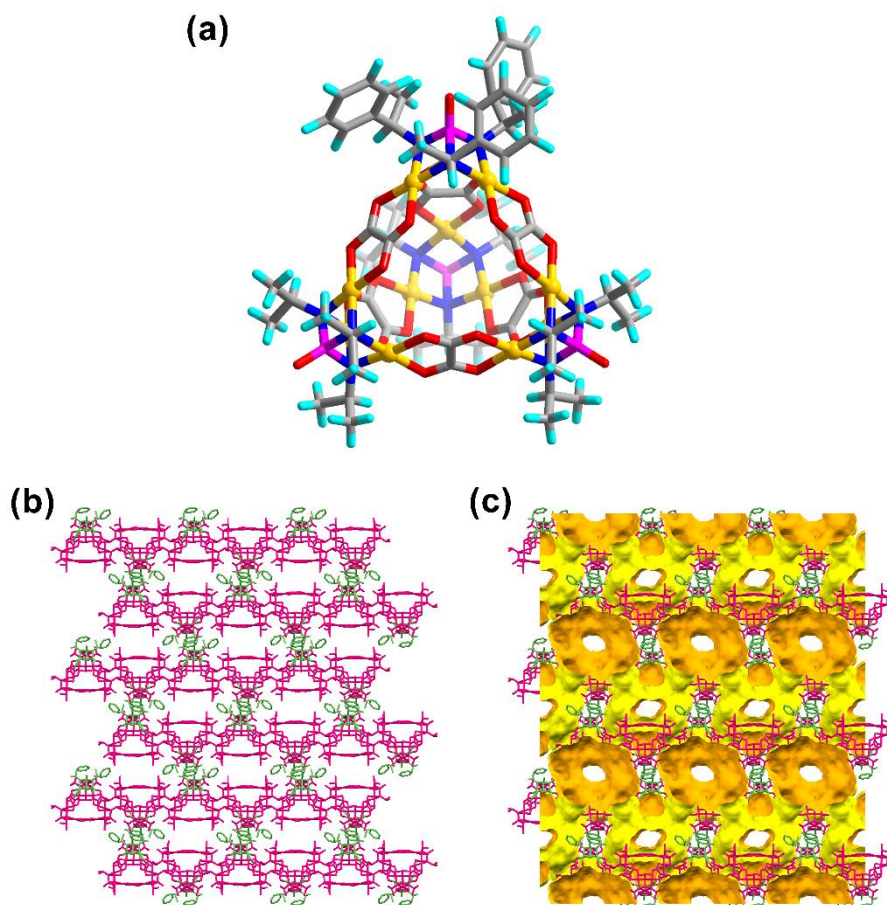


**Figure 5.4.** (a) Molecular structure of racemic cage **5.1-rac** (b) Packing diagram of **5.1-rac** along the b-axis. The green and pink colors denote the respective chiral and achiral subunits of the cage. (c) Presence of intrinsic and extrinsic voids is shown along the c-axis.

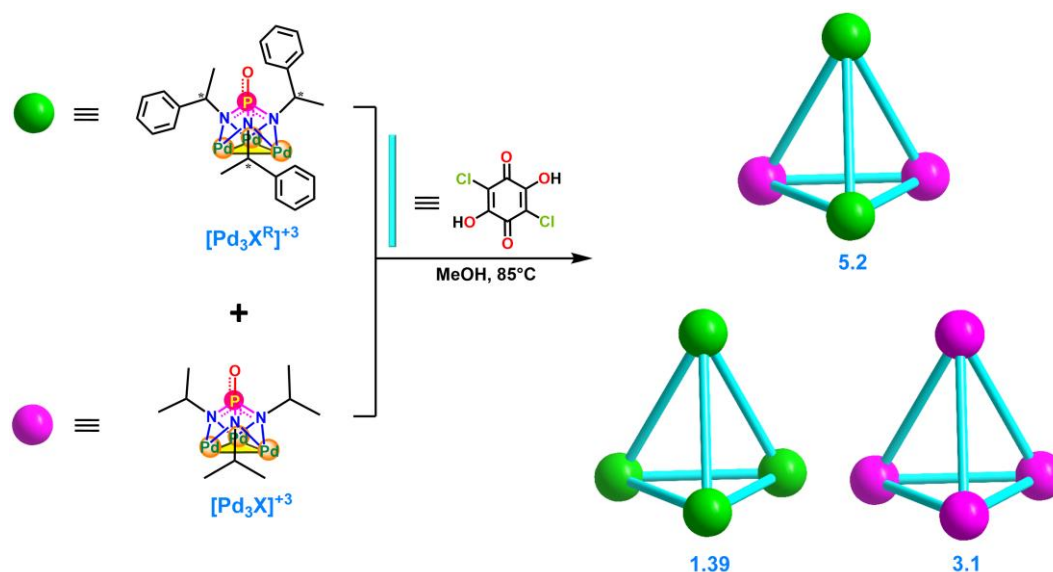
In general, for homoleptic chiral cages in the solid state, the highest symmetry is reached without an inversion center. However, when the homogeneous arrangement of chiral groups is disrupted by heterogeneous groups (achiral subunits in this case), the individual crystals arrange themselves in the most symmetrical way possible. In **5.1** it is achieved by incorporating a glide plane in the crystal structure. Even though the solution-phase CD spectra exhibits the characteristic bisignate bands corresponding to the chiral-phosphoramidate groups of the individual cages **5.1-R** and **5.1-S**, the presence of alternating layers of the cages with the opposite chirality constituted an unexpected racemized crystal packing for **5.1-rac**. This could be attributed to the non-statistical distribution of the chiral and achiral subunits in **5.1-rac**, which leads to a loss of symmetry to the otherwise pure chiral<sup>25</sup> and pure achiral<sup>23</sup> oxalate cages. This lack of symmetry is somewhat compensated by the racemization leading to a centrosymmetric packing in the crystal structure.

Further, as determined by MSROLL software calculations<sup>35,36</sup>, the volume of the central cage cavity in **5.1** was found to be 87.13 Å<sup>3</sup> with a fixed probe radius of 1.4 Å (Table A5.3, Appendix 5). The central cavity in these cages is hydrophobic as observed from the previous reports of the achiral oxalate cage family,<sup>23,27</sup> and hence capable of encapsulating a variety of organic guest molecules within its intrinsic cavity. On the other hand, the chiral oxalate cages<sup>25</sup> has also shown promising enantiomeric separation abilities with various chiral guest molecules. The presence of both flavours in the self-sorted cage system thus prompted us to probe the cage for guest encapsulation and chiral recognition studies (*vide infra*).

With the oxalate linker, the exclusive formation of the 1(chiral):3(achiral) product was mainly driven by steric interactions. The bulkier chiral groups with the  $\alpha$ -methyl benzylamine groups require more duration to react with the small oxalate linker to form a compact tetrahedron. In contrast, the achiral Pd<sub>3</sub>-subunit, lined by the smaller isopropyl groups reacts faster with the oxalate ligands in a competitive manner. This results in the incorporation of three subunits of the achiral PBUs as compared to only one subunit of the chiral PBU in the final heteroleptic tetrahedral product.

**5.3.1.2. Case 2- With chloranilate linker:** Subsequently, to reduce the effect of steric control, a six-membered chloranilate linker [C<sub>6</sub>O<sub>4</sub>Cl<sub>2</sub>]<sup>-2</sup> (Cl-AN)<sup>-2</sup> was used to study the self-sorting pathway with the chiral and achiral PBUs. When the same equimolar mixture of the chiral (R-isomer) and achiral subunits was utilized with a stoichiometric amount of (Cl-AN)<sup>-2</sup>, a dynamic mixture of both social (**5.2**) and narcissistic (**3.1** and **1.39**) sorted products were obtained (Scheme 5.2).

The <sup>31</sup>P{<sup>1</sup>H}-NMR and <sup>1</sup>H-NMR showed peaks in the respective regions of  $\delta$  71.20, 69.71 and 72.6 (Figure A5.5, Appendix 5) corresponding to the phosphoramidate groups present in **5.2**, **1.39**, and **3.1**. These were consistent with those reported for the pure chiral<sup>26</sup> and achiral<sup>24</sup> cages. The presence of **5.2** in the reaction mixture was further confirmed by mass spectrometry and NMR spectral analysis (Figure A5.6-A5.7, Appendix 5). The mass spectra revealed the presence of a statistically sorted product with the incorporation of two chiral and two achiral subunits in the cage.



**Scheme 5.2.** Synthetic pathway depicting the formation of a dynamic mixture of self-sorted tetrahedral cages **5.2**, **1.39**, and **3.1** from an equimolar mixture of chiral and achiral precursors.

$^1\text{H}$  diffusion ordered spectroscopy (DOSY) of the resultant mixture revealed the two distinct diffusion coefficient values for each of the protons pertaining to the chiral subunits as well as the achiral subunits. Thus  $D$ -values of  $4.79 \times 10^{-10} \text{ m}^2/\text{s}$  and  $4.26 \times 10^{-10} \text{ m}^2/\text{s}$  were obtained for the protons in the chiral subunit ( $\delta$  7.75) while  $D$ -values of  $4.81 \times 10^{-10} \text{ m}^2/\text{s}$  and  $5.20 \times 10^{-10} \text{ m}^2/\text{s}$  were observed for those in the achiral subunit ( $\delta$  1.74). While the similar  $D$ -value of  $4.79$  and  $4.81 \times 10^{-10} \text{ m}^2/\text{s}$  pertained to the subunits belonging to the socially sorted cage **5.2**, the comparatively slower value of  $4.26 \times 10^{-10} \text{ m}^2/\text{s}$  and faster value of  $5.20 \times 10^{-10} \text{ m}^2/\text{s}$  were assigned to that of the pure chiral (**1.39**) and pure achiral (**3.1**) cages respectively that were also obtained by the subsequent narcissistic self-sorting of the precursor subunits (Figure A5.8, Appendix 5). Due to the presence of a mixture of products in the solution, the yield and optical purity of **5.2** were not confirmed. However, in the absence of a crystal structure, a single-energy optimized structure of the 2:2 statistically sorted cage **5.2** in R-configuration was constructed by DFT methods with an optimized stabilization energy of  $-8.55 \times 10^6 \text{ kcal/mol}$  (Figure 5.5 and Table A5.4, Appendix 5). The molecular structures of **3.1** and **1.39** have previously been reported.

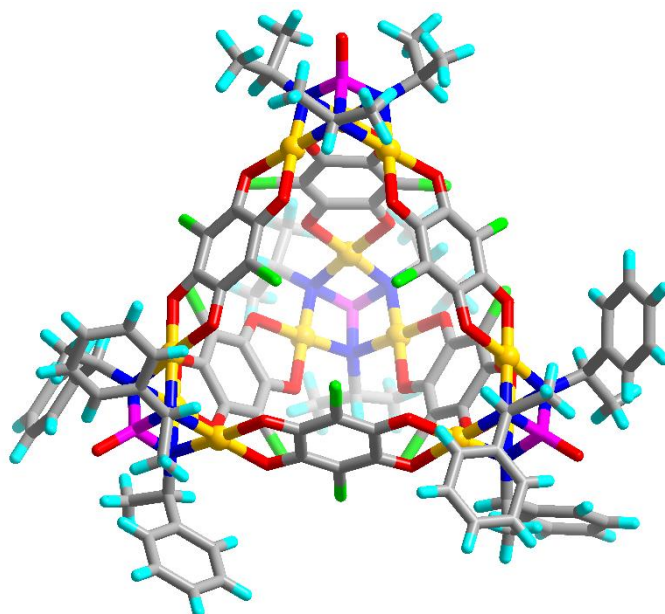
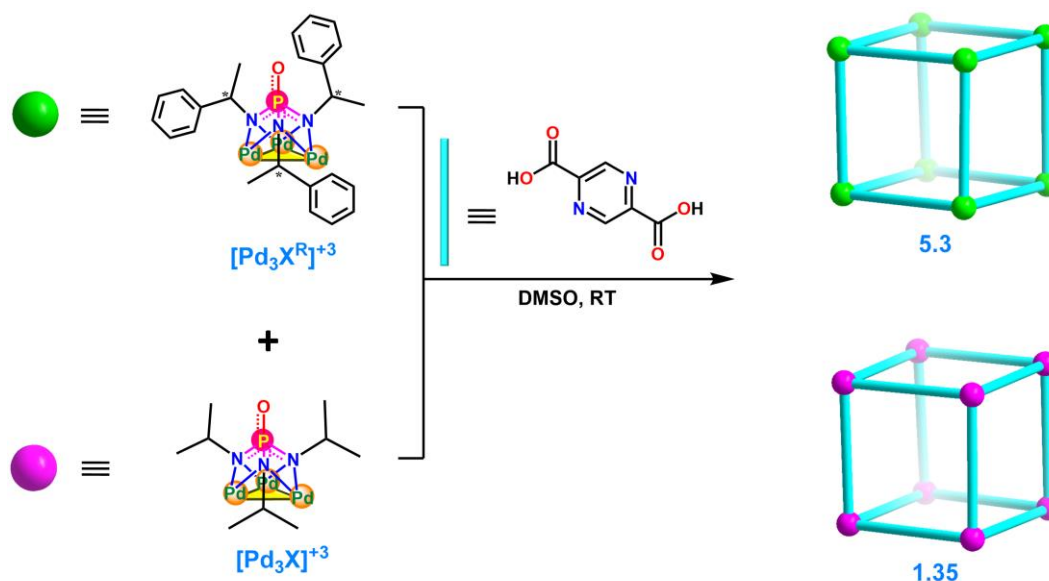


**Figure 5.5.** DFT optimised structure of the 2:2 self-sorted tetrahedral cage **5.2** in R-configuration.

Varying the reaction conditions and the initial stoichiometry of the starting precursors had very little effect on the resultant above-mentioned mixture. While the relative quantities did vary, the three major constituents of the product mixture remained the same. Thus, even though the steric limitations were overcome using a longer Cl-AN<sup>-2</sup> linker and an equal incorporation of both subunits, it failed to produce an exclusive sorted product owing to the similar reactivity of the subcomponents.

**5.3.1.3. Case 3- With pyrazine-dicarboxylate linker:** Limited by both steric and relative reactivity, the final self-sorting study was attempted by employing the 2,5-pyrazine-dicarboxylate (PZDC<sup>-2</sup>) linker with a 120° directing angle. Unlike the previous two cases, this linker was previously known to form a cubical assembly (**1.35**) from the achiral PBUs<sup>37</sup>. However, the synthesis of its chiral counterpart remained unsuccessful due to a major difference in reactivity and solubility issues. Treatment of an equimolar mixture of [Pd<sub>3</sub>X<sup>R</sup>]<sup>+3</sup> and [Pd<sub>3</sub>X]<sup>+3</sup> with a stoichiometric quantity of PZDC<sup>-2</sup>, the hitherto-unknown chiral-PZDC cubical assembly, **5.3** was obtained alongside the reported achiral cubical assembly, **1.35**. Contrary to the expected social sorting, the formation of **5.3** and **1.35** is a result of complete self-recognition, or in another word “narcissistic” self-sorting of the two homoleptic cages (Scheme 5.3)



**Scheme 5.3.** Synthetic pathway depicting the formation of narcissistically self-sorted cubical cages **5.3** from an equimolar mixture of chiral and achiral precursors.

The  $^31P\{^1H\}$ -NMR spectra of the reaction mixture showed the presence of two peaks of equal ratios at  $\delta$  72.7 and 73.7 for **5.3** and **1.35**, respectively (Figure A5.9, Appendix 5). The newly obtained cage **5.3** was further separated from achiral cube, **1.35** by either crystallisation or via extraction with a solvent mixture of  $CHCl_3$ -acetone. The structure of **1.35** has already been reported earlier by our group and its structure in the product mixture was again confirmed by verifying the unit cell parameters of its single crystal (Table 5.2).

It was thus proposed that during the self-sorting pathway, the highly reactive PZDC linkers are self-assembled in a pre-organised fashion by the achiral  $[Pd_3X]^{3+}$  polyhedral building units (PBUs), which was previously not achieved due to higher bulk of the chiral subunits. However, due to the pre-organisational aid by the smaller achiral groups, the reaction proceeded with equal participation from both the subunits leading to the formation of a pair of narcissistically sorted cubes. The absence of any socially self-sorted product can be attributed to the higher order of symmetry present in these complex architectures which unlike the tetrahedral cages, preferred to self-recognise and preserve the symmetry within the same polyhedral cage.

The  $^31P\{^1H\}$ -NMR spectra of the isolated pure cage **5.3** showed a single peak at  $\delta$  72.8 further confirming its formation by the self-sorting pathway (Figure A5.10, Appendix 5). MALDI-TOF mass spectra showed a broad peak centered around the  $m/z$  value of 7820.4, which is the predicted mass of **5.3**. The cage **5.3** was further characterised by  $^1H$ -NMR and DOSY-NMR



analysis which showed a single D-value of  $2.11 \times 10^{-11} \text{ m}^2/\text{s}$  pertaining to the cube (Figure A5.11-A5.13, Appendix 5).

**Table 5.2. Unit Cell Parameters Observed for Achiral PZDC-Linked Cube.**

Compound	1.35 (as narcissistically self-sorted product) (This Work)	1.35 (Reported Earlier) <sup>37</sup>
a (Å); α (°)	42.043(4); 90	23.507(4); 90
b (Å); β(°)	28.314(4); 118.893(4)	37.607(7); 97.638(4)
c (Å); γ(°)	39.341(6); 90	42.296(7); 90
V (Å <sup>3</sup> )	41004(7)	37055(11)

The crystal structure of **5.3** was solved in the chiral tetragonal *I422* space group featuring one-eighth of the molecule in the asymmetric unit (Figure 5.6). The cubic cage comprises eight  $[\text{Pd}_3\text{X}^{\text{R}}]^{3+}$  units wherein each Pd<sup>II</sup> atom of each subunit is chelated by a bidentate N, O-site of bridging PZDC<sup>-2</sup> linker and each PZDC ligand binds two Pd<sup>II</sup> ions in opposite N, O-sites. This results in the cubical assembly comprising of  $[\text{Pd}_3\text{X}^{\text{R}}]^{3+}$  units at the vertices, while the twelve PZDC ligands form its edges. Further, it is also observed that out of the three  $\alpha$ -methylbenzyl groups on each Pd<sub>3</sub> subunit, one of the phenyl rings effectively forms pi-pi stacking interactions with the aromatic ring of the PZDC linker. These additional twelve (one with each PZDC linker at the edge) intra-molecular pi-pi interactions not only give a slightly twisted configuration for the cube **5.3** but also serves as the driving force behind the narcissistic self-sorting taking place in the reaction mixture. The presence of pi-pi interactions gives rise to an additional self-stabilization nature for the highly symmetric cage of **5.3**, reducing the possibility of any social self-sorted product (Figure 5.7).

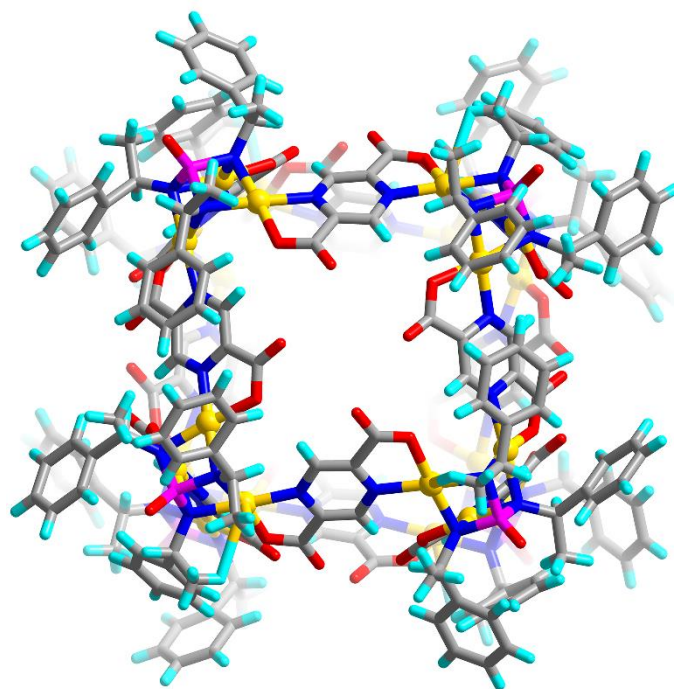


**Figure 5.6.** Molecular structure of cubical assembly **5.3**.

The formation of cube **5.3** was also obtained when a minimum of 0.5 eq of the achiral subunit was employed as compared to the chiral subunit. Thus, in addition to acting as a precursor of its own, the achiral subunit also acted as a template for forming **5.3**. Mechanistically, this pathway can be understood as follows. The bulkier chiral Pd<sub>3</sub>-subunit could not effectively form the self-assembled structure on its own due to the high reactivity of the PZDC<sup>-2</sup> linker. However, the smaller achiral unit can interact with the PZDC linkers and bring them to the most stable cubical arrangement which is then eventually replaced by some of the chiral units due to the presence of additional stability being imparted to the assembly via effective pi-pi stacking interactions.

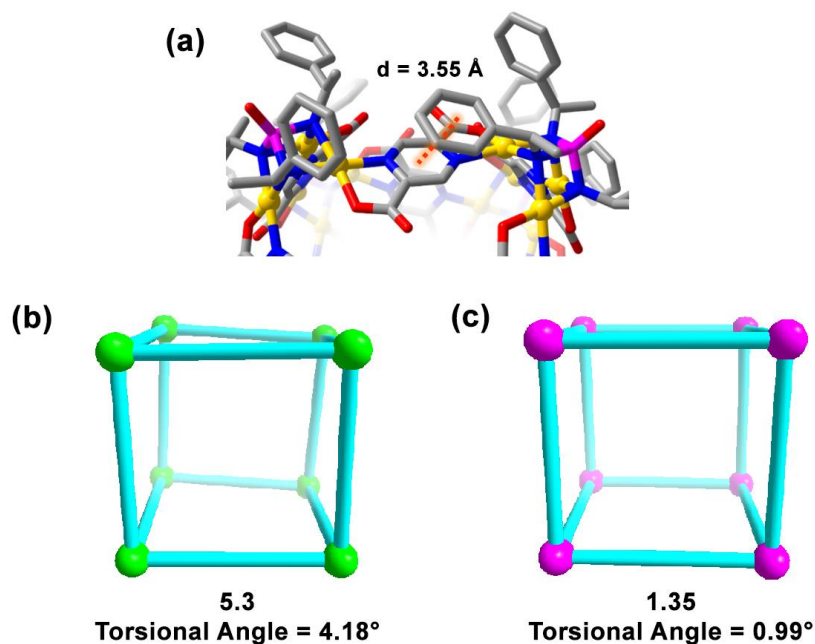


**Figure 5.7.** (a) A fragmental view of the cubical assembly **5.3** showing the intramolecular pi-pi stacking between one of the phenyl rings of the chiral phosphoramidate subunit and the aromatic ring of the PZDC linker. (b) The slightly twisted configuration of the cube **5.3** arising due to the intramolecular pi-stacking vs. (c) no twisted configuration in the achiral cube **1.35** due to the absence of any such intramolecular interactions.

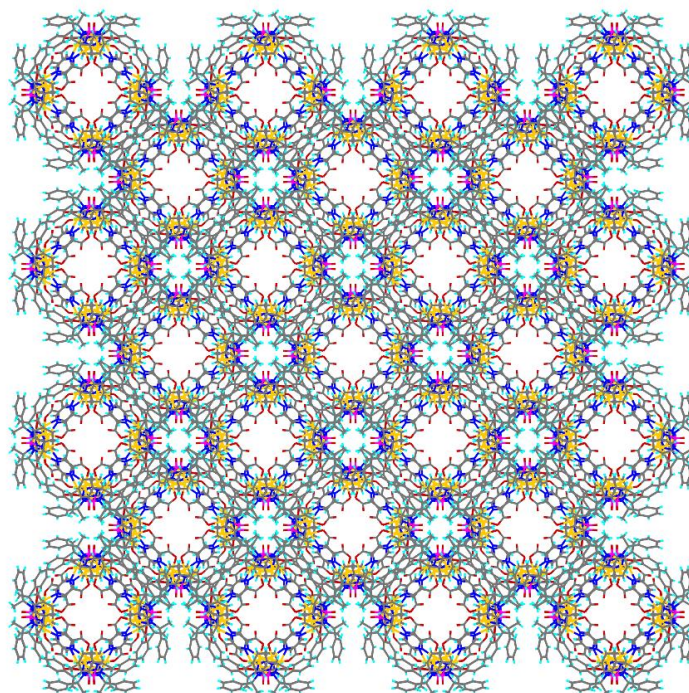


**Figure 5.8.** Packing view of the cubical assembly **5.3** along the c-axis.

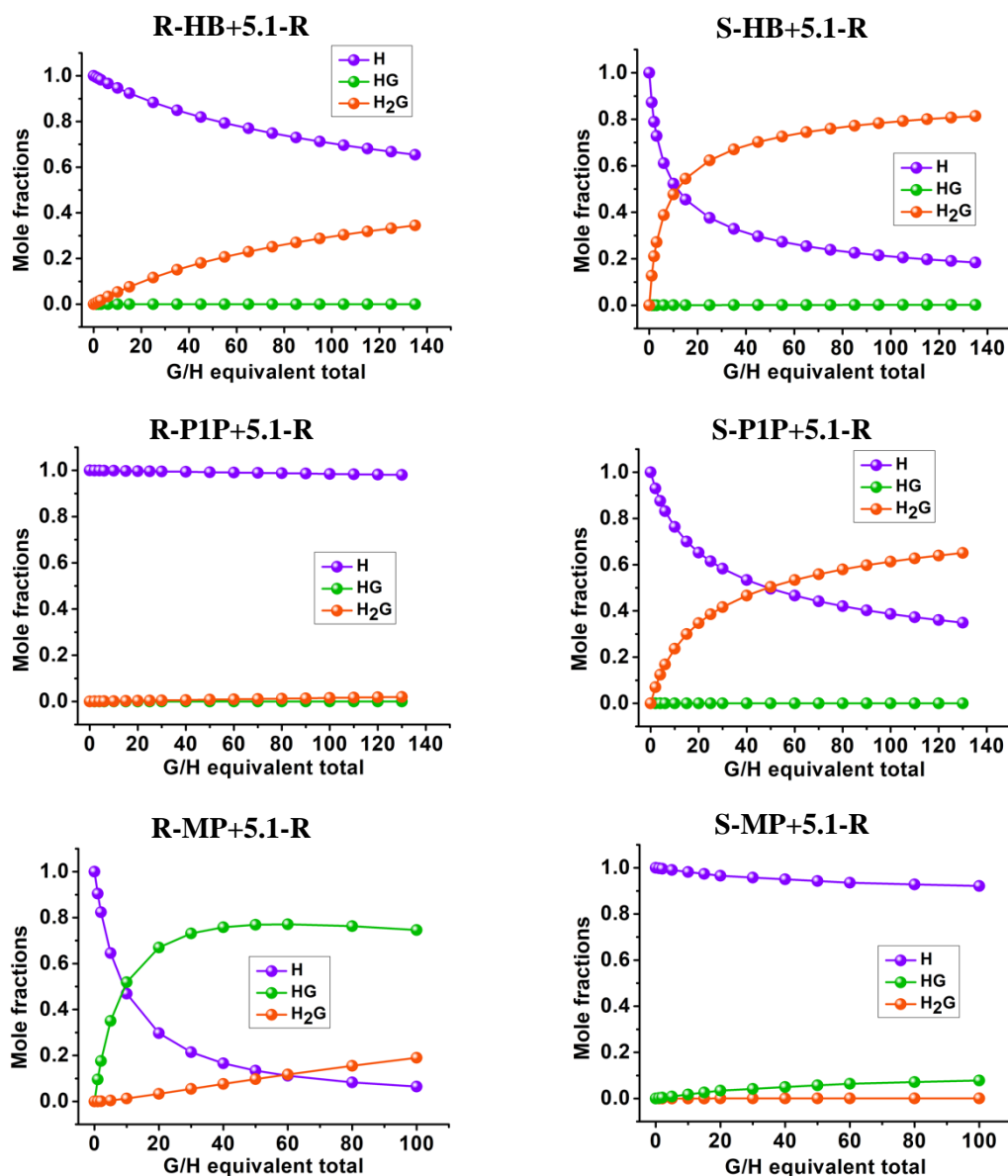
The packing structures of **5.3** indicate a body-centered packed network (BCC lattice) with total solvent-accessible void volumes of  $\sim 8278 \text{ \AA}^3$ , which amounts to  $\sim 42\%$  of their total unit cell volume (Figure 5.8 and Figure A5.14-A5.16, Appendix 5). The intrinsic cavity volume of **5.3** with a probe radius of  $1.5 \text{ \AA}$ , as calculated by the MSROLL software is  $1045.3 \text{ \AA}^3$  which is amongst one of the largest neutral chiral cages reported. Although the usage of PZDC ligands as linkers in coordination polymers is reported in literature<sup>38-40</sup>, the construction of coordination cages, especially chiral ones based on this ligand remains largely unexplored. The large void, charge-neutrality, stability, and chirality of this metal-organic cage set it apart from other similar systems and suggest its potential for further solution-based applications such as chiral recognition and separation studies.

### 5.3.2. Chiral Recognition Studies

After confirming the optical purity of the oxalate-sorted cage, **5.1-R** via optical rotation measurements, the cage was probed for chiral recognition studies. Since both **5.2** and **5.3** were formed alongside other self-sorted products, at this point, the chiral recognition studies were not attempted. The presence of a majority of achiral groups alongside only one chiral subunit prompted us to probe the extent of chiral recognition properties of the cage **5.1-R**. Keeping in mind the presence of both intrinsic and extrinsic voids in the cage, three pairs of chiral (both R- and S-) guest molecules of variable sizes were employed namely, hydrobenzoin (**HB**), 1-phenyl-1-propanol (**P1P**) and 2-methyl morpholine (**MP**). The MALDI-TOF mass-spectrometry of **5.1-R** treated with these guest molecules gave peaks centered at  $m/z$  value of 3124.55, 3022.19 and 2964.60 for the host-guest mixture of **HB + 5.1-R**, **P1P + 5.1-R** and **MP + 5.1-R**, respectively (Figure A5.17-A5.19, Appendix 5). The  $^1\text{H-NMR}$  spectra showed prominent upfield shifts for all the guest protons in the **Guest + 5.1-R** mixture, although the host protons showed minimal to no change at all (Figure A5.20-A5.22, Appendix 5). Among the three guests MP showed the largest upfield shift which could be attributed to the fact that MP, being the smallest in size, could easily get encapsulated within the intrinsic cavity of the cage, irrespective of its chirality, while the larger guests are blocked at the smaller portals of the oxalate window, thereby show sluggish response during encapsulation.

Further to estimate the nature and extent of chiral guest recognition capabilities of **5.1-R**, UV/Visible titrations were performed with the cage in the presence of optically pure guest isomers. The gradual change in the absorbance value was then fitted by the online Bindfit calculator<sup>30-32</sup> (Figure 5.9 and Figure A5.23, Appendix 5). The titration analyses revealed a

prominent 2:1 binding of the host with all the guest molecules and a much weaker 1:1 binding. This suggests that the guest molecules most likely interact with the cage via the externally protruding chiral groups. The crystal packing of **5.1-rac** also shows the presence of chiral voids at the cage exteriors in addition to the intrinsic cavities.

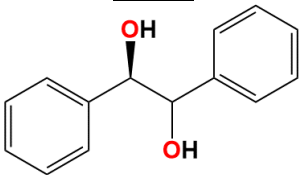
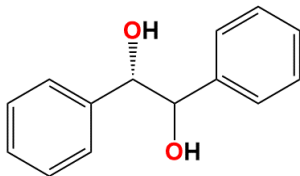
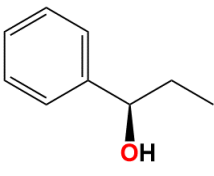


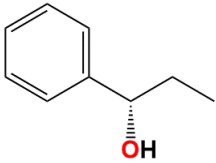
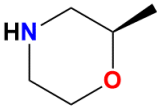
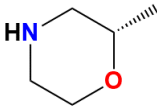
**Figure 5.9.** Bind fit plots for the host-guest systems as derived from the UV-Visible titration experiments.

Of all the guests, the highest binding constant was obtained for the **S-P1P+5.1-R** system with the  $K_a$  value of  $7.2 \times 10^5 \text{ M}^{-1}$ . In contrast, the **R-P1P+5.1-R** system shows a  $K_a$  value of  $4.3 \times 10^4 \text{ M}^{-1}$  thereby giving it the highest selectivity [ $\xi = K_a(\text{larger})/K_a(\text{smaller})$ ] of 16.8. A similar

preferential host-guest binding was observed with the **S-HB+5.1-R** system with a high association constant value of  $K_a = 1.1 \times 10^4 \text{ M}^{-1}$ . However, the **R-HB** isomer also interacts fairly well ( $K_a = 1.5 \times 10^3 \text{ M}^{-1}$ ) with the host **5.1-R**, resulting in an intermediate selectivity of 7.3 (Table 5.3). The lowest chiral recognition with a selectivity of 1.4 was observed with the **MP+5.1-R** systems where the **R-MP** showed slightly higher binding than the **S-MP** with a binding constant values of  $1.2 \times 10^3 \text{ M}^{-1}$  and  $8.5 \times 10^2 \text{ M}^{-1}$  respectively. However, unlike the others, the **MP+5.1-R** systems show a preferential 1:1 binding for the host-guest mixtures. This could again be attributed to the favorable binding of the small **MP** guests within the intrinsic cavities of the cage, thereby, reducing the extent of its enantio-selective recognition. The higher selectivity and high binding affinities of **HB** and **PIP** towards the host can be attributed to possible classical and non-classical hydrogen bonding interactions and pi-pi stacking interactions between the host and guest assemblies. The absence of these interactions in **MP+5.1-R** can be correlated to their much lower association constants.

**Table 5.3. Binding constants  $K_a$  ( $\text{M}^{-1}$ ) and binding selectivity ( $\xi$ ) as derived from the UV-Visible titration experiments**

Guest + 5.1-R	Binding Constant, $K_a$ ( $\text{M}^{-1}$ )	$\xi$
<b>R-HB</b> 	$1.5 \times 10^3$	7.3
<b>S-HB</b> 	$1.1 \times 10^4$	
<b>R-PIP</b> 	$4.3 \times 10^4$	16.7

<p><b>S-P1P</b></p> 	$7.2 \times 10^5$	
<p><b>R-MP</b></p> 	$1.2 \times 10^3$	1.4
<p><b>S-MP</b></p> 	$8.5 \times 10^2$	

## 5.4. Conclusion

In summary, we have studied self-sorting behavior in imido-Pd(II) derived neutral tetrahedral and cubical cages with chiral and achiral subunits. Depending on the dianionic linkers chosen, the sorting pathways were found to be governed by either steric, relative reactivity of the respective sub-components, symmetry and intramolecular interactions. These cages were characterized by NMR, MALDI-TOF-MS, CD, DOSY-NMR and X-ray crystallography and DFT-optimised studies. This mixed-ligand self-sorting phenomenon has not only led to the successful isolation of new heteroleptic tetrahedral cages but has also contributed towards the formation of a hitherto-unknown chiral neutral cage (**5.3**) tethered by PZDC linkers. Furthermore, the oxalate-bound tetrahedral self-sorted cage **5.1-R** was also employed for the enantio-recognition of various chiral guest molecules with distinct sizes. Due to the presence of both intrinsic and extrinsic voids in the cage, the chiral recognition was found to be heavily influenced by the encapsulation of the smaller guests within the cage cavity, thereby reducing their chiral selectivity which is known to occur at the extrinsic cavities of the cage. The occurrence of self-sorting among chemically similar subcomponents in a self-assembly process is essentially a decision-making phenomenon at the molecular level, wherein the statistical distribution and arrangement of the subunits are governed by factors like molecular bulk, symmetry, interactions, etc. Although the linker directionality plays an important role, there are no written rules for the exact outcome of the sorting pathway, making it an interesting technique to pursue.

This can further lead to the formation of newer and sometimes, unusual assemblies with emergent and exciting properties. Further studies on the host–guest chemistry and chiral recognition properties of the chiral cubical cage **5.3** are currently underway.

## 5.5. References

1. G. M. Whitesides, M. Boncheva, *Proc. Natl. Acad. Sci. U.S.A.* **2002**, *99*, 4769-4774.
2. S. Pullen, J. Tessarolo, G. H. Clever, *Chem. Sci.* **2021**, *12*, 7269-7293.
3. T. Jiao, H. Qu, L. Tong, X. Cao, H. Li, *Angew. Chem. Int. Ed.* **2021**, *60*, 9852-9858.
4. T. Tateishi, S. Takahashi, A. Okazawa, V. Martí-Centelles, J. Wang, T. Kojima, P. J. Lusby, H. Sato, S. Hiraoka, *J. Am. Chem. Soc.* **2019**, *141*, 19669-19676.
5. T. Tateishi, M. Yoshimura, S. Tokuda, F. Matsuda, D. Fujita, S. Furukawa, *Coord. Chem. Rev.* **2022**, *467*, 214612.
6. W. M. Bloch, Y. Abe, J. J. Holstein, C. M. Wandtke, B. Dittrich, G. H. Clever, *J. Am. Chem. Soc.* **2016**, *138*, 13750-13755.
7. S. Mukherjee, P. S. Mukherjee, *Chem. Commun.* **2014**, *50*, 2239-2248.
8. R.-J. Li, A. Tarzia, V. Posligua, K. E. Jelfs, N. Sanchez, A. Marcus, A. Baksi, G. H. Clever, F. Fadaei-Tirani, K. Severin, *Chem. Sci.* **2022**, *13*, 11912-11917.
9. R.-J. Li, A. Tarzia, V. Posligua, K. E. Jelfs, N. Sanchez, A. Marcus, A. Baksi, G. H. Clever, F. Fadaei-Tirani, K. Severin, *Chem. Sci.* **2022**, *13*, 11912-11917.
10. L.-L. Yan, C.-H. Tan, G.-L. Zhang, L.-P. Zhou, J.-C. Bünzli, Q.-F. Sun, *J. Am. Chem. Soc.* **2015**, *137*, 8550-8555.
11. F. J. Rizzuto, J. R. Nitschke, *J. Am. Chem. Soc.* **2020**, *142*, 7749-7753.
12. F. J. Rizzuto, J. R. Nitschke, *Nat. Chem.* **2017**, *9*, 903-908.
13. J. Li, P. Nowak, S. Otto, *J. Am. Chem. Soc.* **2013**, *135*, 9222-9239.
14. Z. He, W. Jiang, C. A. Schalley, *Chem. Soc. Rev.* **2015**, *44*, 779-789.
15. M. Schmittel, S. Saha, in *Advances in Inorganic Chemistry, Vol. 71* (Eds.: R. van Eldik, R. Puchta), Academic Press, **2018**, pp. 135-175
16. M. M. J. Smulders, A. Jiménez, J. R. Nitschke, *Angew. Chem. Int. Ed.* **2012**, *51*, 6681-6685.
17. D.-X. Cui, Y. Geng, J.-N. Kou, G.-G. Shan, C.-Y. Sun, K.-H. Zhang, X.-L. Wang, Z.-M. Su, *Nat. Commun.* **2022**, *13*, 4011.
18. T. Tateishi, T. Kojima, S. Hiraoka, *Commun. Chem.* **2018**, *1*, 20.
19. H. Jędrzejewska, A. Szumna, *Chem. Rev.* **2017**, *117*, 4863-4899.



20. C. Li, Y. Zuo, Y.-Q. Zhao, S. Zhang, *Chem. Lett.* **2020**, *49*, 1356-1366.
21. P. Wagner, F. Rominger, W.-S. Zhang, J. H. Gross, S. M. Elbert, R. R. Schröder, M. Mastalerz, *Angew. Chem. Int. Ed.* **2021**, *60*, 8896-8904.
22. F. Esteve, B. Altava, E. García-Verdugo, S. V. Luis, J.-M. Lehn, *Chem* **2022**, *8*, 2023-2042.
23. A. K. Gupta, A. Yadav, A. K. Srivastava, K. R. Ramya, H. Paithankar, S. Nandi, J. Chugh, R. Boomishankar, *Inorg. Chem.* **2015**, *54*, 3196-3202
24. A. Yadav, M. Sarkar, S. Subrahmanyam, A. Chaudhary, E. Hey-Hawkins, R. Boomishankar, *Chem. -Eur. J.* **2020**, *26*, 4209-4213.
25. P. Rajasekar, S. Pandey, H. Paithankar, J. Chugh, A. Steiner, R. Boomishankar, *Chem. Commun.* **2018**, *54*, 1873-1876.
26. P. Rajasekar, S. Pandey, J. D. Ferrara, M. Del Campo, P. Le Magueres, R. Boomishankar, *Inorg. Chem.* **2019**, *58*, 15017-15020.
27. M. Sarkar, R. Boomishankar, *Inorg. Chem.* **2023**, *62*, 1855-1863.
28. A. K. Gupta, S. A. D. Reddy, R. Boomishankar, *Inorg. Chem.* **2013**, *52*, 7608-7614
29. G. Sheldrick, *Acta Crystallogr. Sect. A* **2008**, *64*, 112-122.
30. <http://supramolecular.org>
31. P. Thordarson, *Chem. Soc. Rev.* **2011**, *40*, 1305-1323.
32. D. Brynn Hibbert, P. Thordarson, *Chem. Commun.* **2016**, *52*, 12792-12805.
33. M.J. Frisch et al. *Gaussian 09*, Revision C.01; Gaussian, Inc.: Wallingford, CT, 2016.
34. S. Grimme, *J. Comput. Chem.* **2006**, *27*, 1787-1799.
35. M.L. Connolly, *J. Mol. Graph.* **1993**, *11*, 139-141.
36. L. J. Barbour, *Chem. Commun.* **2006**, 1163-1168.
37. A. Yadav, A. K. Gupta, A. Steiner, R. Boomishankar, *Chem. -Eur. J.* **2017**, *23*, 18296-18302.
38. G. Beobide, O. Castillo, A. Luque, U. García-Couceiro, J. P. García-Terán, P. Román, *Inorg. Chem.* **2006**, *45*, 5367-5382.
39. B. Cai, P. Yang, J.-W. Dai, J.-Z. Wu, *CrystEngComm* **2011**, *13*, 985-991.
40. Y. Pan, D. Ma, H. Liu, H. Wu, D. He, Y. Li, *J. Mater. Chem.* **2012**, *22*, 10834-10839.

 End of Chapter 5 

# Chapter 6



## Thesis Conclusion and Future Perspectives

## Conclusion

*In Summary, this thesis has demonstrated the design, synthetic techniques and host-guest chemistry of a variety of Pd(II) neutral cages. Built on the deprotonation chemistry of imido-phosphate trianions, these Pd(II) containing cages have shown an excellent way of combining main group ligands with transition metal chemistry producing supramolecular self-assembled architectures. Further, all of these cages were probed towards encapsulation of a variety of guest molecules.*

*Chapter 1 began with a general introduction to metallo-supramolecular cage chemistry. Further, the various bonding techniques employed to synthesize these cages have been discussed, followed by a general concept of host-guest chemistry as a pronounced application of these supramolecular cages. Thereafter, the focus shifted onto the neutral cage systems and a detailed description of the various Pd(II) based neutral cage systems being synthesized in our lab. Finally, the chapter ends with a discussion on the aim and objective of this thesis.*

*In Chapter 2, we went on to explore the mechanistic pathway leading to the formation of such neutral assemblies. In the process, two new tetrahedral cages tethered by oxamido and N, N'-dimethyloxamido linkers were reported. These cages were formed by utilizing the less reactive amide-based linkers which slowed down the reaction process, enabling us to isolate two new tetrameric intermediates of these cages based on the said linkers. Further, the reaction pathways were monitored with time and a detailed account of the respective tetrameric intermediates to tetrahedral cages was reported. In the final section, the oximido-linked tetrahedral cage cavity was employed to encapsulate small organic guest molecules. All the studies reported were supported by spectral characterisations such as mass spectrometry, NMR, titration studies, DOSY-NMR etc. and structural characterisations such as SCXRD and DFT-derived theoretical calculations.*

*While the oximido cages could successfully demonstrate the mechanistic pathway that follows behind the multi-component self-assembly, their smaller cavity sizes were unsuitable for larger guest encapsulation. This was overcome in Chapter 3, wherein a family of three larger, isostructural cages based on anilate linkers were probed towards the encapsulation of closo-dicarbododecaboranes, commonly known as carboranes. While traditional guest encapsulation could not occur due to size incompatibility, we employed an in-situ strategy to synthesize the cages in presence of the guest molecules in a one-pot reaction which successfully led to the formation of Guest  $\subset$  Host complexes. A detailed solution-phase study was performed*

aided by mass spectrometry, NMR techniques such as  $^1\text{H}$ -NMR monitoring, 2D-DOSY-NMR and hydrodynamic radii calculations, NOESY/ROESY NMR and IR spectroscopy. Further, extensive DFT-based energy optimisation and binding energy calculation were performed for all the guests.

*Chapter 4* demonstrated the formation of an unusual linker-free Pd(II)-based neutral cube cage via a template-mediated pathway. Here, the usage of an oximido linker in the initial stages of the reaction led to the pre-organisation of the imido-Pd<sub>3</sub> precursor units leading to the formation of the tetrameric complex reported in Chapter 2. However, the introduction of chloride ions in the system quickly escalated the reaction leading to the formation of the tetrahedral cage and its subsequent dimerization to the cube by replacing the weaker oxamide linkers with  $\mu$ -2-chloride linkages. The essentiality of the pre-organisation step template pathway was further proven by removing oxamide from the equation which led to the isolation of a new imido-Pd<sub>3</sub> polyhedral unit. Further, the chloride-linked cube was found to have a large cavity which was studied towards encapsulation of phenolic guest molecules with high binding affinities. Thus, we successfully synthesized a new linker-free polyhedral cage assembly from a non-directing Cl<sup>-</sup> linker and have utilized the same towards effective encapsulation of aromatic polar guest molecules. These studies were accompanied by spectral, theoretical and SCXRD structural analysis techniques.

Finally, in *Chapter 5*, the self-sorting phenomena in Pd-neutral cages were explored. Here, we employed two types of imido-Pd<sub>3</sub> based precursors: chiral and achiral and studied their self-sorting behaviour when exposed to three different kinds of linkers with various sizes, directionality and reactivity. Based on that, three different results were obtained. With a short, linear linker, an exclusive socially sorted tetrahedral cage was obtained with a 1:3 chiral:achiral subunit distribution ratio. Thus, a non-self-recognition bias was inferred. This chiral cage was further fully characterised and was eventually employed towards chiral recognition of three enantiomeric pairs of guests with different sizes and polarities. From the titration analysis, the highest enantioselectivity of 16.7 was obtained for (*S*)-1-phenyl-1-propanol as a guest.

Further, with a longer but lesser reactive linker, a mixture of both socially and narcissistically self-sorted cages was obtained. Due to the lack of product specificity, the self-sorted product was not isolated, however, its presence was confirmed by detailed spectral analysis and the structure was deduced from computational studies.

*In the final section, a longer but 120° directing linker was used which led to the formation of exclusively narcissistic self-sorted cages. This also led to the isolation of an elusive PZDC-linked chiral cube for the first time. This was further attributed to the presence of the achiral subunits in the reaction mixture, which aided in the pre-organisation and subsequent formation of the hitherto-unknown chiral cube. Thus, a template-induced self-sorting pathway was established and while the reactivity of both the chiral and achiral subunits was similar towards PZDC, the self-recognition pathway was strongly favoured due to the formation of highly symmetric resultant assemblies.*

### ***Future Perspectives***

*The final chapter 5 ended with the isolation of newer polyhedral assemblies obtained via the self-sorting pathway. While the mechanistic details behind the formation of homoleptic cages based on neutral imido-Pd<sub>3</sub> motifs have been unravelled, a lot more synthetic principles and further applications of these cages beyond encapsulation and molecular recognition remain to be explored. Especially, the self-sorting phenomena, which is unique to the systems and can be influenced by several factors, is one of the versatile strategies for the construction of complex supramolecular architecture. In addition, there is also plenty of room for the development of the imido-P(V) anions supported by other soft metal ions from both the main group and transition metal series that can give rise to novel structural assemblies and functional materials.*

*Over the years, the understanding of cage chemistry has evolved a lot beyond the simple combination of metal and ligands with suitable coordination sites. With the advent of newer and sophisticated synthetic strategies, design principles and remarkable intricacy, neutral cages, have thus emerged as a prospective class of self-assembled supramolecular materials with interesting functional properties.*

 **End of Chapter 6** 

# Appendix



Structural Characterisation Data**Table A2.1.** Selected bond lengths (Å) and bond angles (°) for **2.1-TM**.

Pd(4)-N(5)	2.02(2)
Pd(4)-N(6)	2.030(17)
Pd(4)-O(3)	2.042(15)
Pd(4)-O(2A)	2.056(16)
O(4)-Pd(3)	2.003(16)
O(4)-Pd(5)	2.018(15)
Pd(2)-O(3)	1.992(15)
Pd(2)-N(1)	2.029(19)
Pd(2)-O(1A)	2.070(16)
Pd(2)-N(2)	2.119(18)
Pd(5)-N(4)	2.01(2)

Pd(5)-O(4A)	2.075(16)
Pd(5)-N(6)	2.085(18)
Pd(3)-N(2)	1.987(17)
Pd(3)-N(3)	2.00(2)
Pd(3)-O(3A)	2.054(16)
Pd(6)-N(2L)	2.02(2)
Pd(6)-O(1L)	2.057(19)
Pd(1)-N(3)	2.02(2)
Pd(1)-N(1)	2.034(19)
Pd(1)-N(1L)	2.04(2)
Pd(1)-O(2L)	2.067(18)

N(5)-Pd(4)-N(6)	74.0(8)
N(5)-Pd(4)-O(3)	171.7(7)
N(6)-Pd(4)-O(3)	97.7(7)
N(5)-Pd(4)-O(2A)	92.5(7)
N(6)-Pd(4)-O(2A)	165.4(7)
O(3)-Pd(4)-O(2A)	95.8(6)
Pd(6)#1-Pd(4)-Pd(2)	103.29(12)
O(3)-Pd(2)-N(1)	171.2(7)
O(3)-Pd(2)-O(1A)	96.2(7)
N(1)-Pd(2)-O(1A)	92.7(7)
O(3)-Pd(2)-N(2)	96.8(7)
N(1)-Pd(2)-N(2)	74.4(8)
O(1A)-Pd(2)-N(2)	166.2(7)
Pd(4)-Pd(2)-Pd(1)	108.21(14)
N(4)-Pd(5)-O(4)	173.4(6)
N(4)-Pd(5)-O(4A)	91.6(7)
O(4)-Pd(5)-O(4A)	95.0(7)
N(4)-Pd(5)-N(6)	74.3(7)

O(4)-Pd(5)-N(6)	99.1(7)
O(4A)-Pd(5)-N(6)	164.7(7)
Pd(3)-Pd(5)-Pd(6)#1	107.06(14)
N(2)-Pd(3)-N(3)	75.6(8)
N(2)-Pd(3)-O(4)	97.5(7)
N(3)-Pd(3)-O(4)	172.8(7)
N(2)-Pd(3)-O(3A)	167.6(8)
N(3)-Pd(3)-O(3A)	93.8(7)
O(4)-Pd(3)-O(3A)	93.3(6)
Pd(1)-Pd(3)-Pd(5)	104.21(10)
N(2L)-Pd(6)-O(1L)	81.4(8)
N(3)-Pd(1)-N(1)	75.7(8)
N(3)-Pd(1)-N(1L)	100.2(8)
N(1)-Pd(1)-N(1L)	171.2(8)
N(3)-Pd(1)-O(2L)	175.6(8)
N(1)-Pd(1)-O(2L)	102.0(7)
N(1L)-Pd(1)-O(2L)	81.7(8)

**Table A2.2.** Selected bond lengths (Å) and bond angles (°) for **2.1-TD**.

Pd(1)-N(1)	2.039(8)
Pd(1)-N(3)	2.040(7)
Pd(1)-N(2L)	2.050(7)
Pd(1)-O(1L)	2.060(6)
Pd(2)-N(1)	2.016(7)
Pd(2)-N(4L)	2.030(6)
Pd(2)-N(2)	2.034(7)
Pd(2)-O(3L)	2.062(6)

Pd(3)-N(3)	2.007(8)
Pd(3)-N(2)	2.014(7)
Pd(3)-O(5L)	2.048(7)
Pd(3)-N(6L)	2.050(7)
Pd(4)-N(4)	2.026(7)
Pd(4)-N(5L)	2.028(6)
Pd(4)-N(6)	2.042(7)
Pd(4)-O(6L)	2.059(6)

Pd(5)-N(5)	2.014(8)
Pd(5)-N(4)	2.035(7)
Pd(5)-N(7L)	2.041(6)
Pd(5)-O(8L)	2.062(6)
Pd(6)-N(6)	2.033(7)
Pd(6)-O(12L)	2.044(6)
Pd(6)-N(11L)	2.046(7)
Pd(6)-N(5)	2.053(8)
Pd(7)-N(8L)	2.020(6)
Pd(7)-N(9)	2.036(7)
Pd(7)-N(7)	2.036(8)
Pd(7)-O(7L)	2.062(7)
Pd(8)-N(7)	2.009(8)
Pd(8)-N(8)	2.029(8)
Pd(8)-N(1L)	2.053(6)
Pd(8)-O(2L)	2.062(6)

Pd(9)-N(8)	2.018(8)
Pd(9)-N(9)	2.019(7)
Pd(9)-N(10L)	2.049(6)
Pd(9)-O(9L)	2.054(7)
Pd(10)-N(10)	2.026(7)
Pd(10)-N(9L)	2.035(7)
Pd(10)-N(12)	2.044(7)
Pd(10)-O(10L)	2.060(7)
Pd(11)-N(10)	2.034(8)
Pd(11)-N(3L)	2.037(6)
Pd(11)-O(4L)	2.065(6)
Pd(11)-N(11)	2.073(8)
Pd(12)-N(11)	2.017(7)
Pd(12)-N(12)	2.031(7)
Pd(12)-N(12L)	2.034(7)
Pd(12)-O(11L)	2.067(7)

N(1)-Pd(1)-N(3)	77.6(3)
N(1)-Pd(1)-N(2L)	99.9(3)
N(3)-Pd(1)-N(2L)	177.1(3)
N(1)-Pd(1)-O(1L)	177.7(3)
N(3)-Pd(1)-O(1L)	100.3(3)
N(2L)-Pd(1)-O(1L)	82.2(3)
Pd(3)-Pd(1)-Pd(2)	59.68(2)
N(1)-Pd(2)-N(4L)	177.2(3)
N(1)-Pd(2)-N(2)	77.1(3)
N(4L)-Pd(2)-N(2)	100.5(3)
N(1)-Pd(2)-O(3L)	99.6(3)
N(4L)-Pd(2)-O(3L)	82.8(2)
N(2)-Pd(2)-O(3L)	176.4(3)
Pd(3)-Pd(2)-Pd(1)	60.14(2)
N(3)-Pd(3)-N(2)	77.4(3)
N(3)-Pd(3)-O(5L)	177.5(3)
N(2)-Pd(3)-O(5L)	100.5(3)
N(3)-Pd(3)-N(6L)	100.6(3)
N(2)-Pd(3)-N(6L)	177.8(3)
O(5L)-Pd(3)-N(6L)	81.5(3)
Pd(2)-Pd(3)-Pd(1)	60.18(2)
N(4)-Pd(4)-N(5L)	176.9(3)
N(4)-Pd(4)-N(6)	76.3(3)
N(5L)-Pd(4)-N(6)	100.7(3)
N(4)-Pd(4)-O(6L)	101.1(3)
N(5L)-Pd(4)-O(6L)	81.9(2)
N(6)-Pd(4)-O(6L)	177.4(3)

Pd(6)-Pd(4)-Pd(5)	59.88(3)
N(5)-Pd(5)-N(4)	76.4(3)
N(5)-Pd(5)-N(7L)	176.5(3)
N(4)-Pd(5)-N(7L)	100.1(3)
N(5)-Pd(5)-O(8L)	101.7(3)
N(4)-Pd(5)-O(8L)	177.3(3)
N(7L)-Pd(5)-O(8L)	81.7(2)
Pd(6)-Pd(5)-Pd(4)	60.03(2)
N(6)-Pd(6)-O(12L)	100.9(3)
N(6)-Pd(6)-N(11L)	177.4(3)
O(12L)-Pd(6)-N(11L)	81.7(3)
N(6)-Pd(6)-N(5)	76.2(3)
O(12L)-Pd(6)-N(5)	176.8(3)
N(11L)-Pd(6)-N(5)	101.2(3)
Pd(5)-Pd(6)-Pd(4)	60.09(3)
N(8L)-Pd(7)-N(9)	100.7(3)
N(8L)-Pd(7)-N(7)	177.4(3)
N(9)-Pd(7)-N(7)	76.9(3)
N(8L)-Pd(7)-O(7L)	82.5(3)
N(9)-Pd(7)-O(7L)	176.6(3)
N(7)-Pd(7)-O(7L)	99.9(3)
Pd(8)-Pd(7)-Pd(9)	60.01(3)
N(7)-Pd(8)-N(8)	76.9(3)
N(7)-Pd(8)-N(1L)	101.7(3)
N(8)-Pd(8)-N(1L)	178.4(3)
N(7)-Pd(8)-O(2L)	176.5(3)
N(8)-Pd(8)-O(2L)	99.8(3)



N(1L)-Pd(8)-O(2L)	81.6(3)
Pd(7)-Pd(8)-Pd(9)	60.00(3)
N(8)-Pd(9)-N(9)	77.0(3)
N(8)-Pd(9)-N(10L)	102.1(3)
N(9)-Pd(9)-N(10L)	178.8(3)
N(8)-Pd(9)-O(9L)	176.4(3)
N(9)-Pd(9)-O(9L)	99.5(3)
N(10L)-Pd(9)-O(9L)	81.5(3)
Pd(7)-Pd(9)-Pd(8)	59.99(2)
N(10)-Pd(10)-N(9L)	177.2(3)
N(10)-Pd(10)-N(12)	77.2(3)
N(9L)-Pd(10)-N(12)	100.3(3)
N(10)-Pd(10)-O(10L)	101.0(3)
N(9L)-Pd(10)-O(10L)	81.6(3)
N(12)-Pd(10)-O(10L)	177.8(3)

Pd(11)-Pd(10)-Pd(12)	59.97(3)
N(10)-Pd(11)-N(3L)	101.3(3)
N(10)-Pd(11)-O(4L)	176.5(3)
N(3L)-Pd(11)-O(4L)	82.0(3)
N(10)-Pd(11)-N(11)	76.4(3)
N(3L)-Pd(11)-N(11)	177.4(3)
O(4L)-Pd(11)-N(11)	100.2(3)
Pd(10)-Pd(11)-Pd(12)	60.72(3)
N(11)-Pd(12)-N(12)	77.4(3)
N(11)-Pd(12)-N(12L)	100.9(3)
N(12)-Pd(12)-N(12L)	177.8(3)
N(11)-Pd(12)-O(11L)	177.0(3)
N(12)-Pd(12)-O(11L)	99.6(3)
N(12L)-Pd(12)-O(11L)	82.1(3)
Pd(11)-Pd(12)-Pd(10)	59.31(3)

### Spectral Characterisation Data

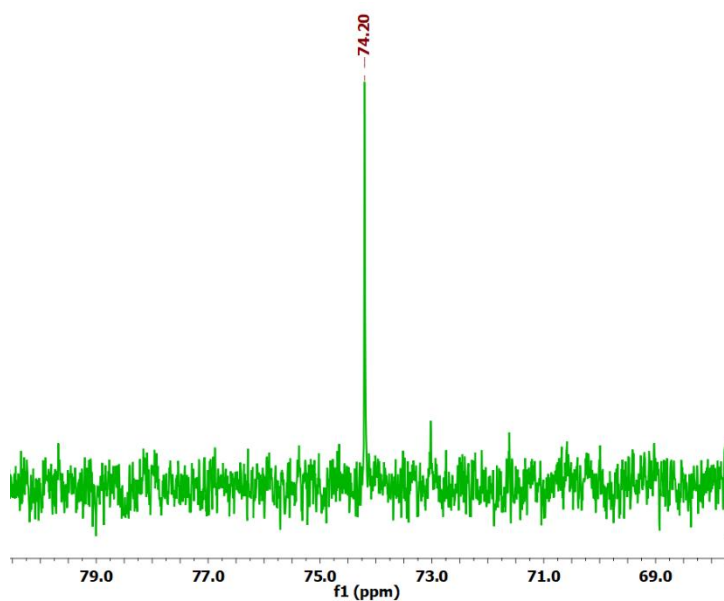


Figure A2.1.  $^{31}\text{P}$ -NMR ( $\text{CDCl}_3$ , 298K) of 2.1-TM.

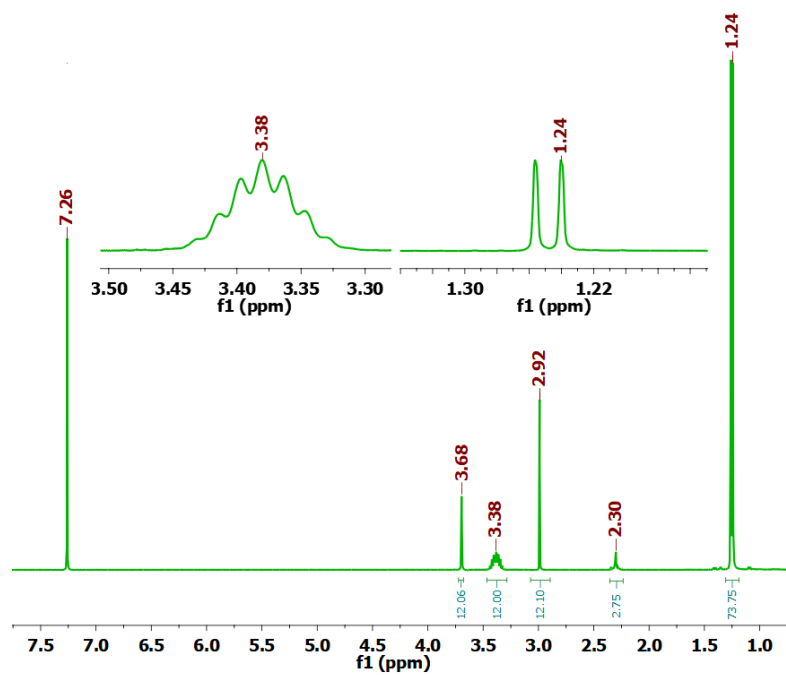


Figure A2.2.  $^1\text{H-NMR}$  ( $\text{CDCl}_3$ , 298K) of 2.1-TM.

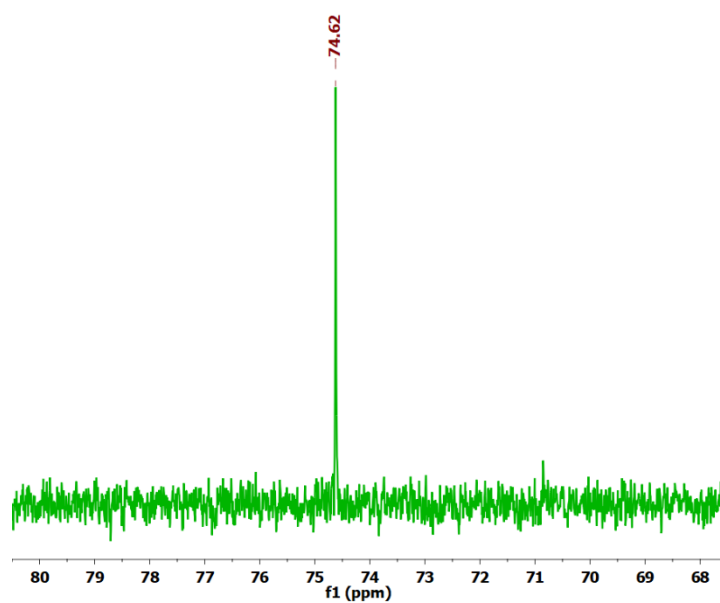


Figure A2.3.  $^{31}\text{P-NMR}$  ( $\text{CDCl}_3$ , 298K) of 2.2-TM.

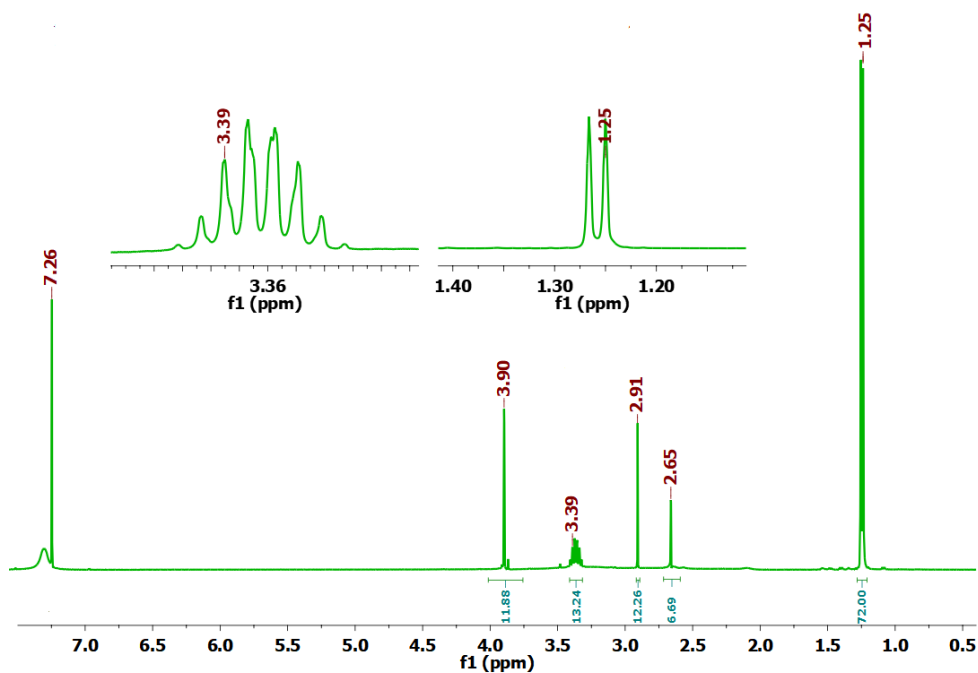


Figure A2.4.  $^1\text{H-NMR}$  ( $\text{CDCl}_3$ , 298K) of 2.2-TM.

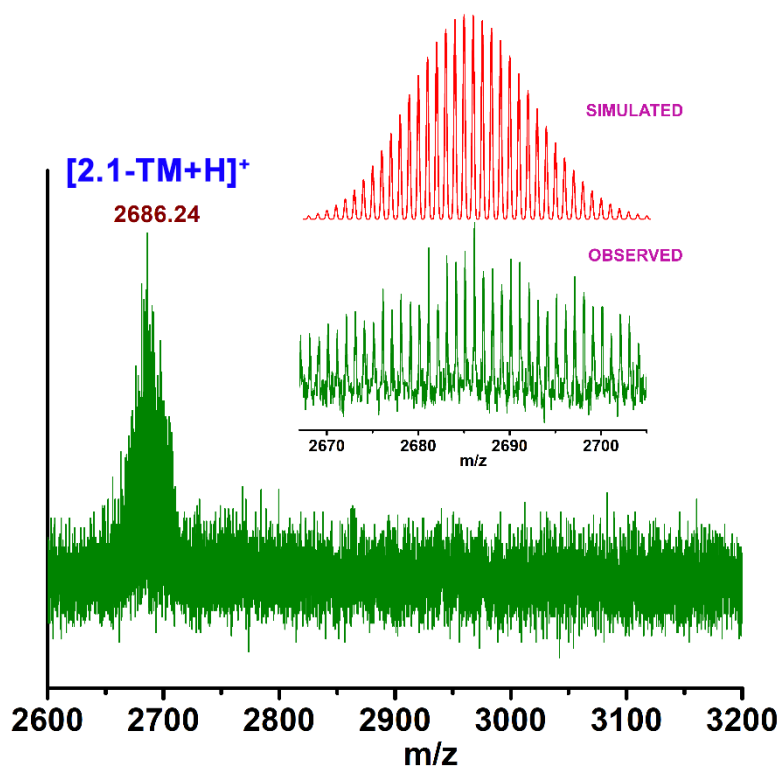


Figure A2.5. MALDI-TOF mass spectrum of 2.1-TM and isotopic distribution of peaks.

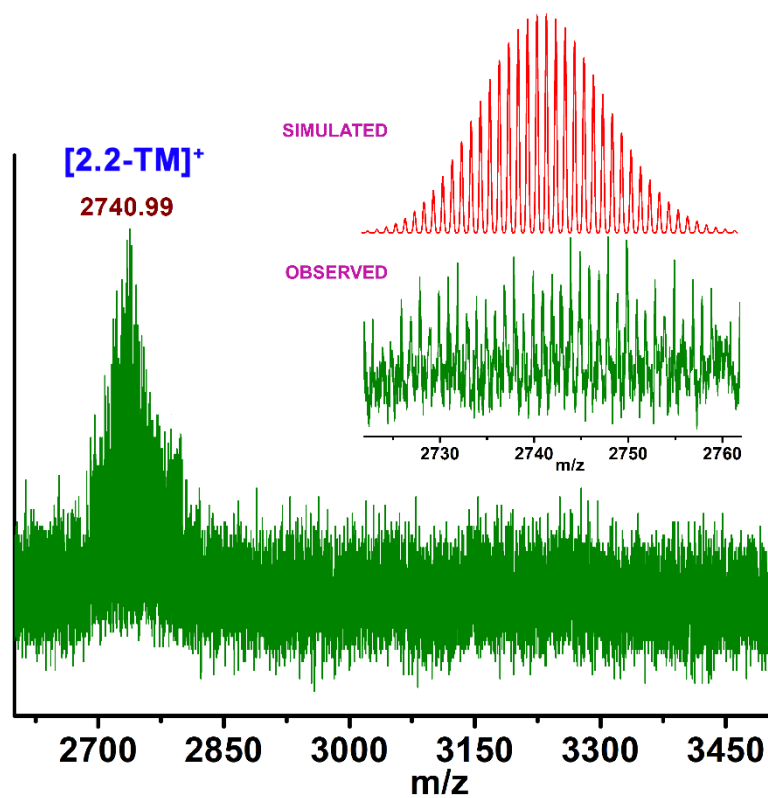


Figure A2.6. MALDI-TOF mass spectrum of 2.2-TM and isotopic distribution of peaks.

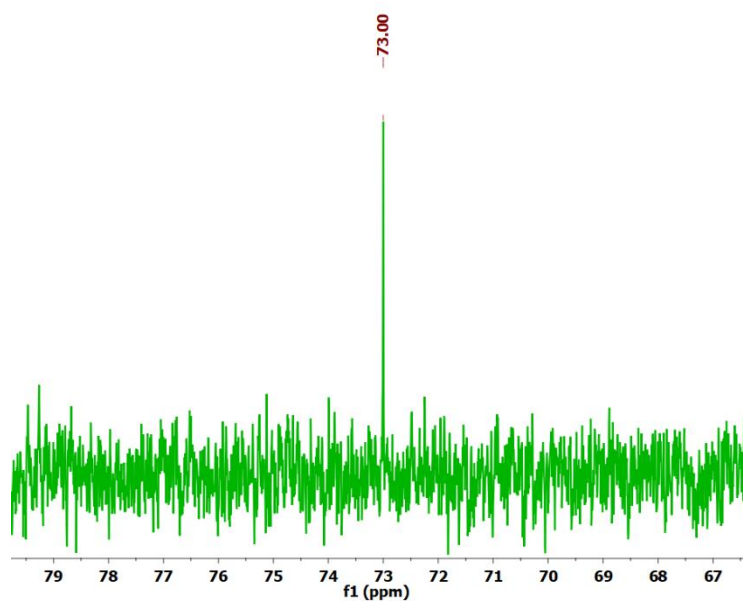


Figure A2.7.  $^{31}\text{P}$ -NMR ( $\text{CDCl}_3$ , 298K) of 2.1-TD.

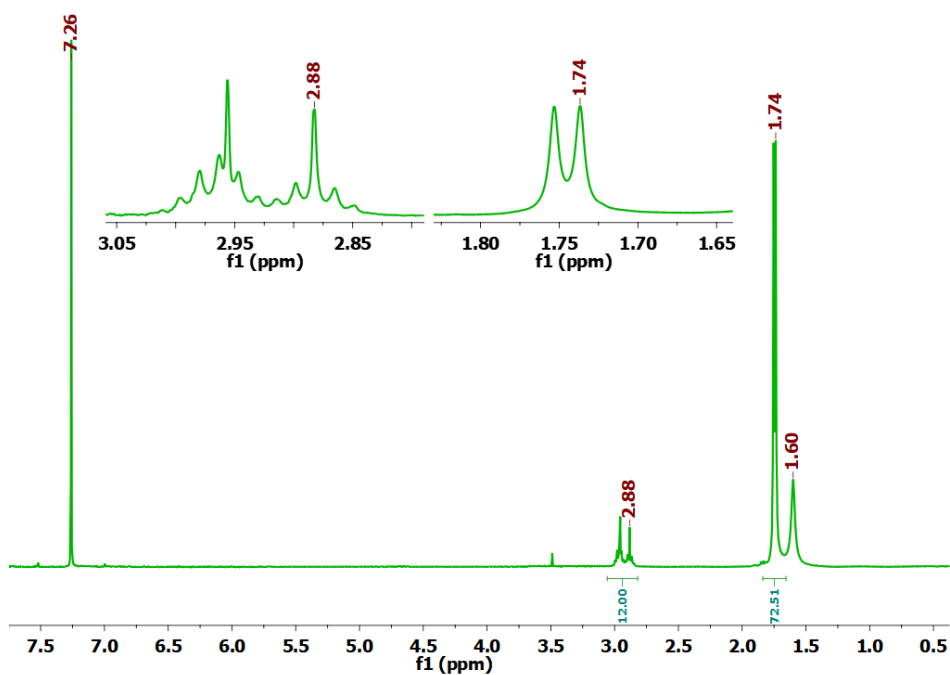


Figure A2.8.  $^1\text{H-NMR}$  ( $\text{CDCl}_3$ , 298K) of **2.1-TD**.

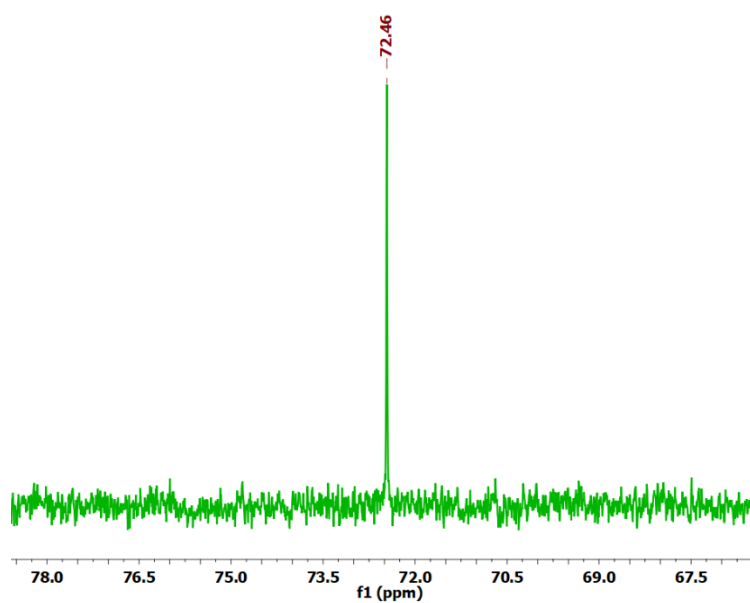


Figure A2.9.  $^{31}\text{P-NMR}$  ( $\delta \text{CDCl}_3$ , 298K) of **2.2-TD**.

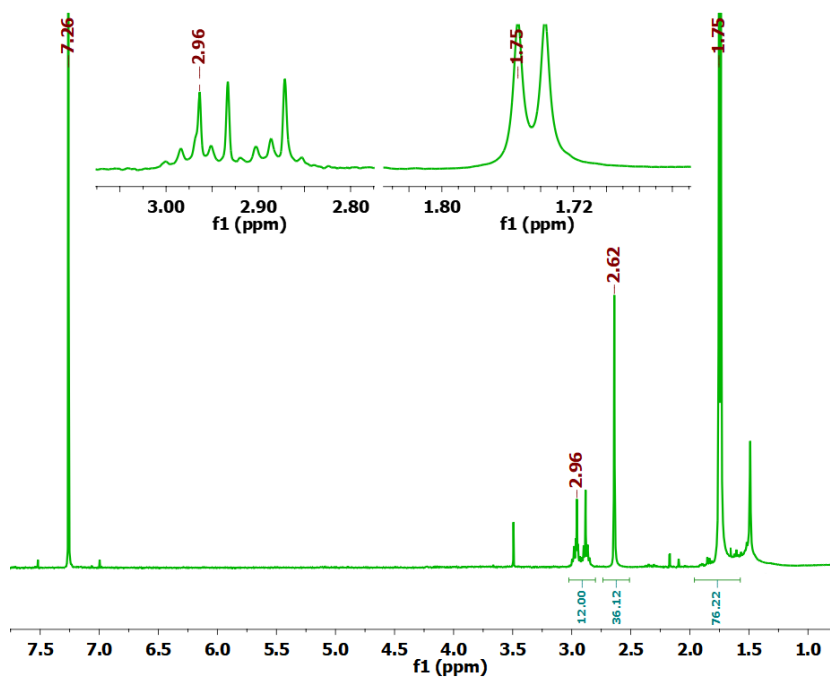


Figure A2.10.  $^1\text{H-NMR}$  ( $\text{CDCl}_3$ , 298K) of 2.2-TD.

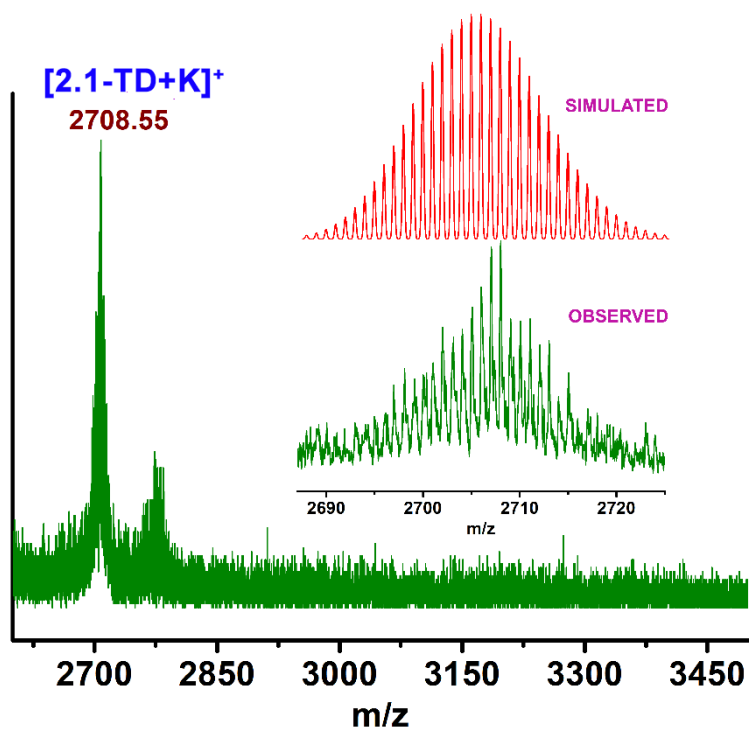


Figure A2.11. MALDI-TOF mass spectrum of 2.1-TD and isotopic distribution of peaks.

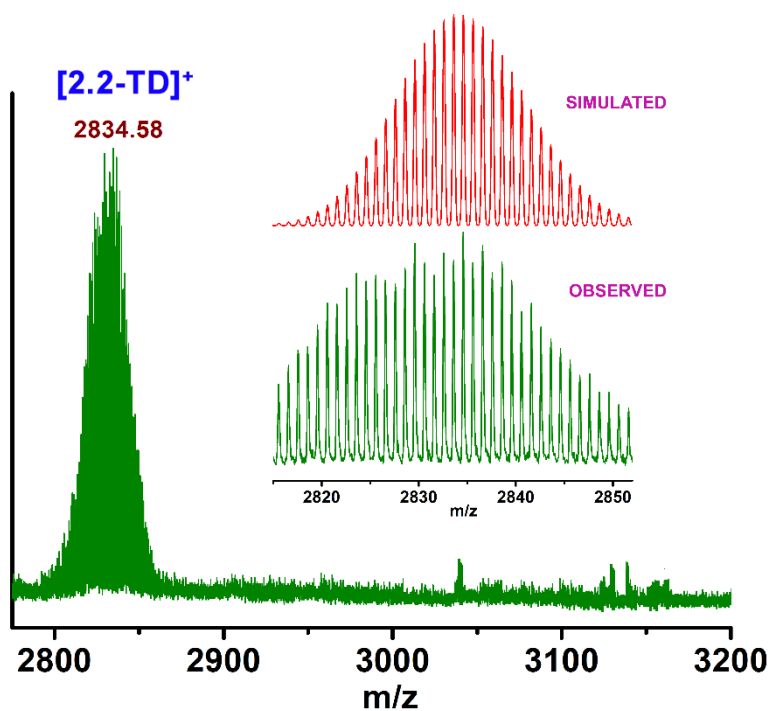


Figure A2.12. MALDI-TOF mass spectrum of 2.2-TD and isotopic distribution of peaks.

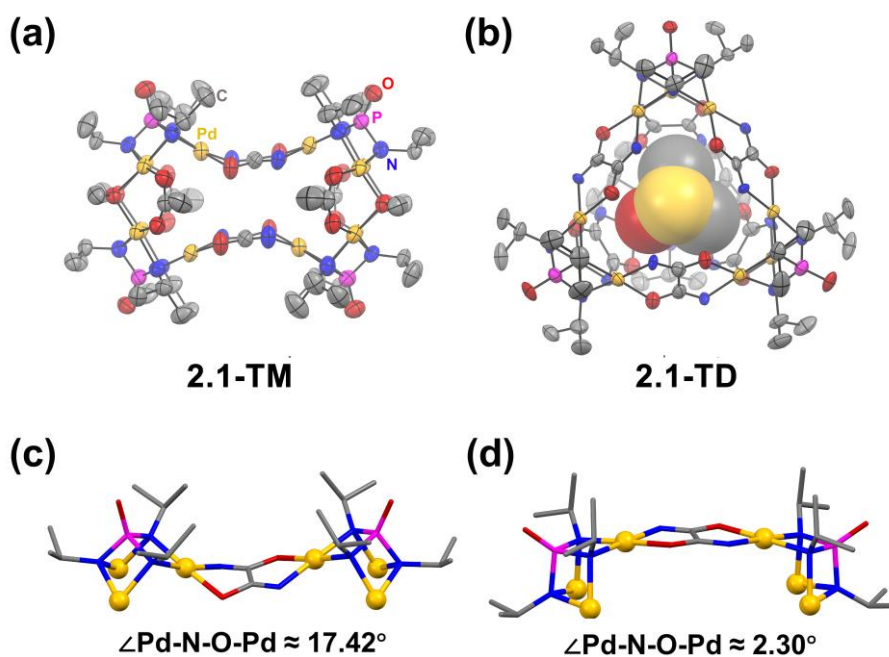
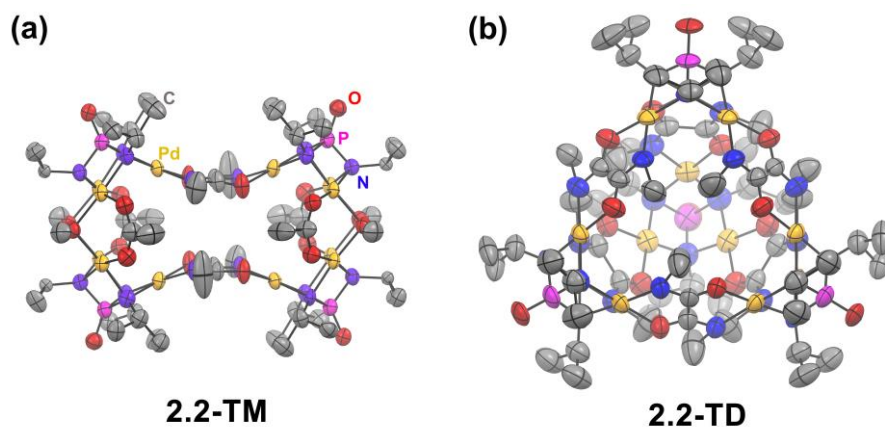
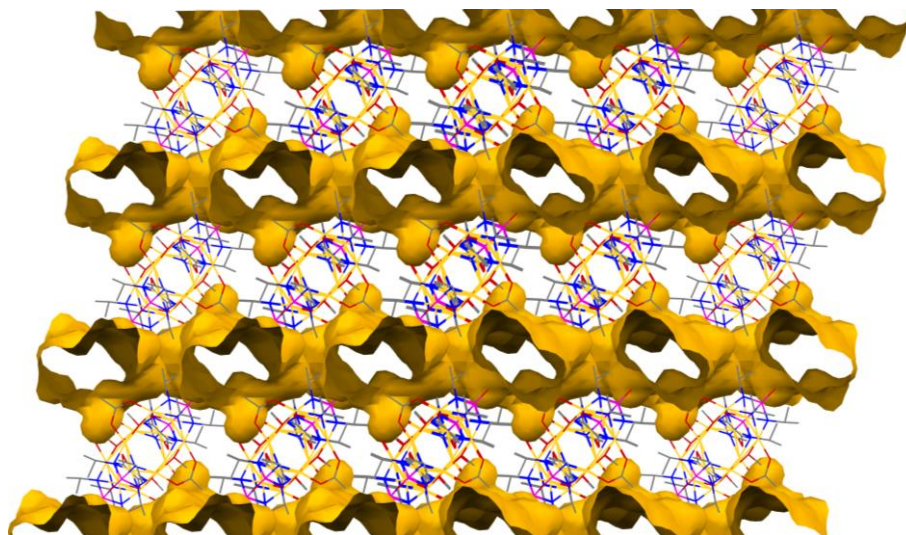


Figure A2.13. ORTEP diagram at 50% ellipsoids depicting the molecular structures of (a) 2.1-TM and (b) 2.1-TD. Average Pd-N-O-Pd dihedral angle in (c) 2.1-TM and (d) 2.1-TD.



**Figure A2.14.** ORTEP diagram at 50% ellipsoids depicting the molecular structures of **2.2-TM** and **2.2-TD**.

### Structural Illustrations Of Intrinsic And Extrinsic Voids



**Figure A2.15.** Connolly surface view of the 3\*3\*3 packing structure of **2.1-TM** computed by Mercury software showing the location and shape of both the intrinsic and extrinsic cavities.



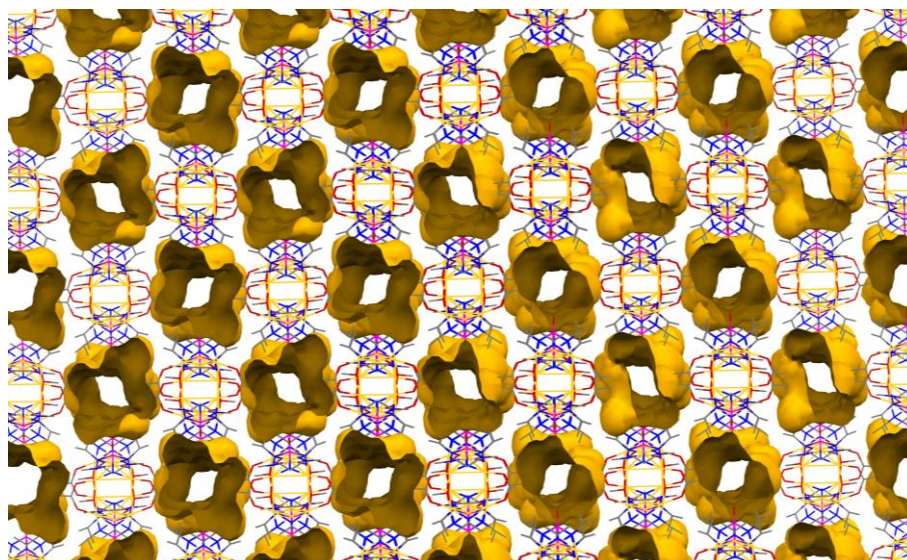


**Figure A2.16.** Connolly surface view of the 3\*3\*3 packing structure of **2.2-TM** computed by Mercury software showing the location and shape of both the intrinsic and extrinsic cavities.

<b>Table A2.3:</b> Molecular cavity volume calculated for <b>2.1-TD</b> from MSROLL calculations.		<b>Table A2.4:</b> Molecular cavity volume calculated for <b>2.2-TD</b> from MSROLL calculations.	
<b>Probe Radius (Å)</b>	<b>Volume (Å<sup>3</sup>)</b>	<b>Probe Radius (Å)</b>	<b>Volume (Å<sup>3</sup>)</b>
1.3	86.92	1.2	85.88
1.4	83.19	1.3	84.68
1.5	78.72	1.35	78.68

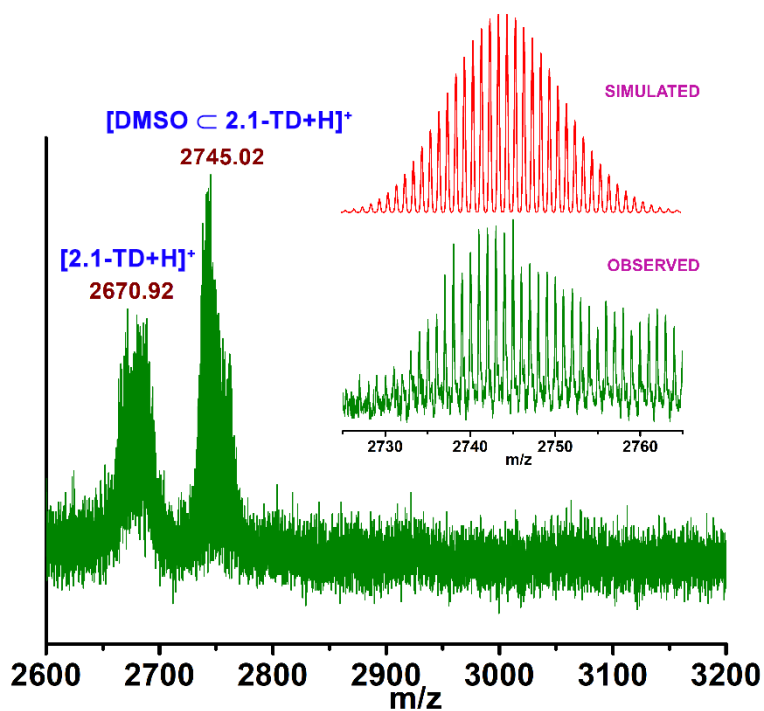


**Figure A2.17.** MALDI-TOF mass spectrum of  $[\text{DMSO} \subset \text{2.1-TD}+\text{H}]^+$  and isotopic distribution of peaks.

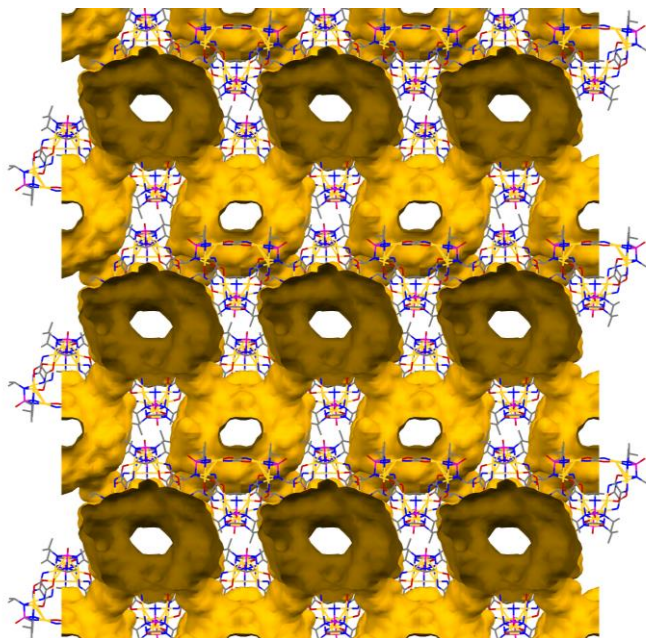


**Figure A2.18.** Connolly surface view of the 3\*3\*3 packing structure of **2.1-TD** computed by Mercury software showing the location and shape of both the intrinsic and extrinsic cavities.

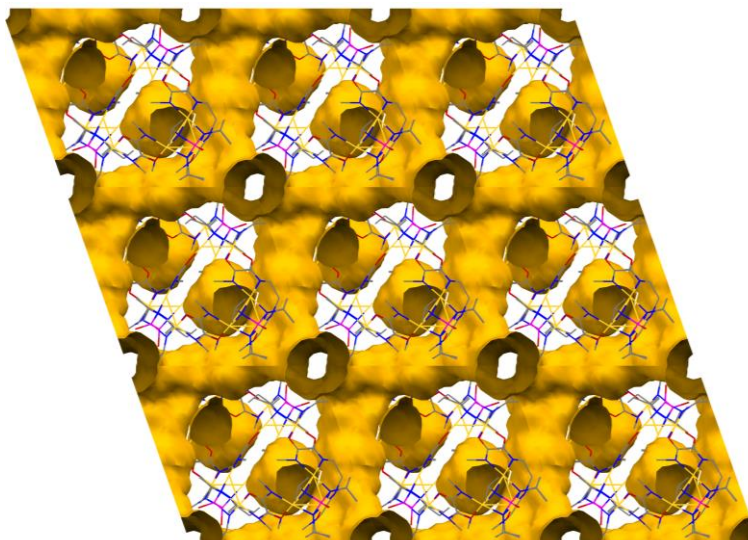


**Figure A2.19.** Connolly surface view of the 3\*3\*3 packing structure of **2.2-TD** computed by Mercury software showing the location and shape of both the intrinsic and extrinsic cavities.

### Spectral Data For Conversion From TM To TD

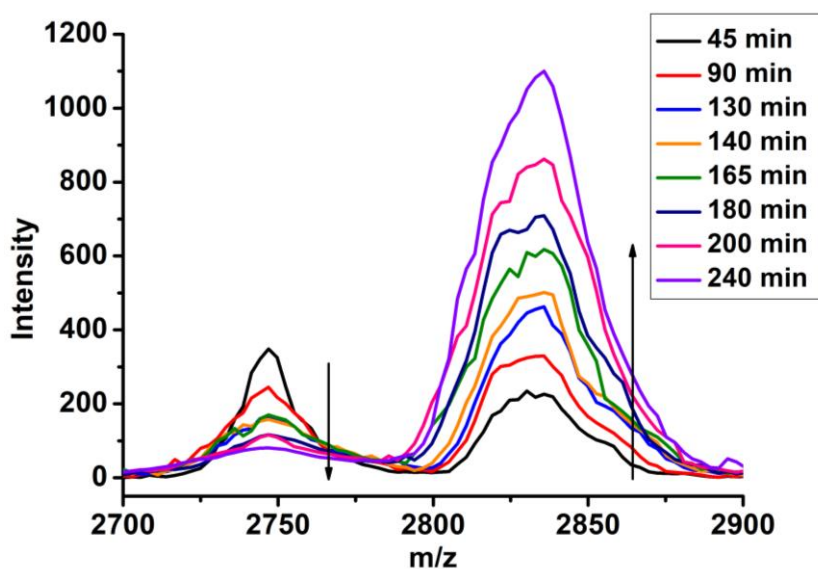


**Figure A2.20.** MALDI-TOF mass spectra showing the conversion of **2.2-TM** to **2.2-TD** in the linear mode.

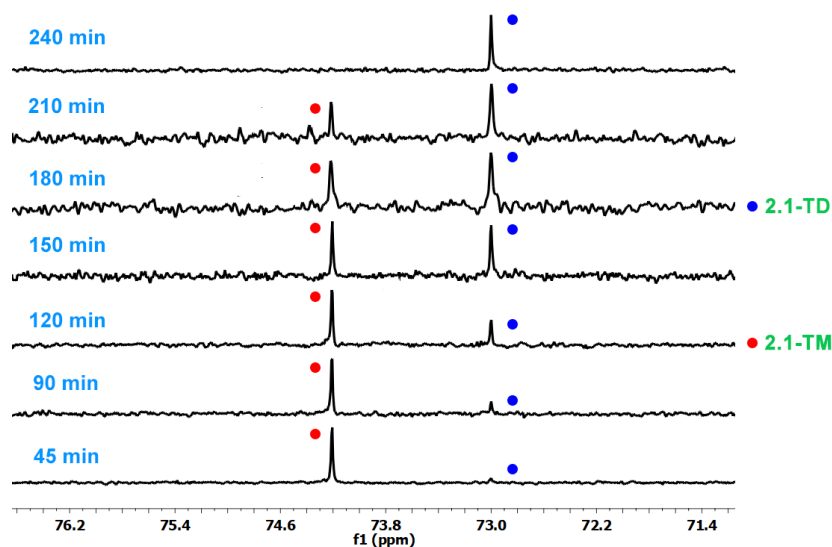


Figure A2.21.  $^{31}\text{P}$ -NMR spectra showing the conversion of 2.1-TM to 2.1-TD ( $\text{CDCl}_3$  in capillary).

### 2D-DOSY NMR

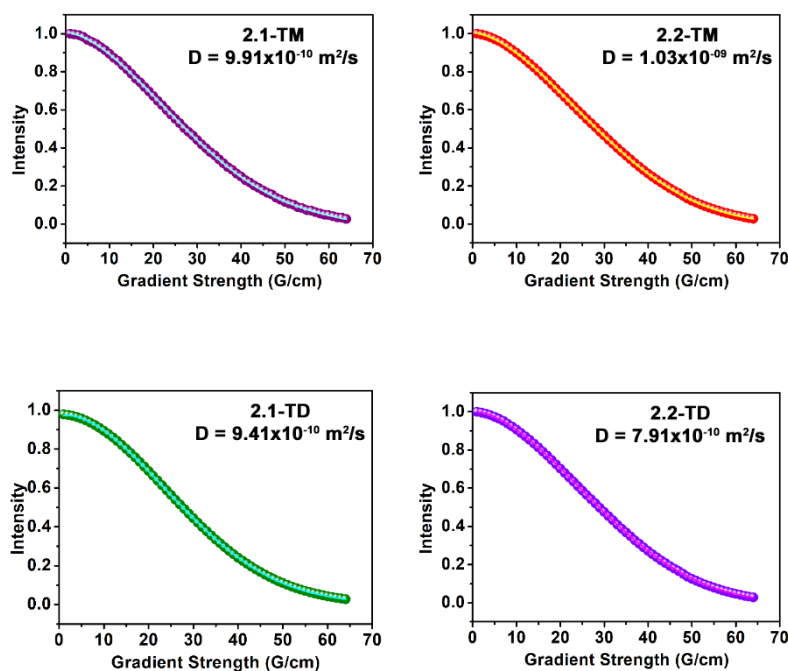
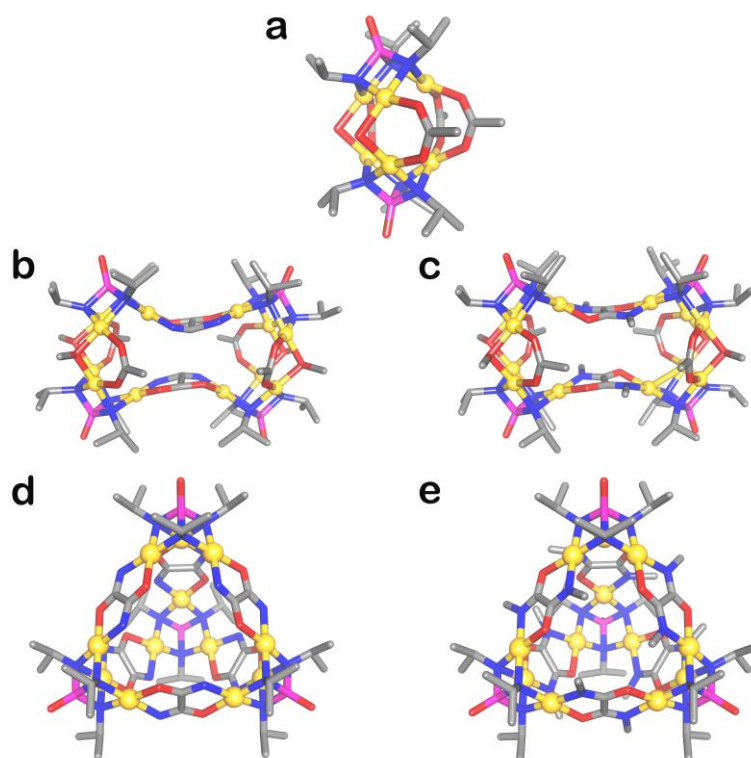


Figure A2.22: Integral decay profile of the tetramers 2.1-TM, 2.2-TM, and tetrahedral cages, 2.1-TD and 2.2-TD plotted as a function of gradient strength. The dots represent experimental data and the lines shows the best fit. Name of the molecule and the diffusion coefficients obtained are shown in the corresponding insets.

### DFT Optimisation Of The Participating Complexes



**Figure A2.23.** DFT optimized structures of the participating complexes (a) **HEXA-Pd** (b) **2.1-TM**, (c) **2.2-TM**, (d) **2.1-TD** and (e) **2.2-TD**

**Table A2.5:** Optimised single molecule energies of the participating complexes

Participating Complexes	Single Molecule Energy (* $\times 10^6$ kcal/mol)
<b>HEXA-Pd</b>	-1.77
<b>2.1-TM</b>	-2.65
<b>2.2-TM</b>	-3.06
<b>2.1-TD</b>	-3.46
<b>2.2-TD</b>	-3.53

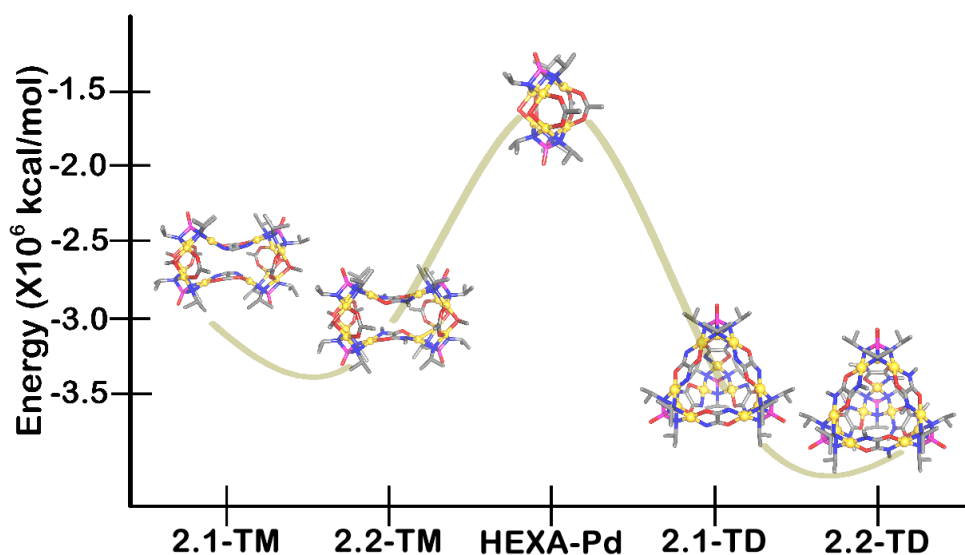


**Figure A2.24.** Schematic representation of the single molecule energies of the participating complexes.

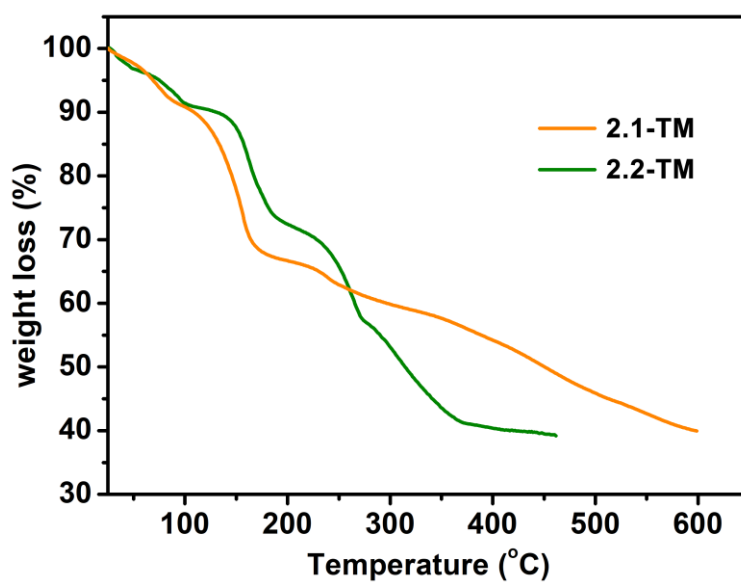


**Figure A2.25.** TGA curves of cages **2.1-TM** and **2.2-TM** showing around 10% weight loss due to the loss of solvents from the system.

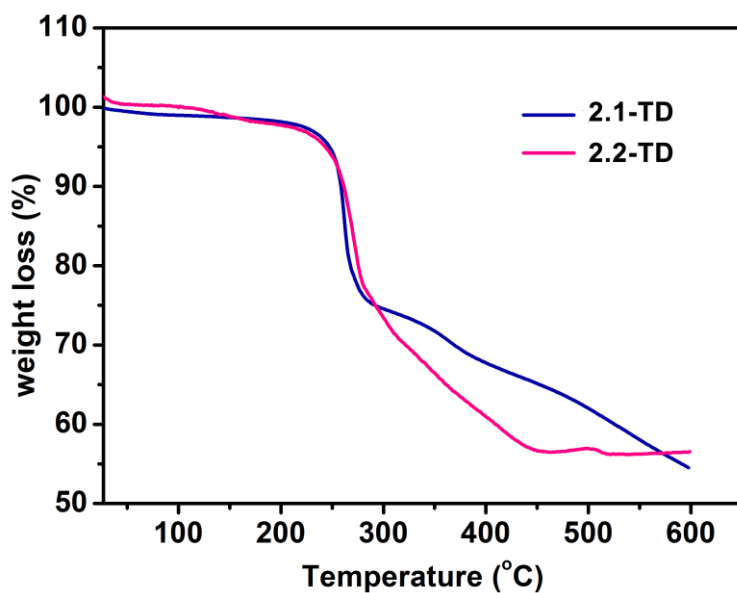


**Figure A2.26.** TGA curves of cages **2.1-TD** and **2.2-TD** showing around 10% weight loss due to the loss of solvents from the system.

### Guest Encapsulation Studies

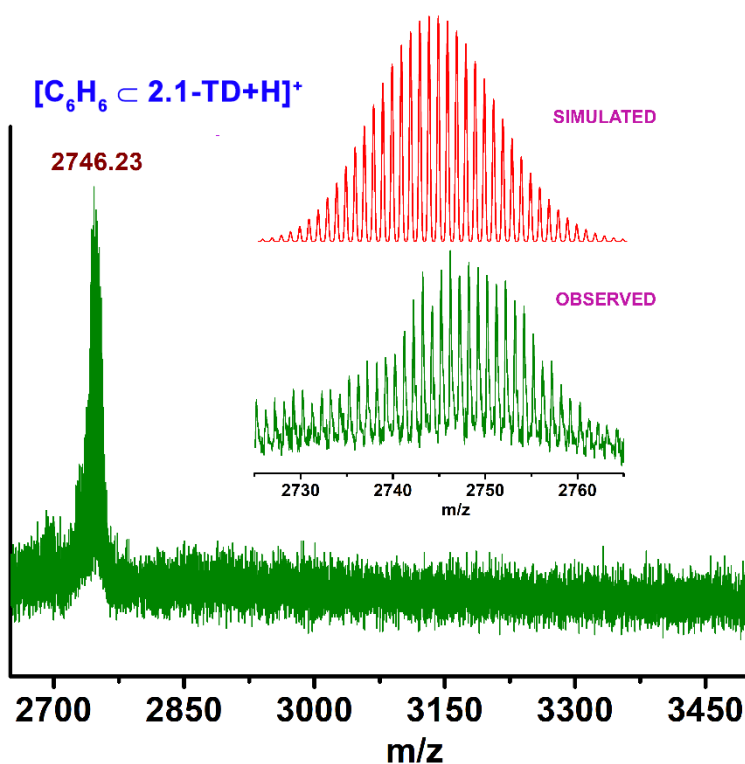


**Figure A2.27.** MALDI-TOF mass spectra of  $[C_6H_6 \subset 2.1-TD+H]^+$  and isotopic distribution of peaks.

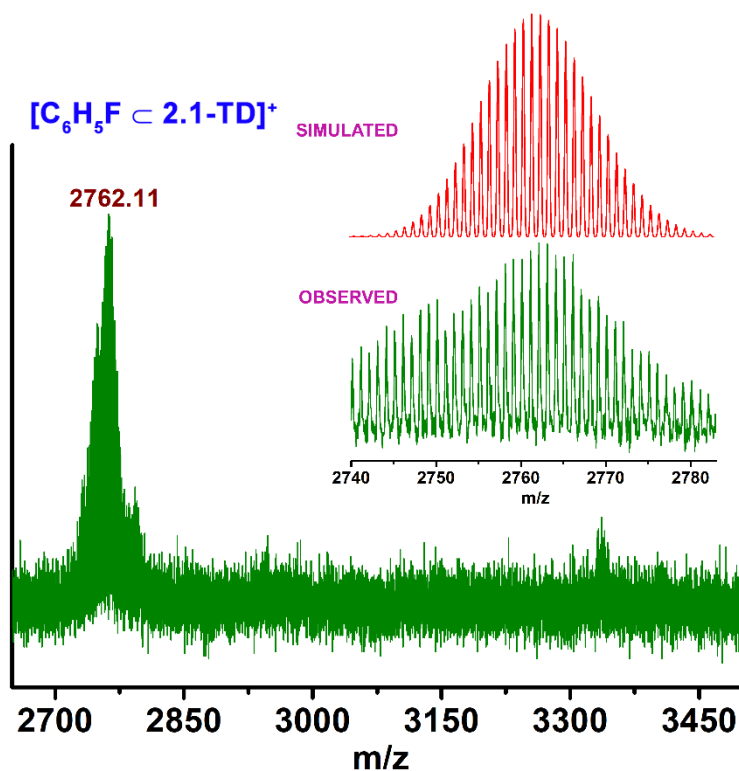


Figure A2.28. MALDI-TOF mass spectra of  $[\text{C}_6\text{H}_5\text{F} \subset 2.1\text{-TD}]^+$  and isotopic distribution of peaks.

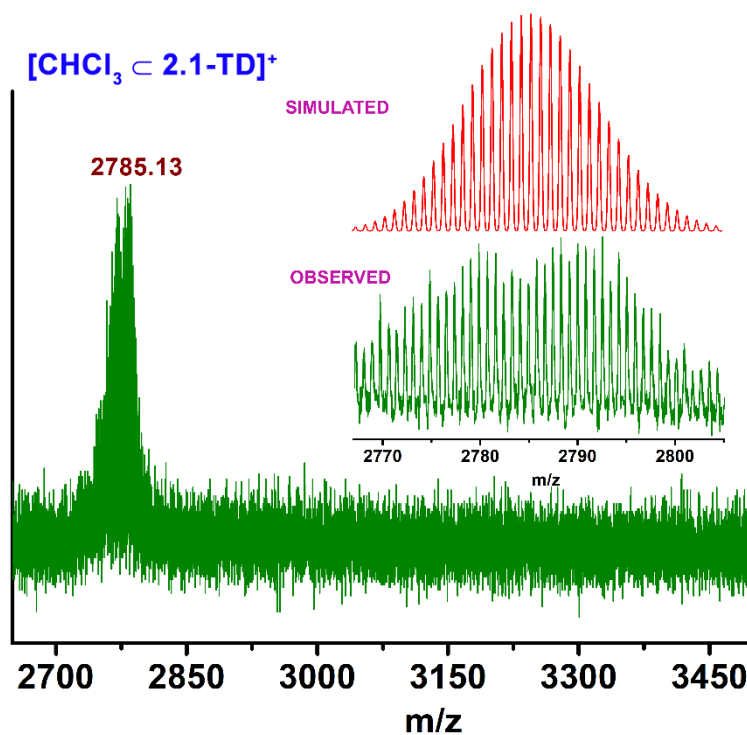
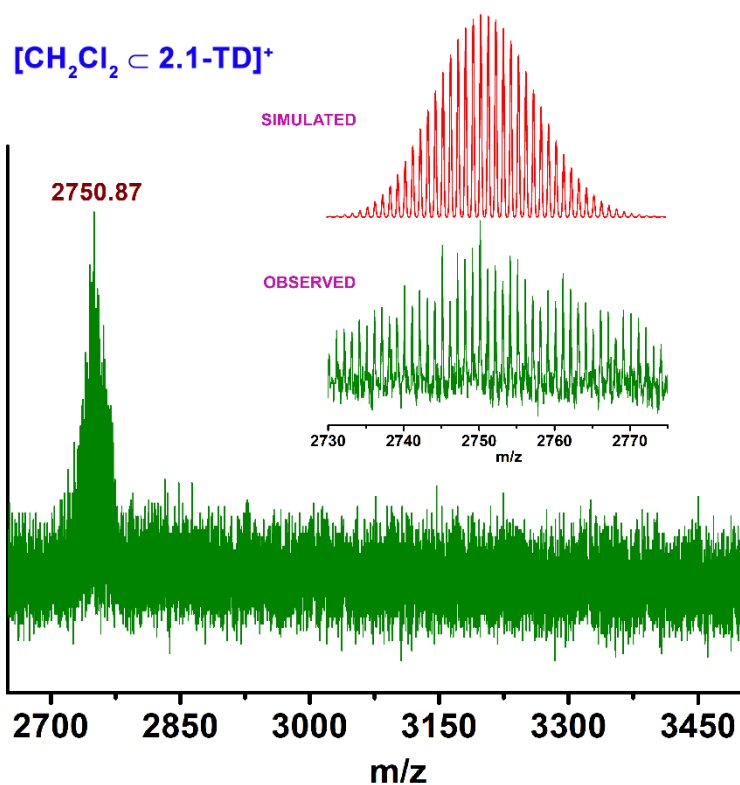
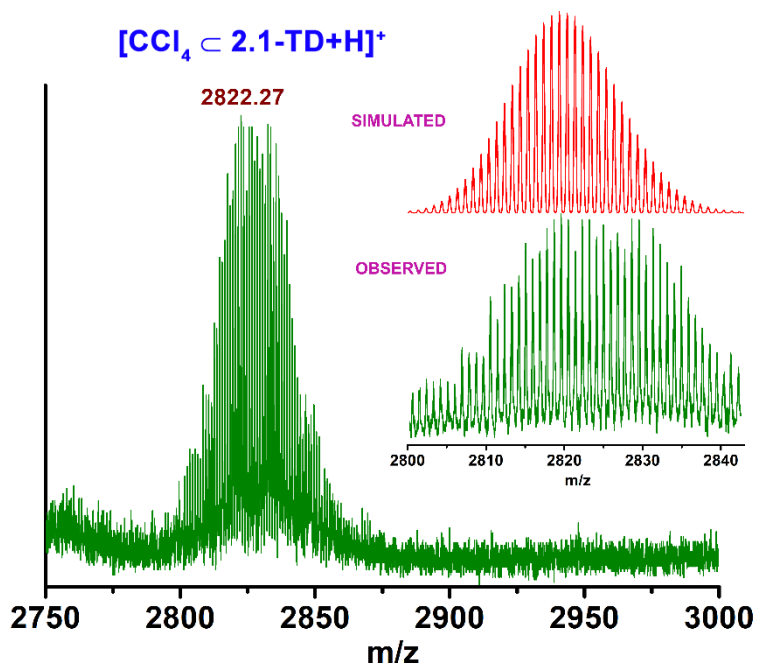


Figure A2.29. MALDI-TOF mass spectra of  $[\text{CHCl}_3 \subset 2.1\text{-TD}]^+$  and isotopic distribution of peaks.

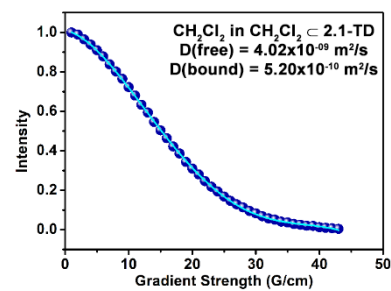
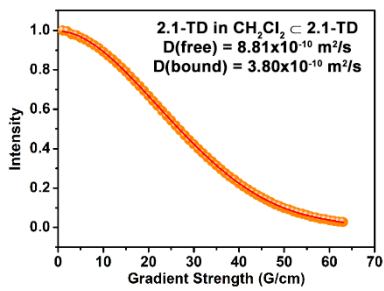
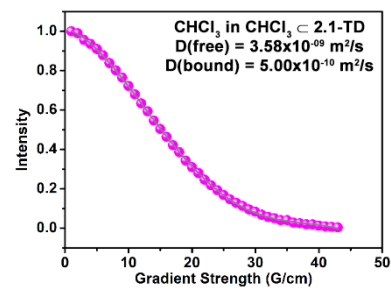
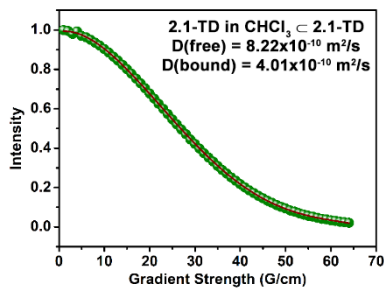
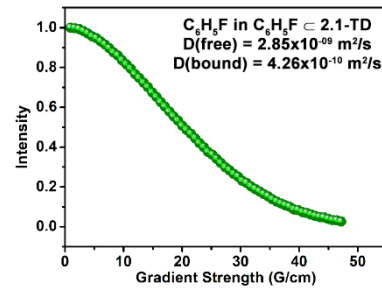
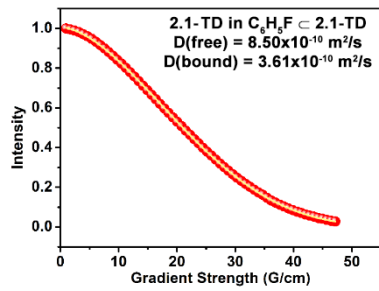
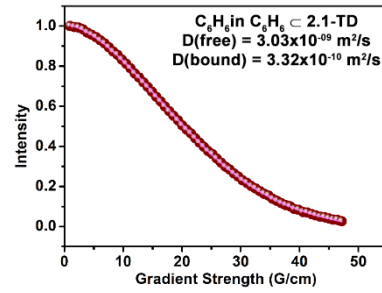
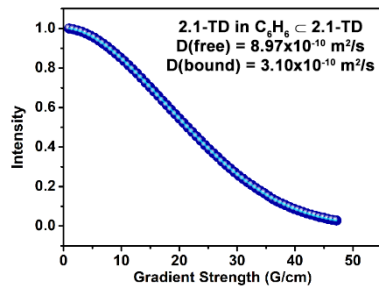




**Figure A2.30.** MALDI-TOF mass spectra of  $[\text{CH}_2\text{Cl}_2 \subset 2.1\text{-TD}]^+$  and isotopic distribution of peaks.



**Figure A2.31.** MALDI-TOF mass spectra of  $[\text{CCl}_4 \subset 2.1\text{-TD+H}]^+$  and isotopic distribution of peaks.



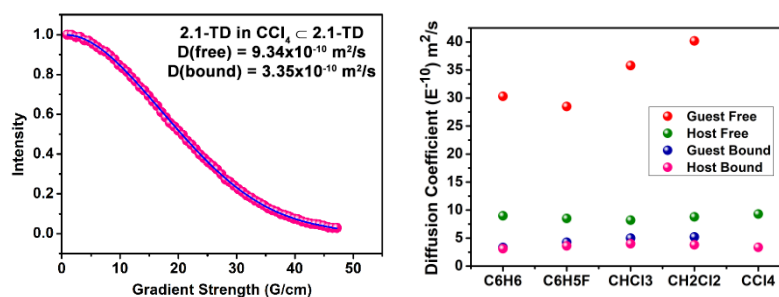


**Figure A2.32:** Integral decay profile of guest protons (left), and host protons (right) in the host-guest system plotted as a function of gradient strength. The dots represent experimental data and the lines shows the best fit using the equation 1. Name of the guest molecule and the diffusion coefficients obtained for free and bound molecule are shown in the corresponding insets.

**Table A2.6:** Diffusion coefficients as obtained from the DOSY experiment for all three hosts and different guests in the studied host-guest systems

Guest $\subset$ 2.1-TD	Diffusion Coefficient ( $\times 10^{-10}$ m <sup>2</sup> /s)			
	Host		Guest	
	Free	Bound	Free	Bound
C <sub>6</sub> H <sub>6</sub>	8.97	3.10	30.30	3.32
C <sub>6</sub> H <sub>5</sub> F	8.50	3.61	28.51	4.26
CHCl <sub>3</sub>	8.22	4.01	35.83	5.00
CH <sub>2</sub> Cl <sub>2</sub>	8.81	3.80	40.21	5.20
CCl <sub>4</sub>	9.34	3.35	-	-
C <sub>6</sub> H <sub>5</sub> Cl	9.21	-	27.06	-

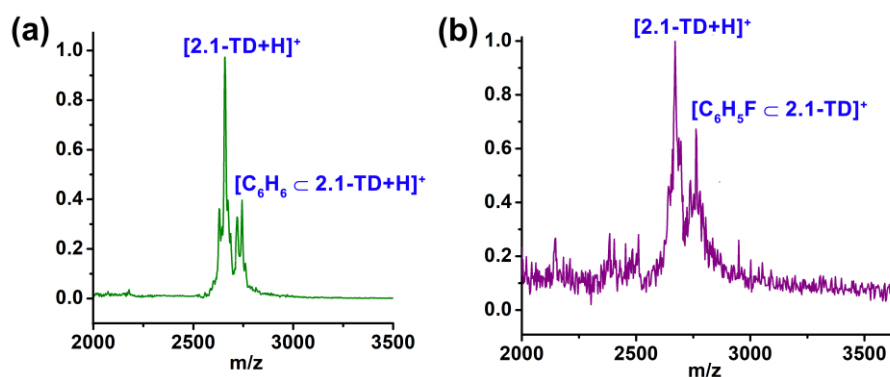


**Figure A2.33.** MALDI-TOF mass spectra of (a)  $[C_6H_6 \subset 2.1-TD+H]^+$  and (b)  $[C_6H_5F \subset 2.1-TD+H]^+$  depicting encapsulation of guest molecules on adding 0.5eq of guest to 1eq of host.

### DFT Optimised Structures Of Host-Guest Complexes

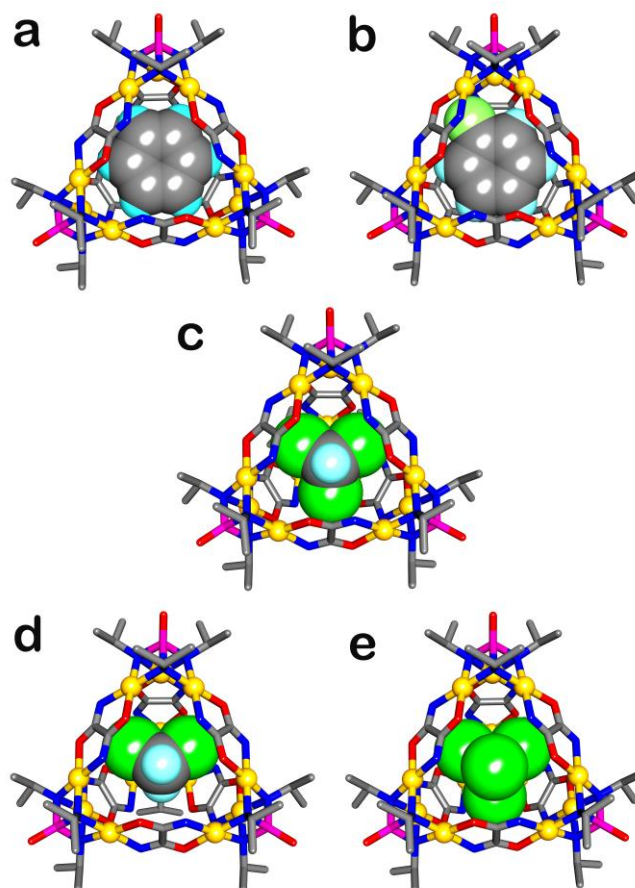


**Figure A2.34.** DFT optimized structures of the host-guest species (a)  $C_6H_6 \subset 2.1-TD$  (b)  $C_6H_5F \subset 2.1-TD$ , (c)  $CHCl_3 \subset 2.1-TD$ , (d)  $CH_2Cl_2 \subset 2.1-TD$  and (e)  $CCl_4 \subset 2.1-TD$

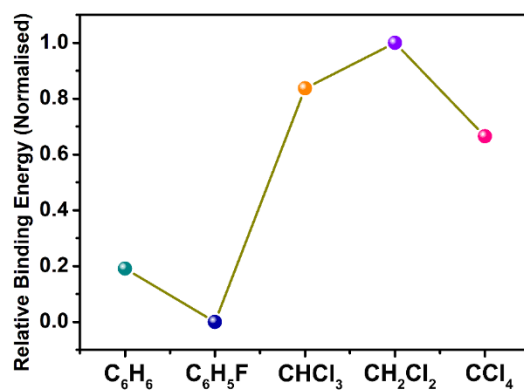


**Figure A2.35.** Relative binding energies of the host-guest species (a)  $C_6H_6 \subset 2.1-TD$  (b)  $C_6H_5F \subset 2.1-TD$ , (c)  $CHCl_3 \subset 2.1-TD$ , (d)  $CH_2Cl_2 \subset 2.1-TD$  and (e)  $CCl_4 \subset 2.1-TD$

\*\*\*\*\*

### Structural Characterisation Data

**Table A3.1.** Selected bond lengths for **3.2-TM**.

<b>Selected Bonds</b>	<b>Bond Length (Å)</b>
Pd(1)-N(1)	2.01(3)
Pd(1)-N(2)	2.02(2)
Pd(1)-O(4)	2.03(2)
Pd(1)-O(3)	2.06(2)
Pd(2)-N(3)	2.00(2)
Pd(2)-N(1)	2.02(2)
Pd(2)-O(9)	2.03(2)
Pd(2)-O(7)	2.06(2)
Pd(3)-N(3)	2.07(3)
Pd(3)-N(2)	2.10(2)
Pd(5)-O(10)	1.99(3)
Pd(5)-N(6)	2.00(3)
Pd(5)-N(4)	2.00(2)
Pd(5)-O(12)	2.01(2)
Pd(4)-N(5)	1.99(3)
Pd(4)-O(5)	2.06(2)
Pd(4)-O(6)	2.06(2)
Pd(4)-N(4)	2.06(2)
Pd(6)-O(8)	2.03(2)
Pd(6)-O(9)	2.05(2)

Table A3.2. Selected bond angles for 3.2-TM.

Selected Angles	Bond Angles (°)
N(1)-Pd(1)-N(2)	74(1)
N(1)-Pd(1)-O(4)	175.5(9)
N(2)-Pd(1)-O(4)	103(1)
N(1)-Pd(1)-O(3)	102.9(9)
N(2)-Pd(1)-O(3)	172.6(9)
O(4)-Pd(1)-O(3)	79.6(8)
Pd(2)-Pd(1)-Pd(3)	58.85(8)
N(3)-Pd(2)-N(1)	76(1)
N(3)-Pd(2)-O(9)	96.0(9)
N(1)-Pd(2)-O(9)	172.2(9)
N(3)-Pd(2)-O(7)	169.8(9)
N(1)-Pd(2)-O(7)	93.8(9)
O(9)-Pd(2)-O(7)	93.8(8)
Pd(3)-Pd(2)-Pd(1)	62.13(8)
Pd(3)-Pd(2)-Pd(6)	88.3(1)
Pd(1)-Pd(2)-Pd(6)	109.2(1)
O(12)#1-Pd(3)-N(3)	94.4(9)
O(12)#1-Pd(3)-N(2)	171.8(9)
N(3)-Pd(3)-N(2)	77(1)
O(10)-Pd(5)-N(6)	170(1)
O(10)-Pd(5)-N(4)	93(1)
N(6)-Pd(5)-N(4)	77(1)
O(10)-Pd(5)-O(12)	95.4(9)
N(6)-Pd(5)-O(12)	94(1)
N(4)-Pd(5)-O(12)	171(1)
N(5)-Pd(4)-O(5)	177(1)
N(5)-Pd(4)-O(6)	101(1)
O(5)-Pd(4)-O(6)	79.1(8)
N(5)-Pd(4)-N(4)	75(1)
O(5)-Pd(4)-N(4)	105(1)
O(6)-Pd(4)-N(4)	176(1)
N(6)#1-Pd(6)-O(8)	169(1)
N(5)#1-Pd(6)-O(9)	172(1)
N(6)#1-Pd(6)-O(9)	95(1)
O(8)-Pd(6)-O(9)	95.3(9)
Pd(5)#1-Pd(6)-Pd(2)	91.7(1)
Pd(4)#1-Pd(6)-Pd(2)	111.9(1)
Pd(5)-Pd(4)-Pd(6)	60.01(9)

## MALDI-TOF Mass Spectra of In-situ Host–Guest Complexes

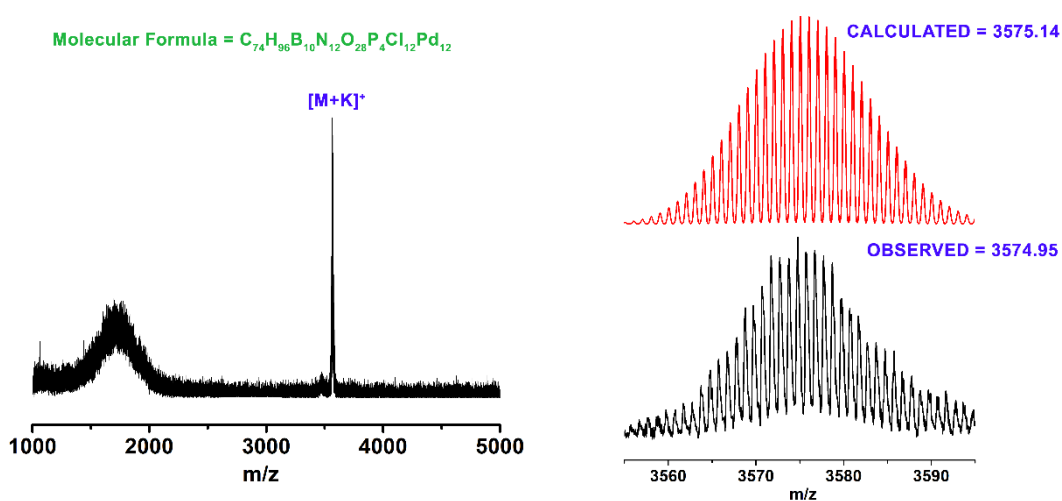


Figure A3.1: MALDI-TOF mass spectrum of host–guest complex *o*-Cb c 3.1.

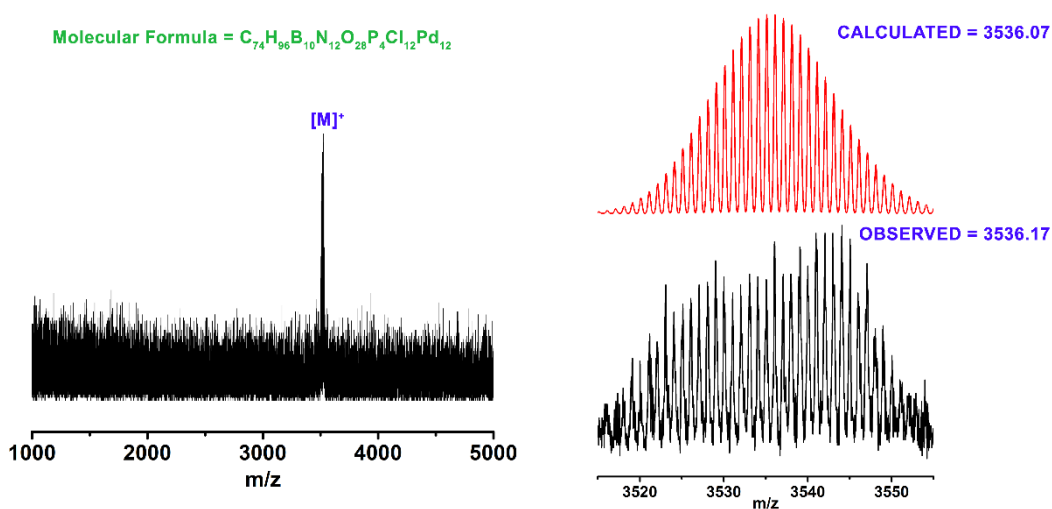


Figure A3.2: MALDI-TOF mass spectrum of host–guest complex *m*-Cb c 3.1.



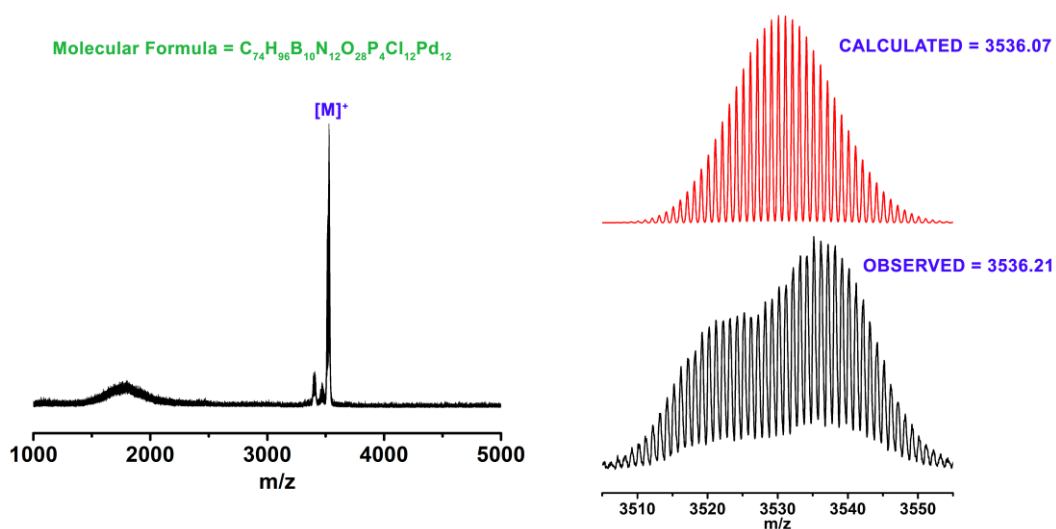


Figure A3.3: MALDI-TOF mass spectrum of host-guest complex *p*-Cb c 3.1.

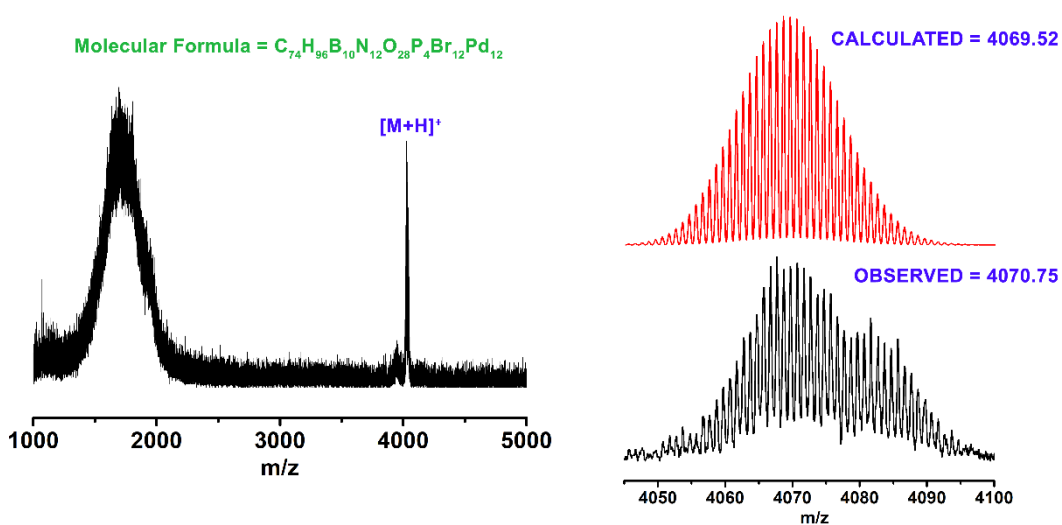


Figure A3.4: MALDI-TOF mass spectrum of host-guest complex *o*-Cb c 3.2.

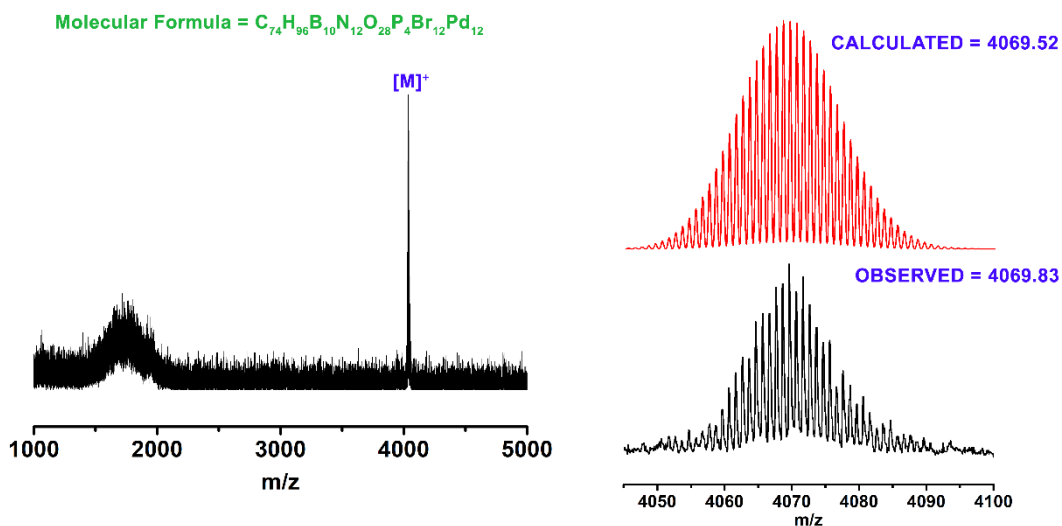


Figure A3.5: MALDI-TOF mass spectrum of host-guest complex *m*-Cb c 3.2.

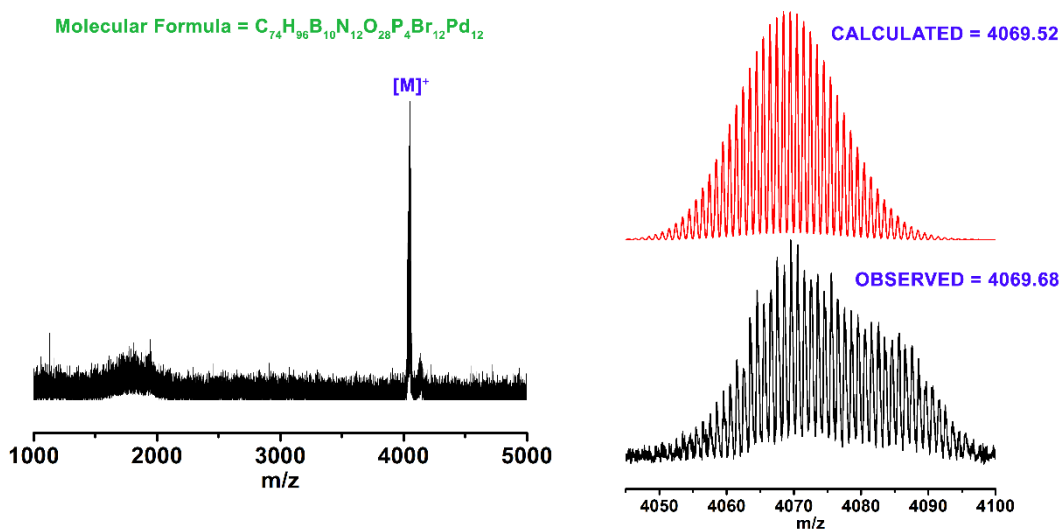


Figure A3.6: MALDI-TOF mass spectrum of host-guest complex *p*-Cb c 3.2.

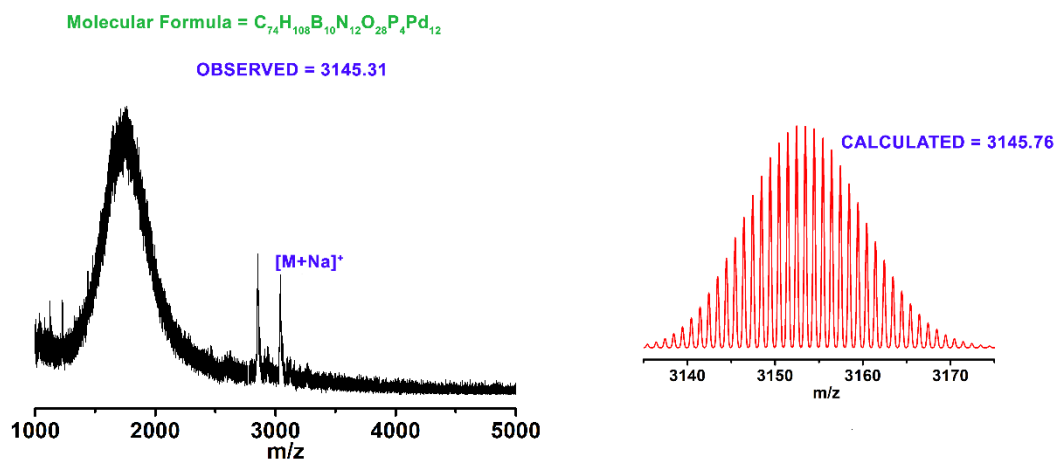


Figure A3.7: MALDI-TOF mass spectrum of host-guest complex *o*-Cb c 3.3.

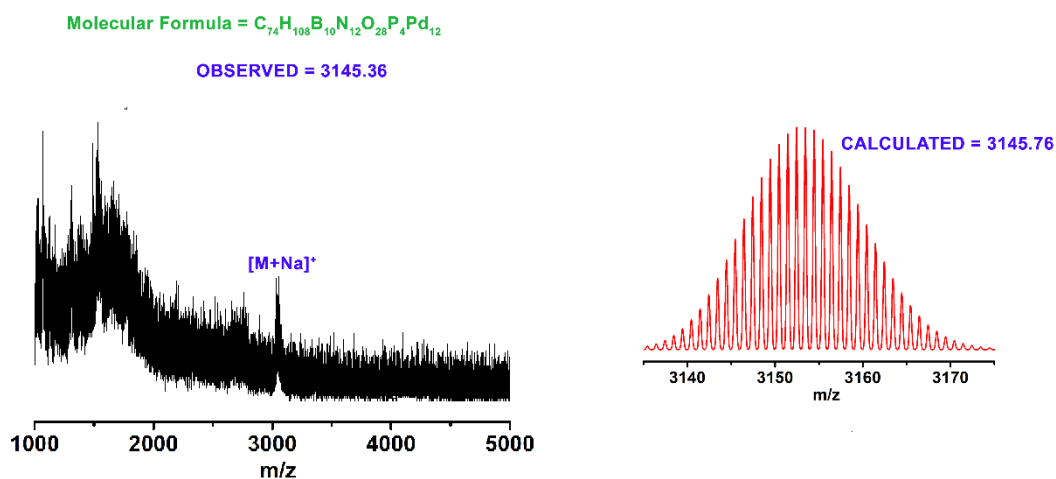


Figure A3.8: MALDI-TOF mass spectrum of host-guest complex *m*-Cb c 3.3.

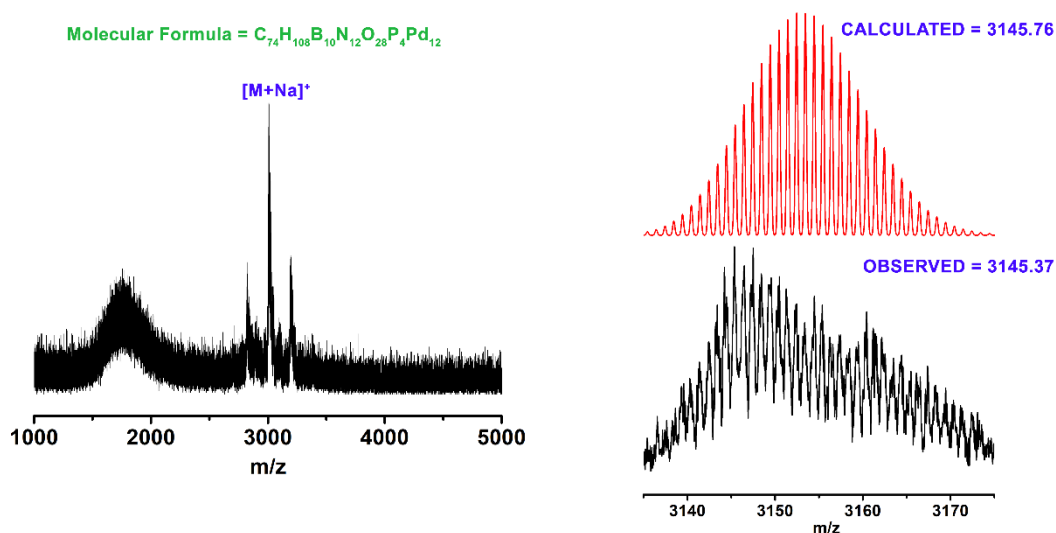


Figure A3.9: MALDI-TOF mass spectrum of host-guest complex *p*-Cb c 3.3.

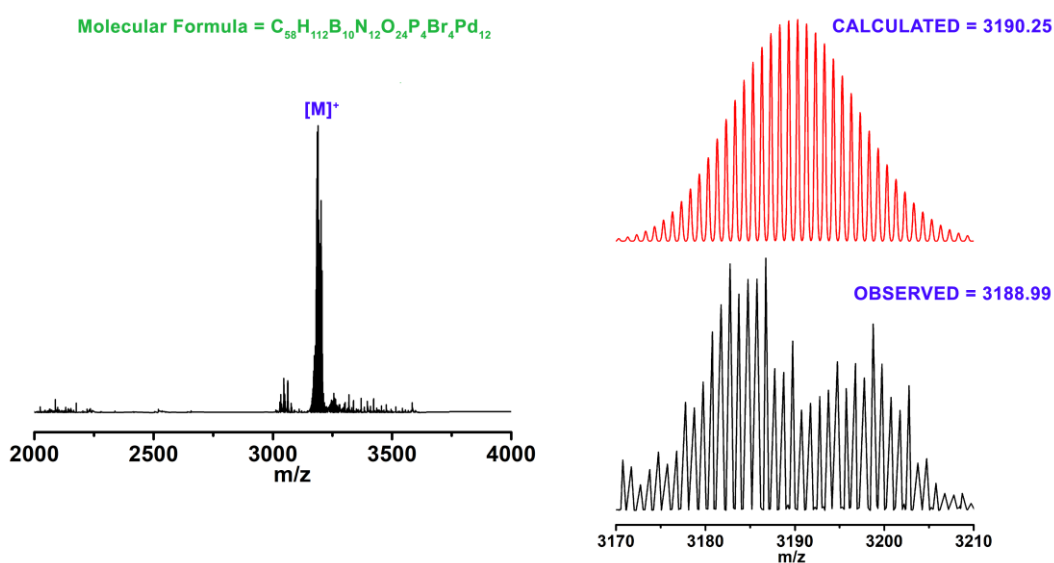
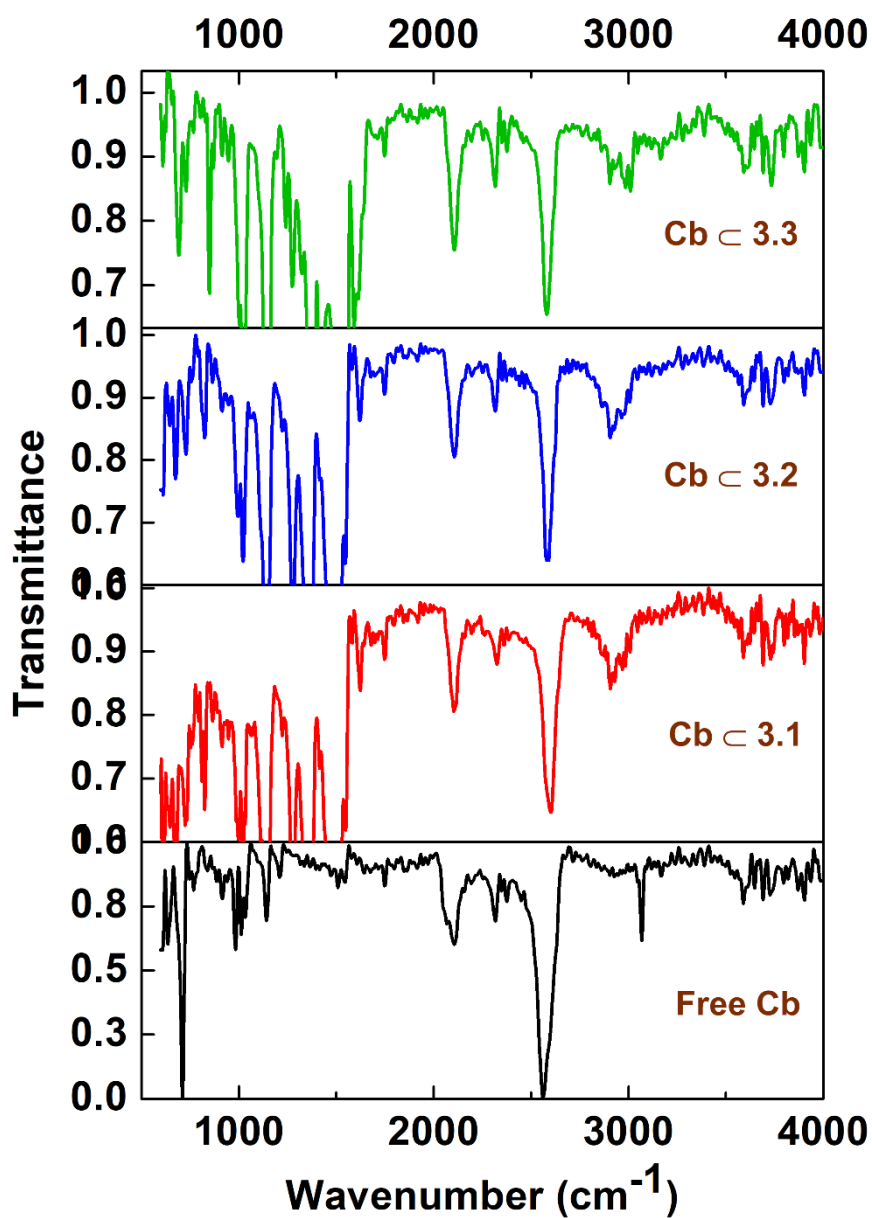
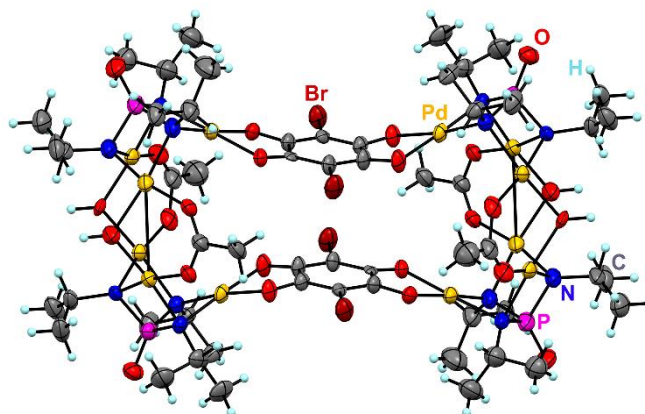


Figure A3.10: MALDI-TOF mass spectrum of host-guest complex 3.2-TM-*o*-Cb.

IR Spectra of Host–Guest Complex  $\text{Cb} \subset \text{Cage}$ Figure A3.11: IR Spectra of Host–Guest Complex  $\text{Cb} \subset \text{Cage}$ .

### Structural and Spectral Characterizations of 3.2-TM



**Figure A3.12:** ORTEP diagram at 50% ellipsoids depicting the molecular structures of **3.2-TM**.

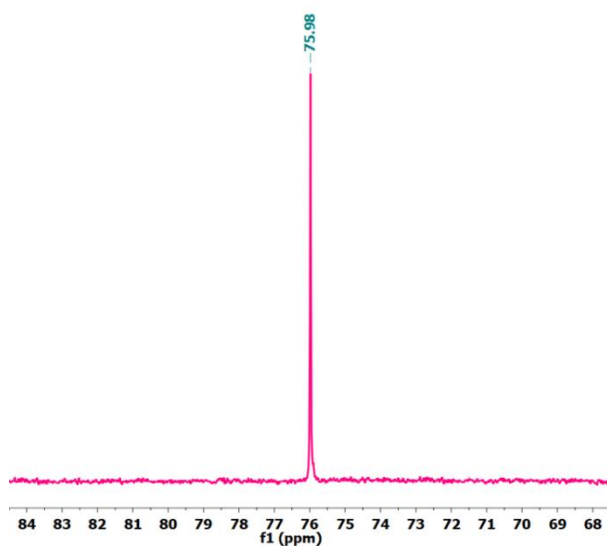


**Figure A3.13:**  $^{31}\text{P}\{^1\text{H}\}$ -NMR spectrum ( $\text{CDCl}_3$ , 298 K) of **3.2-TM**.

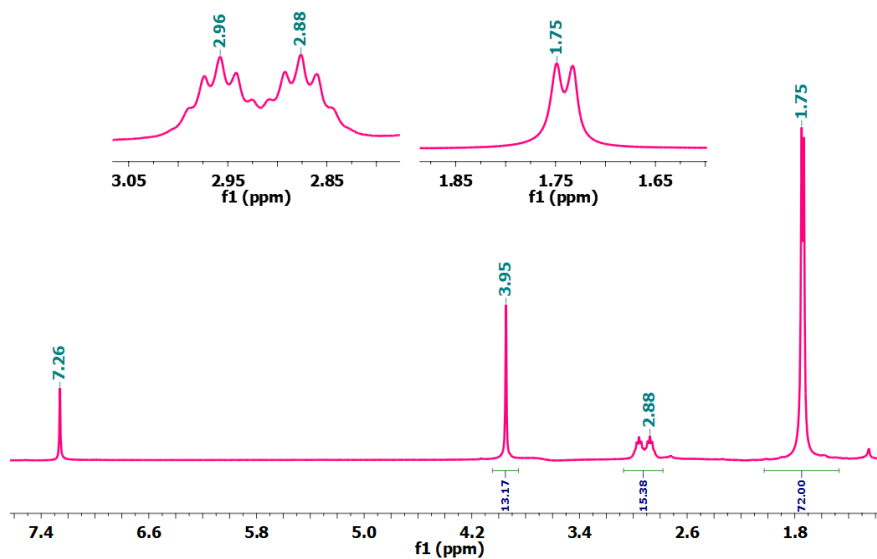


Figure A3.14:  $^1\text{H-NMR}$  spectrum ( $\text{CDCl}_3$ , 298 K) of **3.2-TM**.

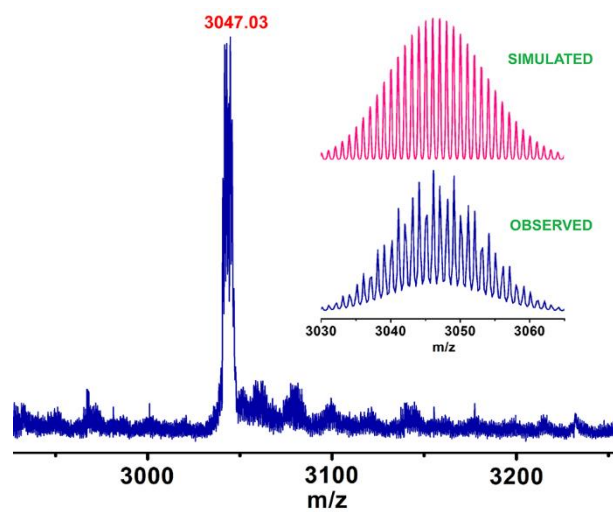
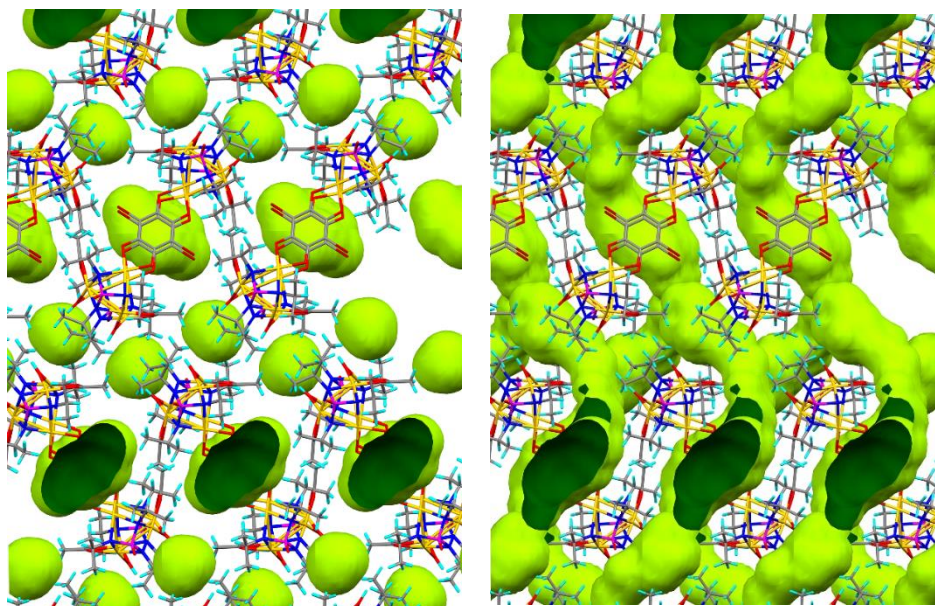
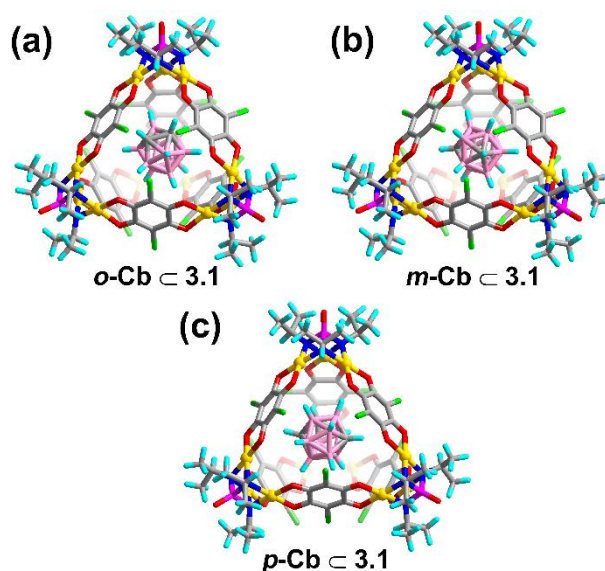


Figure A3.15: MALDI-TOF mass spectrum of **3.2-TM** and isotopic distribution of peaks.



**Figure A3.16:** Connolly surface view of the  $2 \times 2 \times 2$  packing of the structure of **3.2-TM** computed with the Mercury software showing the presence of extrinsic cavities. Left: The surface generated by using 2.1 Å probe radius to show the location of the major packing cavity that can accommodate the **Cb** guests. Right: The surface generated by using 1.4 Å probe radius indicating all possible solvent accessible voids in the structure.

### DFT Optimized Structures of Host–Guest Complexes



**Figure A3.17:** DFT optimized structures of the host–guest species (a) *o*-Cb  $\subset$  3.1, (b) *m*-Cb  $\subset$  3.1, (c) *p*-Cb  $\subset$  3.1.



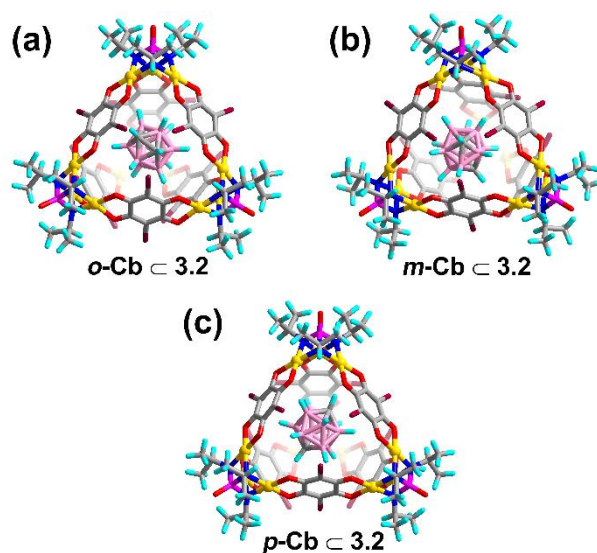


**Figure A3.18:** DFT optimized structures of the host-guest species (a)  $o\text{-Cb} \subset 3.2$ , (b)  $m\text{-Cb} \subset 3.2$ , (c)  $p\text{-Cb} \subset 3.2$ .

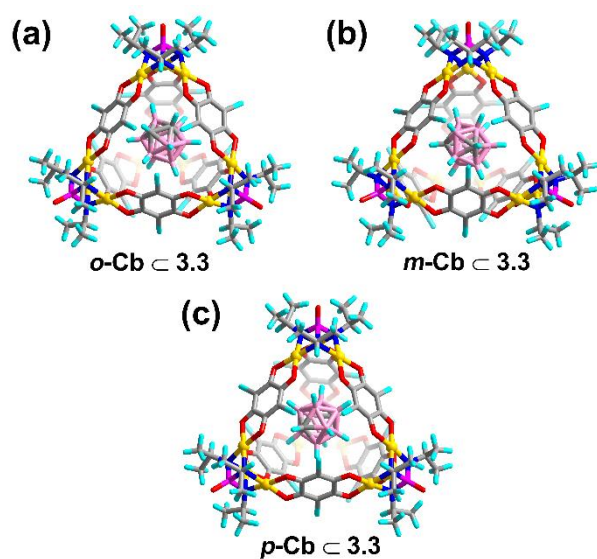


**Figure A3.19:** DFT optimized structures of the host-guest species (a)  $o\text{-Cb} \subset 3.3$ , (b)  $m\text{-Cb} \subset 3.3$ , (c)  $p\text{-Cb} \subset 3.3$ .

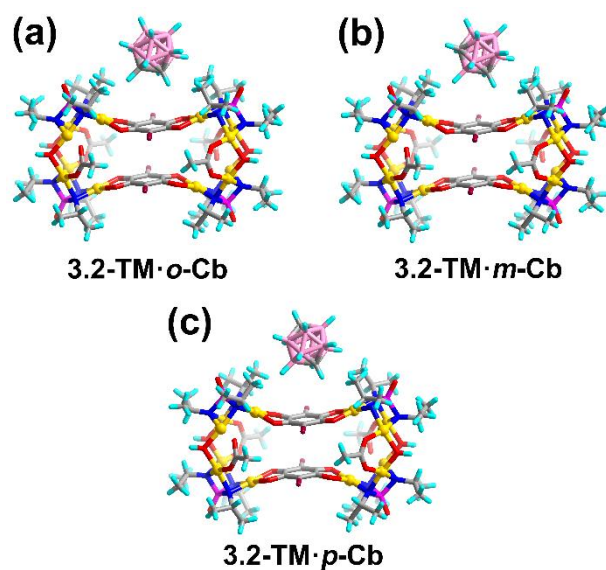


**Figure A3.20:** DFT optimized structures of the host–guest species (a) 3.2-TM·*o*-Cb, (b) 3.2-TM·*m*-Cb, (c) 3.2-TM·*p*-Cb.

### $^{31}\text{P}\{^1\text{H}\}$ -NMR Spectroscopic Characterizations of Host–Guest Complexes

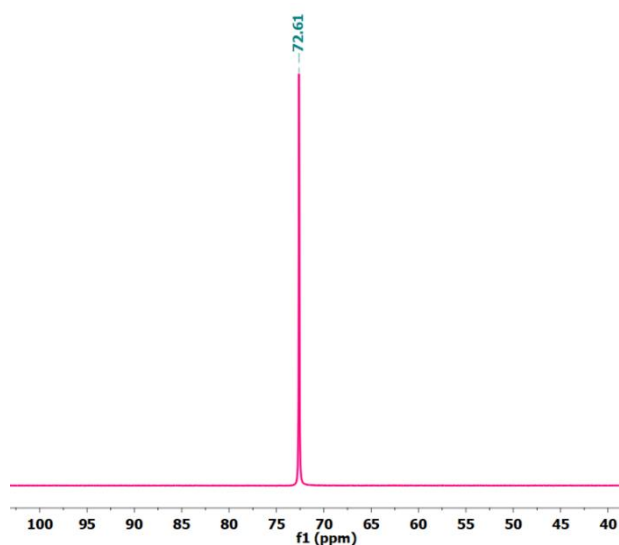


**Figure A3.21:**  $^{31}\text{P}\{^1\text{H}\}$ -NMR spectrum ( $\text{CDCl}_3$ , 298 K) of *o*-Cb  $\subset$  3.1.

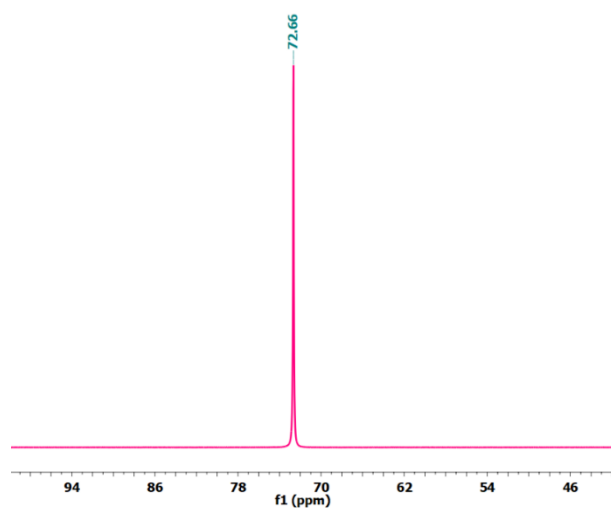


Figure A3.22:  $^{31}\text{P}\{^1\text{H}\}$ -NMR spectrum ( $\text{CDCl}_3$ , 298 K) of *m*-Cb  $\subset$  3.1.

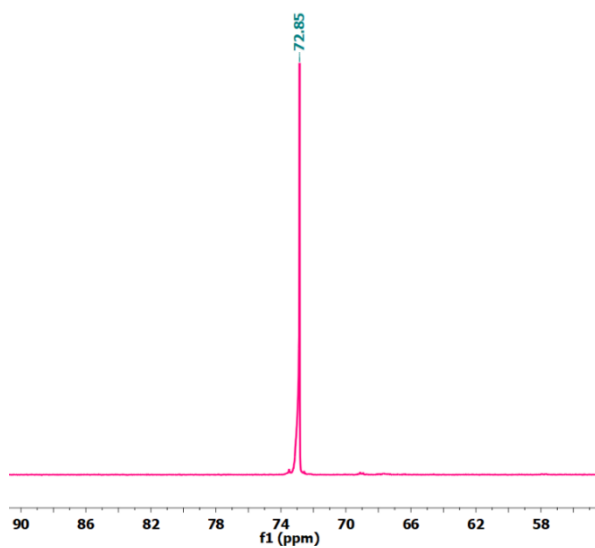
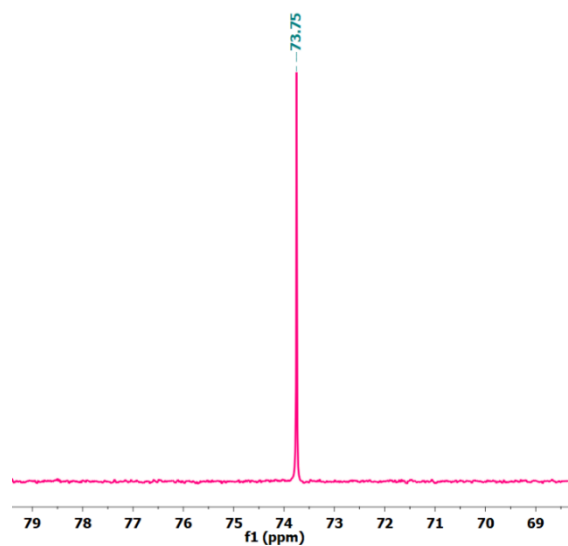
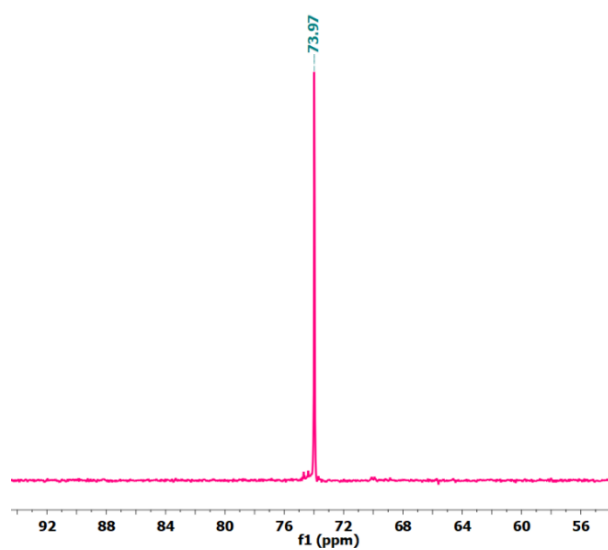


Figure A3.23:  $^{31}\text{P}\{^1\text{H}\}$ -NMR spectrum ( $\text{CDCl}_3$ , 298 K) of *p*-Cb  $\subset$  3.1.



**Figure A3.24:**  $^{31}\text{P}\{^1\text{H}\}$ -NMR spectrum ( $\text{CDCl}_3$ , 298 K) of *o*-Cb c 3.2.



**Figure A3.25:**  $^{31}\text{P}\{^1\text{H}\}$ -NMR spectrum ( $\text{CDCl}_3$ , 298 K) of *m*-Cb c 3.2.

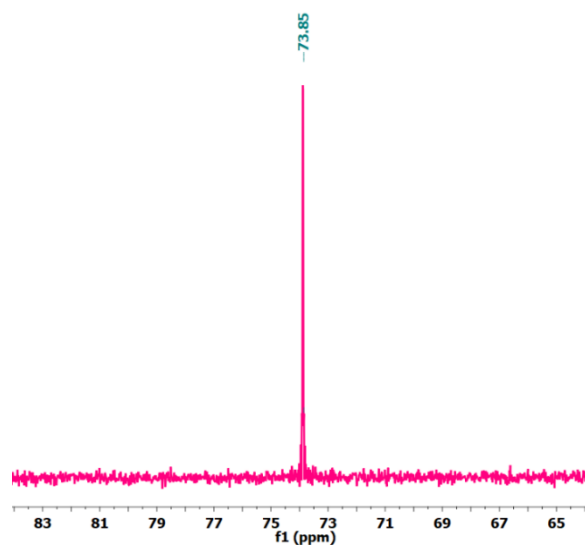


**Figure A3.26:**  $^{31}\text{P}\{^1\text{H}\}$ -NMR spectrum ( $\text{CDCl}_3$ , 298 K) of *p*-Cb c 3.2.

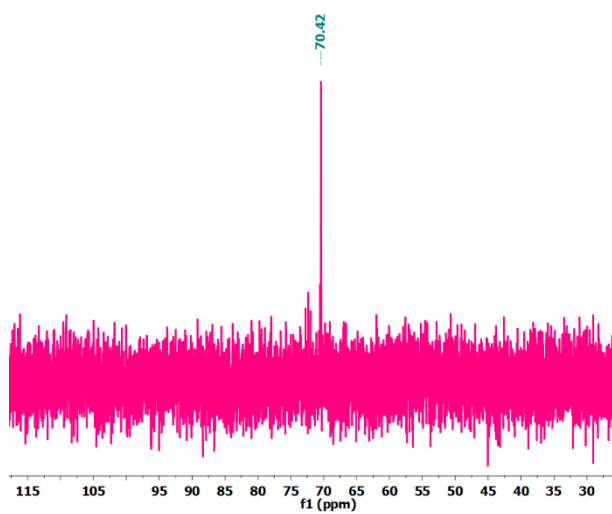


**Figure A3.27:**  $^{31}\text{P}\{^1\text{H}\}$ -NMR spectrum ( $\text{CDCl}_3$ , 298 K) of *o*-Cb c 3.3.

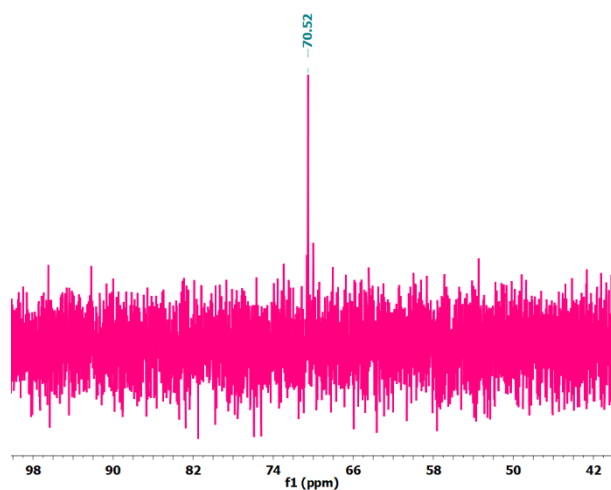


Figure A3.28:  $^{31}\text{P}\{^1\text{H}\}$ -NMR spectrum ( $\text{CDCl}_3$ , 298 K) of *m*-Cb c 3.3.

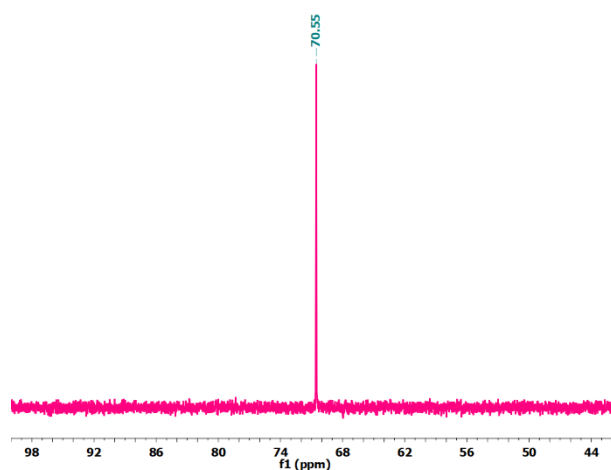


Figure A3.29:  $^{31}\text{P}\{^1\text{H}\}$ -NMR spectrum ( $\text{CDCl}_3$ , 298 K) of *p*-Cb c 3.3.

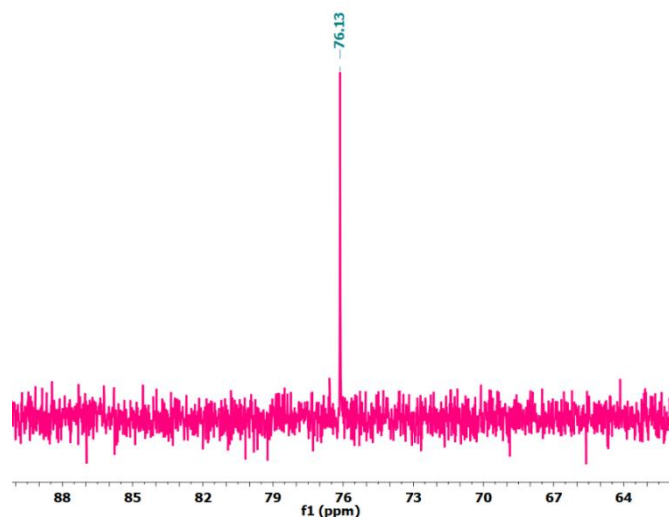


Figure A3.30:  $^{31}\text{P}\{^1\text{H}\}$ -NMR spectrum ( $\text{CDCl}_3$ , 298 K) of 3.2-TM·*o*-Cb.

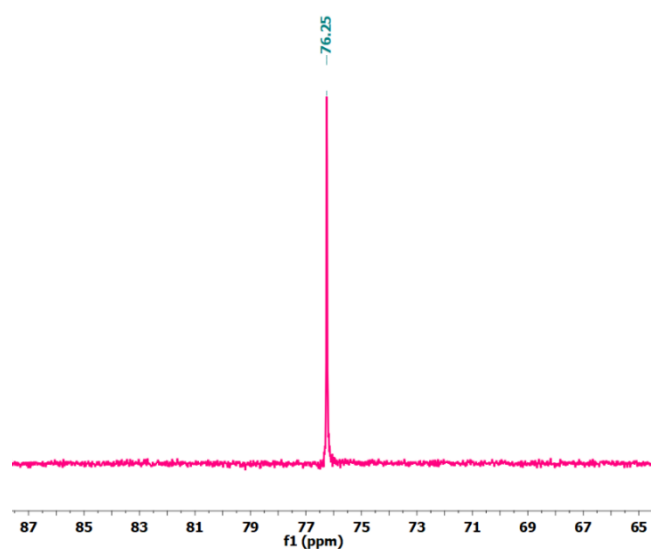


Figure A3.31:  $^{31}\text{P}\{^1\text{H}\}$ -NMR spectrum ( $\text{CDCl}_3$ , 298 K) of 3.2-TM·*m*-Cb.

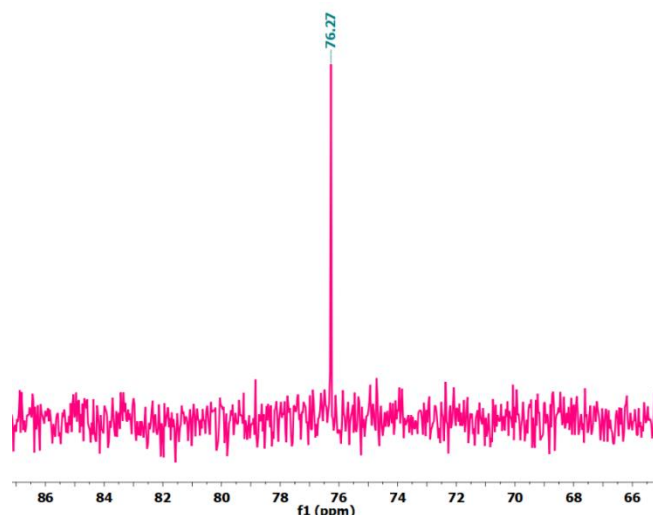


Figure A3.32:  $^{31}\text{P}\{^1\text{H}\}$ -NMR spectrum ( $\text{CDCl}_3$ , 298 K) of **3.2-TM**·*p*-**Cb**.

### Conversion from 3.2-TM to 3.2 followed by $^{31}\text{P}$ -NMR Spectroscopy

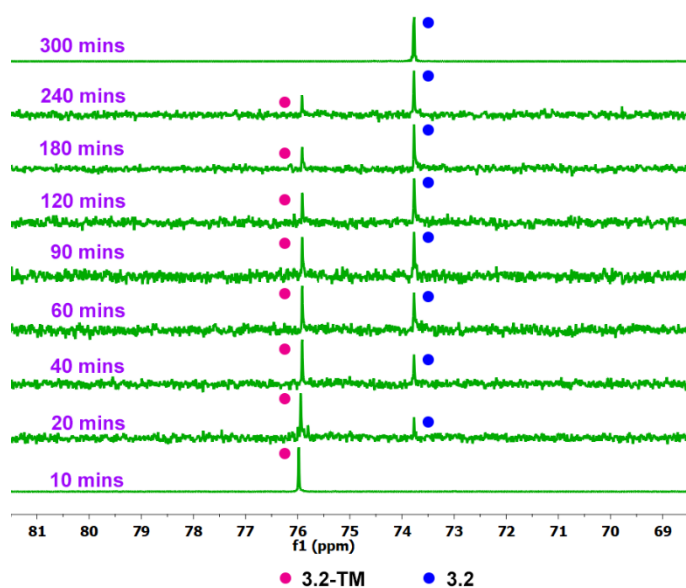
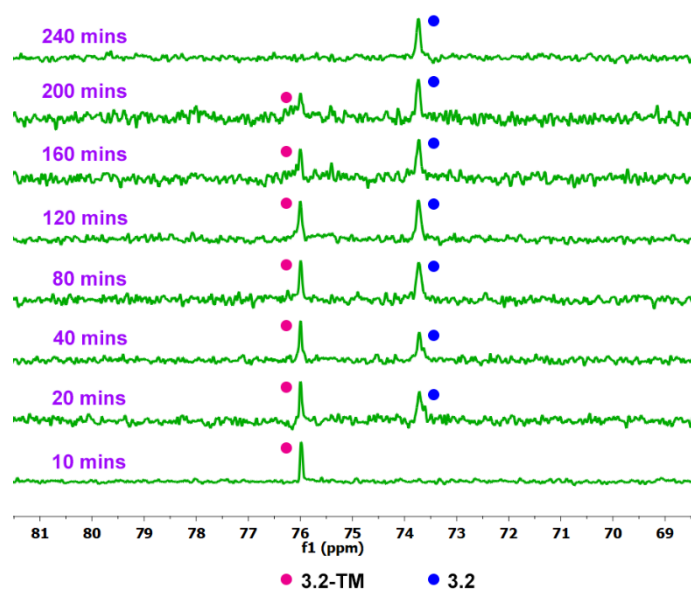


Figure A3.33:  $^{31}\text{P}\{^1\text{H}\}$ -NMR spectra  $\{(\text{CD}_3)_2\text{SO}\}$  showing the conversion of **3.2-TM** to **3.2** in the absence of guest *o*-**Cb**.





**Figure A3.34:**  $^{31}\text{P}\{^1\text{H}\}$ -NMR spectra  $\{(\text{CD}_3)_2\text{SO}\}$  showing the conversion of **3.2-TM** to **3.2** in the presence of guest ***o*-Cb** showing slightly broadened peaks.

## $^1\text{H}$ and $^{11}\text{B}\{^1\text{H}\}$ -NMR Spectroscopic Characterizations of Host–Guest Complexes

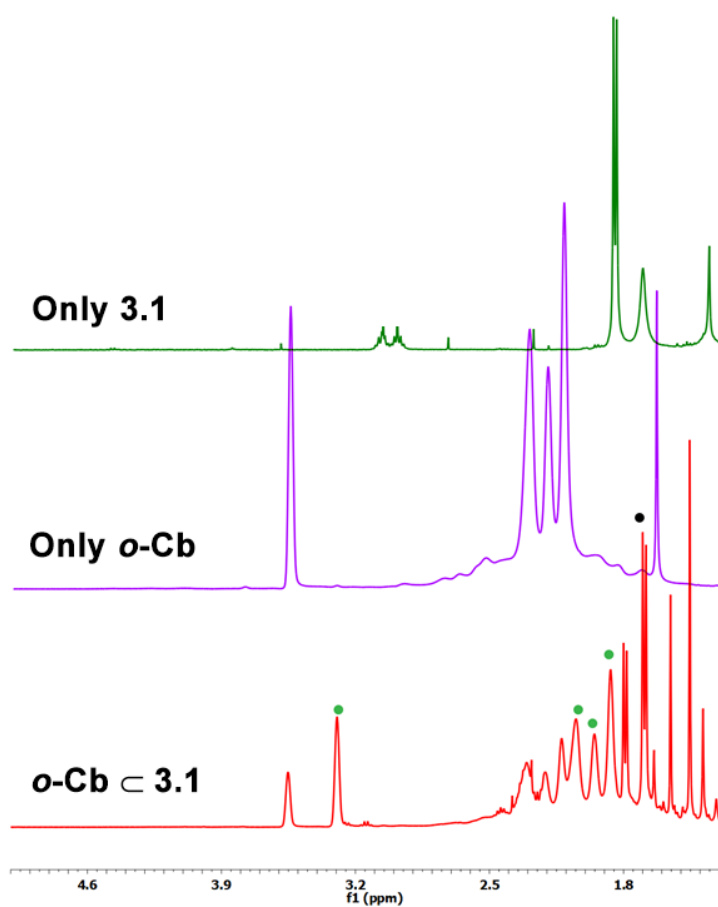


**Figure A3.35:** Partial  $^1\text{H}$ -NMR profile of  $o\text{-Cb} \subset 3.1$  in comparison with pure  $o\text{-Cb}$  and pure cage **3.1**. The black and green dots represent the host and guest protons in their respective bound states

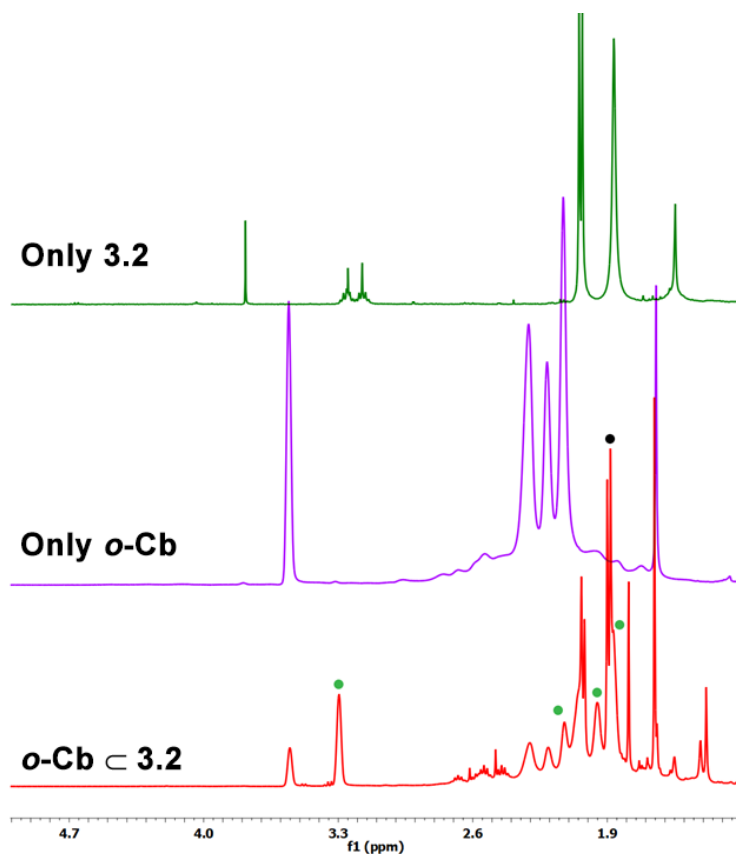


**Figure A3.36:** Partial <sup>1</sup>H-NMR profile of *o*-Cb c 3.2 in comparison with pure *o*-Cb and pure cage 3.2. The black and green dots represent the host and guest protons in their respective bound states.

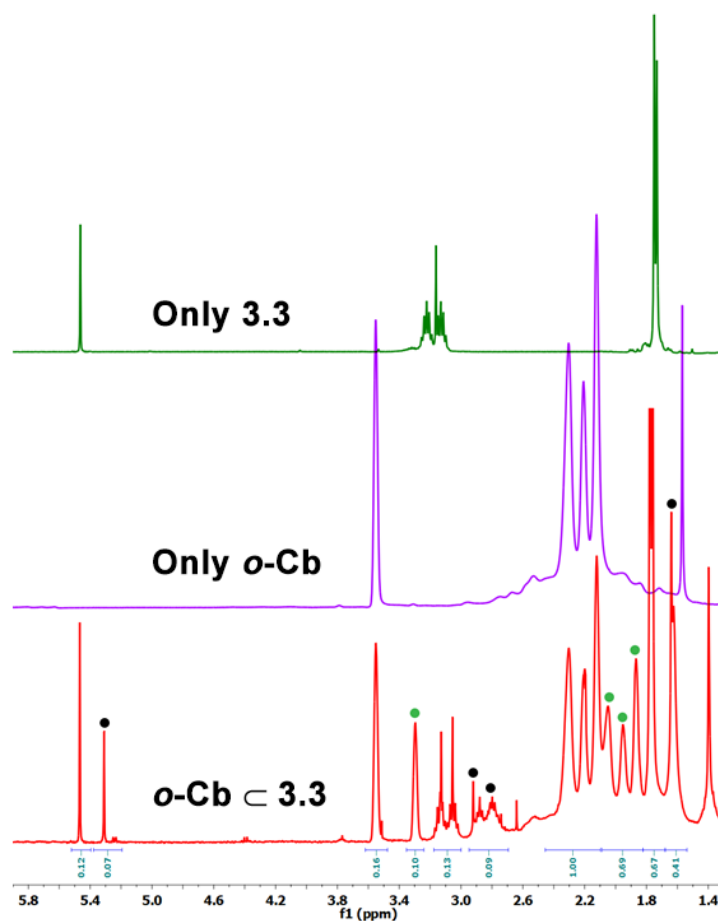


**Figure A3.37:** Partial <sup>1</sup>H-NMR profile of *o*-Cb ⊂ 3.3 in comparison with pure *o*-Cb and pure cage 3.3. The black and green dots represent the host and guest protons in their respective bound states

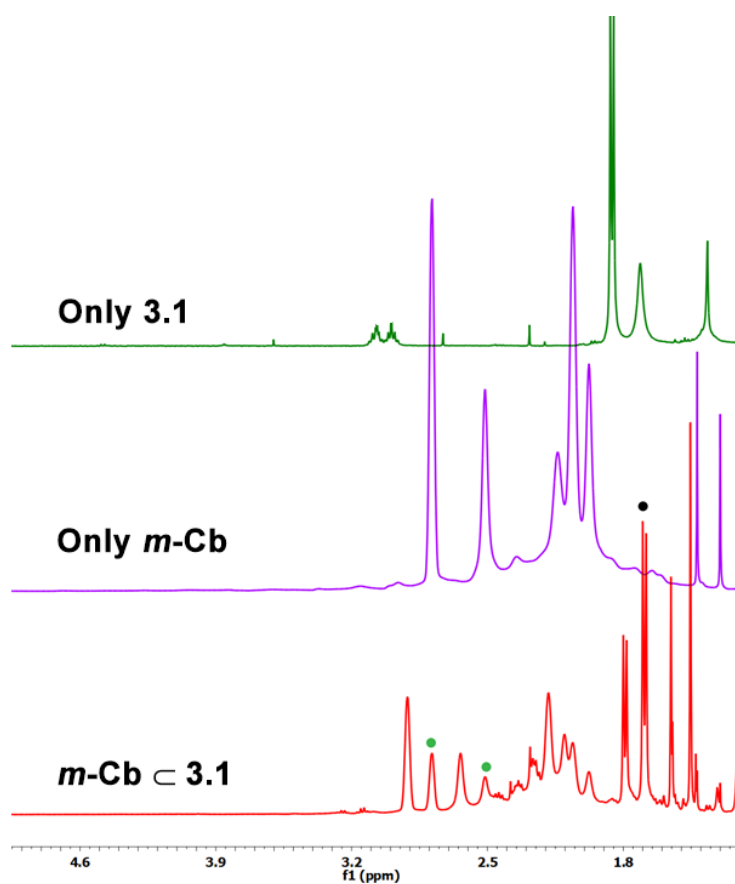


**Figure A3.38:** Partial <sup>1</sup>H-NMR profile of *m-Cb* ⊂ **3.1** in comparison with pure *m-Cb* and pure cage **3.1**. The black and green dots represent the host and guest protons in their respective bound states

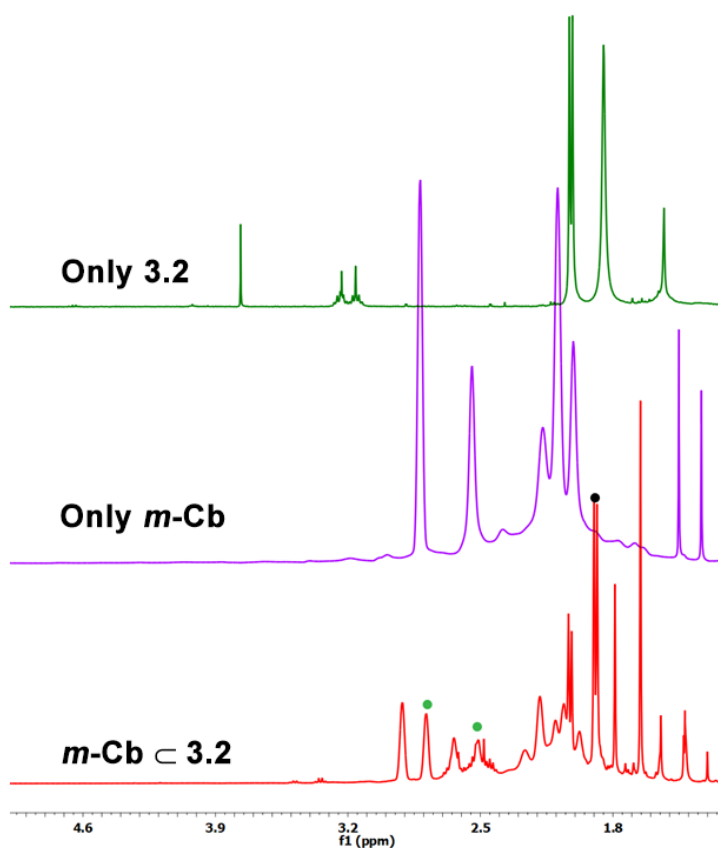


**Figure A3.39:** Partial <sup>1</sup>H-NMR profile of *m*-Cb ⊂ 3.2 in comparison with pure *m*-Cb and pure cage 3.2. The black and green dots represent the host and guest protons in their respective bound states

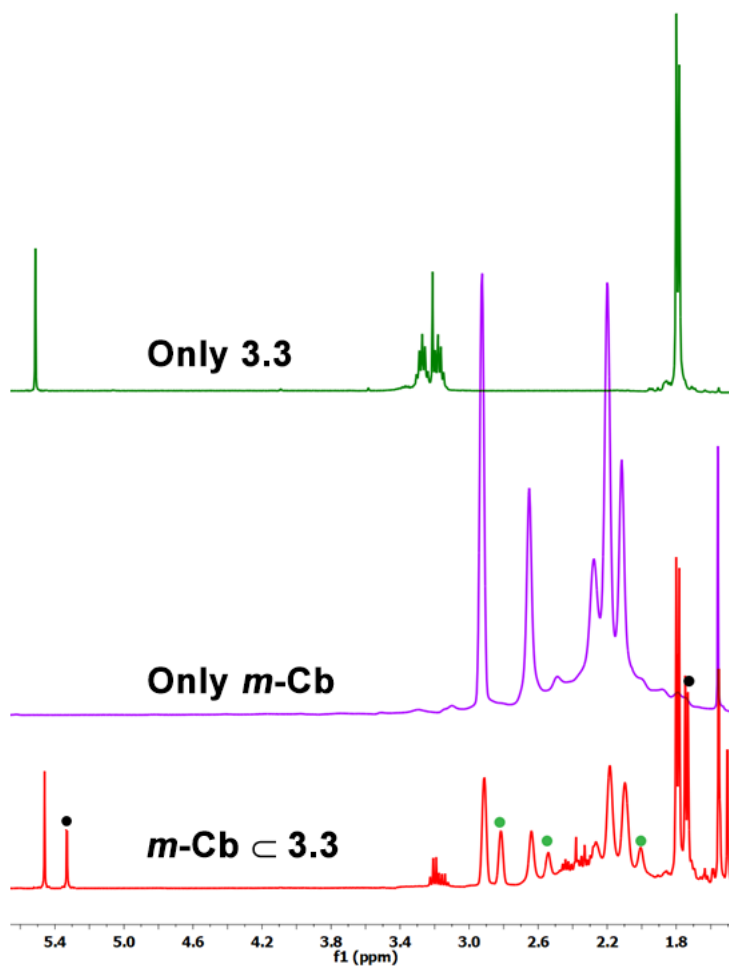


**Figure A3.40:** Partial <sup>1</sup>H-NMR profile of *m-Cb* ⊂ **3.3** in comparison with pure *m-Cb* and pure cage **3.3**. The black and green dots represent the host and guest protons in their respective bound states

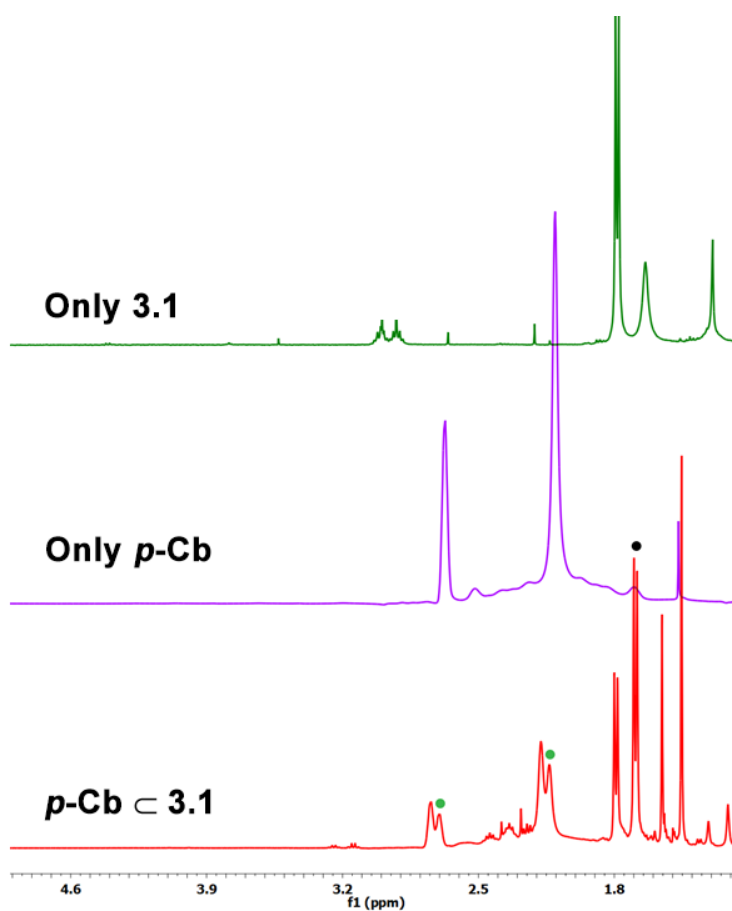


**Figure A3.41:** Partial <sup>1</sup>H-NMR profile of *p*-Cb ⊂ 3.1 in comparison with pure *p*-Cb and pure cage 3.1. The black and green dots represent the host and guest protons in their respective bound states



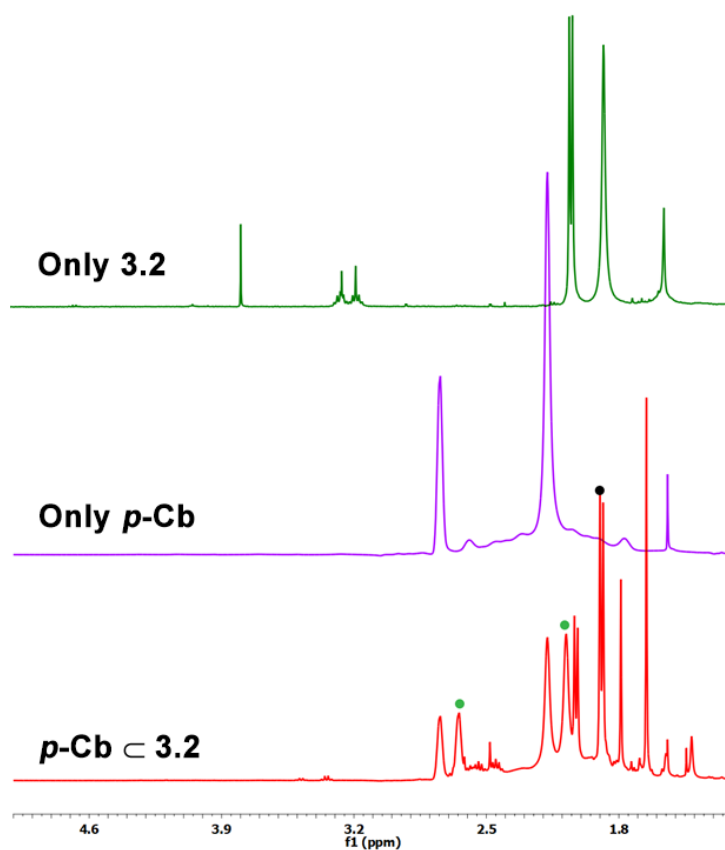


**Figure A3.42:** Partial <sup>1</sup>H-NMR profile of *p*-Cb ⊂ 3.2 in comparison with pure *p*-Cb and pure cage 3.2. The black and green dots represent the host and guest protons in their respective bound states

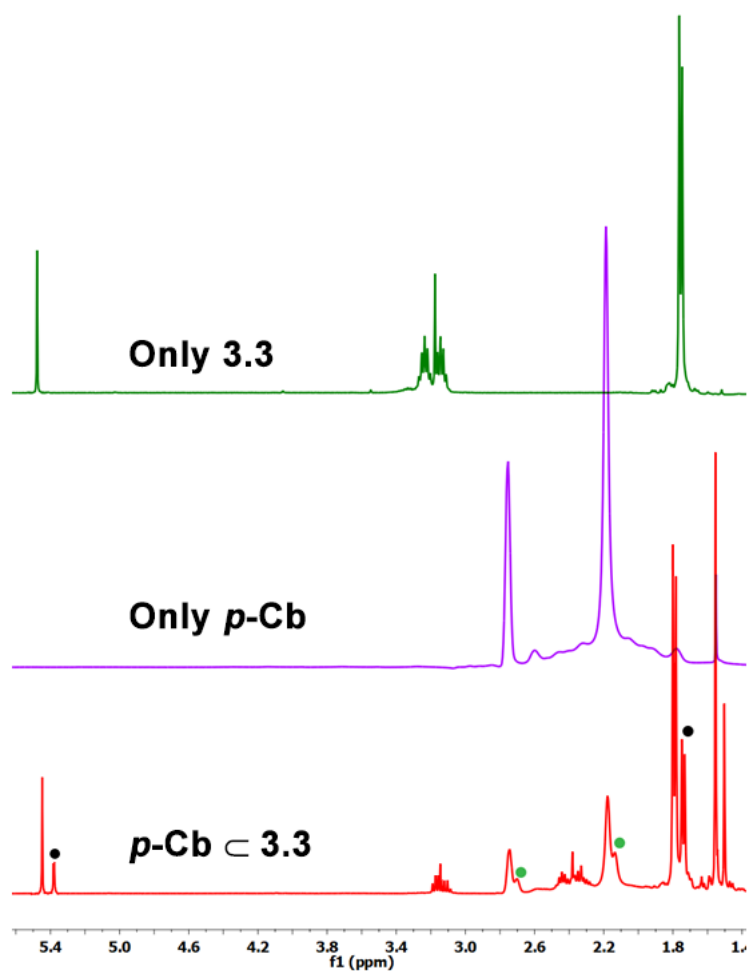


**Figure A3.43:** Partial  $^1\text{H-NMR}$  profile of  $p\text{-Cb} \subset 3.3$  in comparison with pure  $p\text{-Cb}$  and pure cage 3.3. The black and green dots represent the host and guest protons in their respective bound states

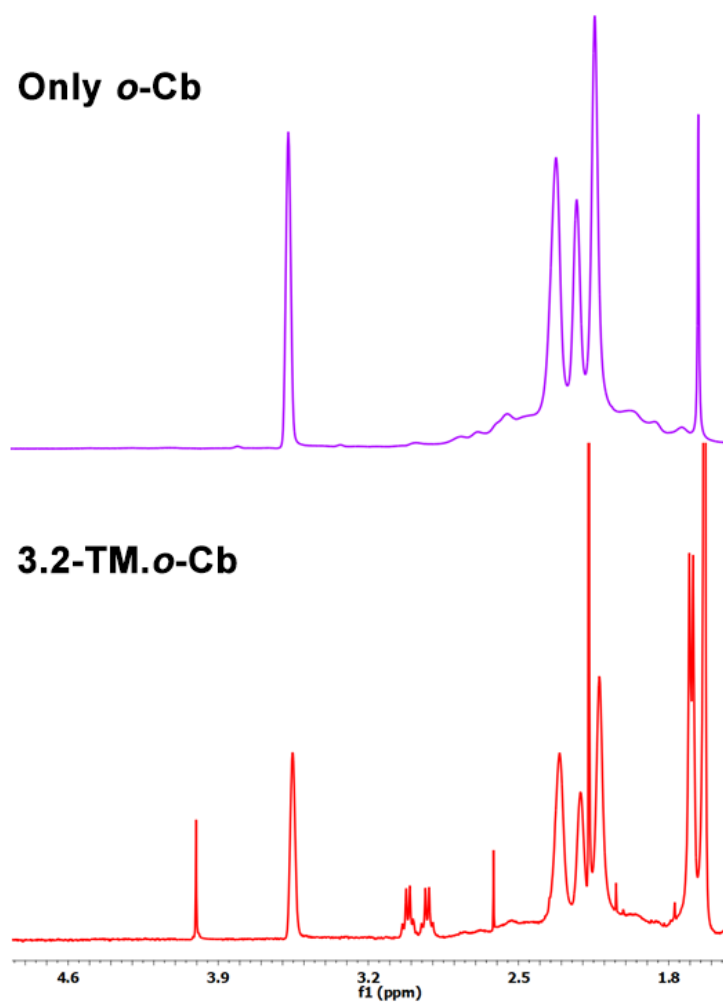


**Figure A3.44:** Partial <sup>1</sup>H-NMR profile of **3.2-TM.o-Cb** in comparison with pure **o-Cb** and pure **3.2-TM**.

Time-dependent NMR spectral conversion of 3.2-TM to 3.2 in the presence of guest Cb

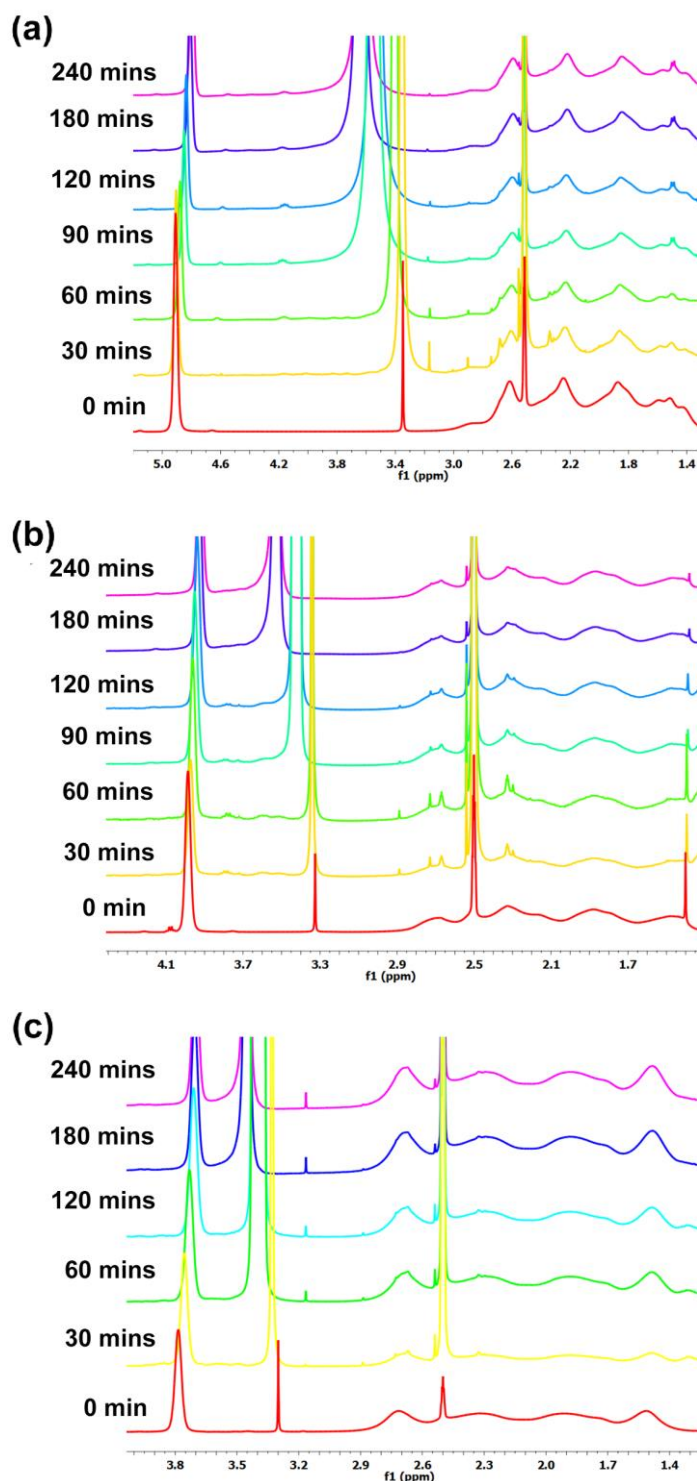


**Figure A3.45:** Time-dependent NMR spectral changes during the conversion of 3.2-TM to 3.2 in the presence of (a) *o*-Cb, (b) *m*-Cb and (c) *p*-Cb.

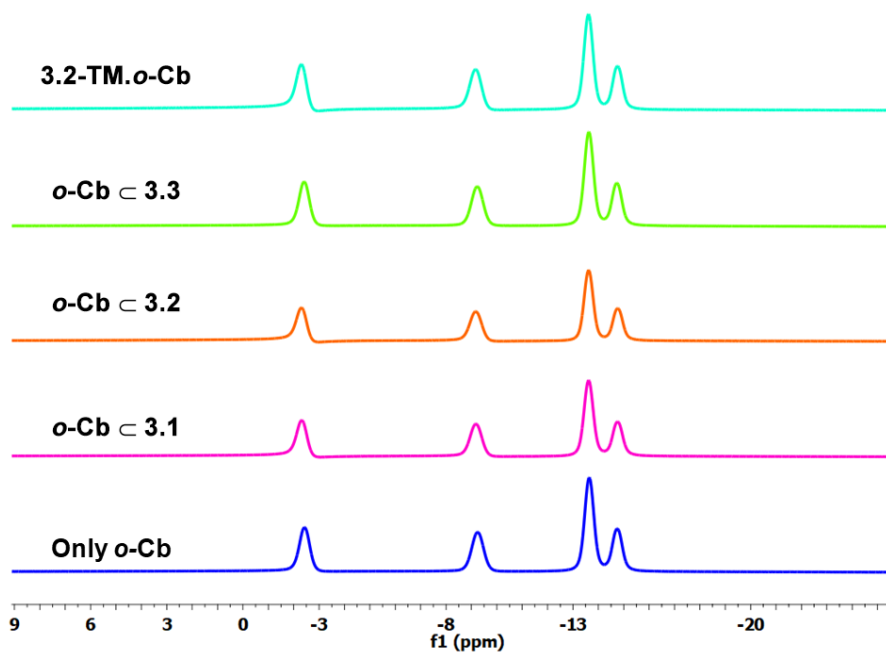
$^{11}\text{B}\{^1\text{H}\}$ -NMR Spectroscopic Characterizations of Host–Guest Complexes

Figure A3.46:  $^{11}\text{B}\{^1\text{H}\}$ -NMR spectrum ( $\text{CDCl}_3$ , 298 K) of *o*-Cb with all hosts.

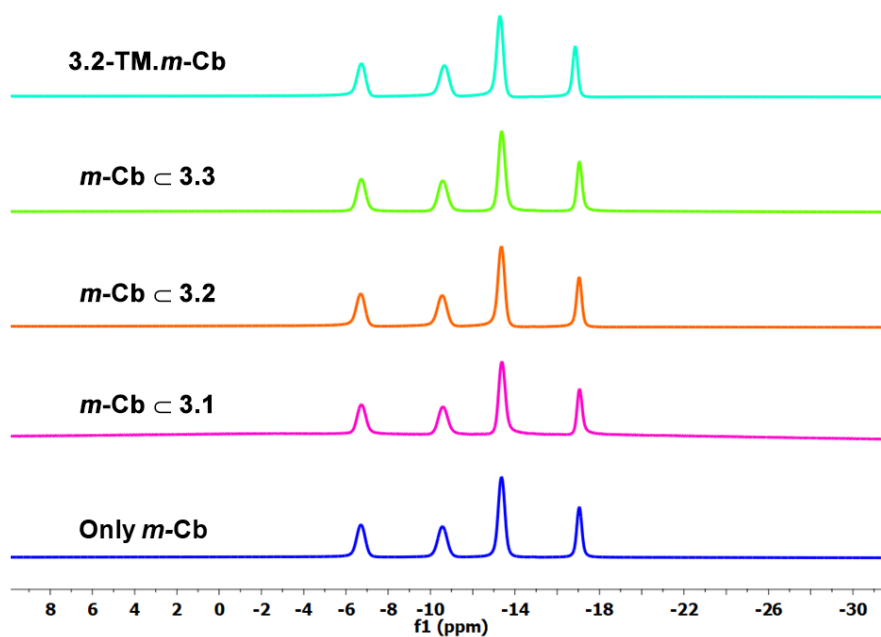


Figure A3.47:  $^{11}\text{B}\{^1\text{H}\}$ -NMR spectrum ( $\text{CDCl}_3$ , 298 K) of *m*-Cb with all hosts.

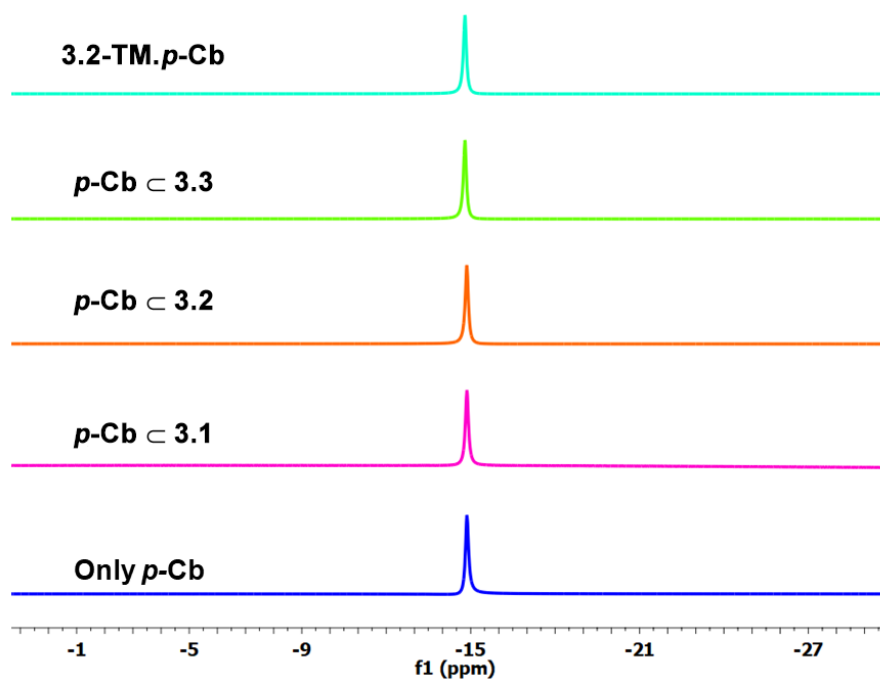


Figure A3.48:  $^{11}\text{B}\{^1\text{H}\}$ -NMR spectrum ( $\text{CDCl}_3$ , 298 K) of  $p\text{-Cb}$  with all hosts.

### $^1\text{H}$ - $^1\text{H}$ -NOESY/ROESY-NMR Spectral Characterizations of $\text{Cb} \subset 3.3$ Host-Guest Complexes

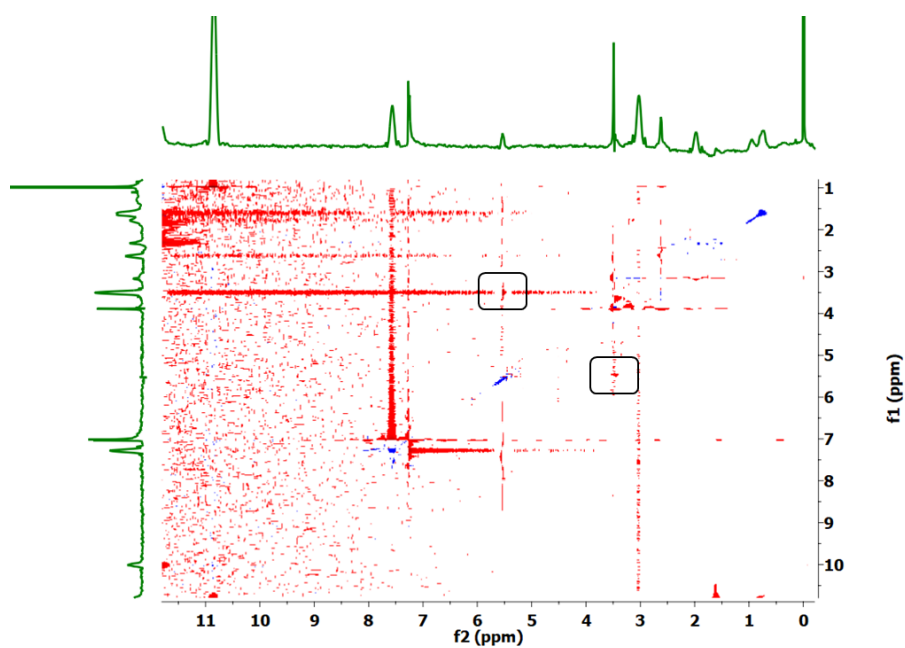


Figure A3.49:  $^1\text{H}$ - $^1\text{H}$ -NOESY-NMR spectra of  $o\text{-Cb} \subset 3.3$  complex.

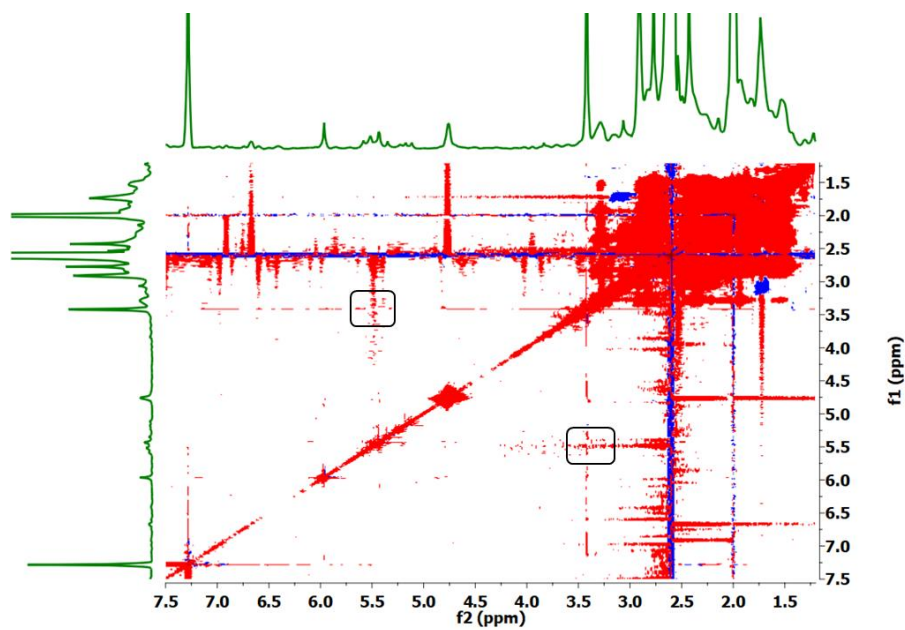


Figure A3.50:  $^1\text{H}$ - $^1\text{H}$ -ROESY-NMR spectra of *m*-Cb c 3.3 complex.

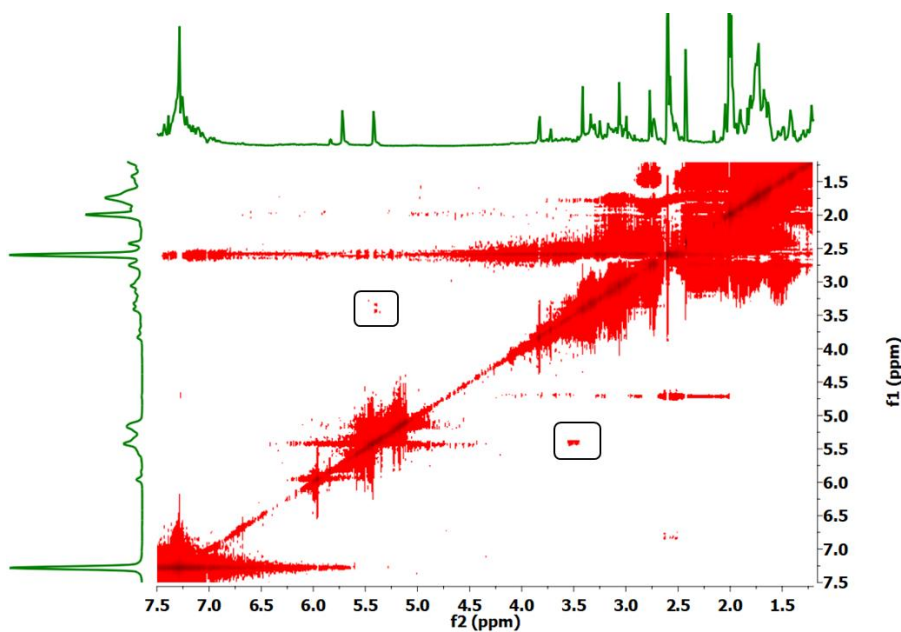
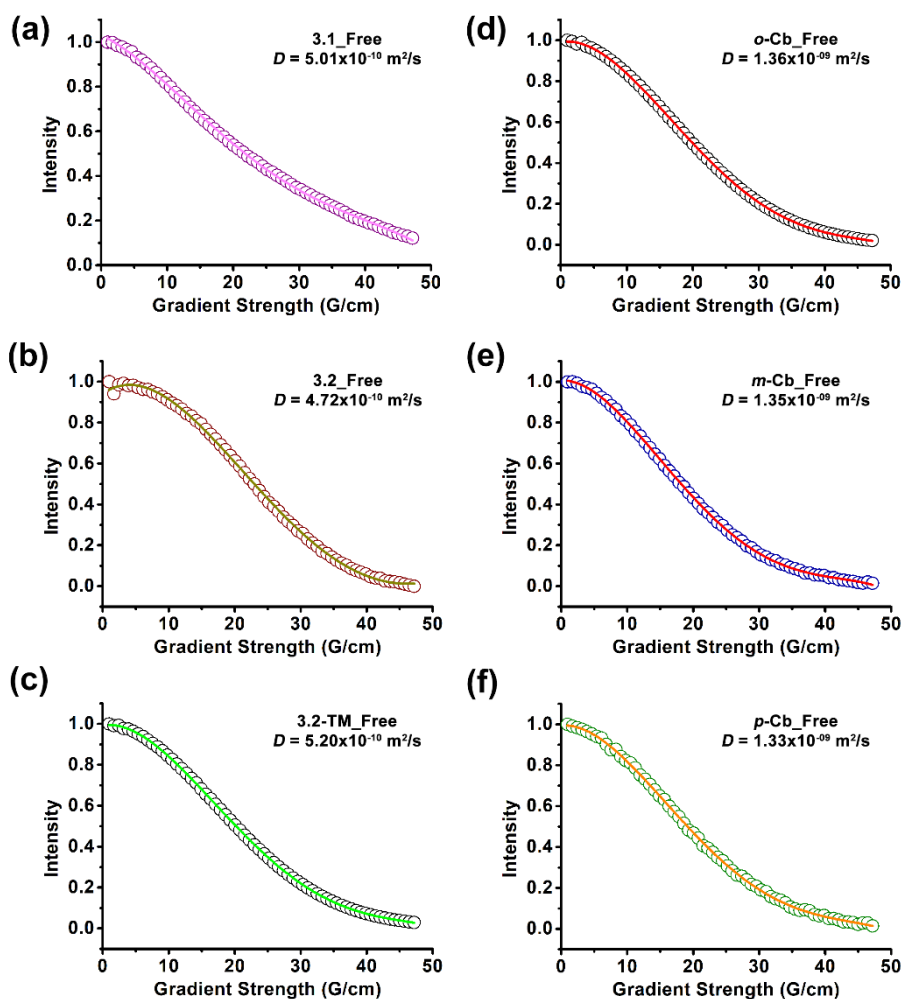


Figure A3.51:  $^1\text{H}$ - $^1\text{H}$ -ROESY-NMR spectra of *p*-Cb c 3.3 complex.

## 2D-DOSY-NMR Characterizations of Host–Guest Complexes



**Figure A3.52.** Integral decay profile of all free host protons (left), and free guest hydrogen atoms (right) plotted as a function of gradient strength. The circles represent experimental data and the lines show the best fit using equation 1. The name of the molecules and the diffusion coefficients obtained are shown in the corresponding insets. The reported diffusion coefficients were obtained using the T1/T2 relaxation module in TopSpin 4.1 software.



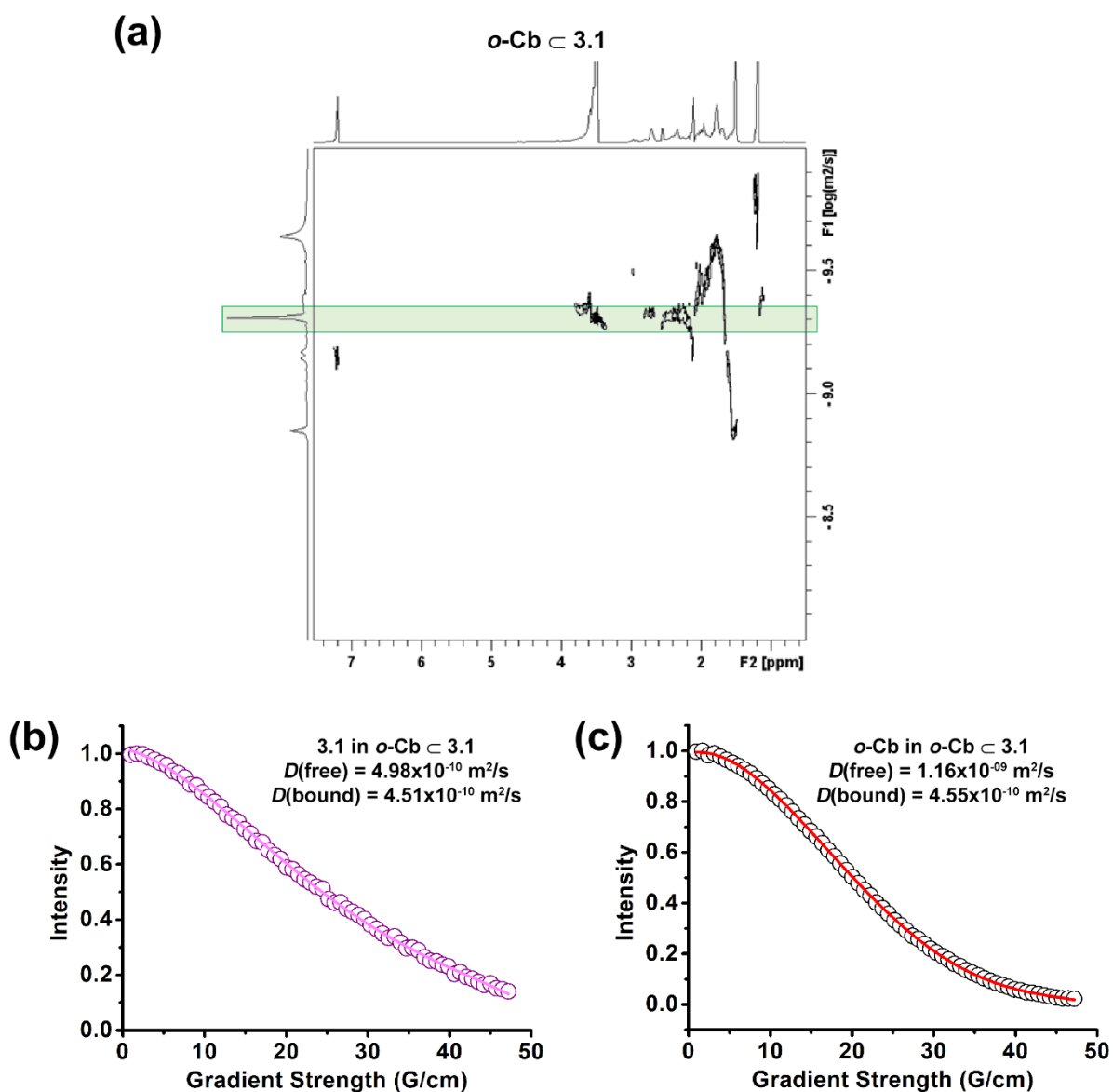


**Figure A3.53:** (a) 2D-DOSY-NMR spectra of  $o\text{-Cb} \subset 3.1$  complex. The green highlighted region corresponds to the diffusion of  $o\text{-Cb} \subset 3.1$  in the bound state. Due to the very broad nature of the peaks, the reported  $D$  values were extracted by using the T1/T2 relaxation module in TopSpin 4.1 software as follows: integral decay profile of (b) the i-Pr CH<sub>3</sub> of host **3.1**, and (c) guest  $o\text{-Cb}$  C-H atoms in the host-guest system plotted as a function of gradient strength. The circles represent experimental data and the lines show the best fit using equation 2. The name of the molecules and the diffusion coefficients obtained for free and bound moieties are shown in the corresponding insets.

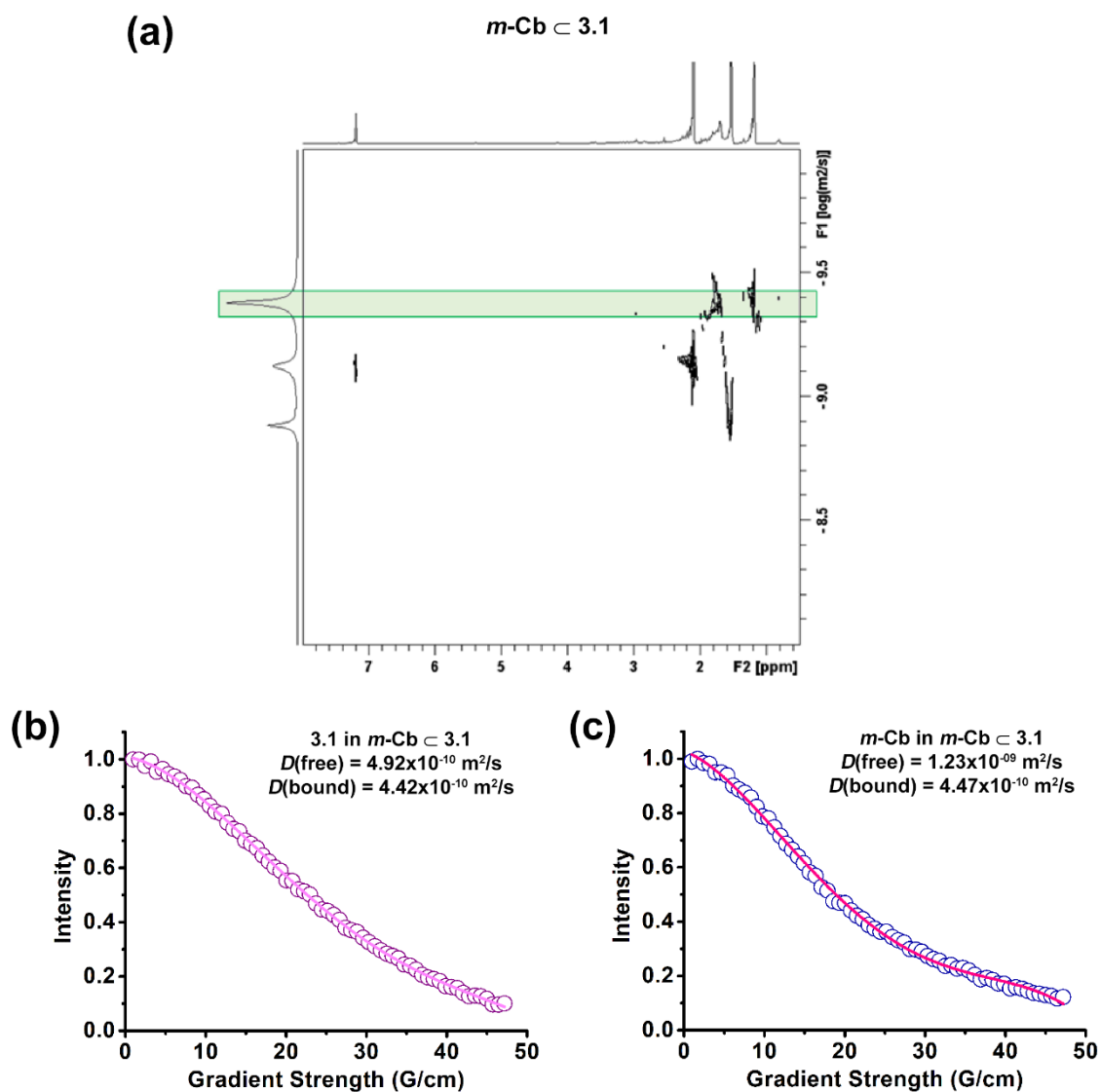


**Figure A3.54:** (a) 2D-DOSY-NMR spectra of  $m\text{-Cb} \subset 3.1$  complex. The green highlighted region corresponds to the diffusion of  $m\text{-Cb} \subset 3.1$  in the bound state. Due to the very broad nature of the peaks, the reported  $D$  values were extracted by using the T1/T2 relaxation module in TopSpin 4.1 software as follows: integral decay profile of (b) the  $i\text{-Pr } \text{CH}_3$  of host **3.1**, and (c) guest  $m\text{-Cb}$  C-H atoms in the host-guest system plotted as a function of gradient strength. The circles represent experimental data and the lines show the best fit using equation 2. The name of the molecules and the diffusion coefficients obtained for free and bound moieties are shown in the corresponding insets.

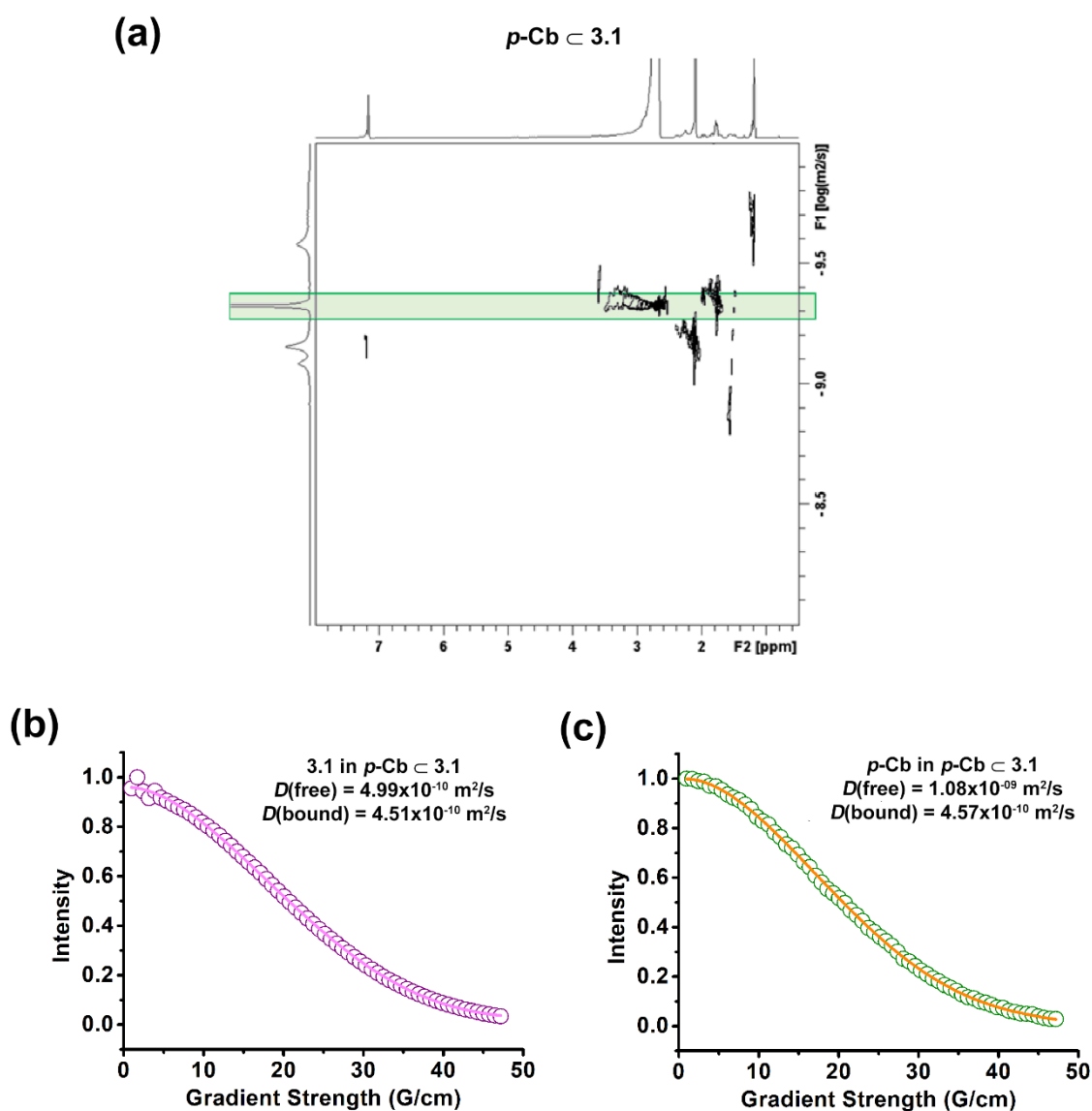


**Figure A3.55:** (a) 2D-DOSY-NMR spectra of  $p\text{-Cb} \subset 3.1$  complex. The green highlighted region corresponds to the diffusion of  $p\text{-Cb} \subset 3.1$  in the bound state. Due to the very broad nature of the peaks, the reported  $D$  values were extracted by using the T1/T2 relaxation module in TopSpin 4.1 software as follows: integral decay profile of (b) the  $i\text{-Pr } \text{CH}_3$  of host **3.1**, and (c) guest  $p\text{-Cb}$  C-H atoms in the host-guest system plotted as a function of gradient strength. The circles represent experimental data and the lines show the best fit using equation 2. The name of the molecules and the diffusion coefficients obtained for free and bound moieties are shown in the corresponding insets.

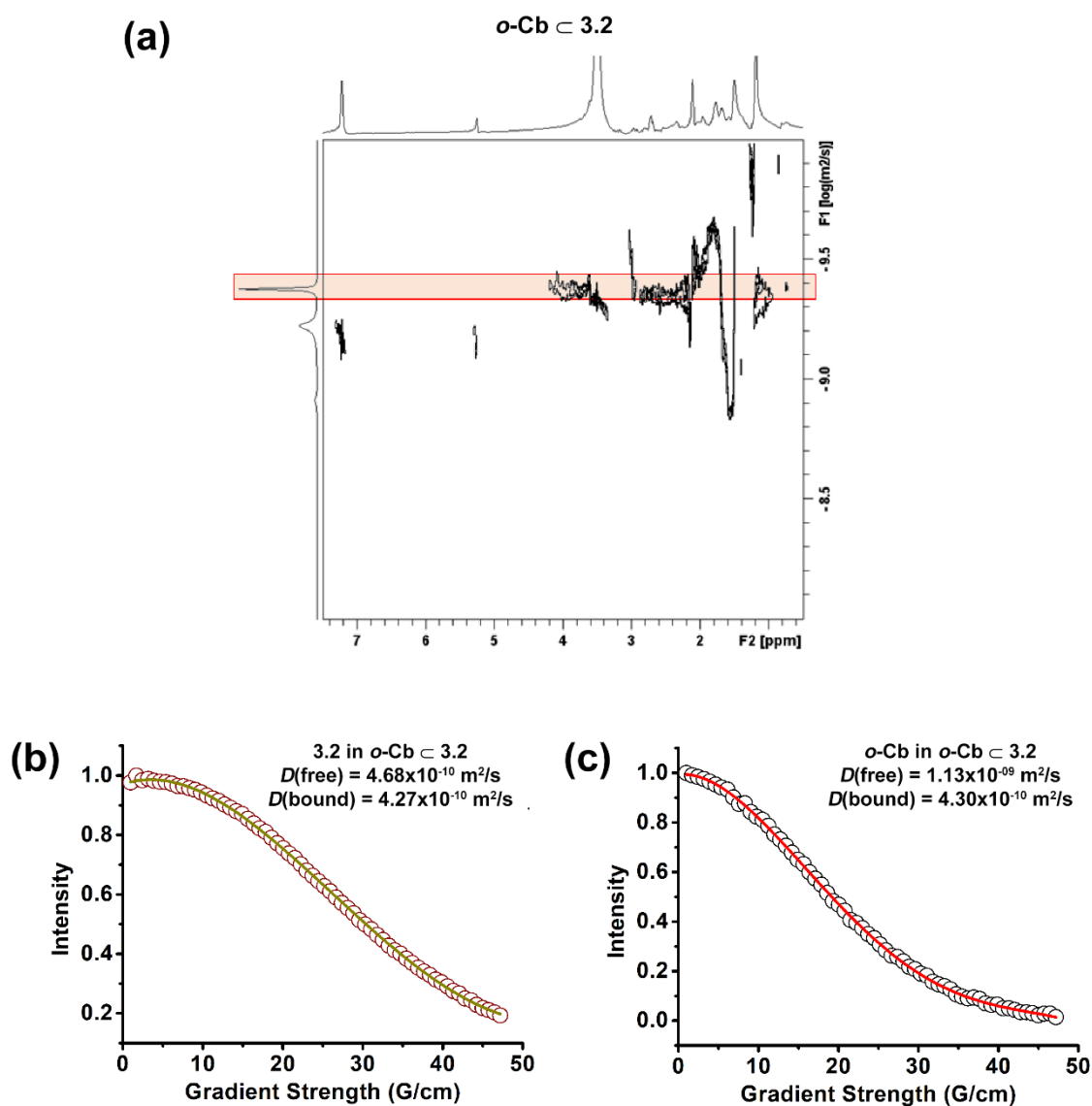


**Figure A3.56:** (a) 2D-DOSY-NMR spectra of  $o\text{-Cb} \subset 3.2$  complex. The red highlighted region corresponds to the diffusion of  $o\text{-Cb} \subset 3.2$  in the bound state. Due to the very broad nature of the peaks, the reported  $D$  values were extracted by using the T1/T2 relaxation module in TopSpin 4.1 software as follows: integral decay profile of (b) the  $i\text{-Pr CH}_3$  of host **3.2**, and (c) guest  $o\text{-Cb}$  C-H atoms in the host-guest system plotted as a function of gradient strength. The circles represent experimental data and the lines show the best fit using equation 2. The name of the molecules and the diffusion coefficients obtained for free and bound moieties are shown in the corresponding insets.

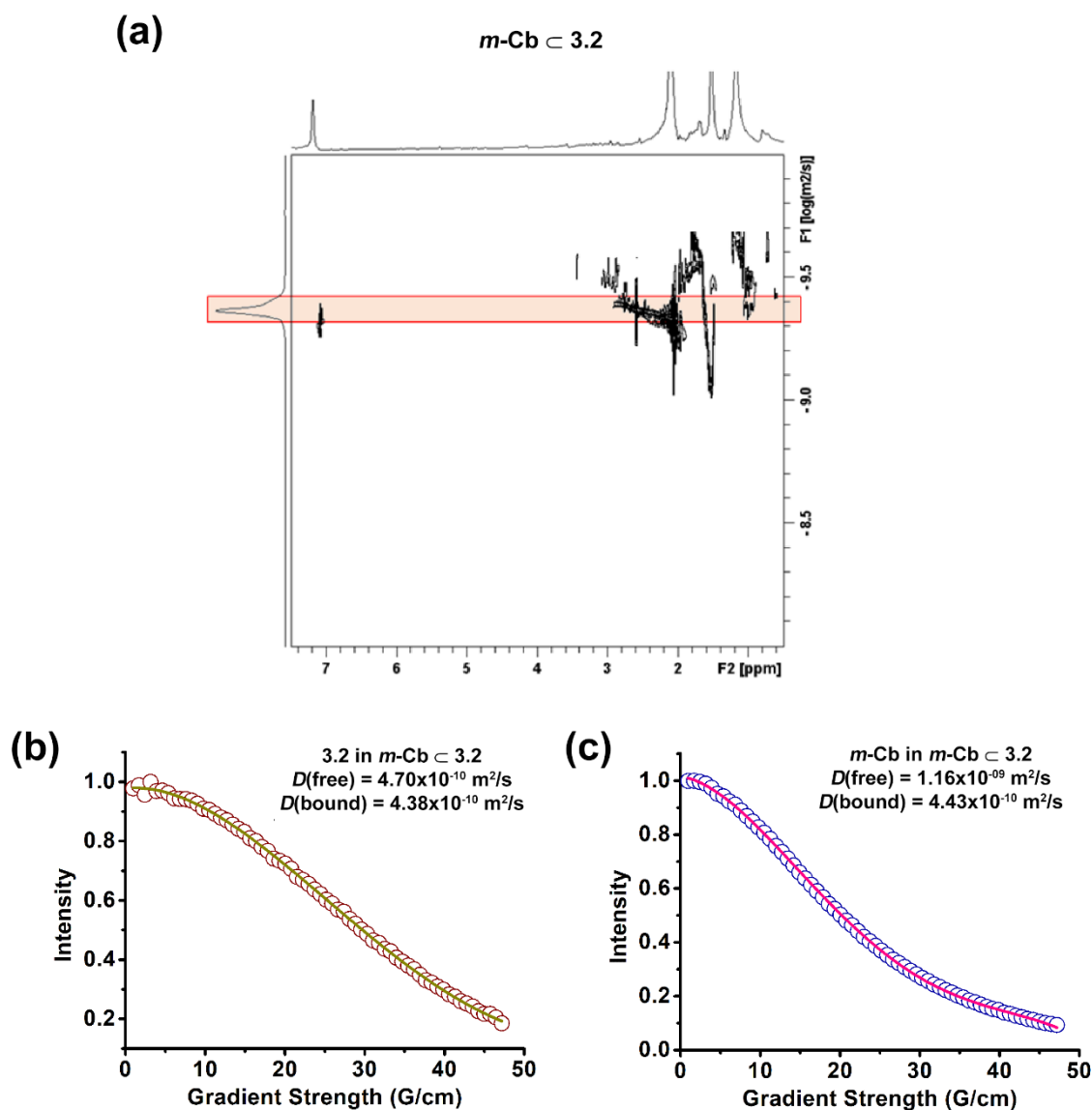


**Figure A3.57:** (a) 2D-DOSY-NMR spectra of  $m\text{-Cb} \subset 3.2$  complex. The red highlighted region corresponds to the diffusion of  $m\text{-Cb} \subset 3.2$  in the bound state. Due to the very broad nature of the peaks, the reported  $D$  values were extracted by using the T1/T2 relaxation module in TopSpin 4.1 software as follows: integral decay profile of (b) the  $i\text{-Pr } \text{CH}_3$  of host **3.2**, and (c) guest  $m\text{-Cb}$  C-H atoms in the host-guest system plotted as a function of gradient strength. The circles represent experimental data and the lines show the best fit using equation 2. The name of the molecules and the diffusion coefficients obtained for free and bound moieties are shown in the corresponding insets.

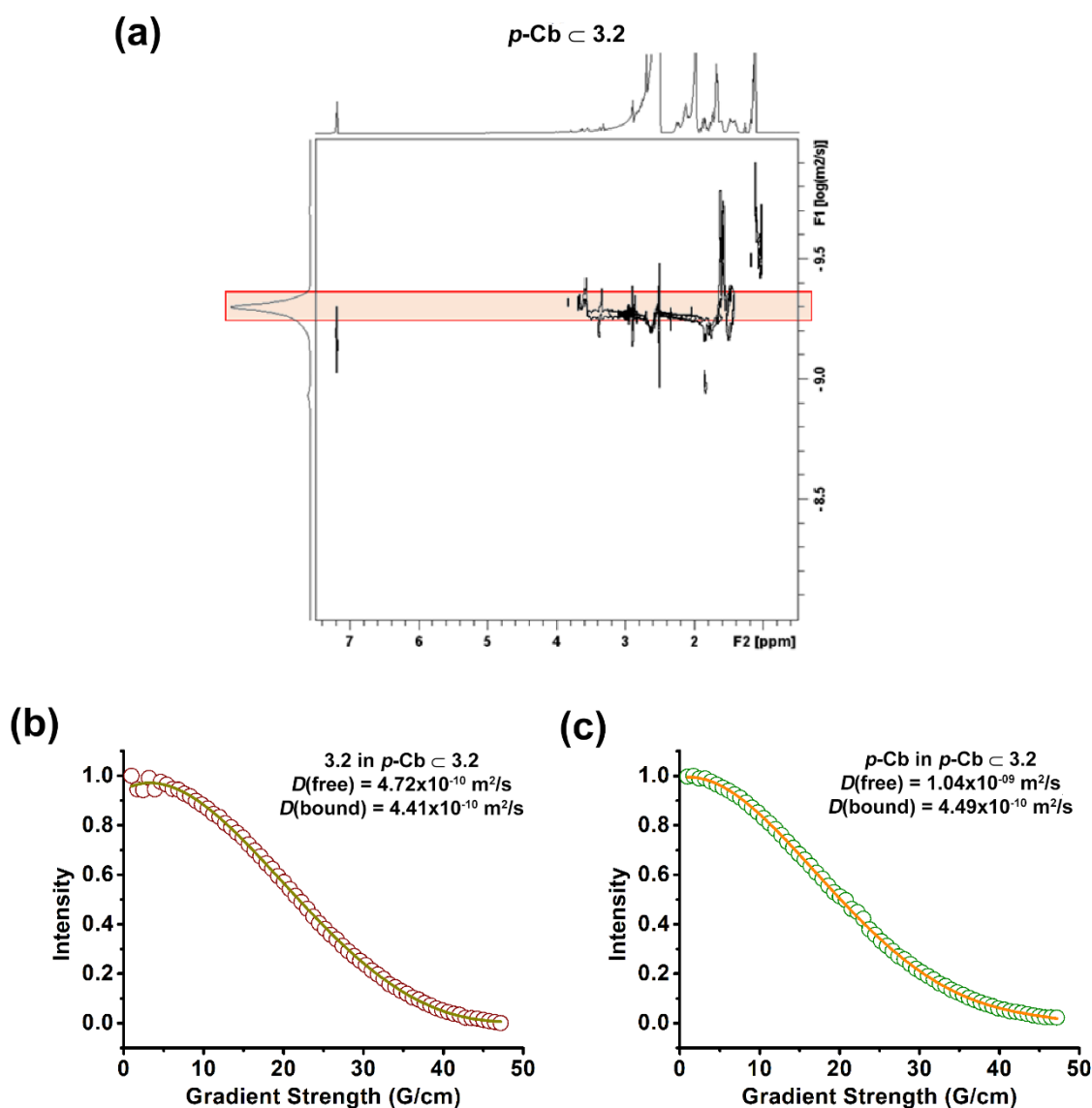


**Figure A3.58:** (a) 2D-DOSY-NMR spectra of  $p\text{-Cb} \subset 3.2$  complex. The red highlighted region corresponds to the diffusion of  $p\text{-Cb} \subset 3.2$  in the bound state. Due to the very broad nature of the peaks, the reported  $D$  values were extracted by using the T1/T2 relaxation module in TopSpin 4.1 software as follows: integral decay profile of (b) the  $i\text{-Pr } \text{CH}_3$  of host  $3.2$ , and (c) guest  $p\text{-Cb}$  C-H atoms in the host-guest system plotted as a function of gradient strength. The circles represent experimental data and the lines show the best fit using equation 2. The name of the molecules and the diffusion coefficients obtained for free and bound moieties are shown in the corresponding insets.

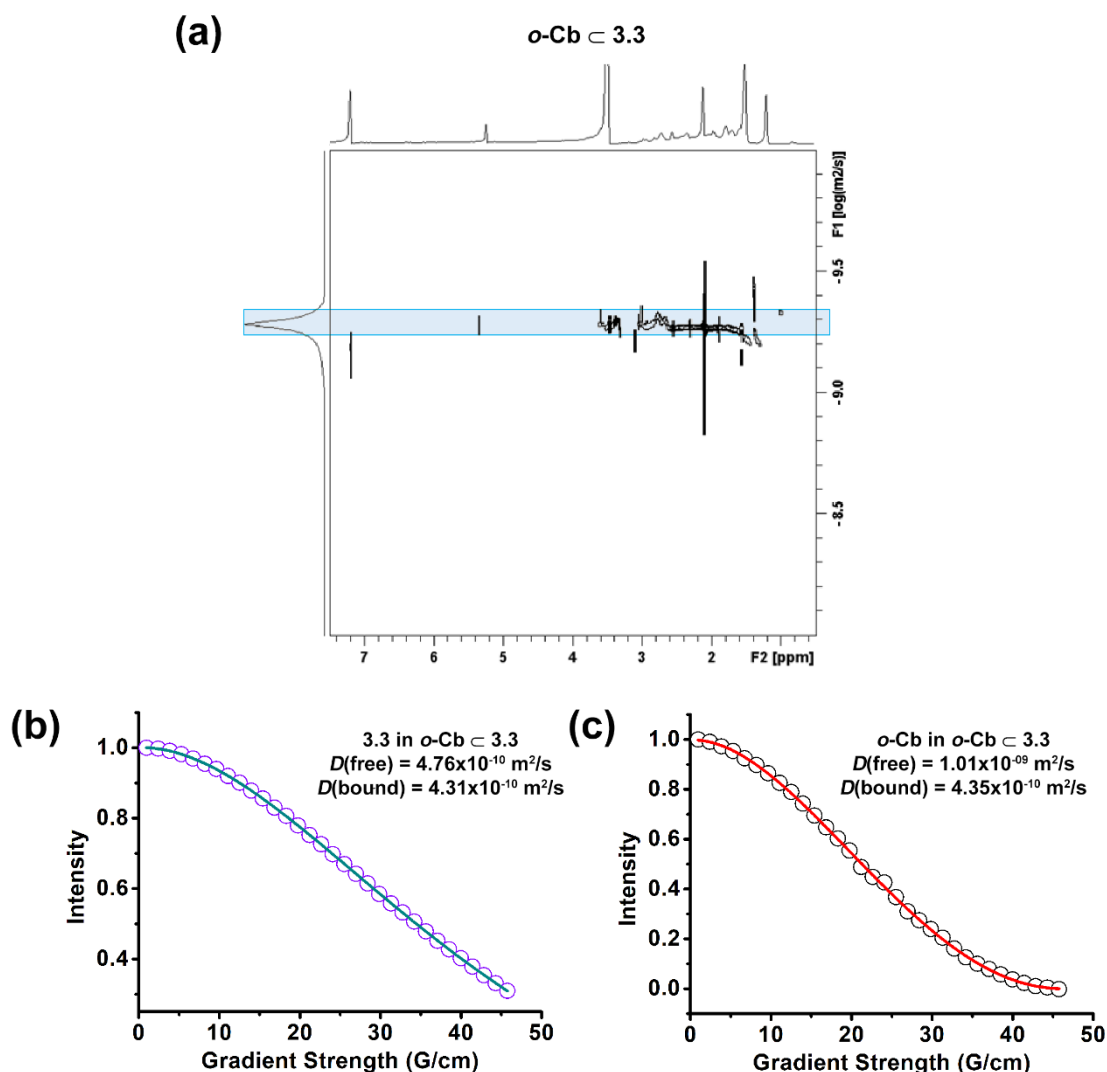


**Figure A3.59:** (a) 2D-DOSY-NMR spectra of  $o\text{-Cb} \subset 3.3$  complex. The blue highlighted region corresponds to the diffusion of  $o\text{-Cb} \subset 3.3$  in the bound state. Due to the very broad nature of the peaks, the reported  $D$  values were extracted by using the T1/T2 relaxation module in TopSpin 4.1 software as follows: integral decay profile of (b) the i-Pr  $CH_3$  of host **3.3**, and (c) guest  $o\text{-Cb}$  C-H atoms in the host-guest system plotted as a function of gradient strength. The circles represent experimental data and the lines show the best fit using equation 2. The name of the molecules and the diffusion coefficients obtained for free and bound moieties are shown in the corresponding insets.

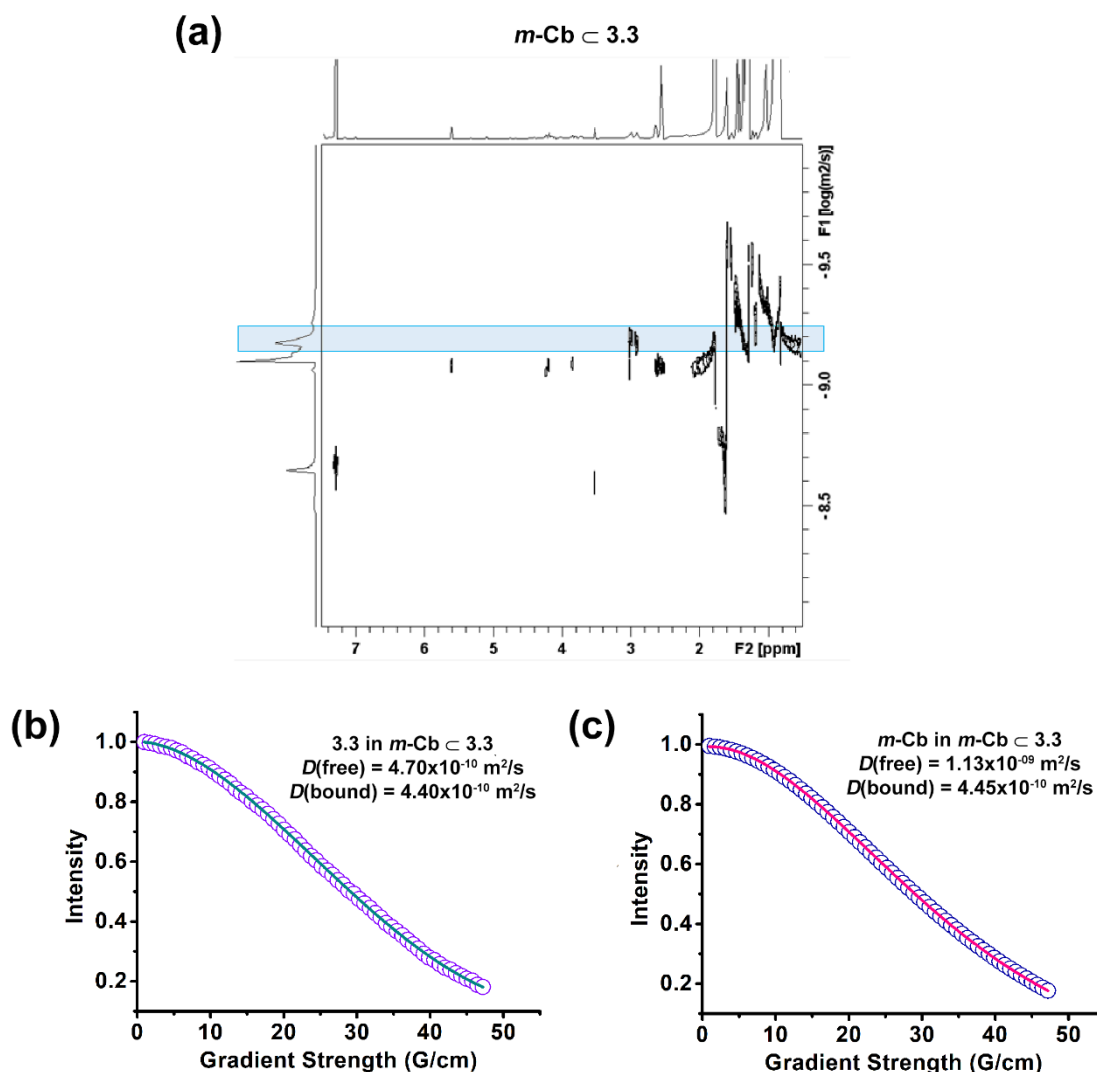


**Figure A3.60:** (a) 2D-DOSY-NMR spectra of  $m\text{-Cb} \subset 3.3$  complex. The blue highlighted region corresponds to the diffusion of  $m\text{-Cb} \subset 3.3$  in the bound state. Due to the very broad nature of the peaks, the reported  $D$  values were extracted by using the T1/T2 relaxation module in TopSpin 4.1 software as follows: integral decay profile of (b) the  $i\text{-Pr } \text{CH}_3$  of host  $3.3$ , and (c) guest  $m\text{-Cb}$  C-H atoms in the host-guest system plotted as a function of gradient strength. The circles represent experimental data and the lines show the best fit using equation 2. The name of the molecules and the diffusion coefficients obtained for free and bound moieties are shown in the corresponding insets.



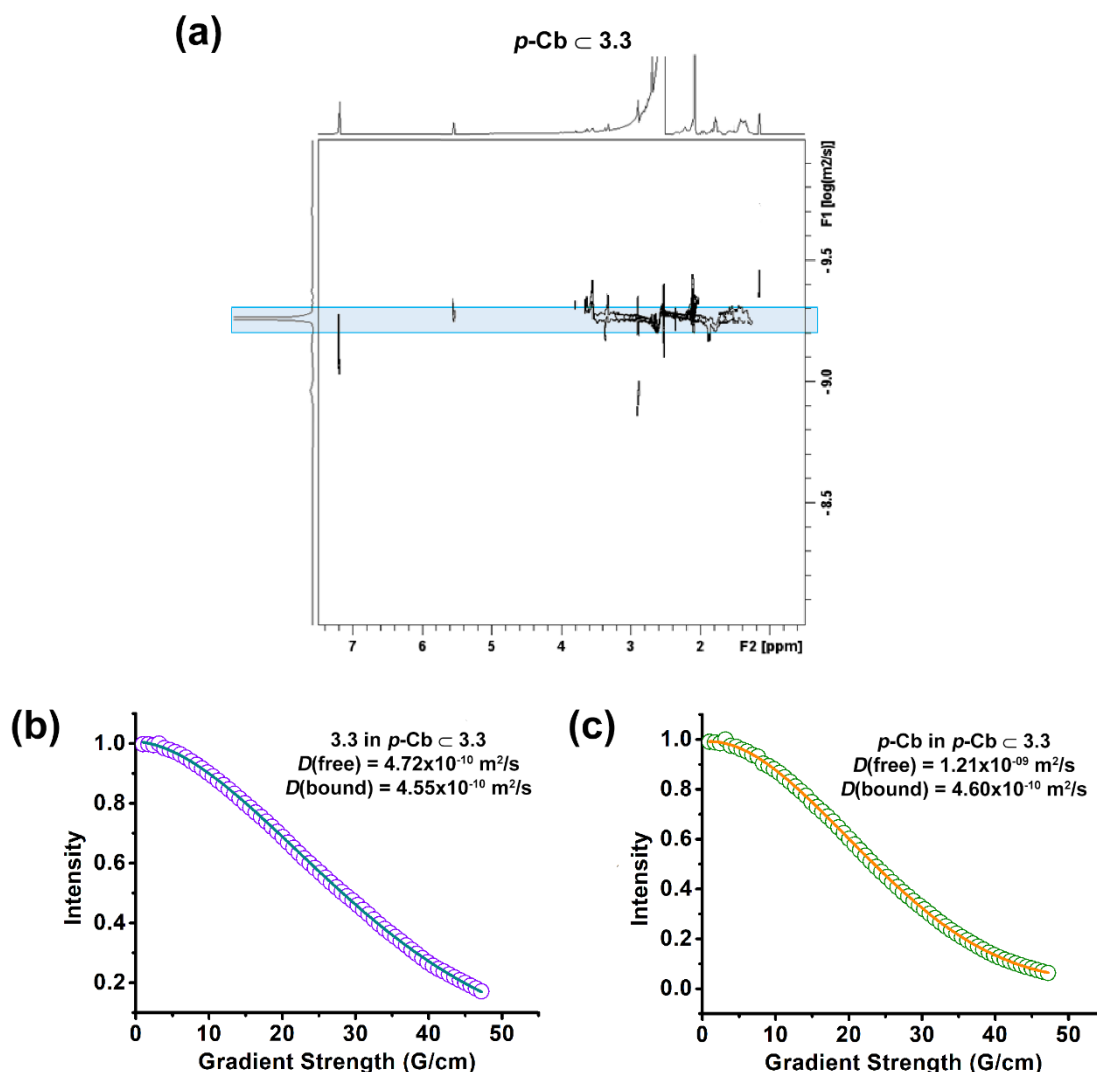


**Figure A3.61:** (a) 2D-DOSY-NMR spectra of  $p\text{-Cb} \subset 3.3$  complex. The blue highlighted region corresponds to the diffusion of  $p\text{-Cb} \subset 3.3$  in the bound state. Due to the very broad nature of the peaks, the reported  $D$  values were extracted by using the T1/T2 relaxation module in TopSpin 4.1 software as follows: integral decay profile of (b) the  $i\text{-Pr CH}_3$  of host  $3.3$ , and (c) guest  $p\text{-Cb}$  C-H atoms in the host-guest system plotted as a function of gradient strength. The circles represent experimental data and the lines show the best fit using equation 2. The name of the molecules and the diffusion coefficients obtained for free and bound moieties are shown in the corresponding insets.

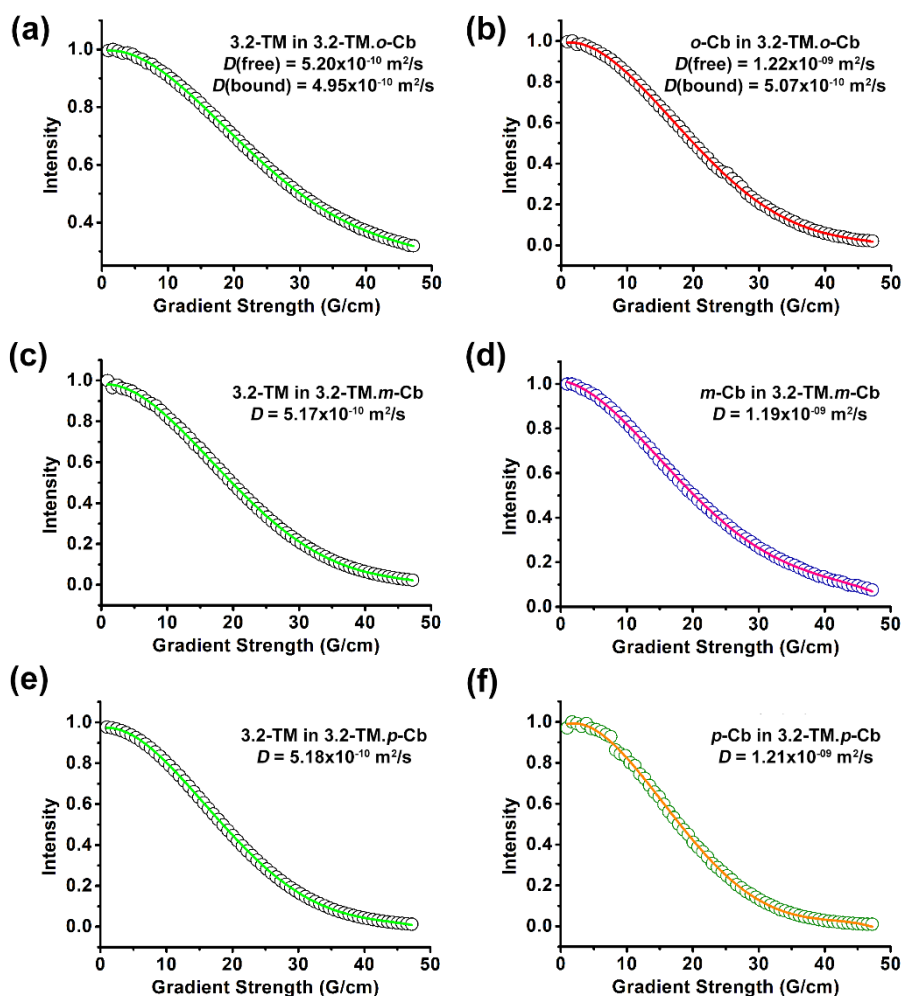


**Figure A3.62.** Integral decay profile of the  $i$ -Pr  $\text{CH}_3$  of host **3.2-TM** (left) and guest C- $H$  atoms (right) in the host–guest system plotted as a function of gradient strength. The circles represent experimental data and the lines show the best fit using equation 2. The name of the molecules and the diffusion coefficients obtained for free and bound moieties are shown in the corresponding insets. The reported diffusion coefficients were obtained using the T1/T2 relaxation module in TopSpin 4.1 software.

**Table A3.4.** Diffusion coefficients as obtained from the DOSY experiment for all host–guest systems. All the reported diffusion coefficients were obtained using the T1/T2 relaxation module in TopSpin 4.1 software. The standard deviations ( $\pm$ )<sup>a</sup> are given in parentheses.

Host–Guest Systems	Diffusion Coefficient ( $\times 10^{-10}$ m <sup>2</sup> /s)			
	Host		Guest	
	Free	Bound	Free	Bound
<i>o</i> -Cb $\subset$ 3.1	4.98(1) <sup>a</sup>	4.51(1)	11.60(4)	4.55(1)
<i>m</i> -Cb $\subset$ 3.1	4.92(2)	4.42(1)	12.31(3)	4.47(1)
<i>p</i> -Cb $\subset$ 3.1	4.99(1)	4.51(1)	10.84(4)	4.57(2)
<i>o</i> -Cb $\subset$ 3.2	4.68(3)	4.27(1)	11.33(2)	4.30(1)
<i>m</i> -Cb $\subset$ 3.2	4.70(1)	4.38(1)	11.26(6)	4.43(2)
<i>p</i> -Cb $\subset$ 3.2	4.72(4)	4.41(2)	10.41(6)	4.49(1)
<i>o</i> -Cb $\subset$ 3.3	4.76(6)	4.31(2)	10.15(4)	4.35(1)
<i>m</i> -Cb $\subset$ 3.3	4.70(1)	4.40(2)	11.28(4)	4.45(2)
<i>p</i> -Cb $\subset$ 3.3	4.72(1)	4.55(4)	12.11(1)	4.60(6)
3.2-TM· <i>o</i> -Cb	5.20(3)	4.95(1)	12.21(4)	5.07(2)
3.2-TM· <i>m</i> -Cb	5.17(6)	-	12.21(2)	-
3.2-TM· <i>p</i> -Cb	5.18(2)	-	12.16(8)	-

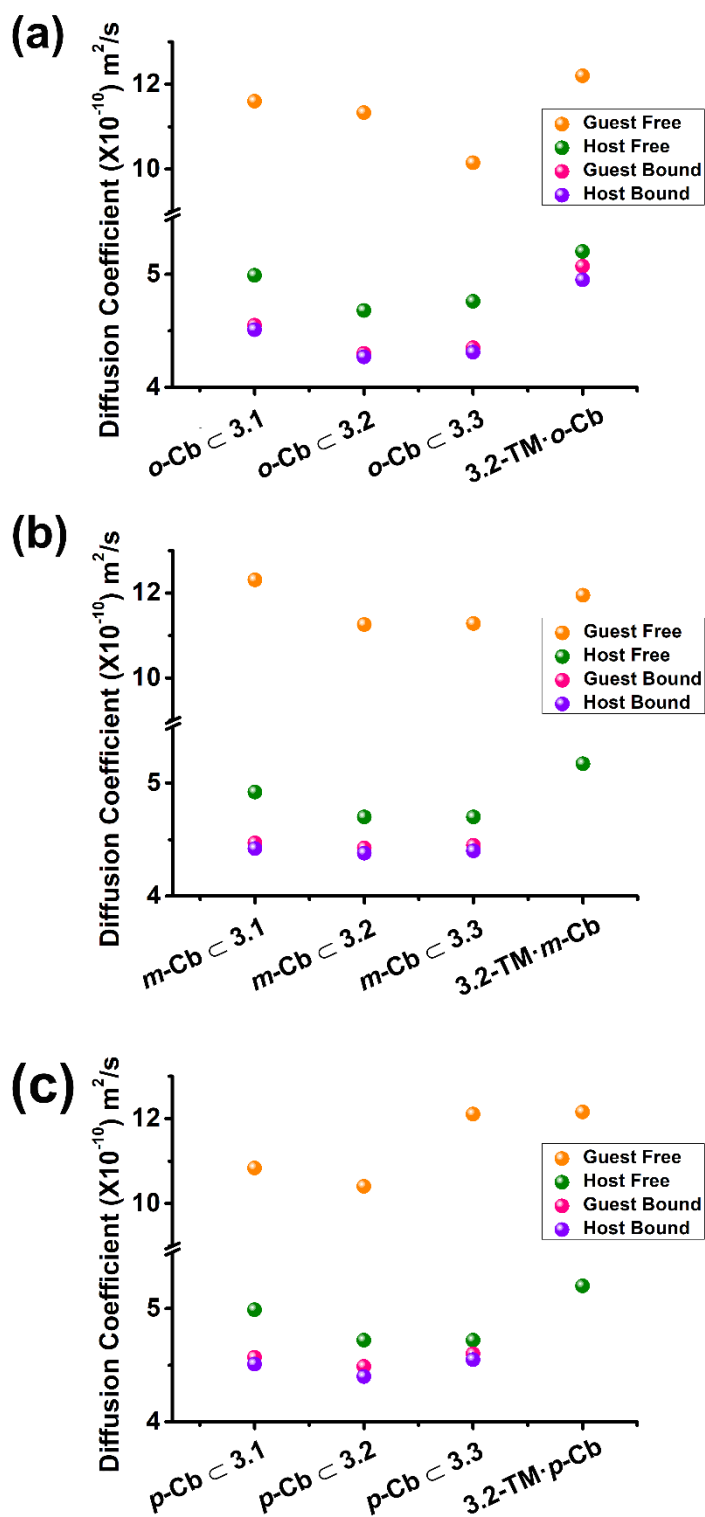


**Figure A3.63.** Summary of the  $D$  values for the host and guest hydrogen atoms studied for the systems of (a) *o*-Cb with all hosts, (b) *m*-Cb with all hosts and (c) of *p*-Cb with all hosts.

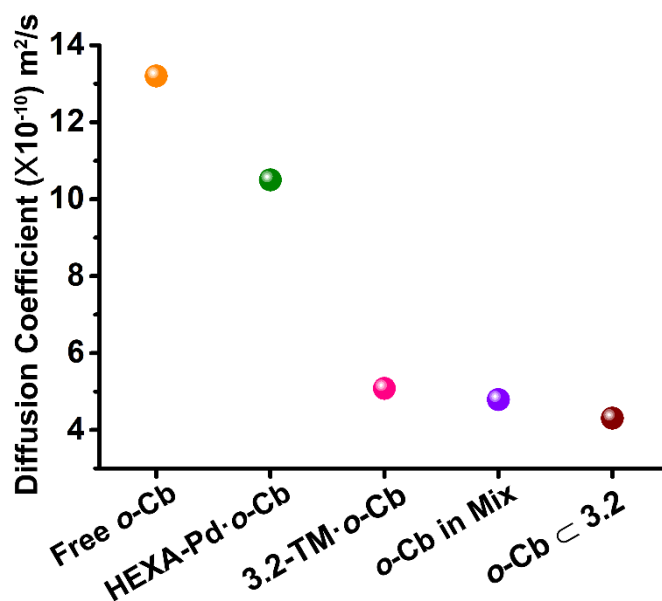


**Figure A3.64:** In-situ encapsulation of *o*-Cb causes the diffusion coefficient of *o*-Cb to decrease with the gradual formation of *o*-Cb c 3.2 from HEXA-Pd via pathways B and C.

### Calculation of Hydrodynamic Radii of Host–Guest Complexes

**Table A3.5.** Hydrodynamic radii as obtained from the DOSY experiment for all host–guest systems. The standard deviations ( $\pm$ )<sup>a</sup> are given in parentheses.

Host–Guest Systems	Hydrodynamic Radii (Å)			
	Host		Guest	
	Free	Bound	Free	Bound
<i>o</i> -Cb c 3.1	10.61(2) <sup>a</sup>	11.44(1)	5.80(1)	11.38(2)
<i>m</i> -Cb c 3.1	10.71(2)	11.62(1)	5.58(1)	11.54(2)
<i>p</i> -Cb c 3.1	10.59(2)	11.44(1)	6.07(1)	11.33(1)
<i>o</i> -Cb c 3.2	11.12(1)	11.95(2)	5.89(1)	11.90(3)
<i>m</i> -Cb c 3.2	11.09(1)	11.72(2)	5.91(1)	11.62(2)
<i>p</i> -Cb c 3.2	11.06(2)	11.66(2)	6.24(1)	11.52(4)
<i>o</i> -Cb c 3.3	10.98(2)	11.87(3)	6.34(6)	11.78(8)
<i>m</i> -Cb c 3.3	11.09(6)	11.68(3)	5.91(2)	11.58(5)
<i>p</i> -Cb c 3.3	11.06(4)	11.38(2)	5.64(6)	11.28(4)
3.2-TM· <i>o</i> -Cb	10.26(1)	10.66(2)	5.61(1)	10.46(1)
3.2-TM· <i>m</i> -Cb	10.31(2)	-	5.61(1)	-
3.2-TM· <i>p</i> -Cb	10.29(1)	-	5.62(1)	-

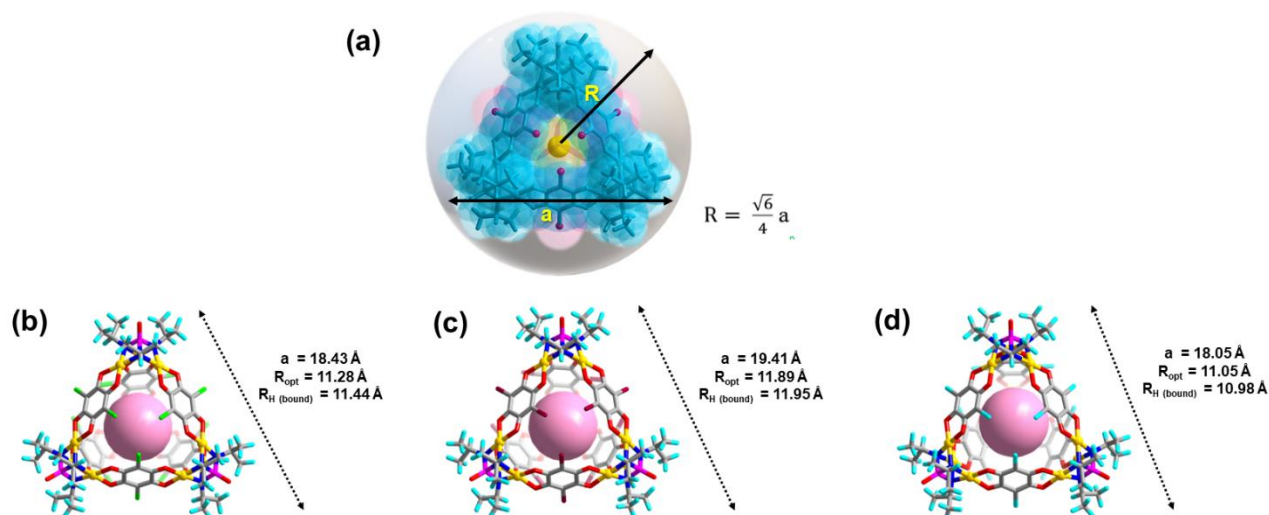


**Figure A3.65.** (a) Schematic representation of hydrodynamic radii and molecular models of systems (b)  $\text{Cb} \subset 3.1$  (c)  $\text{Cb} \subset 3.2$  and (d)  $\text{Cb} \subset 3.3$ . The  $R_H$  values depicted pertains to  $o\text{-Cb} \subset \text{Cage}$  systems.

**Table A3.6.** Comparison of the hydrodynamic radii as obtained from DOSY experiment and radii of the circumscribed sphere calculated from the respective energy-minimized models of the guest-bound cage systems.

Host–Guest Systems	Host Bound Hydrodynamic Radii (Å)	Optimized Radii (Å) of $\text{Cb} \subset \text{Cage}$	Guest Bound Hydrodynamic Radii (Å)
	$o\text{-Cb} \subset 3.1$	11.44(1)	11.28(1)
$m\text{-Cb} \subset 3.1$	11.62(1)	11.29(3)	11.54(2)
$p\text{-Cb} \subset 3.1$	11.44(1)	11.29(3)	11.33(1)
$o\text{-Cb} \subset 3.2$	11.95(2)	11.89(4)	11.90(3)
$m\text{-Cb} \subset 3.2$	11.72(2)	11.91(2)	11.62(2)
$p\text{-Cb} \subset 3.2$	11.66(2)	11.92(2)	11.52(4)
$o\text{-Cb} \subset 3.3$	11.87(3)	10.99(1)	11.78(8)
$m\text{-Cb} \subset 3.3$	11.68(3)	11.02(6)	11.58(5)
$p\text{-Cb} \subset 3.3$	11.38(2)	11.01(2)	11.28(4)

### Calculation of Binding Energy of Host–Guest Complexes

**Table A3.7.** Binding energy of the host–guest complex calculated using DFT by G09 software.

Hosts	Host–Guest Systems	Binding Energy (kcal/mol)
3.1	<i>o</i> -Cb ⊂ 3.1	-661.54
	<i>m</i> -Cb ⊂ 3.1	-619.49
	<i>p</i> -Cb ⊂ 3.1	-595.76
3.2	<i>o</i> -Cb ⊂ 3.2	-660.28
	<i>m</i> -Cb ⊂ 3.2	-621.13
	<i>p</i> -Cb ⊂ 3.2	-605.60
3.3	<i>o</i> -Cb ⊂ 3.3	-500.12
	<i>m</i> -Cb ⊂ 3.3	-480.08
	<i>p</i> -Cb ⊂ 3.3	-470.25
3.2-TM	3.2-TM· <i>o</i> -Cb	-101.47
	3.2-TM· <i>m</i> -Cb	-84.31
	3.2-TM· <i>p</i> -Cb	-81.13

**Table A3.8.** Deformation energy of the host–guest complex calculated using DFT by G09 software.

Hosts	Host–Guest Systems	Deformation Energy (kcal/mol)
3.1	<i>o</i> -Cb ⊂ 3.1	0.98
	<i>m</i> -Cb ⊂ 3.1	1.12
	<i>p</i> -Cb ⊂ 3.1	0.87
3.2	<i>o</i> -Cb ⊂ 3.2	1.15
	<i>m</i> -Cb ⊂ 3.2	1.03
	<i>p</i> -Cb ⊂ 3.2	0.92
3.3	<i>o</i> -Cb ⊂ 3.3	1.14
	<i>m</i> -Cb ⊂ 3.3	1.08
	<i>p</i> -Cb ⊂ 3.3	1.05
3.2-TM	3.2-TM· <i>o</i> -Cb	0.19
	3.2-TM· <i>m</i> -Cb	0.16
	3.2-TM· <i>p</i> -Cb	0.16

## Possible Non-Classical Interactions Present in the Host–Guest Complexes

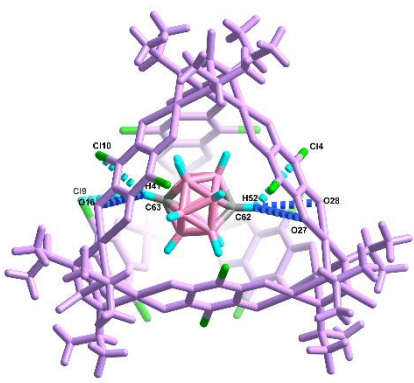
	D-H...A	d(H...A) (Å)	d(D...A) (Å)	< (D-H...A) (°)
	C62- H42...O10	2.801(2)	3.775(2)	142.9(4)
	C62- H42...Cl11	3.211(5)	4.298(9)	148.7(4)
	C62- H42...O12	3.577(8)	4.304(9)	122.8(7)
	C63- H46...O17	2.858(9)	3.921(3)	160.9(2)
	C63- H46...O9	3.290(2)	4.243(3)	144.9(2)

**Figure A3.66.** Potential non-covalent interactions responsible for the stabilization of the host–guest assemblies and a summary of the computed non-classical H-bonds in *o*-Cb c 3.1.

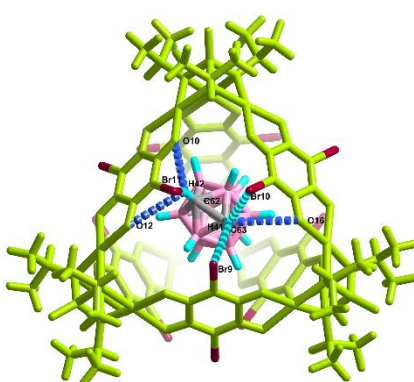
	D-H...A	d(H...A) (Å)	d(D...A) (Å)	< (D-H...A) (°)
	C62- H47...O13	3.397(6)	4.305(9)	135.4(5)
	C62- H47...Cl15	3.715(4)	4.471(3)	129.7(9)
	C63- H41...Cl9	3.769(5)	4.812(5)	141.7(8)
	C63- H41...O16	3.581(2)	4.271(5)	120.8(1)
	C63- H41...Cl10	3.083(6)	4.076(2)	147.1(2)

**Figure A3.67.** Potential non-covalent interactions responsible for the stabilization of the host–guest assemblies and a summary of the computed non-classical H-bonds in *m*-Cb c 3.1.

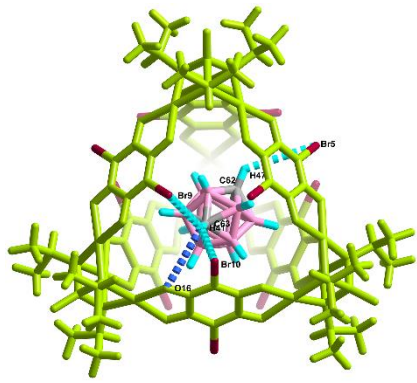


	D-H...A	d(H...A) (Å)	d(D...A) (Å)	< (D-H...A) (°)
	C62-H52...O27	3.776(9)	4.601(4)	132.9(9)
	C62-H52...O28	3.302(9)	4.390(6)	173.3(6)
	C62-H52...C14	3.770(9)	4.534(2)	128.7(3)
	C63-H41...C19	3.763(4)	4.701(6)	141.7(8)
	C63-H41...O16	3.571(5)	4.271(3)	120.8(5)
	C63-H41...C110	3.083(9)	4.075(9)	146.9(3)

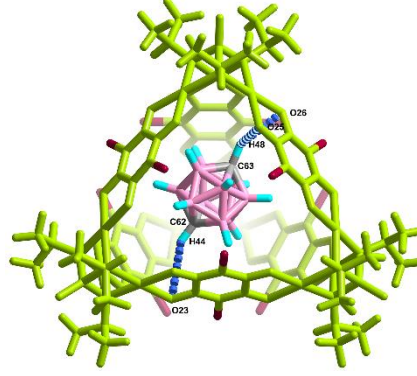
**Figure A3.68.** Potential non-covalent interactions responsible for the stabilization of the host-guest assemblies and a summary of the computed non-classical H-bonds in *p*-Cb **3.1**.

	D-H...A	d(H...A) (Å)	d(D...A) (Å)	< (D-H...A) (°)
	C62-H42...O10	2.801(5)	3.775(2)	142.9(2)
	C62-H42...Br11	3.282(5)	4.301(5)	148.7(9)
	C62-H42...O12	3.577(8)	4.305(2)	122.9(7)
	C63-H41...Br9	3.761(3)	4.708(6)	141.7(8)
	C63-H41...O16	3.581(6)	4.271(3)	120.8(5)
	C63-H41...Br10	3.084(4)	4.076(2)	146.9(3)

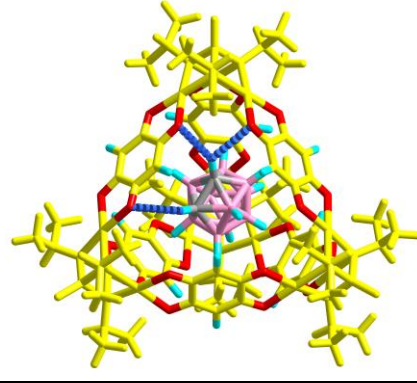
**Figure A3.69.** Potential non-covalent interactions responsible for the stabilization of the host-guest assemblies and a summary of the computed non-classical H-bonds in *o*-Cb **3.2**.

	<b>D-H...A</b>	<b>d(H...A) (Å)</b>	<b>d(D...A) (Å)</b>	<b>&lt; (D-H...A) (°)</b>
	C62- H47...Br5	3.515(6)	4.371(6)	129.7(9)
	C63- H41...Br10	3.084(2)	4.076(3)	146.9(3)
	C63- H41...O16	3.581(6)	4.171(6)	120.8(5)
	C63- H41...Br9	3.771(4)	4.707(6)	141.7(8)

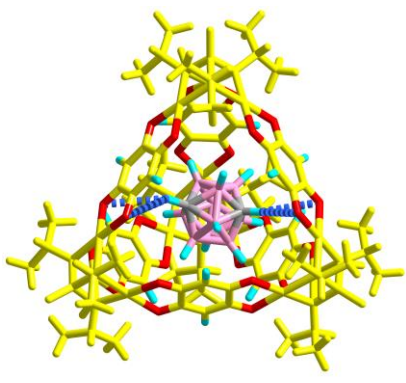
**Figure A3.70.** Potential non-covalent interactions responsible for the stabilization of the host–guest assemblies and a summary of the computed non-classical H-bonds in *m*-Cb c 3.2.

	<b>D-H...A</b>	<b>d(H...A) (Å)</b>	<b>d(D...A) (Å)</b>	<b>&lt; (D-H...A) (°)</b>
	C62- H44...O23	3.406(5)	4.204(2)	131.3(3)
	C63- H48...O25	3.482(2)	4.178(9)	119.9(8)
	C63- H48...O26	2.751(6)	3.795(2)	149.7(4)

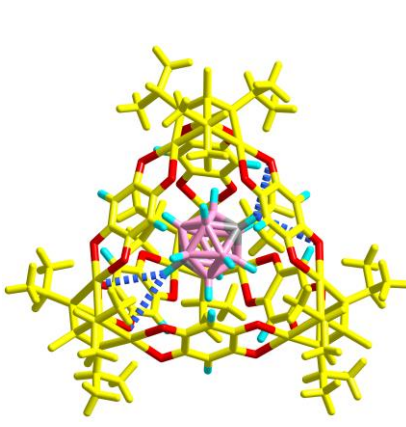
**Figure A3.71.** Potential non-covalent interactions responsible for the stabilization of the host–guest assemblies and a summary of the computed non-classical H-bonds in *p*-Cb c 3.2.

	<b>D-H...A</b>	<b>d(H...A) (Å)</b>	<b>d(D...A) (Å)</b>	<b>&lt; (D-H...A) (°)</b>
	C74- H92...O26	2.910(1)	3.965(1)	151.3(1)
	C74- H92...O11	3.142(1)	4.004(3)	131.5(1)
C73- H96...O28	3.360(2)	4.440(1)	169.1(2)	

**Figure A3.72.** Potential non-covalent interactions responsible for the stabilization of the host–guest assemblies and a summary of the computed non-classical H-bonds in *o*-Cb c 3.3.

	<b>D-H...A</b>	<b>d(H...A) (Å)</b>	<b>d(D...A) (Å)</b>	<b>&lt; (D-H...A) (°)</b>
	C73- H94...O21	3.225(6)	4.334(5)	147.0(1)
	C73- H94...O22	3.389(9)	4.450(1)	142.2(3)
	C74- H90...O9	3.543(4)	4.498(0)	145.3(4)
	C74- H90...O17	3.036(4)	4.112(3)	168.4(5)

**Figure A3.73.** Potential non-covalent interactions responsible for the stabilization of the host–guest assemblies and a summary of the computed non-classical H-bonds in *m*-Cb  $\subset$  **3.3**.

	<b>D-H...A</b>	<b>d(H...A) (Å)</b>	<b>d(D...A) (Å)</b>	<b>&lt; (D-H...A) (°)</b>
	C73- H94...O22	3.406(1)	4.450(1)	142.2(3)
	C73- H94...O21	3.225(6)	4.334(7)	147.0(6)
	C74- H86...O10	2.977(8)	3.917(8)	139.5(1)
	C74- H86...O12	3.482(3)	4.251(1)	125.7(0)

**Figure A3.74.** Potential non-covalent interactions responsible for the stabilization of the host–guest assemblies and a summary of the computed non-classical H-bonds in *p*-Cb  $\subset$  **3.3**.

	<b>D-H...A</b>	<b>d(H...A)</b> (Å)	<b>d(D...A)</b> (Å)	<b>&lt; (D-H...A)</b> (°)
	C57-H105...O4	3.548(3)	4.571(9)	153.9(2)
	C58-H110...O7	3.895(6)	4.989(6)	142.9(4)

**Figure A3.75.** Potential non-covalent interactions responsible for the stabilization of the host-guest assemblies and a summary of the computed non-classical H-bonds in **3.2-TM·o-Cb**.

	<b>D-H...A</b>	<b>d(H...A)</b> (Å)	<b>d(D...A)</b> (Å)	<b>&lt; (D-H...A)</b> (°)
	C57-H105...O4	3.605(8)	4.622(2)	153.9(2)

**Figure A3.76.** Potential non-covalent interactions responsible for the stabilization of the host-guest assemblies and a summary of the computed non-classical H-bonds in **3.2-TM·m-Cb**.

	<b>D-H...A</b>	<b>d(H...A)</b> (Å)	<b>d(D...A)</b> (Å)	<b>&lt; (D-H...A)</b> (°)
	C57-H105...O4	3.603(2)	4.621(9)	153.9(2)

**Figure A3.77.** Potential non-covalent interactions responsible for the stabilization of the host-guest assemblies and a summary of the computed non-classical H-bonds in **3.2-TM·p-Cb**.

\*\*\*\*\*

Structural Characterisation Data**Table A4.1.** Selected bond lengths (Å) and bond angles (°) for **4.1**.

Selected Bonds	Bond lengths (Å)
Pd(5)-N(6)	2.011(19)
Pd(5)-N(5)	2.017(19)
Pd(5)-Cl(7)	2.326(7)
Pd(8)-N(9)	2.031(19)
Pd(8)-N(8)	2.043(19)
Pd(8)-Cl(8)	2.344(7)
Pd(11)-N(12)	2.00(2)
Pd(11)-N(11)	2.06(2)
Pd(11)-Cl(9)	2.335(7)
Pd(11)-Cl(10)	2.349(7)
Pd(12)-N(10)	2.032(19)
Pd(12)-N(12)	2.064(19)
Pd(12)-Cl(12)	2.328(7)
Pd(12)-Cl(11)	2.341(7)
Pd(7)-N(8)	2.006(19)
Pd(7)-N(7)	2.062(19)
Pd(2)-N(2)	1.994(19)
Pd(2)-N(3)	2.023(18)
Pd(2)-Cl(3)	2.329(6)
Pd(2)-Cl(4)	2.332(7)
Pd(4)-N(4)	2.01(2)

Pd(4)-N(5)	2.032(19)
Pd(4)-Cl(5)	2.333(7)
Pd(4)-Cl(6)	2.339(7)
Pd(9)-N(7)	2.00(2)
Pd(9)-N(9)	2.033(19)
Pd(9)-Cl(2)	2.337(7)
Pd(9)-Cl(1)	2.346(7)
Pd(3)-N(3)	2.04(2)
Pd(3)-N(1)	2.05(2)
Pd(3)-Cl(5)	2.332(7)
Pd(3)-Cl(6)	2.344(7)
Pd(10)-N(11)	2.037(19)
Pd(10)-N(10)	2.060(19)
Pd(10)-Cl(3)	2.326(7)
Pd(10)-Cl(4)	2.327(7)
Pd(6)-N(4)	2.040(19)
Pd(6)-N(6)	2.056(19)
Pd(1)-N(1)	2.024(18)
Pd(1)-N(2)	2.06(2)
Pd(1)-Cl(1)	2.326(7)
Pd(1)-Cl(2)	2.349(6)

Selected Angles	Bond angles (°)
N(6)-Pd(5)-N(5)	77.1(8)
Pd(6)-Pd(5)-Pd(4)	60.70(7)
Cl(7)#1-Pd(8)-Cl(8)	86.1(2)
Pd(7)-Pd(8)-Pd(9)	60.92(6)
N(12)-Pd(11)-N(11)	76.4(8)
Cl(9)-Pd(11)-Cl(10)	87.4(2)
Pd(10)-Pd(11)-Pd(12)	59.00(7)
N(10)-Pd(12)-N(12)	76.1(8)
Cl(12)-Pd(12)-Cl(11)	87.4(2)
Pd(10)-Pd(12)-Pd(11)	59.85(7)
Pd(8)-Pd(7)-Pd(9)	59.57(7)
Pd(3)-Pd(2)-Pd(1)	61.29(7)
N(4)-Pd(4)-N(5)	77.2(8)

Pd(5)-Pd(4)-Pd(6)	59.65(6)
N(7)-Pd(9)-N(9)	76.9(8)
Pd(8)-Pd(9)-Pd(7)	59.51(7)
N(3)-Pd(3)-N(1)	75.1(8)
Pd(2)-Pd(3)-Pd(1)	59.60(7)
N(11)-Pd(10)-N(10)	75.4(8)
Pd(12)-Pd(10)-Pd(11)	61.15(6)
N(4)-Pd(6)-N(6)	77.1(8)
Cl(12)#1-Pd(6)-Cl(11)#1	87.2(2)
N(4)-Pd(6)-Pd(5)	80.5(6)
N(6)-Pd(6)-Pd(5)	38.7(5)
Pd(5)-Pd(6)-Pd(4)	59.65(7)
N(1)-Pd(1)-N(2)	76.5(8)
Pd(2)-Pd(1)-Pd(3)	59.11(7)

Pd(4)-Cl(6)-Pd(3)	91.4(2)	Pd(10)-Cl(4)-Pd(2)	89.0(2)
Pd(7)#1-Cl(9)-Pd(11)	91.9(2)	Pd(5)#1-Cl(8)-Pd(8)	90.2(2)
Pd(10)-Cl(3)-Pd(2)	89.1(2)	Pd(9)-Cl(2)-Pd(1)	91.5(2)
Pd(5)-Cl(7)-Pd(8)#1	90.6(2)	Pd(1)-Cl(1)-Pd(9)	91.9(3)
Pd(12)-Cl(11)-Pd(6)#1	91.0(3)	Pd(12)-Cl(12)-Pd(6)#1	91.4(2)
Pd(3)-Cl(5)-Pd(4)	91.8(2)	Pd(7)#1-Cl(10)-Pd(11)	91.2(2)

**Table A4.2.** Selected bond lengths (Å) and bond angles (°) for **4.2**.

Selected Bonds	Bond lengths (Å)
Pd(1)-N(2)	2.091(3)
Pd(1)-N(1)	2.098(3)
N(2)-Pd(2)	2.025(3)
Pd(2)-N(3)	2.039(3)
Pd(2)-O(3)	2.060(3)
Pd(2)-O(4)	2.149(3)
O(2)-Pd(3)	2.047(3)
N(1)-Pd(3)	2.026(3)
Pd(3)-N(3)	2.045(3)
Pd(3)-O(5)	2.055(3)

Selected Angles	Bond angles (°)
Pd(2)#1-Pd(1)-Pd(3)	88.599(13)
Pd(2)-Pd(1)-Pd(3)	63.464(10)
Pd(2)#1-Pd(1)-Pd(3)#1	63.464(10)
Pd(2)-Pd(1)-Pd(3)#1	88.597(13)
Pd(3)-Pd(1)-Pd(3)#1	54.539(15)
Pd(2)-N(2)-Pd(1)	94.72(13)
Pd(1)-Pd(2)-Pd(3)	58.436(12)
Pd(3)-N(1)-Pd(1)	94.94(13)
Pd(1)-Pd(3)-Pd(2)	58.099(11)
Pd(2)-N(3)-Pd(3)	102.78(14)

### Spectral Characterisation Data

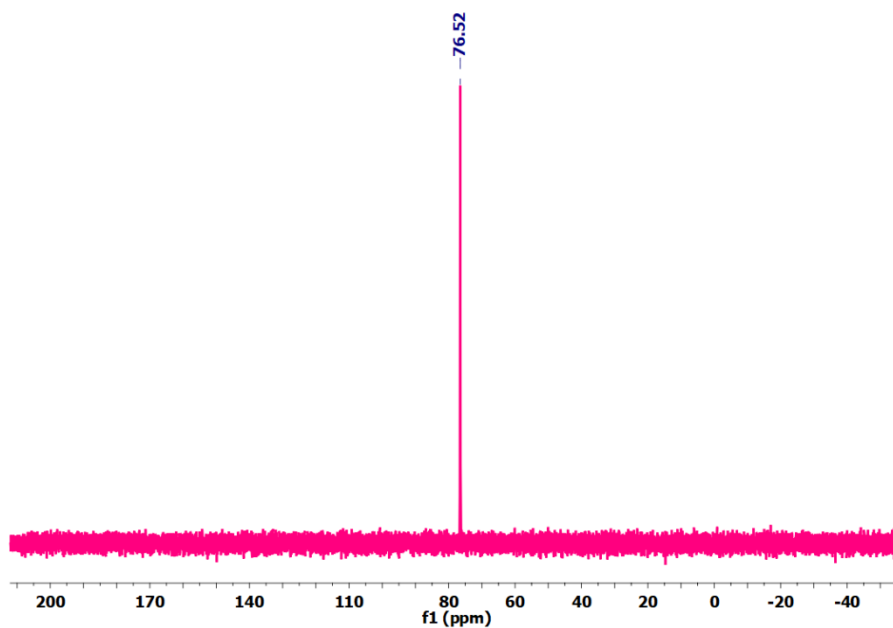


Figure A4.1.  $^{31}\text{P}\{^1\text{H}\}$ -NMR ( $\text{CDCl}_3$ , 298K) of **4.1**.

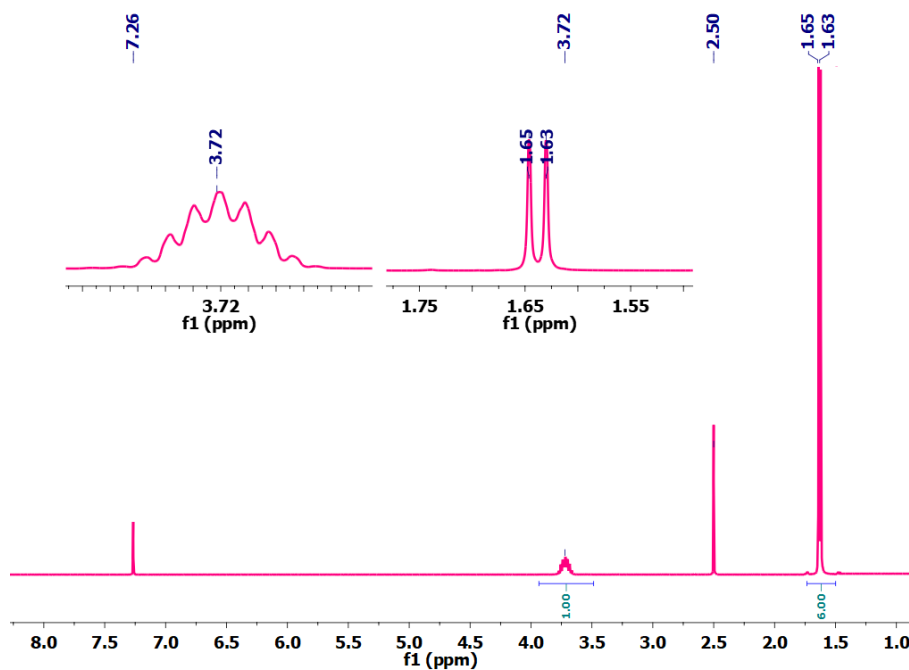


Figure A4.2.  $^1\text{H}$ -NMR ( $\text{CDCl}_3$ , 298K) of **4.1**.

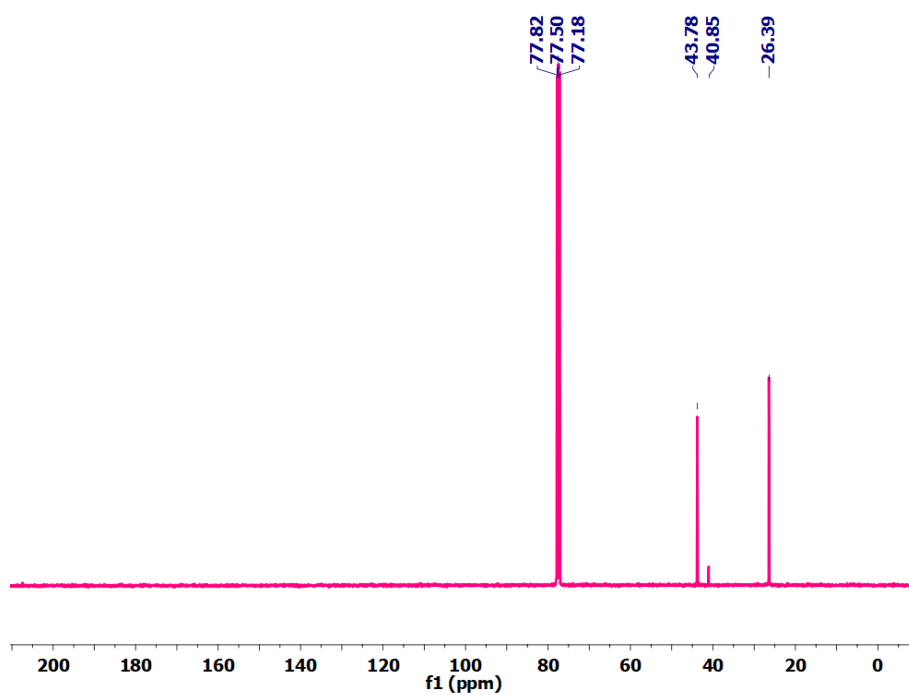


Figure A4.3.  $^{13}\text{C}$ -NMR ( $\text{CDCl}_3$ , 298K) of 4.1.

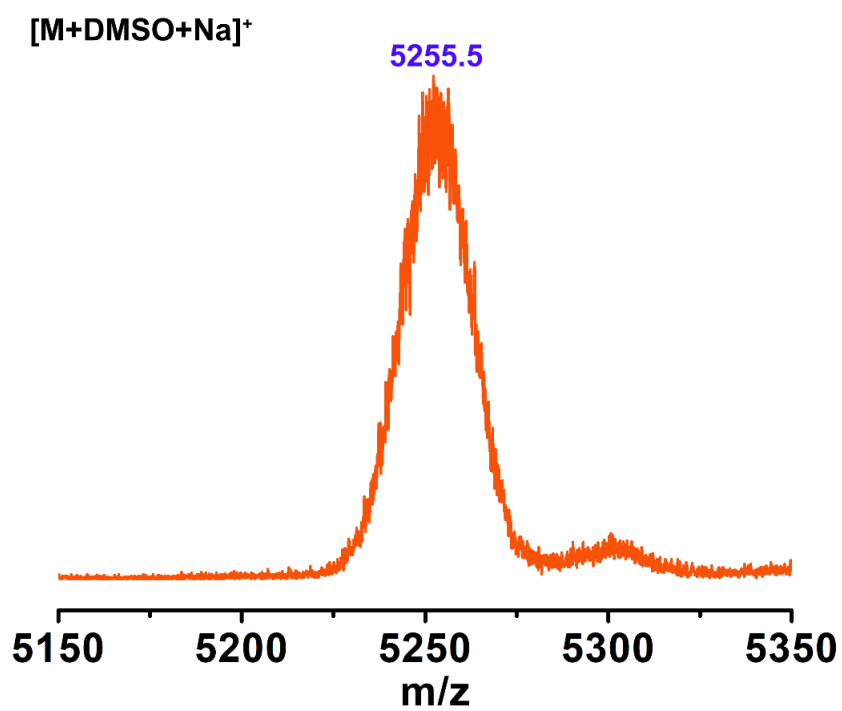
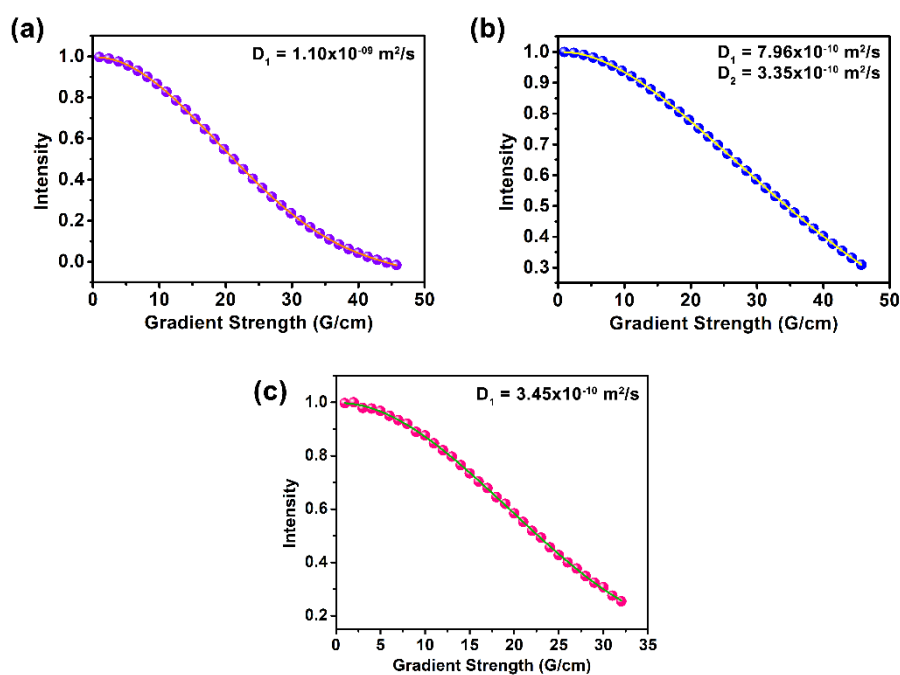
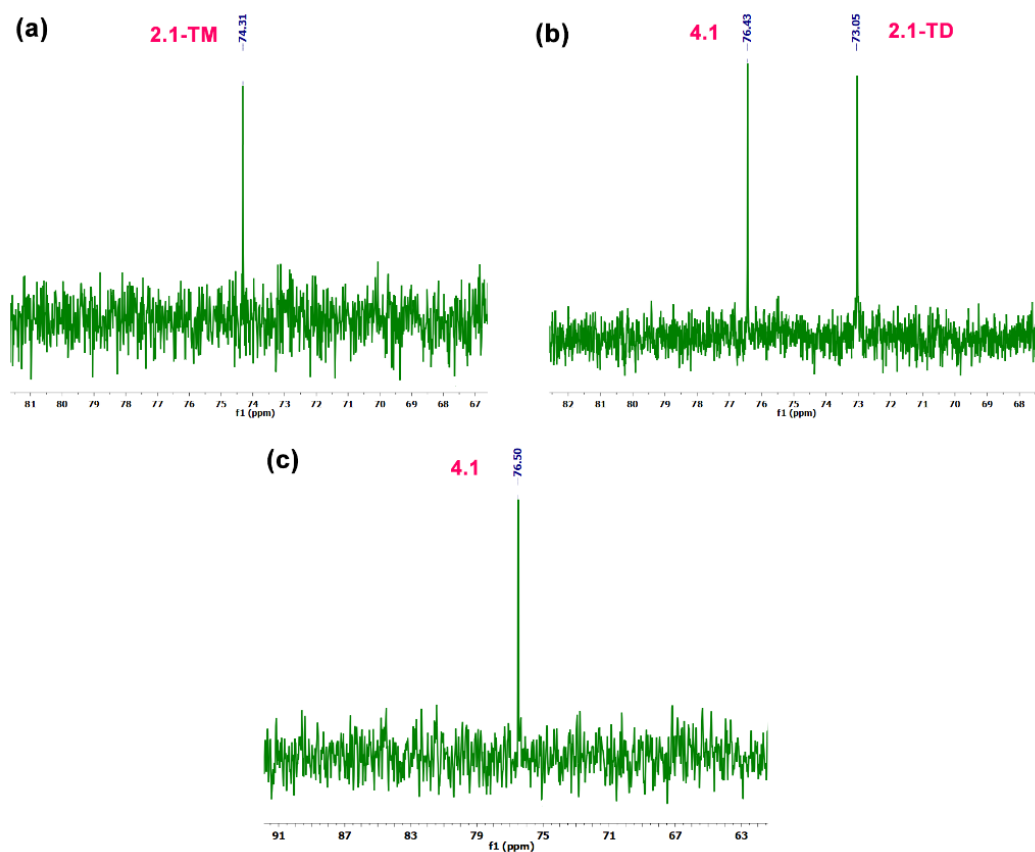


Figure A4.4. MALDI-TOF mass spectrum of 4.1.





**Figure A4.5.** Integral decay profile of the i-Pr CH<sub>3</sub> group of the various host systems present in the reaction mixture after (a) 1 hour (b) 5 hours (c) 15 hours, plotted as a function of gradient strength. The circles represent experimental data and the lines show the best fit using equations 1 or 2. The name of the molecules and the diffusion coefficients obtained for free and bound moieties are shown in the corresponding insets. The reported diffusion coefficients were obtained using the T1/T2 relaxation module in TopSpin 4.1 software.



**Figure A4.6.**  $^{31}\text{P}\{^1\text{H}\}$  NMR spectral changes during the formation of **4.1** via the intermediate templates **2.1-TM** and **2.1-TD**, recorded at the following stages of reaction: (a) 1 hour, (b) 5 hours, and (c) 15 hours.

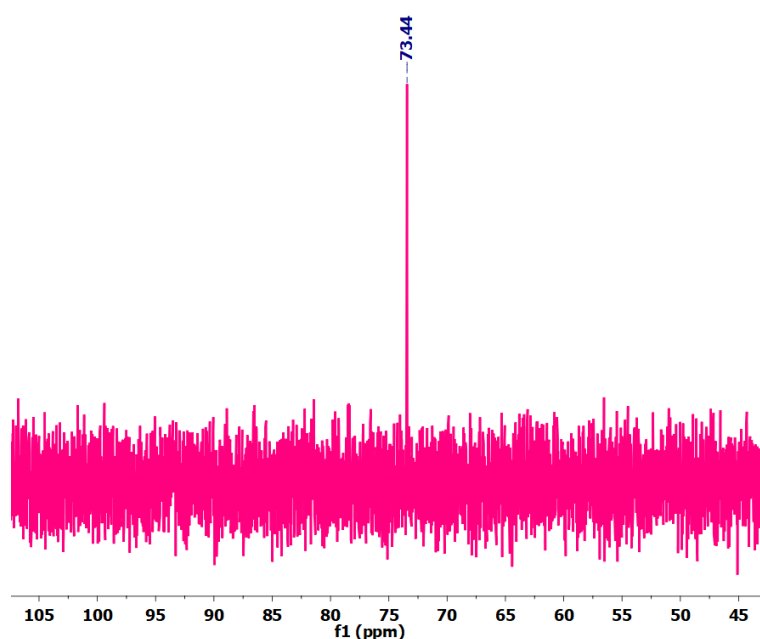


**Figure A4.7.**  $^{31}\text{P}\{^1\text{H}\}$ -NMR ( $\text{CDCl}_3$ , 298K) of **4.2**.

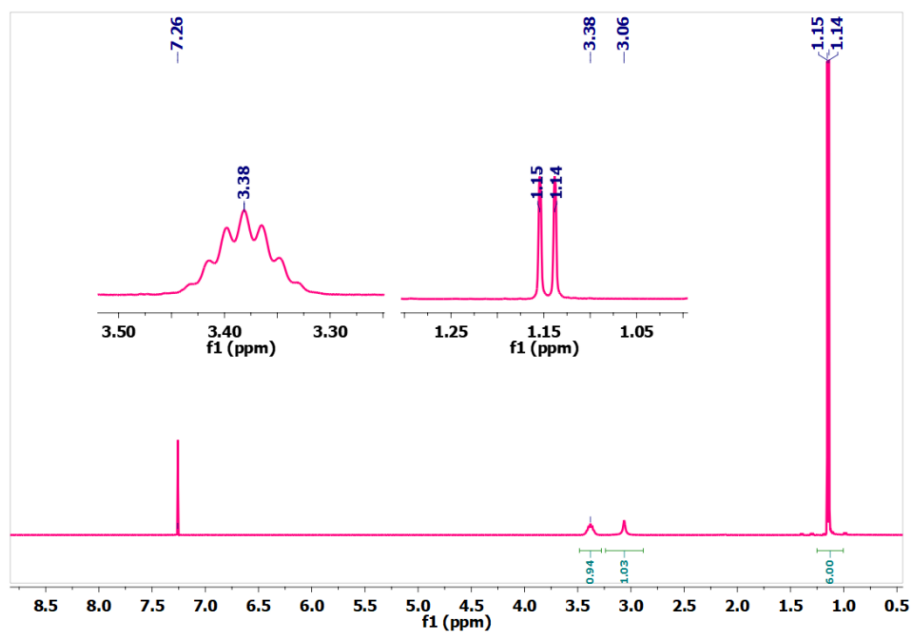


Figure A4.8.  $^1\text{H-NMR}$  ( $\text{CDCl}_3$ , 298K) of 4.2.

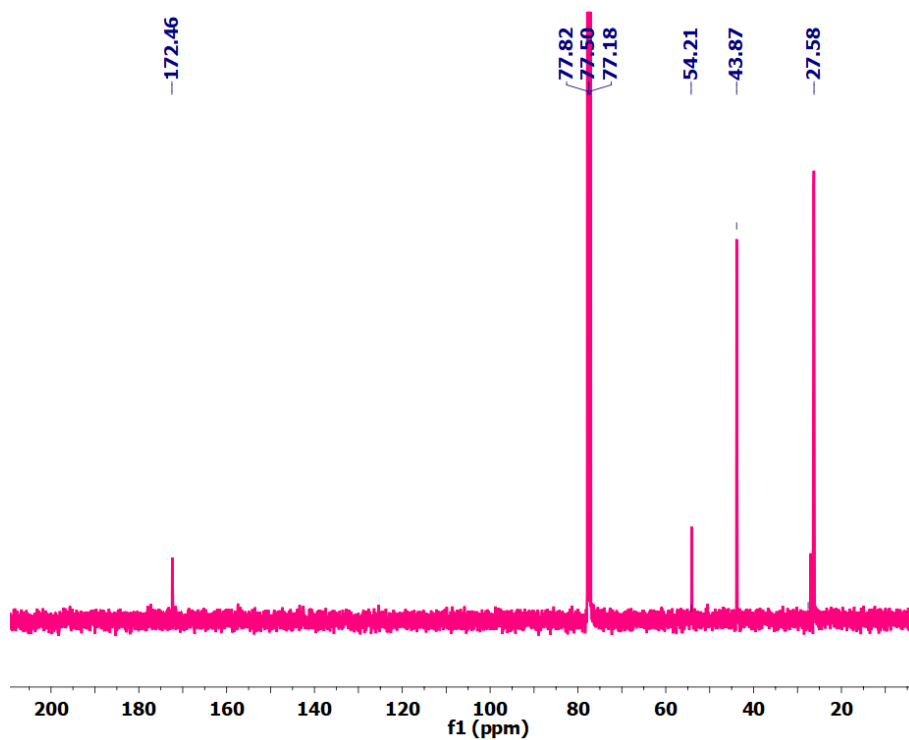
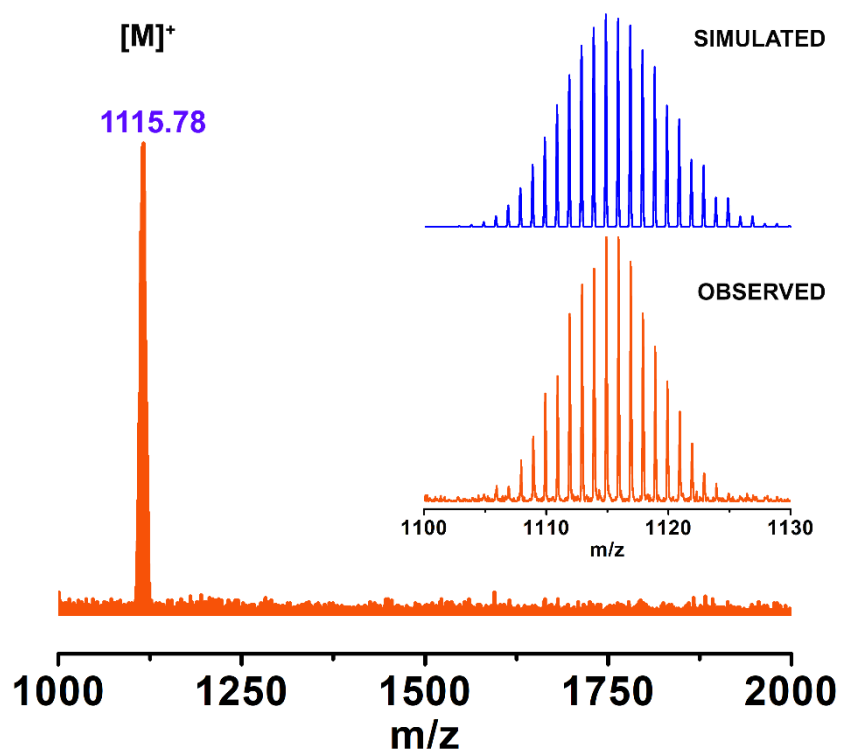
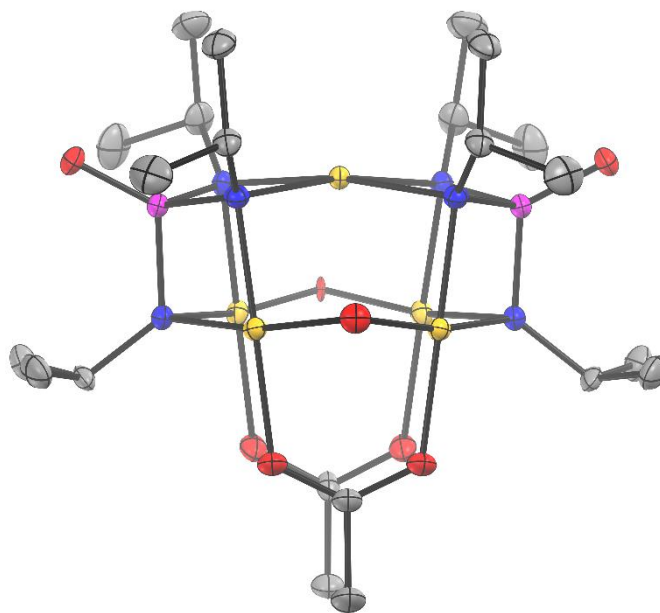


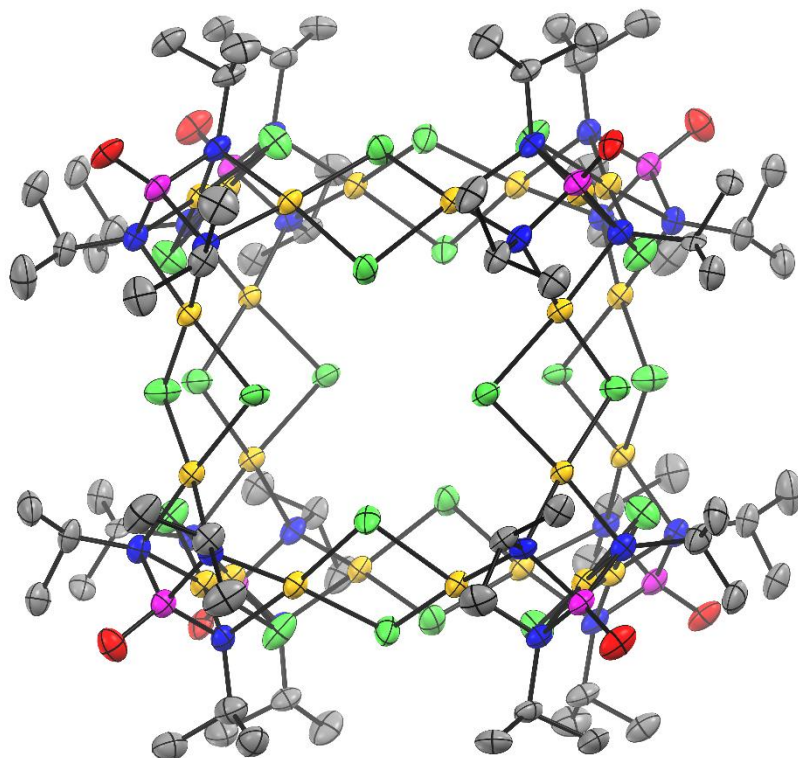
Figure A4.9.  $^{13}\text{C-NMR}$  ( $\text{CDCl}_3$ , 298K) of 4.1.



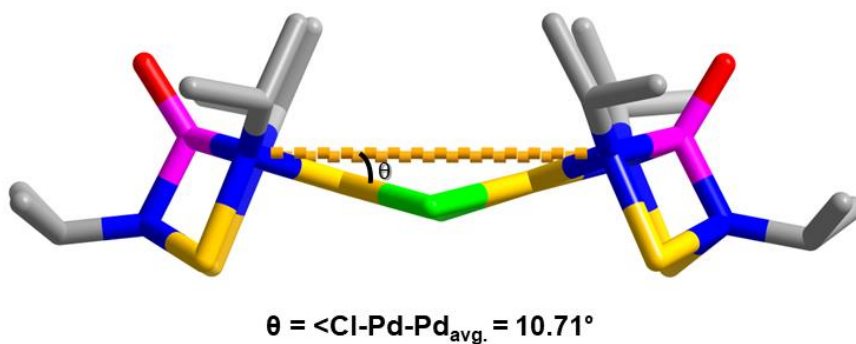
**Figure A4.10.** MALDI-TOF mass spectrum of **4.2** and isotopic distribution of peaks.



**Figure A4.11.** ORTEP diagram at 50% ellipsoids depicting the molecular structures of **4.2**.

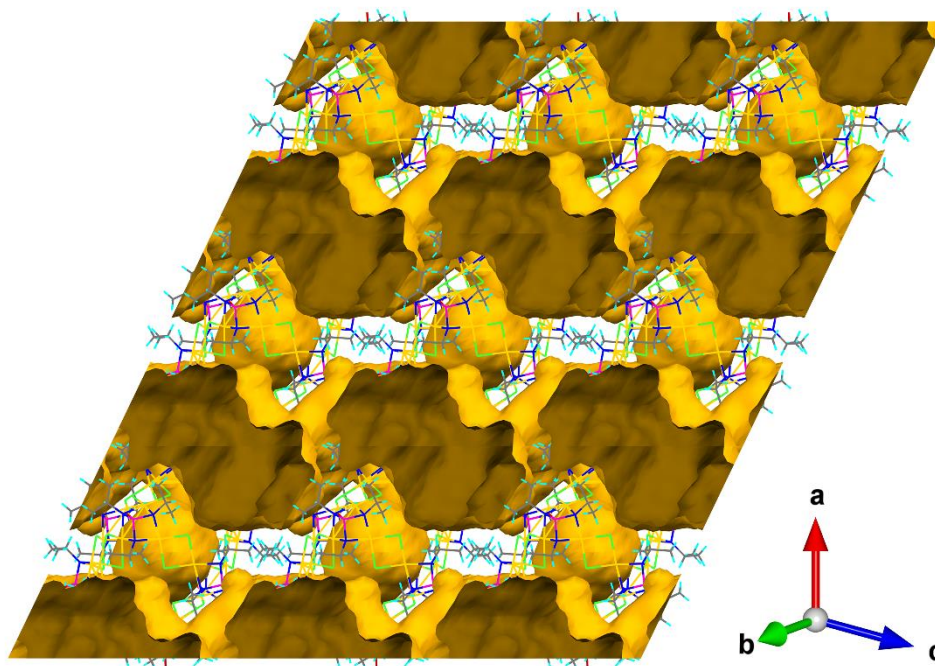


**Figure A4.12.** ORTEP diagram at 50% ellipsoids depicting the molecular structures of **4.1**.



**Figure A4.13.** Average Cl-Pd-Pd angle in **4.1** shows the slight concaving of the Pd-Cl panels by an average angle of  $10.71^\circ$ .

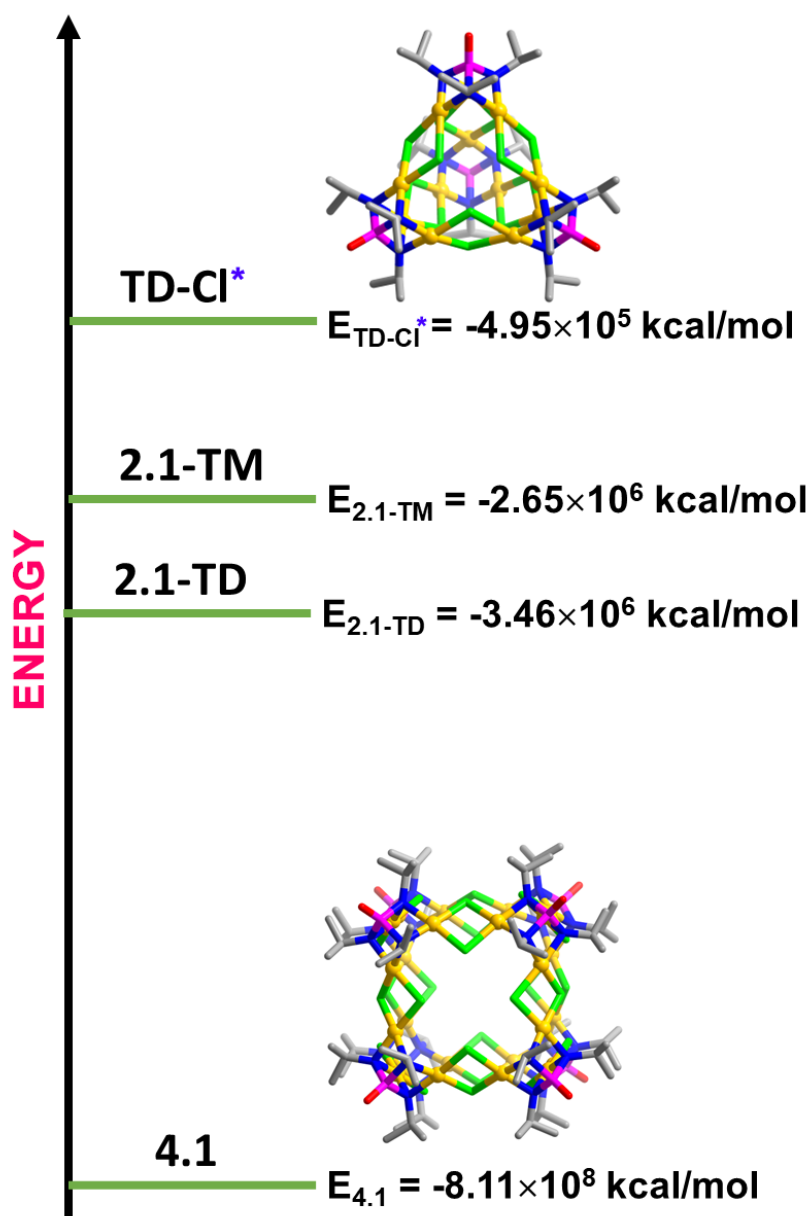
### Structural Illustrations Of Intrinsic And Extrinsic Voids



**Figure A4.14.** Connolly surface view of the 3\*3\*3 packing structure of **4.1** computed by Mercury software showing the location and shape of both the intrinsic and extrinsic cavities.

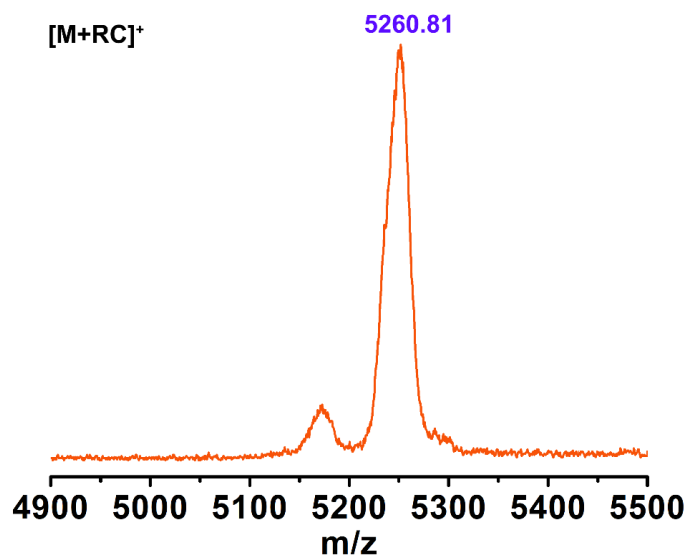
**Table A4.3:** Molecular cavity volume calculated for **4.1** from MSROLL calculations.

Probe Radius (Å)	Volume (Å <sup>3</sup> )
1.3	278.41
1.4	275.09
1.5	273.11

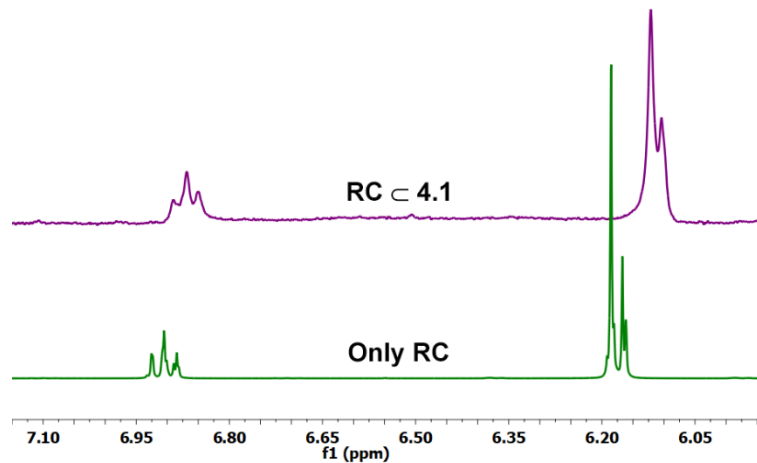


**Figure A4.15.** Schematic representation of the single molecule optimized energies of the various stable and transient intermediates existing in the reaction mixture. The energy of the hypothetical  $\mu_2$ -Cl bridged tetrahedral cage **TD-Cl\*** has been denoted by \* as it is the least possible optimized energy that could be obtained for this cage. Due to the close proximity of the  $[\text{Pd}_3\text{X}]^{+3}$  units and chloride ions, the structure is heavily strained and soon collapses on further cycles of geometry optimization.

### Guest Encapsulation Studies

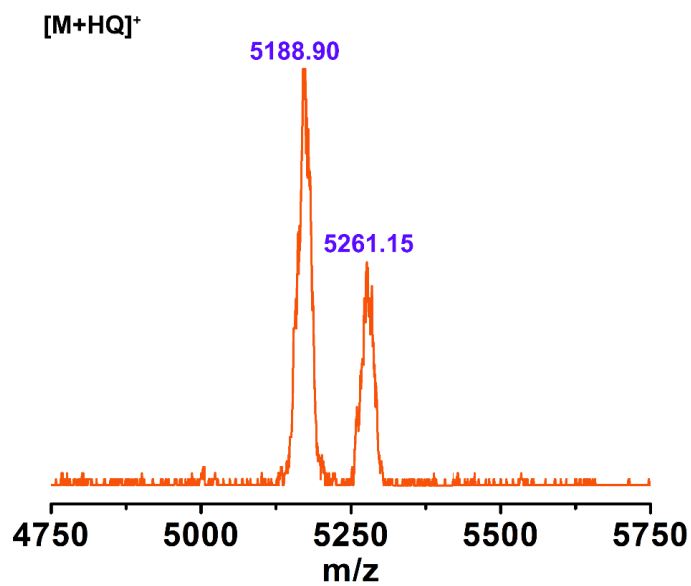


**Figure A4.16.** MALDI-TOF mass spectra of  $[RC \subset 4.1]^+$  (linear mode) where M = molecular mass of 4.1.

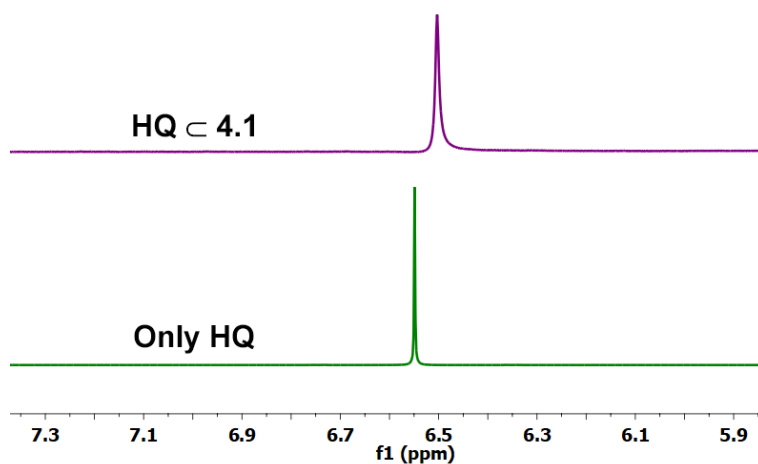


**Figure A4.17.**  $^1\text{H-NMR}$  spectra of RC  $\subset$  4.1 showing upfield shift of the guest protons.

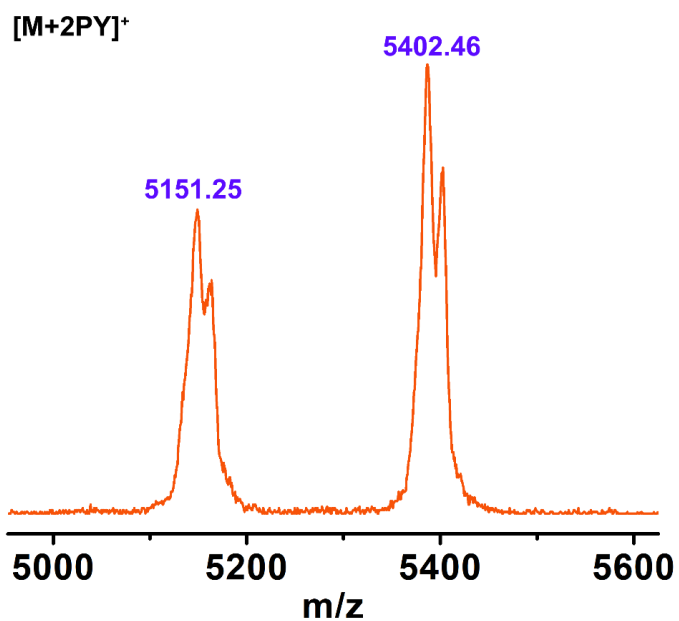




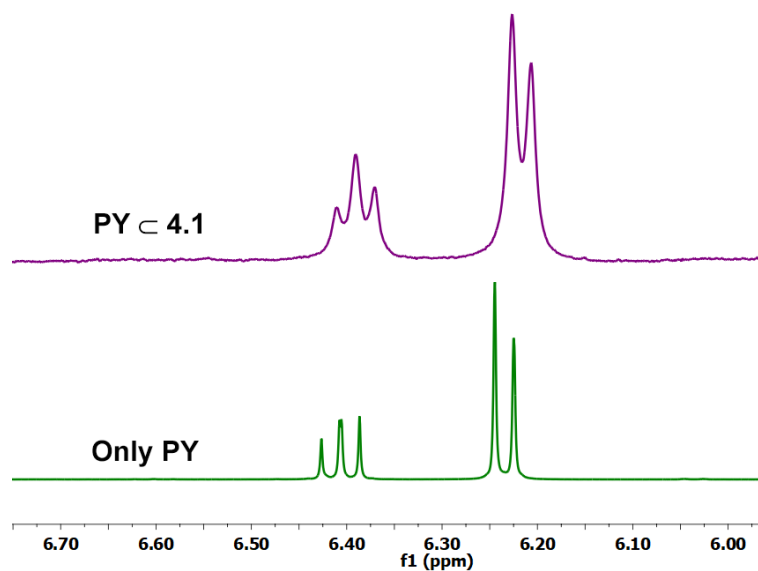
**Figure A4.18.** MALDI-TOF mass spectra of  $[\text{HQ} \subset \mathbf{4.1}]^+$  (linear mode) where M = molecular mass of **4.1**.



**Figure A4.19.** <sup>1</sup>H-NMR spectra of HQ ⊂ **4.1** showing upfield shift of the guest protons.

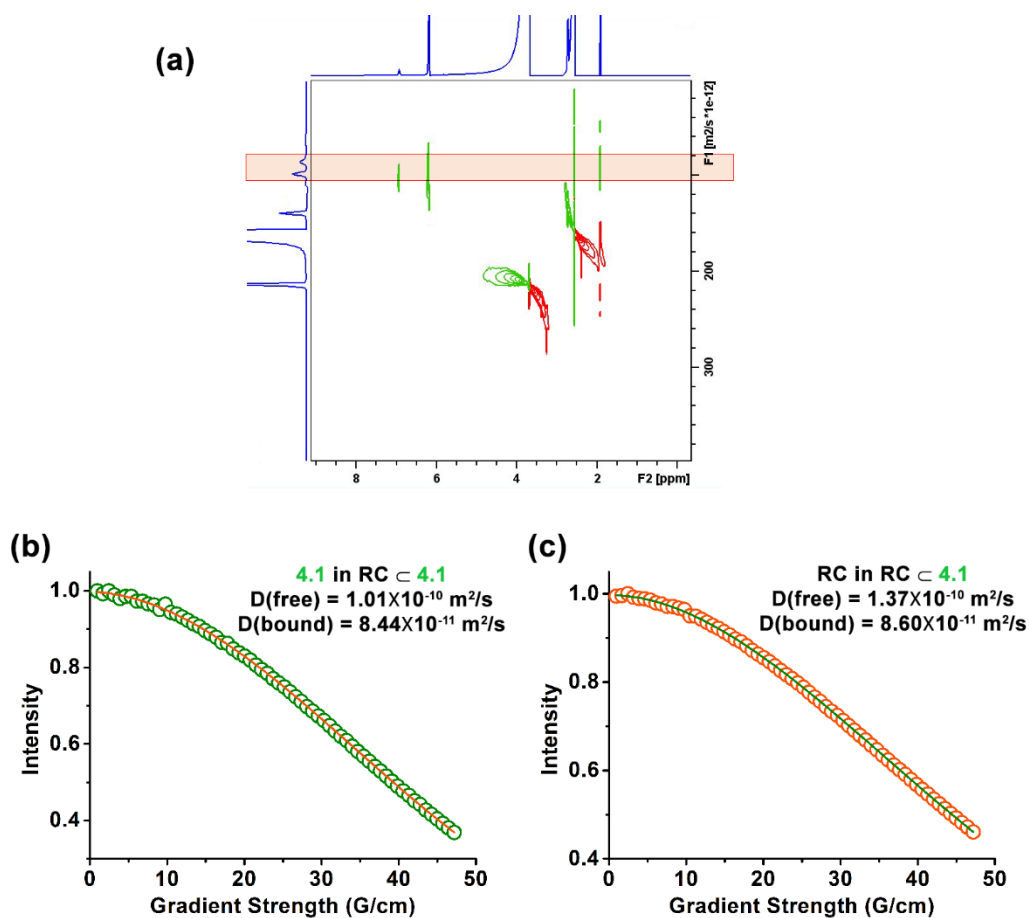


**Figure A4.20.** MALDI-TOF mass spectra of  $[2PY \subset 4.1]^+$  (linear mode) where M = molecular mass of **4.1**.

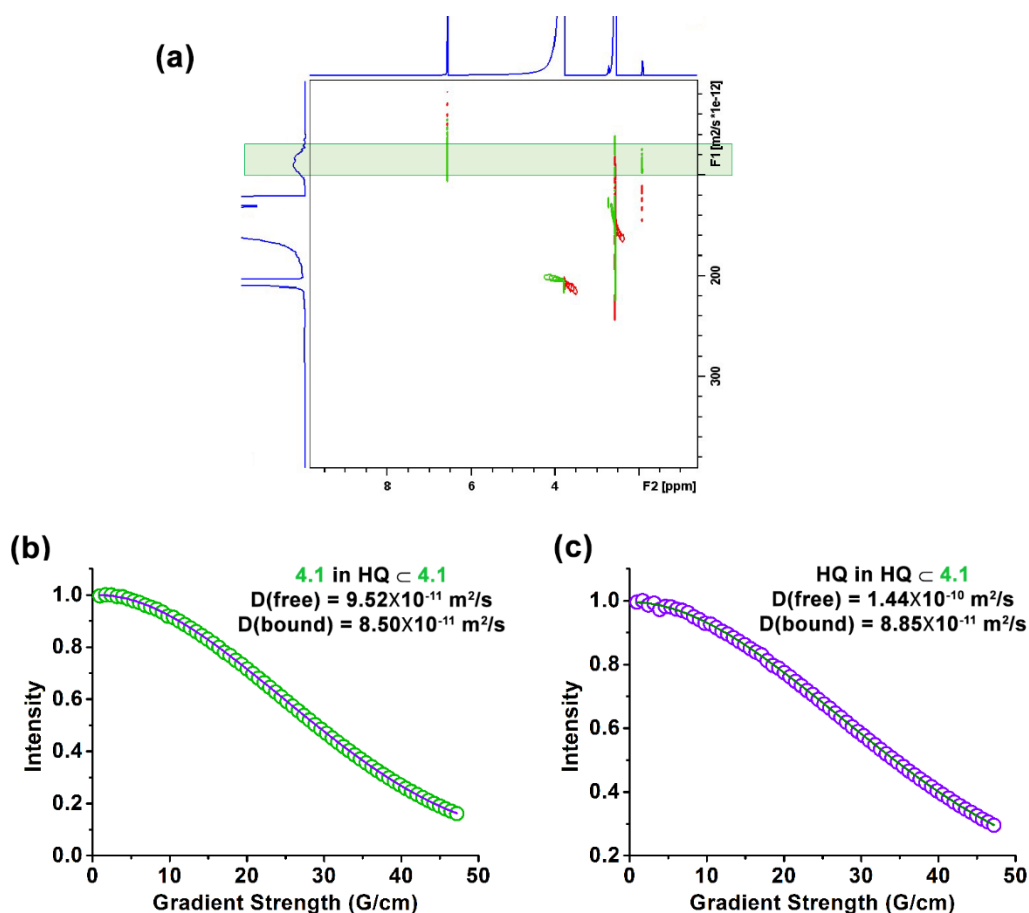


**Figure A4.21.**  $^1\text{H-NMR}$  spectra of  $\text{PY} \subset 4.1$  showing upfield shift of the guest protons.

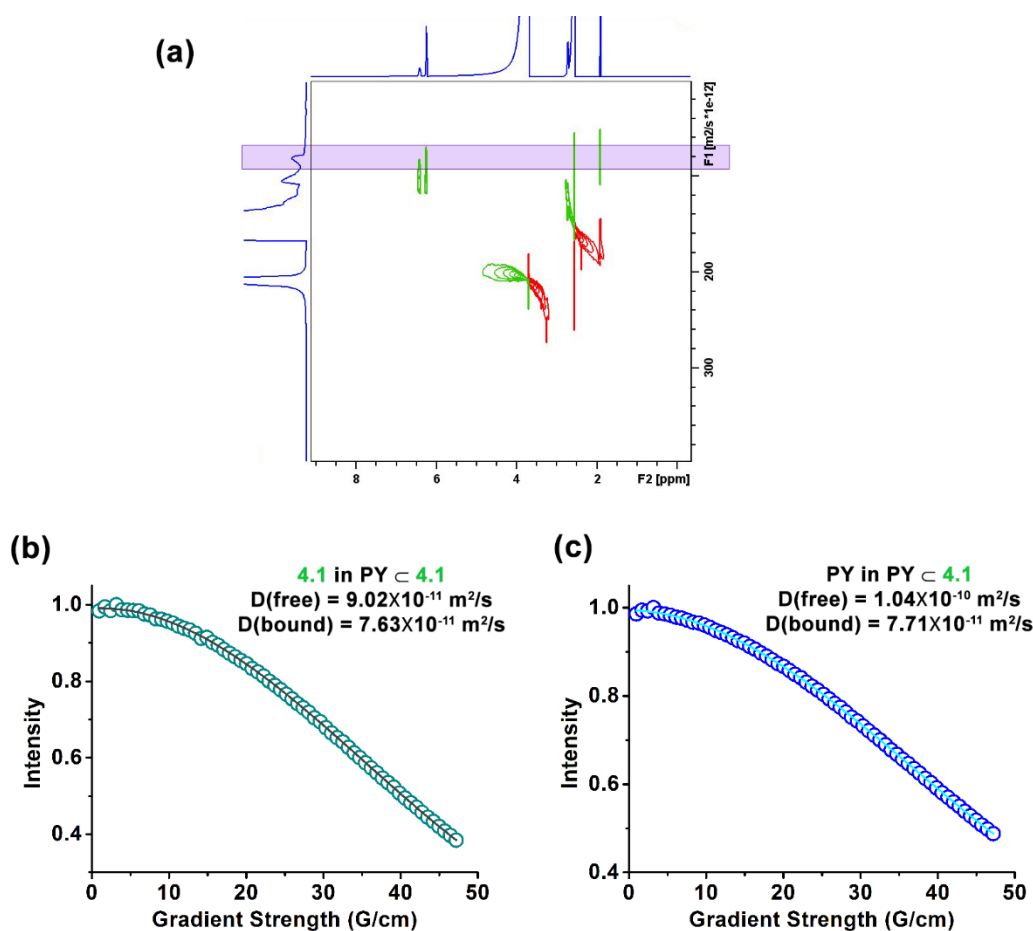
## 2D-DOSY-NMR Characterizations of Host–Guest Complexes



**Figure A4.22:** (a) 2D-DOSY-NMR spectra of  $\text{RC} \subset \mathbf{4.1}$  complex. The green highlighted region corresponds to the diffusion of  $\text{RC} \subset \mathbf{4.1}$  in the bound state. Due to the broad nature of the peaks, the reported  $D$  values were extracted by using the T1/T2 relaxation module in TopSpin 4.1 software as follows: integral decay profile of (b) the  $i$ -Pr  $CH_3$  of host **4.1**, and (c) guest aromatic  $C-H$  atoms in the host–guest system are plotted as a function of gradient strength. The circles represent experimental data and the lines show the best fit using equation 2. The name of the molecules and the diffusion coefficients obtained for free and bound moieties are shown in the corresponding insets.



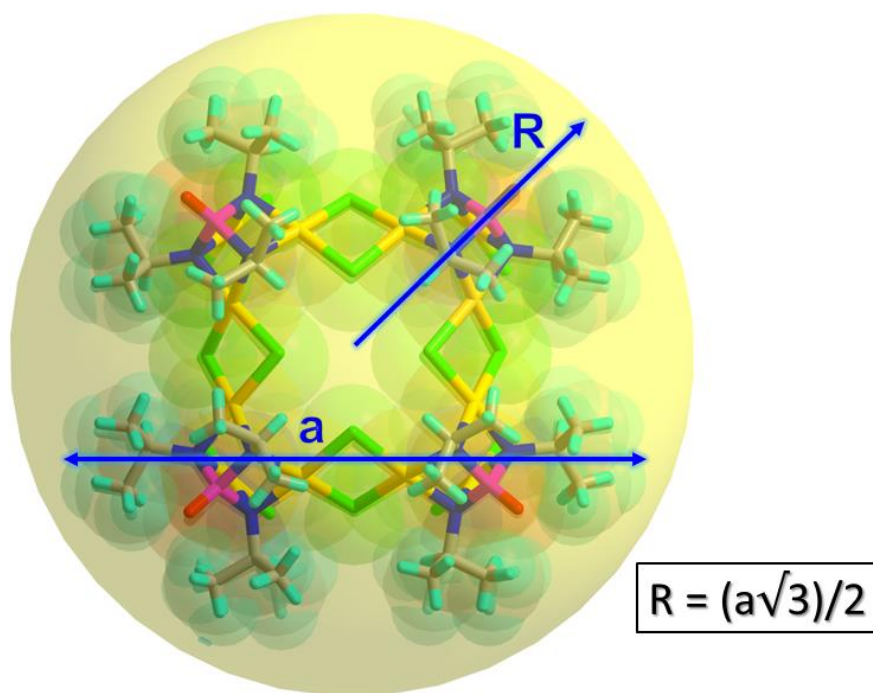
**Figure A4.23:** (a) 2D-DOSY-NMR spectra of  $\text{HQ} \subset 4.1$  complex. The green highlighted region corresponds to the diffusion of  $\text{HQ} \subset 4.1$  in the bound state. Due to the broad nature of the peaks, the reported  $D$  values were extracted by using the T1/T2 relaxation module in TopSpin 4.1 software as follows: integral decay profile of (b) the  $i\text{-Pr } \text{CH}_3$  of host  $4.1$ , and (c) guest aromatic C-H atoms in the host-guest system are plotted as a function of gradient strength. The circles represent experimental data and the lines show the best fit using equation 2. The name of the molecules and the diffusion coefficients obtained for free and bound moieties are shown in the corresponding insets.



**Figure A4.24:** (a) 2D-DOSY-NMR spectra of  $PY \subset 4.1$  complex. The green highlighted region corresponds to the diffusion of  $PY \subset 4.1$  in the bound state. Due to the broad nature of the peaks, the reported  $D$  values were extracted by using the T1/T2 relaxation module in TopSpin 4.1 software as follows: integral decay profile of (b) the  $i\text{-Pr } CH_3$  of host  $4.1$ , and (c) guest aromatic  $C-H$  atoms in the host-guest system are plotted as a function of gradient strength. The circles represent experimental data and the lines show the best fit using equation 2. The name of the molecules and the diffusion coefficients obtained for free and bound moieties are shown in the corresponding insets.

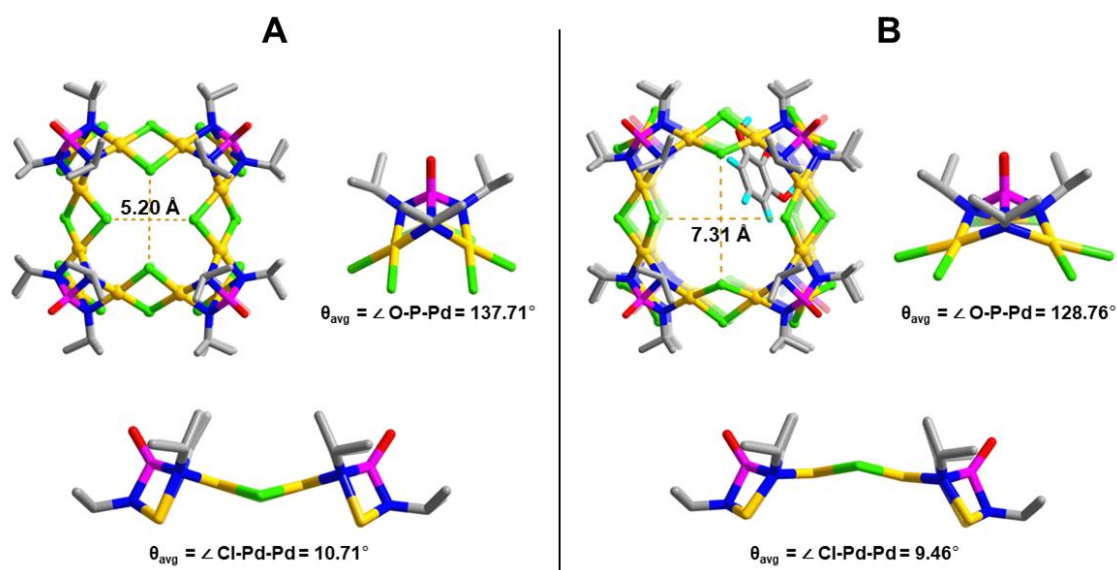
**Table 4.4.** Diffusion coefficients as obtained from the DOSY experiment for all host–guest systems. All the reported diffusion coefficients were obtained using the T1/T2 relaxation module in TopSpin 4.1 software. The standard deviations ( $\pm$ )<sup>a</sup> are given in parentheses.

Host–Guest Systems	Diffusion Coefficient ( $\times 10^{-11}$ m <sup>2</sup> /s)			
	Host		Guest	
	Free	Bound	Free	Bound
RC $\subset$ 4.1	10.10(1) <sup>a</sup>	8.44(2)	13.70(1)	8.60(3)
HQ $\subset$ 4.1	9.52(2)	8.50(1)	14.42(2)	8.85(1)
PY $\subset$ 4.1	9.02(3)	7.63(2)	10.41(1)	7.71(2)

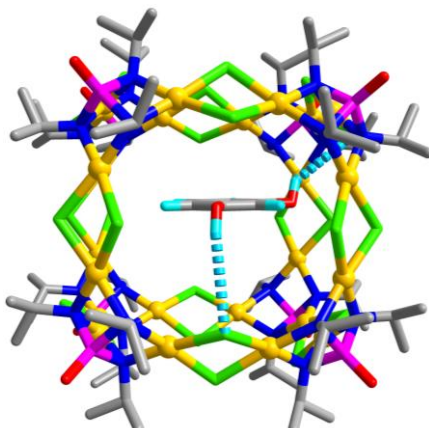


**Figure A4.25.** Schematic representation of hydrodynamic radii of Guest  $\subset$  4.1 systems

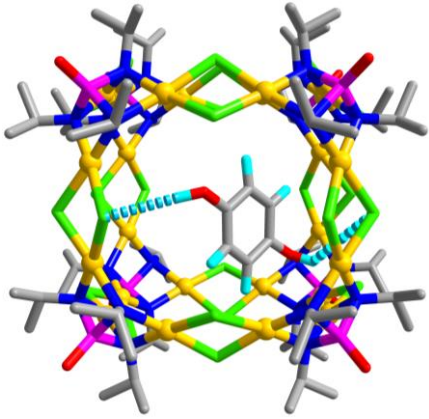
## DFT Optimised Structures and Possible Non-Classical Interactions Present within the Host-Guest Complexes



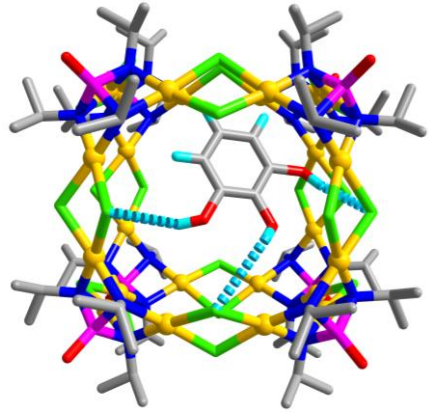
**Figure A4.26.** Comparison of the structural features of the cube **4.1** in absence of guest (A) and in presence of guest (B).

	<b>D-H...A</b>	<b>d(H...A)</b> (Å)	<b>d(D...A)</b> (Å)	<b>&lt; (D-H...A)</b> (°)
	O9-H173...Cl21	3.406(6)	4.411(2)	170.3(1)
	O10-H174...Cl14	3.471(1)	3.131(2)	142.1(2)

**Figure A4.27.** Potential non-covalent interactions responsible for the stabilization of the host-guest assemblies and a summary of the computed non-classical H-bonds in **RC**  $\subset$  **4.1**.

	<b>D-H...A</b>	<b>d(H...A) (Å)</b>	<b>d(D...A) (Å)</b>	<b>&lt; (D-H...A) (°)</b>
	O10- H174...Cl7	2.301(1)	4.310(3)	123.4(1)
	O9- H171...Cl16	2.851(1)	3.566(3)	160.3(1)

**Figure A4.28.** Potential non-covalent interactions responsible for the stabilization of the host–guest assemblies and a summary of the computed non-classical H-bonds in **HQ**  $\subset$  **4.1**.

	<b>D-H...A</b>	<b>d(H...A) (Å)</b>	<b>d(D...A) (Å)</b>	<b>&lt; (D-H...A) (°)</b>
	O11- H174...Cl16	3.101(1)	3.783(2)	129.3(2)
	O9- H173...Cl7	2.488(1)	3.431(4)	170.9(2)
	O10- H172...Cl11	3.451(1)	4.264(2)	142.1(4)

**Figure A4.29.** Potential non-covalent interactions responsible for the stabilization of the host–guest assemblies and a summary of the computed non-classical H-bonds in **PY**  $\subset$  **4.1**.

\*\*\*\*\*



Structural Characterisation Data: 5.1-rac and 5.3**Table A5.1.** Selected bond lengths (Å) and bond angles (°) for **5.1-rac**.

Selected Bonds	Bond lengths (Å)
Pd(1)-N(1)	2.007(8)
Pd(1)-N(2)	2.030(7)
Pd(1)-O(1)	2.064(7)
Pd(1)-O(2)	2.080(7)
N(1)-Pd(4)	2.025(9)
Pd(2)-N(3)	2.015(7)
Pd(2)-N(2)	2.025(7)
Pd(2)-O(3)	2.064(7)
Pd(2)-O(4)	2.070(7)
Pd(3)-N(1)	2.035(8)
Pd(3)-N(3)	2.037(8)
Pd(3)-O(5)	2.064(7)
Pd(3)-O(6)	2.065(7)
Pd(4)-N(4)	1.980(9)
Pd(4)-N(5)	2.006(9)
Pd(4)-O(7)	2.054(7)
Pd(4)-O(8)	2.056(7)
Pd(4)-P(2)	2.718(3)
Pd(4)-Pd(4)	3.1070(14)
Pd(4)-Pd(3)	3.1272(13)
Pd(5)-N(6)	2.014(9)
Pd(5)-N(7)	2.018(8)
Pd(5)-O(9)	2.069(7)

Pd(5)-O(10)	2.070(7)
Pd(6)-N(8)	2.019(8)
Pd(6)-N(7)	2.019(9)
Pd(6)-O(11)	2.058(8)
Pd(6)-O(12)	2.075(7)
Pd(7)-N(10)	2.029(9)
Pd(7)-N(11)	2.045(9)
Pd(7)-O(13)	2.063(8)
Pd(7)-O(14)	2.065(7)
Pd(8)-N(9)	2.017(9)
Pd(8)-N(10)	2.030(8)
Pd(8)-O(15)	2.063(8)
Pd(8)-O(16)	2.064(8)
Pd(4)-N(4)	2.033(8)
Pd(4)-O(17)	2.063(7)
Pd(4)-O(18)	2.068(8)
Pd(3)-N(5)	2.038(9)
Pd(9)-N(11)	2.026(8)
Pd(9)-N(9)	2.040(9)
Pd(10)-N(6)	2.013(9)
Pd(10)-N(8)	2.025(8)
Pd(10)-O(19)	2.060(8)
Pd(10)-O(20)	2.068(7)

Selected Angles	Bond angles (°)
N(20)-Pd(1)-N(21)	77.8(3)
N(20)-Pd(1)-O(1)	177.3(3)
N(21)-Pd(1)-O(1)	99.5(3)
N(20)-Pd(1)-O(2)	99.9(3)
N(21)-Pd(1)-O(2)	177.1(3)
O(1)-Pd(1)-O(2)	82.8(3)
Pd(3)-Pd(1)-Pd(2)	60.65(2)
Pd(3)-N(1)-Pd(4)	101.6(4)
N(3)-Pd(2)-N(21)	77.6(3)
N(3)-Pd(2)-O(3)	100.1(3)
N(21)-Pd(2)-O(3)	177.7(3)
N(3)-Pd(2)-O(4)	177.1(3)
N(21)-Pd(2)-O(4)	99.7(3)

O(3)-Pd(2)-O(4)	82.6(3)
Pd(1)-Pd(2)-Pd(3)	58.88(3)
N(20)-Pd(3)-N(3)	77.5(3)
N(20)-Pd(3)-O(5)	99.3(3)
N(3)-Pd(3)-O(5)	176.6(3)
N(20)-Pd(3)-O(6)	177.7(3)
N(3)-Pd(3)-O(6)	100.5(3)
O(5)-Pd(3)-O(6)	82.7(3)
Pd(1)-Pd(3)-Pd(2)	60.47(2)
N(4)-Pd(4)-N(5)	77.9(4)
N(4)-Pd(4)-O(7)	99.7(3)
N(5)-Pd(4)-O(7)	177.6(3)
N(4)-Pd(4)-O(8)	177.1(3)
N(5)-Pd(4)-O(8)	99.8(3)

O(7)-Pd(4)-O(8)	82.6(3)
Pd(4)-Pd(4)-Pd(3)	60.32(3)
N(6)-Pd(5)-N(7)	77.0(4)
N(6)-Pd(5)-O(9)	177.5(3)
N(7)-Pd(5)-O(9)	100.6(3)
N(6)-Pd(5)-O(10)	99.9(3)
N(7)-Pd(5)-O(10)	176.3(3)
O(9)-Pd(5)-O(10)	82.6(3)
Pd(10)-Pd(5)-Pd(6)	59.38(3)
N(8)-Pd(6)-N(7)	77.1(4)
N(8)-Pd(6)-O(11)	99.4(3)
N(7)-Pd(6)-O(11)	176.5(3)
N(8)-Pd(6)-O(12)	177.8(3)
N(7)-Pd(6)-O(12)	101.1(3)
O(11)-Pd(6)-O(12)	82.4(3)

N(10)-Pd(7)-N(11)	77.1(4)
N(10)-Pd(7)-O(13)	176.9(4)
N(11)-Pd(7)-O(13)	100.0(3)
N(10)-Pd(7)-O(14)	100.0(3)
N(11)-Pd(7)-O(14)	176.6(3)
O(13)-Pd(7)-O(14)	82.9(3)
Pd(9)-Pd(7)-Pd(8)	60.99(3)
N(9)-Pd(8)-N(10)	77.3(4)
N(9)-Pd(8)-O(15)	100.0(4)
N(10)-Pd(8)-O(15)	177.1(4)
N(9)-Pd(8)-O(16)	177.7(4)
N(10)-Pd(8)-O(16)	100.4(3)
O(15)-Pd(8)-O(16)	82.3(3)
Pd(7)-Pd(8)-Pd(9)	59.45(3)
N(1)-Pd(4)-N(4)	77.4(3)

**Table A5.2.** Selected bond lengths (Å) and bond angles (°) for **5.3**.

Selected Bonds	Bond lengths (Å)
Pd(1)-O(9)	2.023(7)
Pd(1)-N(4)	2.028(8)
Pd(1)-N(3)	2.033(8)
Pd(1)-N(1)#1	2.080(9)
N(1)-Pd(2)	2.009(9)
Pd(2)-O(10)	2.014(8)

Pd(2)-N(2)	2.030(9)
Pd(2)-N(5)	2.067(10)
N(4)-Pd(3)#1	2.051(8)
Pd(3)-N(5)	2.014(10)
Pd(3)-O(11)#3	2.044(8)
Pd(3)-N(4)#2	2.051(8)
Pd(3)-N(6)	2.060(9)

Selected Angles	Bond angles (°)
O(9)-Pd(1)-N(4)	96.8(3)
O(9)-Pd(1)-N(3)	81.9(3)
N(4)-Pd(1)-N(3)	178.3(4)
O(9)-Pd(1)-N(1)#1	172.5(3)
N(4)-Pd(1)-N(1)#1	76.6(4)
N(3)-Pd(1)-N(1)#1	104.8(4)

Pd(2)#1-Pd(1)-Pd(3)#1	60.20(3)
N(1)-Pd(2)-N(2)	175.2(4)
O(10)-Pd(2)-N(2)	81.1(3)
N(1)-Pd(2)-N(5)	76.4(4)
O(10)-Pd(2)-N(5)	170.1(4)
N(2)-Pd(2)-N(5)	106.9(4)

### Spectral Characterisation Data: 5.1

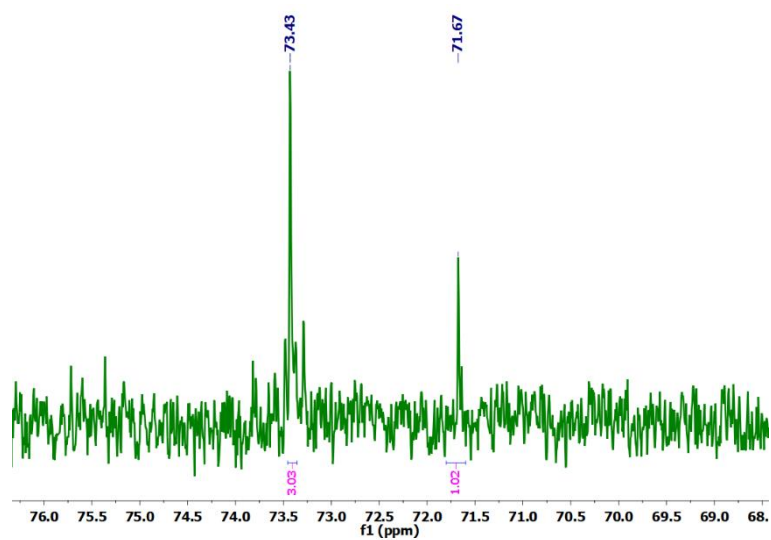


Figure A5.1.  $^{31}\text{P}\{^1\text{H}\}$ -NMR ( $\text{CDCl}_3$ , 298K) of **5.1**.

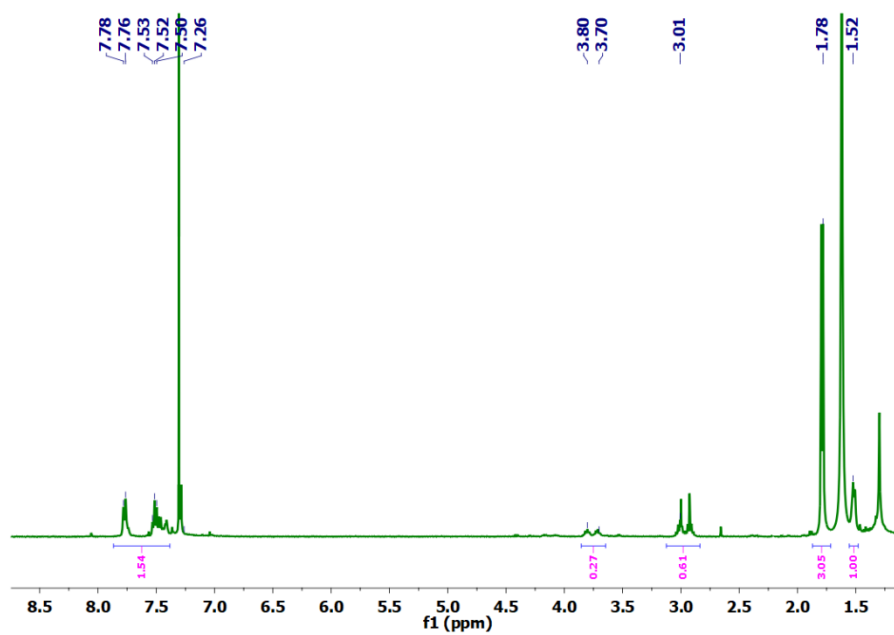


Figure A5.2.  $^1\text{H}$ -NMR ( $\text{CDCl}_3$ , 298K) of **5.1**.

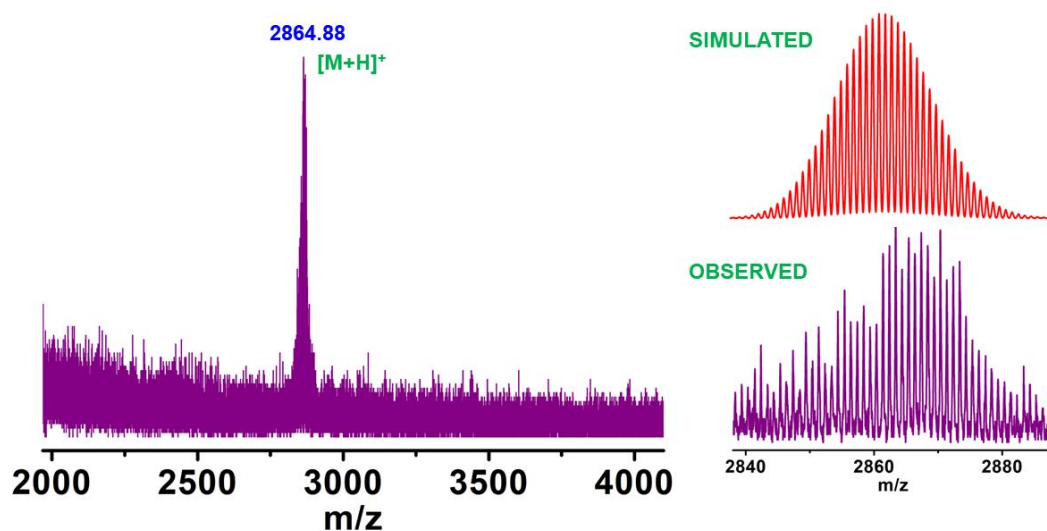


Figure A5.3. MALDI-TOF mass spectrum of **5.1** showing the isotopic distribution of peaks.

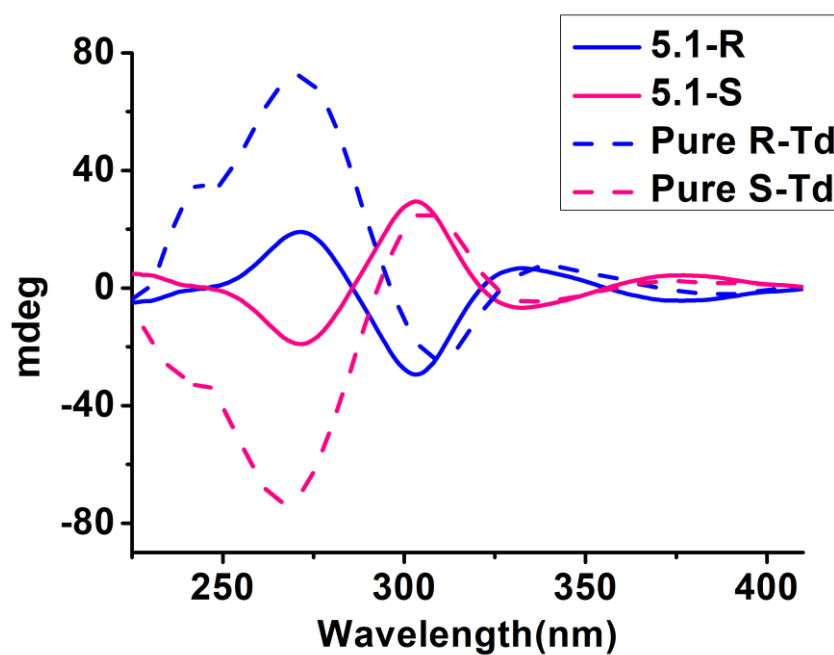
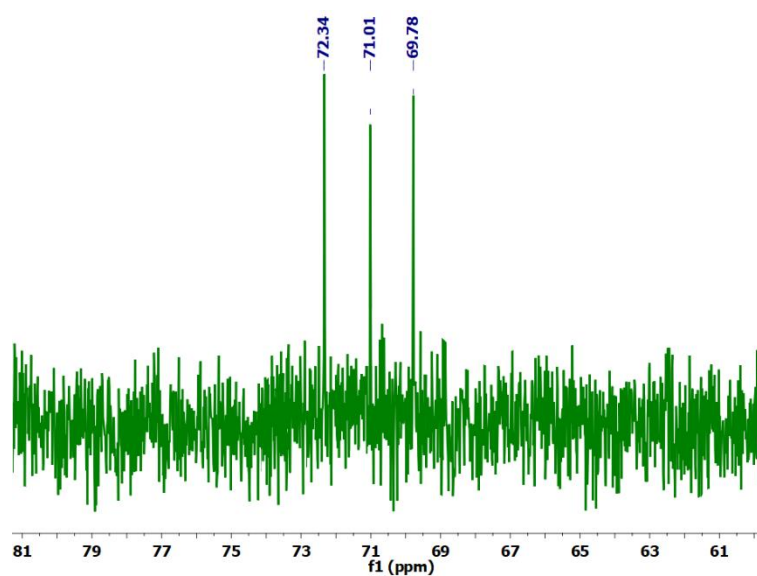


Figure A5.4. Circular dichroism spectra of the self-sorted tetrahedral cages **5.1-R** and **5.1-S** in comparison with the pure chiral cages.

**Table A5.3:** Molecular cavity volume calculated for **5.1-rac** from MSROLL calculations.

Probe Radius (Å)	Volume (Å <sup>3</sup> )
1.3	88.50
1.4	87.13
1.5	86.71

### Spectral Characterisation Data: 5.2

**Figure A5.5.** <sup>31</sup>P{<sup>1</sup>H}-NMR (CDCl<sub>3</sub>, 298K) of **5.2**.

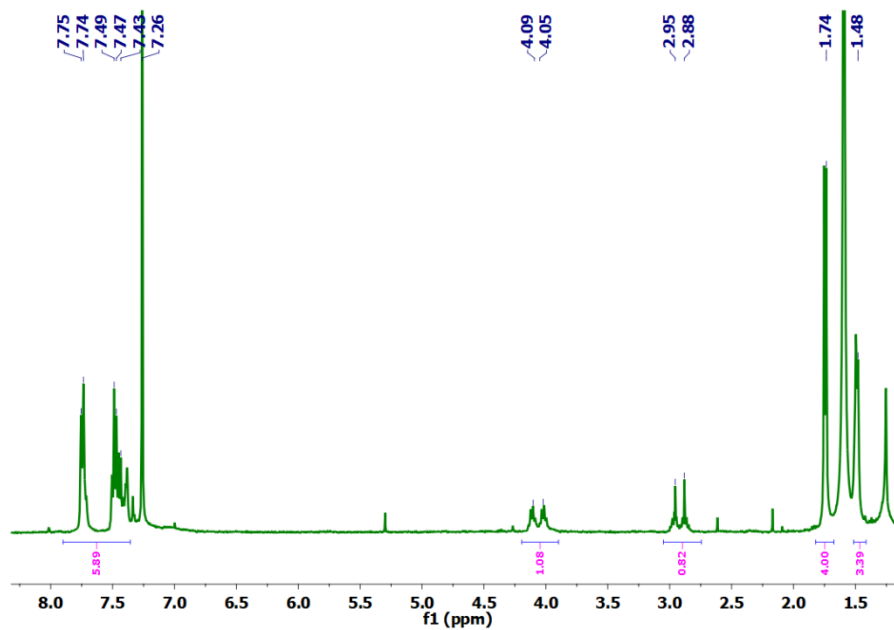


Figure A5.6. <sup>1</sup>H-NMR (CDCl<sub>3</sub>, 298K) of **5.2**.

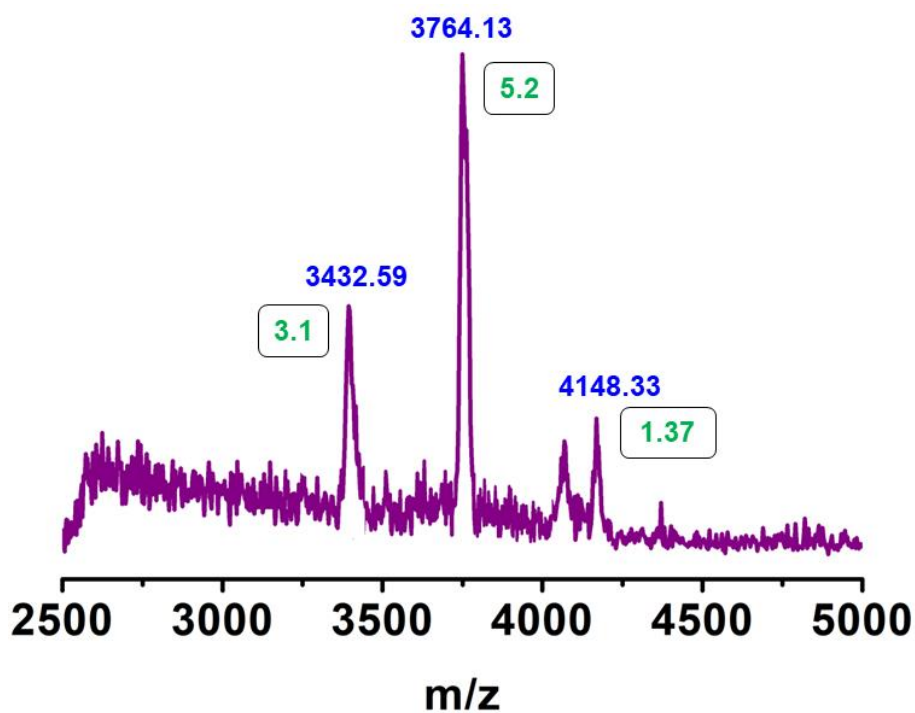
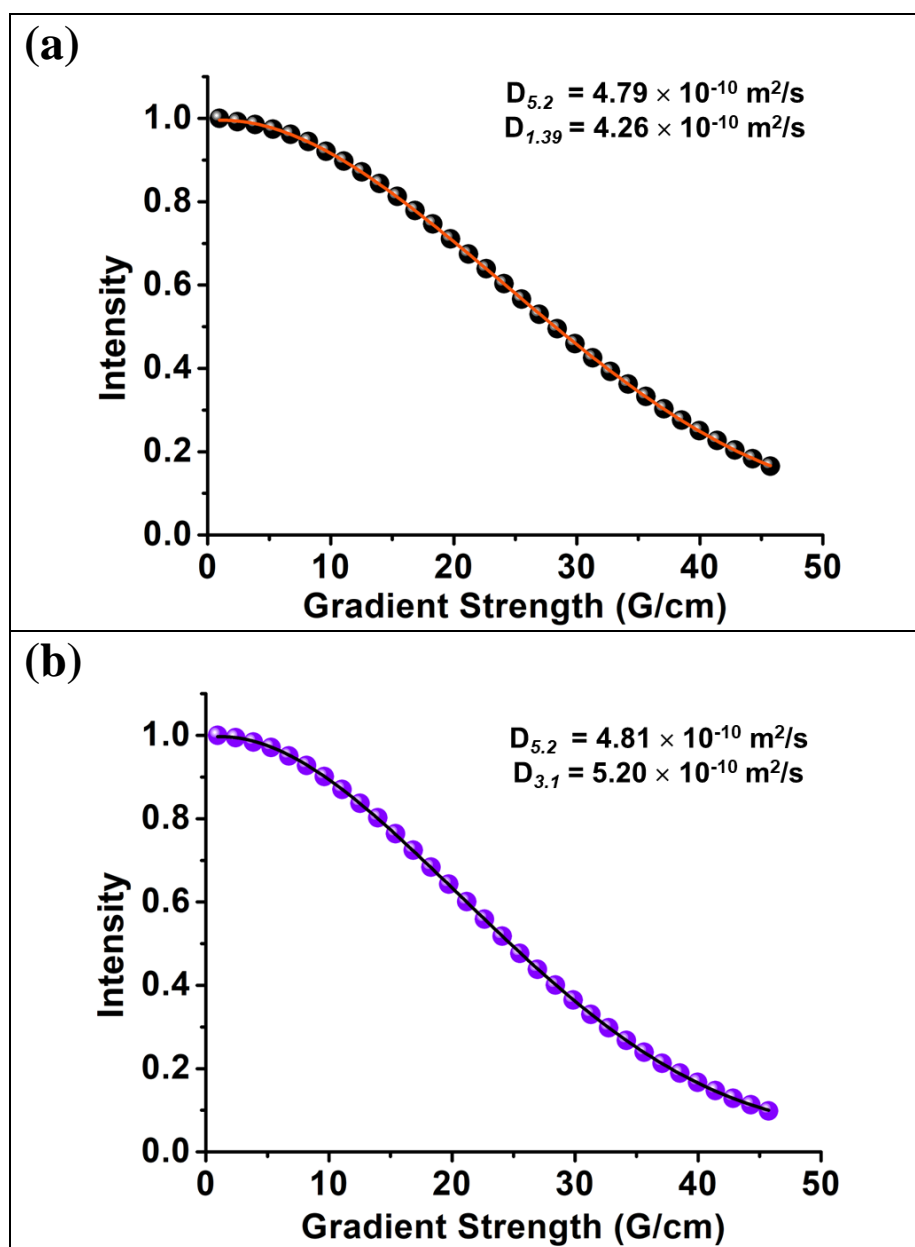


Figure A5.7. MALDI-TOF mass spectrum of **5.2** (linear mode).



**Figure A5.8.** Integral decay profile of the protons (a)  $\delta$  7.75 (chiral) and (b)  $\delta$  1.74 (achiral) ( $\text{CDCl}_3$ , 298 K) in the product mixture containing **5.2** plotted as a function of gradient strength. The circles represent experimental data and the lines show the best fit using equation 2. The name of the corresponding molecules and the diffusion coefficients obtained are shown in the corresponding insets. The reported diffusion coefficients were obtained using the T1/T2 relaxation module in TopSpin 4.1 software.

**Table A5.4.** xyz coordinates of the atoms of the DFT optimized structure of **5.2**.

	266			H	7.93120	14.91980	17.89530
	<b>5.2</b>			H	7.07710	16.23350	17.84470
Pd	5.59760	13.32040	13.26310	H	8.57440	16.28840	18.30860
N	5.82660	15.32680	13.50260	H	9.29980	15.74220	16.23140
O	5.40270	11.30740	13.11880	C	8.47530	17.46300	15.92350
O	5.47230	13.16310	11.22090	H	9.36990	17.62470	15.35920
N	5.76120	13.50260	15.26140	H	7.62610	17.73220	15.33080
Pd	7.82490	15.49040	13.32040	H	8.49800	18.06450	16.80810
Pd	7.76760	13.26310	15.49040	C	4.80170	12.70340	16.08800
Cl	5.49340	8.29940	12.79490	C	3.37410	13.13570	15.86240
C	5.43230	9.50860	11.58360	H	3.19270	13.15680	14.91980
P	5.86330	15.22470	15.22470	H	3.24330	14.01090	16.23350
O	5.02530	16.06270	16.06270	H	2.77940	12.51360	16.28840
N	7.58540	15.26140	15.32680	H	4.89740	11.66930	15.83050
C	5.00000	16.28630	12.70340	C	5.15110	12.88430	17.57690
C	5.42590	11.94210	10.84560	N	5.82660	5.76120	7.58540
C	5.39430	10.87300	11.96110	N	5.76120	7.58540	5.82660
C	5.43230	11.57940	9.50440	Pd	7.82490	5.59760	7.76760
C	5.42590	9.14590	10.24240	Pd	7.76760	7.82490	5.59760
C	5.22560	17.71390	13.13570	P	5.86330	5.86330	5.86330
H	6.16820	17.89530	13.15680	O	5.02530	5.02530	5.02530
H	4.85450	17.84470	14.01090	N	7.58540	5.82660	5.76120
H	4.79960	18.30860	12.51360	C	5.00000	4.80170	8.38460
H	5.25750	16.19060	11.66930	C	5.22560	3.37410	7.95230
C	3.51110	15.93690	12.88430	H	6.16820	3.19270	7.93120
Cl	5.49340	12.78860	8.29310	H	4.85450	3.24330	7.07710
C	5.39430	10.21500	9.12690	H	4.79960	2.77940	8.57440
O	5.47230	7.92490	9.86710	H	5.25750	4.89740	9.41870
O	5.40270	9.78060	7.96920	C	3.51110	5.15110	8.20370
Pd	5.59760	7.76760	7.82490	C	8.38460	5.00000	4.80170
C	8.38460	16.08800	16.28630	C	7.95230	5.22560	3.37410
C	7.95230	15.86240	17.71390	H	7.93120	6.16820	3.19270



H	7.07710	4.85450	3.24330
H	8.57440	4.79960	2.77940
H	9.41870	5.25750	4.89740
C	8.20370	3.51110	5.15110
C	4.80170	8.38460	5.00000
C	3.37410	7.95230	5.22560
H	3.19270	7.93120	6.16820
H	3.24330	7.07710	4.85450
H	2.77940	8.57440	4.79960
H	4.89740	9.41870	5.25750
C	5.15110	8.20370	3.51110
O	7.96920	15.68530	11.30740
O	9.86710	15.61570	13.16310
Cl	8.29310	15.59460	8.29940
C	9.50440	15.65570	9.50860
C	10.24240	15.66210	11.94210
C	9.12690	15.69370	10.87300
C	11.58360	15.65570	11.57940
C	10.84560	15.66210	9.14590
Cl	12.79490	15.59460	12.78860
C	11.96110	15.69370	10.21500
O	11.22090	15.61570	7.92490
O	13.11880	15.68530	9.78060
Pd	13.26310	15.49040	7.76760
O	7.96920	5.40270	9.78060
O	9.86710	5.47230	7.92490
Cl	8.29310	5.49340	12.78860
C	9.50440	5.43230	11.57940
C	10.24240	5.42590	9.14590
C	9.12690	5.39430	10.21500
C	11.58360	5.43230	9.50860
C	10.84560	5.42590	11.94210
Cl	12.79490	5.49340	8.29940

C	11.96110	5.39430	10.87300
O	11.22090	5.47230	13.16310
O	13.11880	5.40270	11.30740
Pd	13.26310	5.59760	13.32040
O	9.78060	13.11880	15.68530
O	7.92490	11.22090	15.61570
Cl	12.78860	12.79490	15.59460
C	11.57940	11.58360	15.65570
C	9.14590	10.84560	15.66210
C	10.21500	11.96110	15.69370
C	9.50860	9.50440	15.65570
C	11.94210	10.24240	15.66210
Cl	8.29940	8.29310	15.59460
C	10.87300	9.12690	15.69370
O	13.16310	9.86710	15.61570
O	11.30740	7.96920	15.68530
Pd	13.32040	7.82490	15.49040
N	15.32680	7.58540	15.26140
N	13.50260	5.82660	15.32680
Pd	15.49040	7.76760	13.26310
P	15.22470	5.86330	15.22470
O	16.06270	5.02530	16.06270
N	15.26140	5.76120	13.50260
C	16.28630	8.38460	16.08800
C	17.71390	7.95230	15.86240
H	17.89530	7.93120	14.91980
H	17.84470	7.07710	16.23350
H	18.30860	8.57440	16.28840
H	16.23140	9.29980	15.74220
C	15.92350	8.47530	17.46300
C	16.08800	7.38920	18.31490
H	16.41700	6.58370	17.98380
C	15.75700	7.50520	19.66030

C	15.43220	9.67730	17.95640
H	15.32250	10.40480	17.38710
C	15.10110	9.79330	19.30180
H	14.77210	10.59880	19.63290
C	15.26560	8.70720	20.15380
H	15.04420	8.78530	21.05430
H	15.86660	6.77770	20.22970
C	16.08800	4.80170	12.70340
C	15.86240	3.37410	13.13570
H	14.91980	3.19270	13.15680
H	16.23350	3.24330	14.01090
H	16.28840	2.77940	12.51360
H	15.74220	4.85660	11.78820
C	17.46300	5.16450	12.61270
C	18.31490	5.00000	13.69880
H	17.98380	4.67100	14.50430
C	19.66030	5.33100	13.58280
C	17.95640	5.65580	11.41070
H	17.38710	5.76550	10.68320
C	19.30180	5.98690	11.29470
H	19.63290	6.31590	10.48920
C	20.15380	5.82240	12.38080
H	21.05430	6.04380	12.30270
H	20.22970	5.22140	14.31030
C	12.70340	5.00000	16.28630
C	13.13570	5.22560	17.71390
H	13.15680	6.16820	17.89530
H	14.01090	4.85450	17.84470
H	12.51360	4.79960	18.30860
H	11.78820	5.34580	16.23140
C	12.61270	3.62500	15.92350
C	13.69880	2.77310	16.08800
H	14.50430	3.10420	16.41700

C	13.58280	1.42770	15.75700
C	11.41070	3.13160	15.43220
H	10.68320	3.70090	15.32250
C	11.29470	1.78620	15.10110
H	10.48920	1.45510	14.77210
C	12.38080	0.93420	15.26560
H	12.30270	0.03370	15.04420
H	14.31030	0.85830	15.86660
O	9.78060	7.96920	5.40270
O	7.92490	9.86710	5.47230
Cl	12.78860	8.29310	5.49340
C	11.57940	9.50440	5.43230
C	9.14590	10.24240	5.42590
C	10.21500	9.12690	5.39430
C	9.50860	11.58360	5.43230
C	11.94210	10.84560	5.42590
Cl	8.29940	12.79490	5.49340
C	10.87300	11.96110	5.39430
O	13.16310	11.22090	5.47230
O	11.30740	13.11880	5.40270
Pd	13.32040	13.26310	5.59760
O	15.68530	9.78060	13.11880
O	15.61570	7.92490	11.22090
Cl	15.59460	12.78860	12.79490
C	15.65570	11.57940	11.58360
C	15.66210	9.14590	10.84560
C	15.69370	10.21500	11.96110
C	15.65570	9.50860	9.50440
C	15.66210	11.94210	10.24240
Cl	15.59460	8.29940	8.29310
C	15.69370	10.87300	9.12690
O	15.61570	13.16310	9.86710
O	15.68530	11.30740	7.96920

Pd	15.49040	13.32040	7.82490
N	15.26140	15.32680	7.58540
N	15.32680	13.50260	5.82660
P	15.22470	15.22470	5.86330
O	16.06270	16.06270	5.02530
N	13.50260	15.26140	5.76120
C	16.08800	16.28630	8.38460
C	15.86240	17.71390	7.95230
H	14.91980	17.89530	7.93120
H	16.23350	17.84470	7.07710
H	16.28840	18.30860	8.57440
H	15.74220	16.23140	9.29980
C	17.46300	15.92350	8.47530
C	18.31490	16.08800	7.38920
H	17.98380	16.41700	6.58370
C	19.66030	15.75700	7.50520
C	17.95640	15.43220	9.67730
H	17.38710	15.32250	10.40480
C	19.30180	15.10110	9.79330
H	19.63290	14.77210	10.59880
C	20.15380	15.26560	8.70720
H	21.05430	15.04420	8.78530
H	20.22970	15.86660	6.77770
C	12.70340	16.08800	4.80170
C	13.13570	15.86240	3.37410
H	13.15680	14.91980	3.19270
H	14.01090	16.23350	3.24330
H	12.51360	16.28840	2.77940
H	11.78820	15.74220	4.85660
C	12.61270	17.46300	5.16450
C	13.69880	18.31490	5.00000
H	14.50430	17.98380	4.67100
C	13.58280	19.66030	5.33100

C	11.41070	17.95640	5.65580
H	10.68320	17.38710	5.76550
C	11.29470	19.30180	5.98690
H	10.48920	19.63290	6.31590
C	12.38080	20.15380	5.82240
H	12.30270	21.05430	6.04380
H	14.31030	20.22970	5.22140
C	16.28630	12.70340	5.00000
C	17.71390	13.13570	5.22560
H	17.89530	13.15680	6.16820
H	17.84470	14.01090	4.85450
H	18.30860	12.51360	4.79960
H	16.23140	11.78820	5.34580
C	15.92350	12.61270	3.62500
C	16.08800	13.69880	2.77310
H	16.41700	14.50430	3.10420
C	15.75700	13.58280	1.42770
C	15.43220	11.41070	3.13160
H	15.32250	10.68320	3.70090
C	15.10110	11.29470	1.78620
H	14.77210	10.48920	1.45510
C	15.26560	12.38080	0.93420
H	15.04420	12.30270	0.03370
H	15.86660	14.31030	0.85830
H	4.31620	12.58920	18.17760
H	5.99800	12.27750	17.82080
H	5.38180	13.91170	17.76690
H	2.91100	16.77750	12.60470
H	3.26330	15.10020	12.26510
H	3.32450	15.69030	13.90860
H	4.31610	8.49850	2.91040
H	5.99780	8.81070	3.26720
H	5.38210	7.17640	3.32120

H	8.50680	2.91020	4.31920
H	8.80400	3.26920	6.00320
H	7.17480	3.31940	5.37350

H	2.91090	4.31120	8.48520
H	3.26380	5.98910	8.82130
H	3.32410	5.39570	7.17900

### Spectral Characterisation Data: 5.3

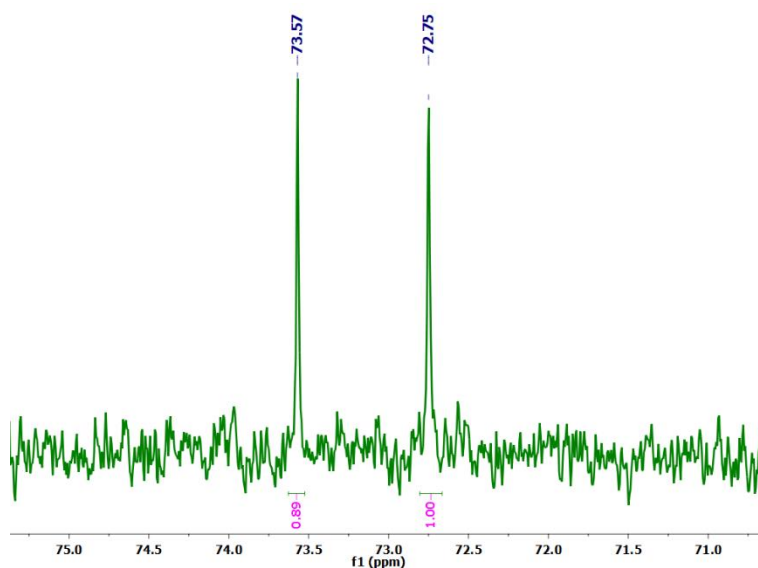


**Figure A5.9.**  $^{31}\text{P}\{^1\text{H}\}$ -NMR ( $\text{CDCl}_3$ , 298K) of the reaction mixture showing the peaks pertaining to both **5.3** and **1.35**.

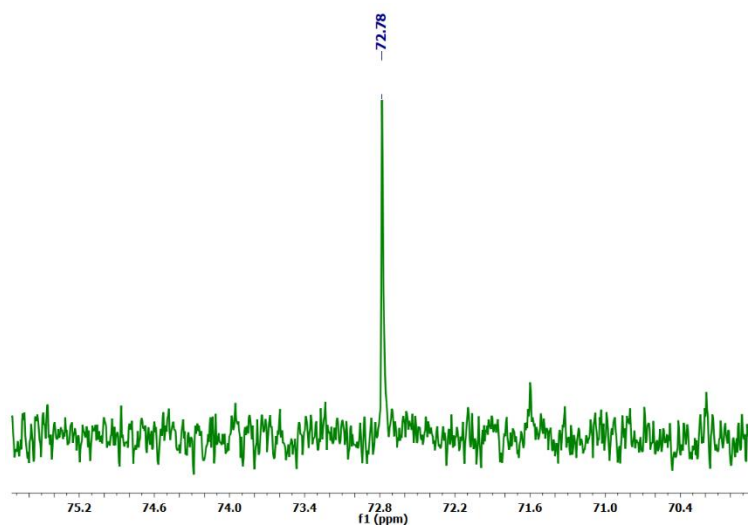


**Figure A5.10.**  $^{31}\text{P}\{^1\text{H}\}$ -NMR ( $\text{CDCl}_3$ , 298K) of the pure cage **5.3**.

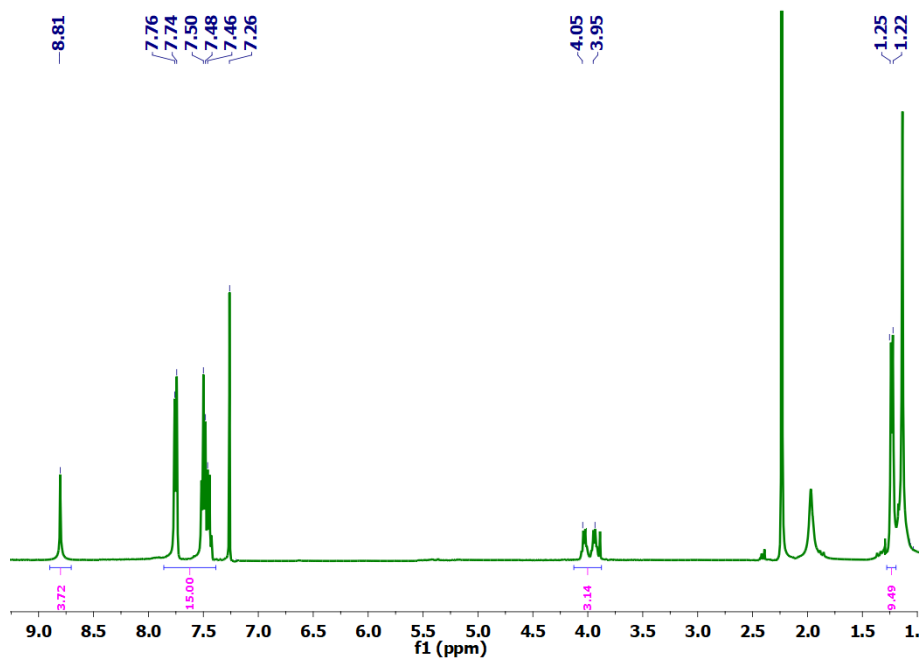


Figure A5.11.  $^1\text{H-NMR}$  ( $\text{CDCl}_3$ , 298K) of pure cage **5.3**.

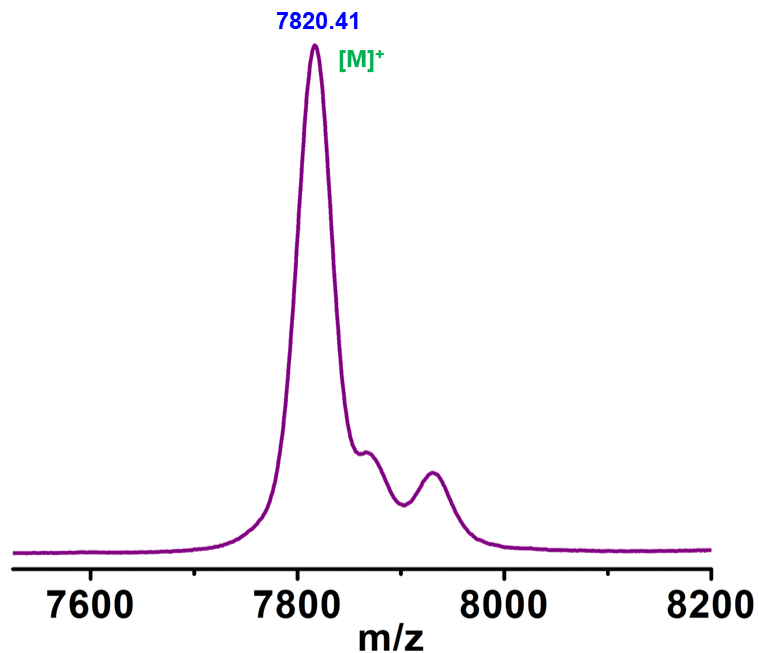
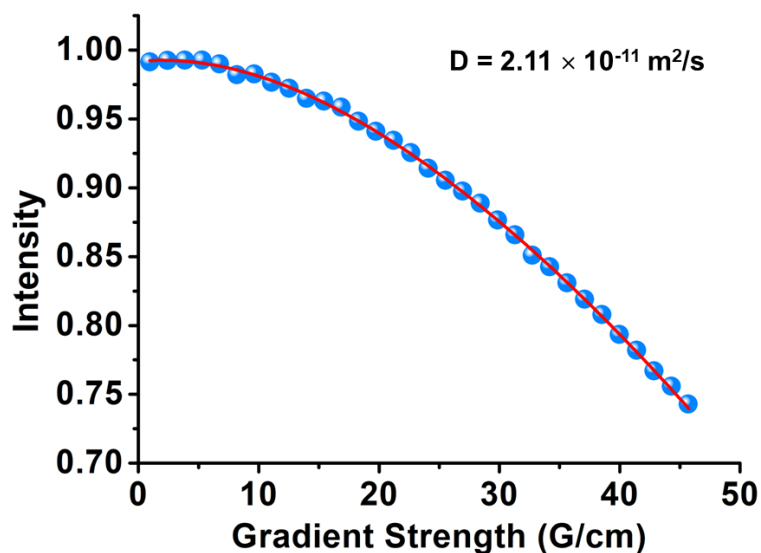
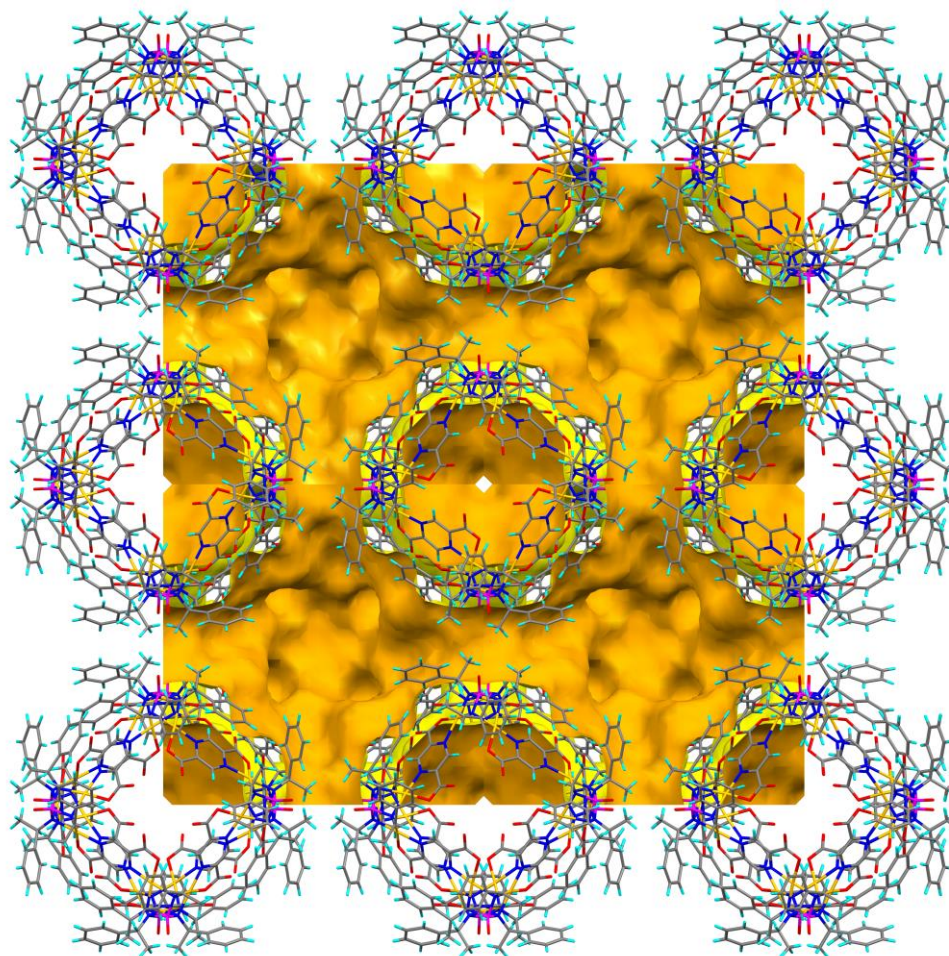


Figure A5.12. MALDI-TOF mass spectrum (linear mode) of **5.3**.



**Figure A5.13.** Integral decay profile of the protons  $\delta$  8.81 ( $\text{CDCl}_3$ , 298 K) in the tetrahedral cage **5.3** plotted as a function of gradient strength. The circles represent experimental data and the lines show the best fit using equation 1. The diffusion coefficient obtained is shown in the corresponding insets. The reported diffusion coefficient has been obtained using the T1/T2 relaxation module in TopSpin 4.1 software.

### Structural Illustrations Of Intrinsic And Extrinsic Voids in 5.3



**Figure A5.14.** Connolly surface view (along the c-axis) of the  $2 \times 2 \times 2$  packing structure of **5.3** computed by Mercury software along with its solvent accessible surface in tetragonal  $I422$  phase.

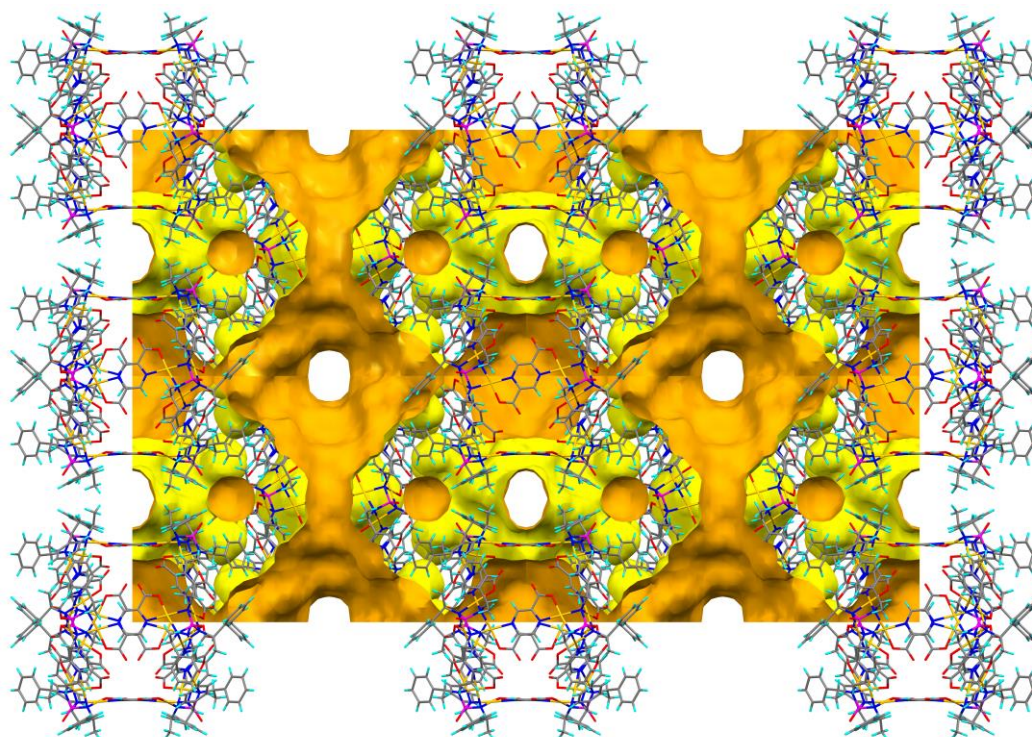


**Figure A5.15.** Connolly surface view (along the b-axis) of the  $2 \times 2 \times 2$  packing structure of **5.3** computed by Mercury software along with its solvent accessible surface in tetragonal  $I422$  phase.



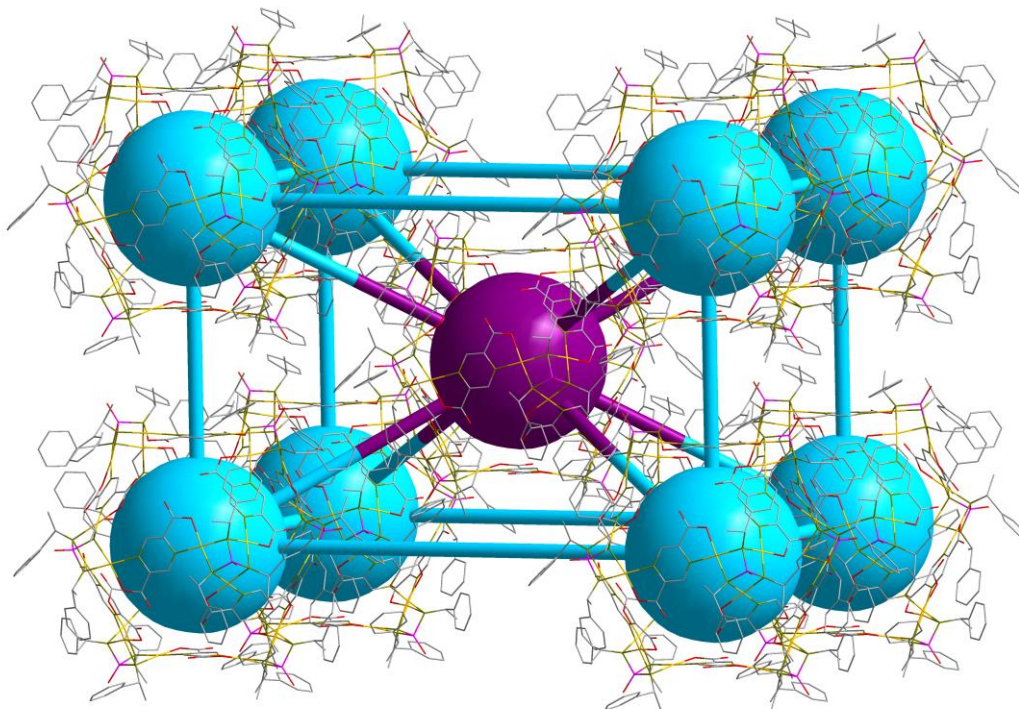


**Figure A5.16.** Packing Structure of **5.3** in  $I422$  showing the Intrinsic cavities. The spheres depict the intrinsic voids of the individual cages: the blue spheres depict the intrinsic voids of the cages that lie in the corner of the unit cell while the violet sphere depicts the intrinsic void of the cage in the center of the unit cell.

### Chiral Recognition Studies with 5.1-R

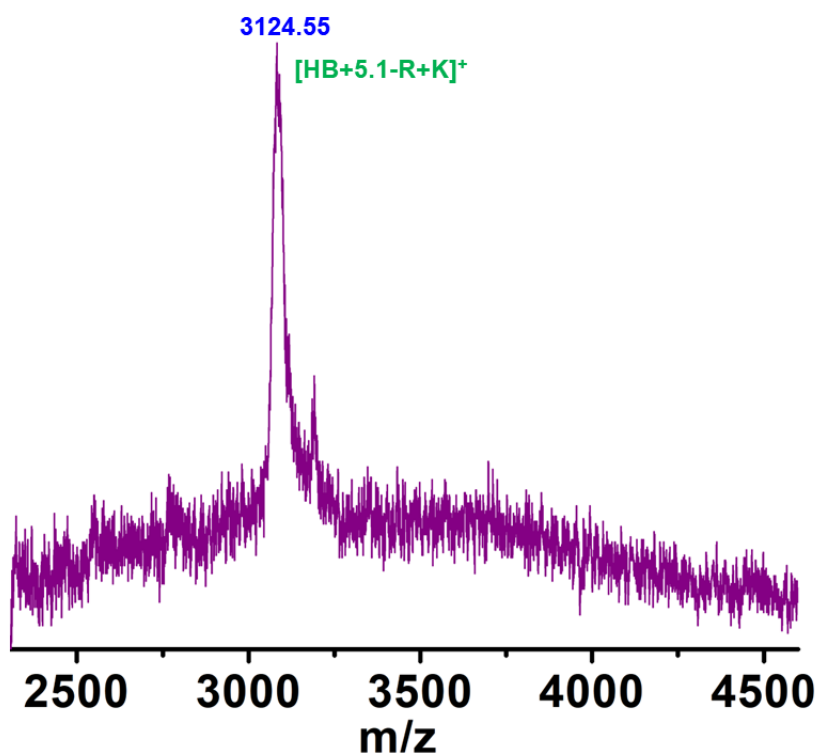


Figure A5.17. MALDI-TOF mass spectrum (linear mode) of  $\pm$ HB + 5.1-R.

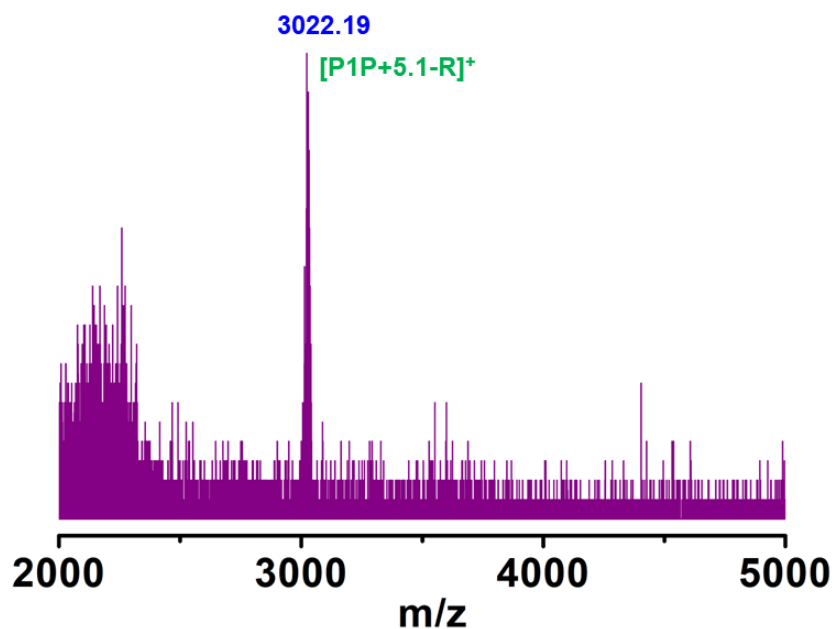


Figure A5.18. MALDI-TOF mass spectrum (linear mode) of  $\pm$ PIP + 5.1-R.

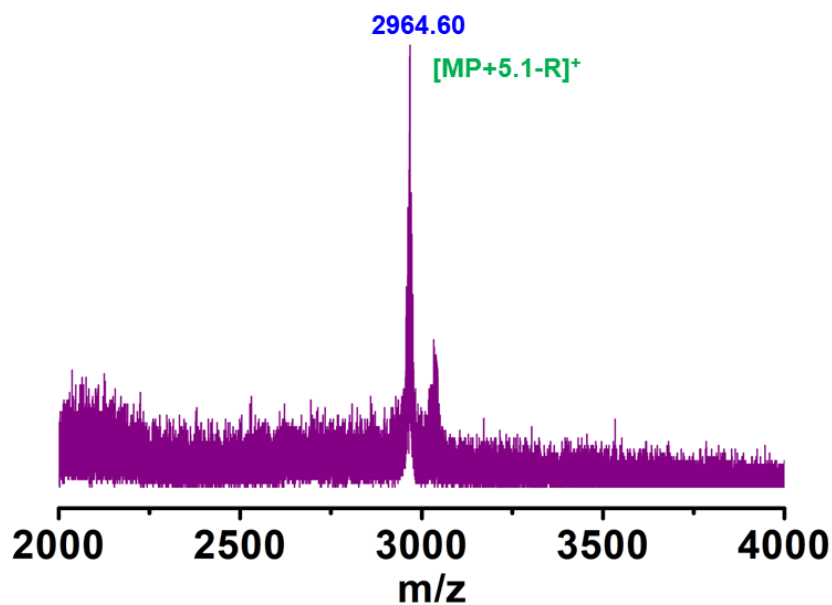


Figure A5.19. MALDI-TOF mass spectrum of  $\pm MP + 5.1-R$ .

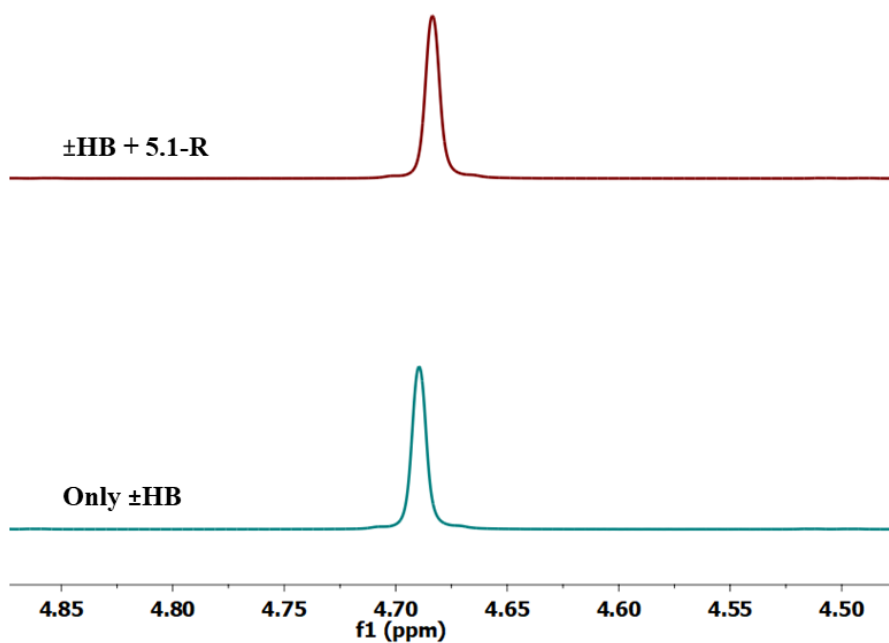
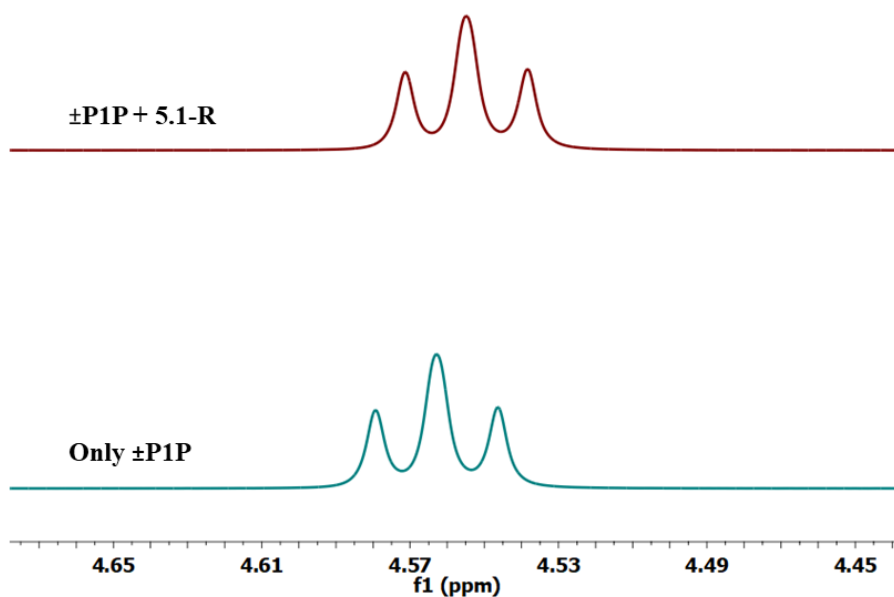
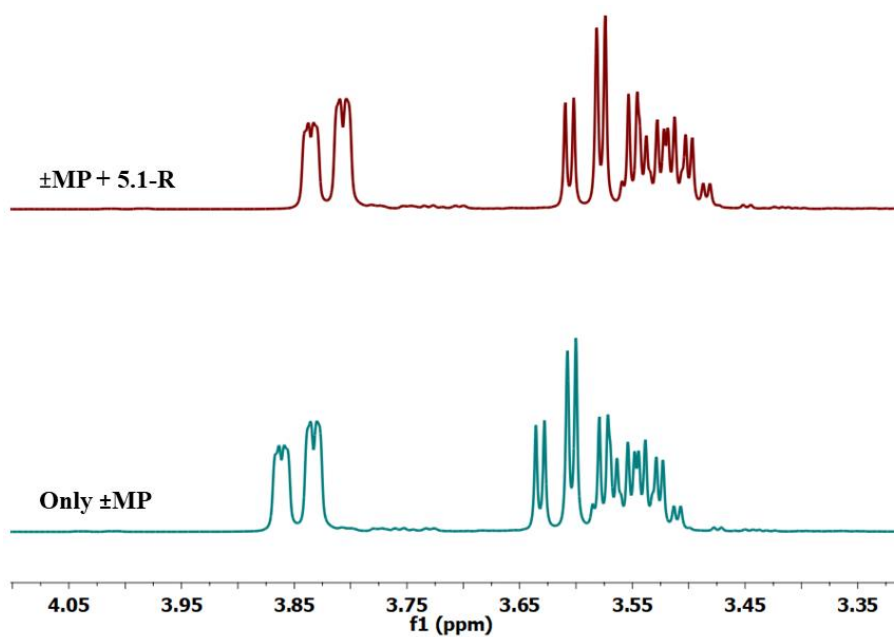


Figure A5.20. Partial  $^1H$ -NMR ( $CDCl_3$ , 298K) spectrum showing upfield shift of **HB** proton peaks in  $\pm HB + 5.1-R$  as compared to free **HB**.

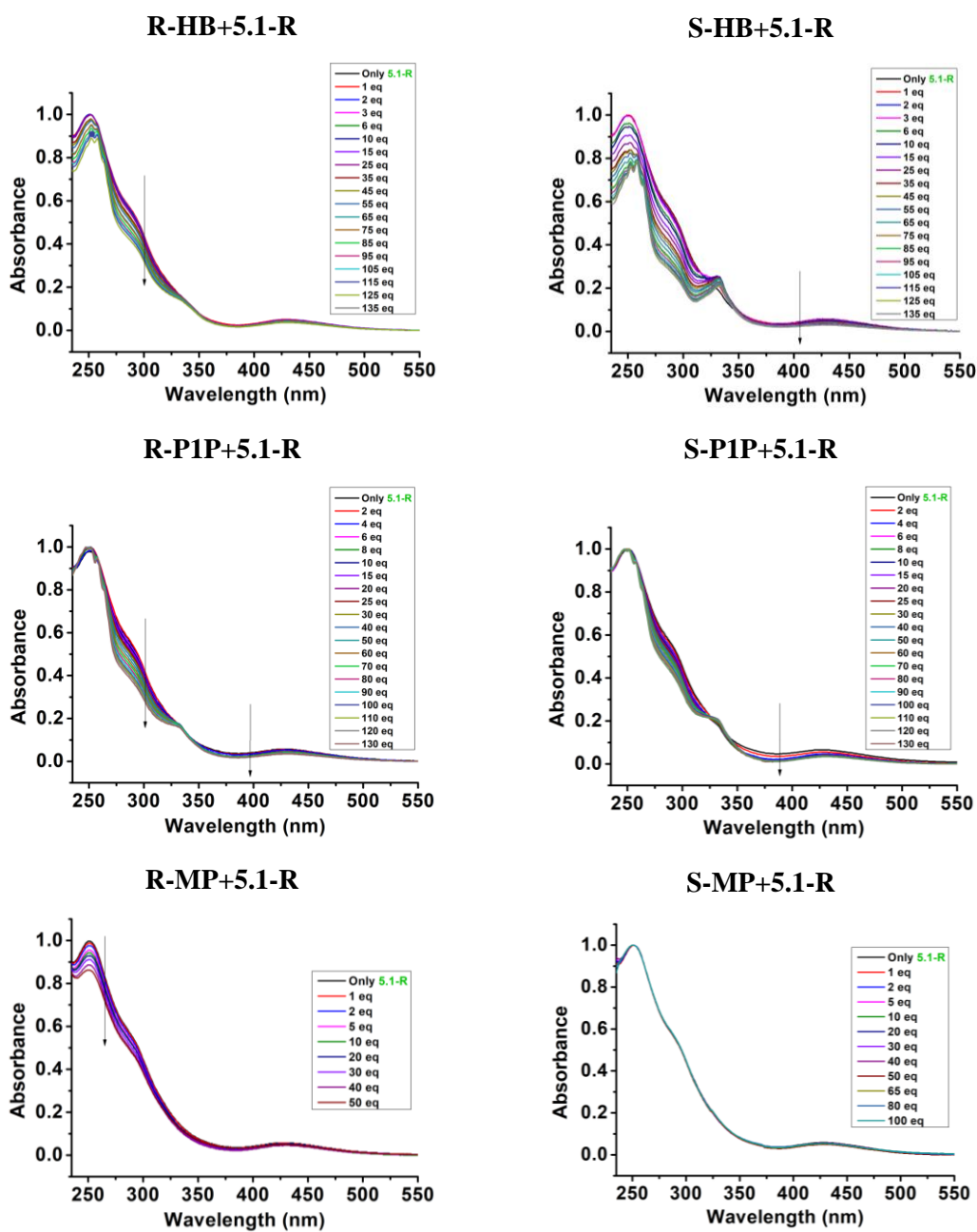


**Figure A5.21.** Partial <sup>1</sup>H-NMR (CDCl<sub>3</sub>, 298K) spectrum showing upfield shift of **P1P** proton peaks in **±P1P + 5.1-R** as compared to free **P1P**.



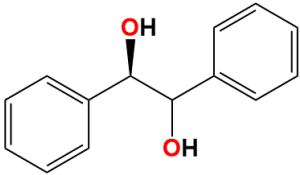
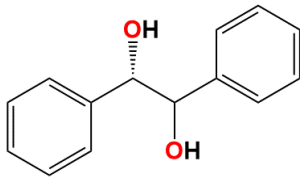
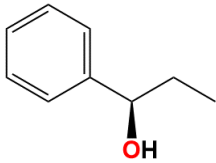
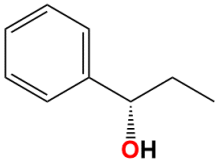
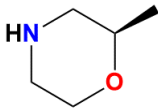
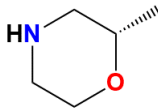
**Figure A5.22.** Partial <sup>1</sup>H-NMR (CDCl<sub>3</sub>, 298K) spectrum showing upfield shift of **MP** proton peaks in **±MP + 5.1-R** as compared to free **MP**.

## UV-Visible Titration Plots of the Host-Guest Complexes



**Figure 5.23.** UV-VIS titration plots for the host-guest complex of respective guests upon addition to the **5.1-R**.

**Table A5.4. Binding constants  $K_a$  ( $M^{-1}$ ) and binding selectivity ( $\xi$ ) as derived from the UV-Visible titration experiments**

Guest + 5.1-R	Binding Constant, $K_a$ ( $M^{-1}$ )	$\xi$
<p><b><u>R-HB</u></b></p> 	$1.5 \times 10^3$ (7)	7.3 (S)
<p><b><u>S-HB</u></b></p> 	$1.1 \times 10^4$ (11)	
<p><b><u>R-P1P</u></b></p> 	$4.3 \times 10^4$ (9)	16.7 (S)
<p><b><u>S-P1P</u></b></p> 	$7.2 \times 10^5$ (4)	
<p><b><u>R-MP</u></b></p> 	$1.2 \times 10^3$ (14)	1.4 (R)
<p><b><u>S-MP</u></b></p> 	$8.5 \times 10^2$ (11)	

\*\*\*\*\*